Solvation and Ion Specificity in Complex Media

Mario Spadina

THÈSE POUR OBTENIR LE GRADE DE DOCTEUR DE L'UNIVERSITÉ DE MONTPELLIER

en Chimie

École doctorale Sciences Chimiques Balard ED 459

Institut de Chimie Séparative de Marcoule - ICSM
Laboratoire Modélisation Mésoscopique & Chimie Théorique - LMCT

Solvation and Ion Specificity in Complex Media

Présentée par Mario Špadina
Le 24/06/2019

Sous la direction de Jean-François Dufrêche et Klemen Bohinc

Devant le jury composé de

Jean-François JOANNY, Professeur, Collège de France	Président du jury
Jean-François DUFRÊCHE, Professeur, Université Montpellier	Directeur
Klemen BOHINC, Professeur, University of Ljubljana (Slovénie)	Co-Directeur
Virginie MARRY, Professeur, Sorbonne Université	Rapporteur
Christophe LABBEZ, Chargé de Recherche, CNRS/Université de Bourgogne	Rapporteur
Gilles BORDIER, Docteur, CEA	Examinateur
Martin IN, Directeur de Recherche, CNRS/Université Montpellier	Examinateur
Daniel HARRIES, Professeur, The Hebrew University of Jerusalem (Israël)	Examinateur
Thomas ZEMB, Professeur, CEA/INSTN président du jury	Invité

UNIVERSITÉ DE MONTPELLIER

Acknowledgements / Zahvale

Ah, where to begin? Indeed, I found myself asking the very same question did as the famous character Bilbo Baggins from even more famous book by J.R.R. Tolkein. Well, I suppose it is best to start from the beginning.

I would like to thank all members of the jury, to Madame Virginie Marry, and Messieur Christophe Labbez for accepting to serve as *rapporteurs* of my thesis manuscript, and to Messieurs Martin In, Daniel Harries, Gilles Bordier, and Jean-François Joanny who showed the interest in my work and accepted to serve as judges.

During the past three years, apart from being in Ljubljana as a part of the project, the majority of time I spent at Institute for Separation Chemistry (ICSM) in Marcoule, where I was part of the Mesoscopic Modelling and Theoretical Chemistry (LMCT) laboratory. The scientific part of my PhD thesis depended on its everyday life counterpart. The staff of ICSM, as well as the colleagues students made me feel welcome and help me to overcome difficulties of everyday life. To all of them, I want to express my gratitude. To name the few is to neglect the most, which at this point strictly is forbidden. Thank you ICSM.

A part of the work done during my thesis came in a form of the collaboration between multiple groups scattered across the Europe. I would like to acknowledge Dr. Drazić on the experimental HR-TEM measurements done at National Institute for Chemistry in Ljubljana, Slovenia. Furthermore, I would like to thank Prof. Kovačević from the Science and Mathematical Faculty in Zagreb for measurements of decontamination process. Acknowledgments to Borna Kovačević for his contribution on the structural characterization of nanotubes samples. I would like to thank Simon Gourdin-Bertin on the help in modellization of the charging process of nanomaterials in aqueous solutions. Last but far from least, I would like to express my gratitude to Atiđa Selmani, my first Mentor dating all the way back to student days. Apart from the fact that she has played one of the crucial roles in scientific part presented in this thesis, she is also indirectly responsible for my arrival at ICSM in first place. It was she who forced me, and eventually introduced me to Prof. Bohinc which in the end led to all of this. Thank you Atiđa, and I hope we continue like this for time to come.

I would like to thank Magali Duvail, Olivier Diat, Damien Bourgeois, Jérémy Causse, Bertrand Siboulet, and Stéphane Pellet-Rostaing on useful scientific discussions. Many thanks to the famous Prof. Epameinondas Leontidis on the scientific discussions, but also on the indirect strong motivation. To Prof. Leontidis: the *Chemistry* in colloidal community is not dead, and I hope we have proved it within this thesis work. I am very grateful to Prof. Stjepan

Marčelja, for all the discussions, advises, and kind words that helped me to reach the primal goal of PhD - to propose a novelty in science.

I would especially like to thank Prof. Thomas Zemb. Since he did not only participate in scientific discussions with me, advised me, guided me to some extent, and worked together on within ERC project, he also directly helped me to learn how to put the work in the perspective. It is only natural to exclude Prof. Zemb from mutual-acknowledgments paragraph and dedicate to him this new one entirely. Thank you Prof. Zemb, and I hope we will continue with the job.

One may think that three years is quite short period to meet a lot of good people, but I claim otherwise, which is in my case an empirically obtained fact. There is a 'bunch' of people I would like to mention and thank so I will start with this extensive (but not nearly exhaustive!) list. I would like to thank the members of LMCT group (and the office): Lolita, Mathilde, Asmae, Marin, Tristan, Amaury, Simon, Pavel, Michael, Magali, and Bertrand for positive and relaxing atmosphere in the laboratory (or the office, whatever one prefers). Since a positive atmosphere was not only the property of LMCT laboratory, I am obliged and honored to give my gratitude to Ran, Markus, Simon, Michael, Maximilian, Aureglio, Simone, Zijun, Zije, Max, David, Remy, Temim, and many more. Many thank also to people I met apart from work in both France and Slovenia. Thank you: Karim, Hassan, Reza, Miroslav, Slavko, Dragana, Dušan, Marijan, guys from basketball teams, and many other.

I would like to thank Bertrand Siboulet, the person who was responsible for me within CEA. I have especially enjoyed our lunches together (I have enjoyed less actually walking to the lunch), and discussions of all sorts we had there. The conversation is always easy, when the belly is full. Bertrand I would like you to memorize this phrase: *This is the last time I ate like this*!

To my Co-supervisor and the friend, Prof. Klemen Bohinc I would like to express my highest gratitude. From the student days, up to know, he has always been kind and encouraging. He helped when was needed, and inspired when was needed. An example of his personality is his profound eye for details which made my writing of pretty much everything troublesome. Because of this, I truly learned. Hvala Klemen.

How to properly thank my Thesis Supervisor? Well, for start I would like to thank Prof. Jean-François Dufrêche. But this does not really do the job. Therefore, I will go into detail. Jean-François thank you for all the patience that you had with me, thank you all the dozens of hours that you spent teaching me (from science to whatever) in your office, thank you help with everyday stuff like giving me your charger for computer when I forget my own (a recently made mistake), thank you allowing me my days of 'reduced' productivity, thank you for constantly

pushing me to expand the view of science, and finally thank you for being kind and making me feel welcome and important, at all times.

Finally, I would like to thank my girlfriend Ana, to my friends back home who were involved in this work, and to my family. The nature of it demands that I do this properly on my native language. Barbara, Atiđa, Stipe, i Tomislave želim Vam se zahvaliti od srca što ste sudjelovali samnom u svemu ovome. Pogurali ste me kad je trebalo, i napumpali mi ego kada je trebalo. Zmija je zmija, a ja sam na kraju napravio skroz ok. Vaš Špaco.

Mama, Tata, Luka, Mare i ostatak šire obitelji... Želim Vam se zahvaliti što ste me stavili na ovaj put, koji traje od 2010. godine kada ste prvi put iskrcali more stvari u Palmotićevoj ulici. I evo, skoro desetljeće kasnije, dolazi kraj mom školovanju. Stoga i priliči da, baš kako sam završio i zahvale Diplomskog rada, zavrsim i disertaciju sada. Hvala Vam što ste mi uvijek bili vjetar u leđa, *forza* kada je trebalo.

Ana... Nakon svega, teško mi je i sažeti u par rečenica sve ono što ti želim reci. Hvala ti za ove godine. Hvala ti za svaki put kada si me morala iznova ohrabrivati da bih izgurao kroz sljedeći dan. Hvala ti i što si me s vremena na vrijeme natjerala da uzmem odmor i mislim na sebe. I ova disertacija je dio tvog projekta i nadam se da si ponosna na mene, kao što sam ja ponosan na tebe. Hvala ti Ana.

Aear cen ven a mar.

Elrond of Rivindel

Abstract - English Version

The object of this thesis was to create models for two applications which readily appear in separation chemistry, namely the solid-liquid and the liquid-liquid extractions. The benefit of modelling in both cases is twofold. Studying the fundamental properties of ions and their solvation properties in the complex media, and simplifying the expression for important effects, enables us to construct the framework which can be used by both chemists in the laboratory, as well as the chemical engineers in the process design. For two applications we adapted two different systems, both of which can be considered as complex. The model system to study the solid-liquid separation was the suspension of TiO_2 nanotubes dispersed in the aqueous solution. This system was studied by the means of Classical Density Functional Theory coupled with the charge regulation method, within the Grand-canonical ensemble. Indeed, the method proved to be successful in establishing the full description of the charge properties of TiO_2 nanotubes. In this case, we were interested in obtaining the description of ion inside the charged nanotubes under influence by the electric field (exhibited by nanotubes). Calculations predicted effects such as the difference in surface charge between the outer and the inner surface, or the violation of electroneutrality inside the nanotubes. It was demonstrated that the model was in the agreement with the experimental data. Moreover, the method can be directly used to predict titration for various techniques. A simple generalization of the proposed approach can be used to study the actual adsorption efficiency of the solid-liquid separation process. The model system to study the liquid-liquid extraction process included three distinct parts. The three parts were devoted to the cases on non-ionic, acidic ion exchangers, and finally the synergistic mixtures of extractants. Simple bulk statistical thermodynamics model, in which we incorporated some of the well-established concepts in colloidal chemistry provided a soft-matter approach for the calculation of actual engineering-scale processes. Were have expanded a classical simple equilibria approach to broader, more intuitive polydisperse aggregates formation that underlines the liquid-liquid extraction. The key finding can be presented as a current opinion or newly-proposed paradigm: at equilibrium, many aggregates completely different in composition but similar in free energy coexist. With obtained polydispersity, we were equipped with tool to study a more 'global' behavior of liquid-liquid extraction. This urged us to pass our considerations of historical extraction isotherms to extraction 'maps'. Great care was devoted to the study of synergy since it is a 60-year old ongoing question in the separation industrial and science community. To our best knowledge, the first quantitative rationalization total synergistic extraction was proposed within this thesis. Underlying effects of enthalpy

and entropy control on the organic phase structuring were decoupled and studied in detail. Hopefully, this thesis demonstrated the importance of mesoscopic modelling to assist both chemists and chemical engineers in practical examples.

Résumé – Version en français

Le but de cette thèse était de créer des modèles pour deux applications qui apparaissent couramment en chimie séparative, à savoir la séparation solide-liquide et la séparation liquide-liquide. L'avantage de la modélisation est manifeste dans les deux cas. L'étude fondamentale des propriétés des ions et de leur solvatation dans les milieux complexes, en tenant compte de façon simplifié des différents effets mis en jeu, nous a permis de construire un cadre qui utile aussi bien aux chimistes en laboratoire qu'aux ingénieurs lors de la conception des procédés. Nous avons adapté cette stratégie sur deux systèmes différents, qui peuvent tous deux être considérés comme complexes. Le premier système modèle pour étudier la séparation solide-liquide était des nanotubes de TiO_2 dispersés dans une solution aqueuse. Ce système a été étudié au moyen de la Théorie de la Fonctionnelle de la Densité Classique couplée à une méthode de régulation de charge, au sein de l'ensemble Grand-Canonique. La méthode s'est avérée efficace pour établir la description complète des propriétés de charge des nanotubes de TiO_2. Dans ce cas, nous nous sommes intéressés à obtenir la description de l'ion à l'intérieur des nanotubes chargés sous l'influence du champ électrique (créé par les nanotubes). Les calculs ont prédit des effets tels que la différence de charge de surface entre la surface externe et la surface interne, ou la violation de l'électroneutralité à l'intérieur des nanotubes. Il a été démontré que le modèle était en accord avec les données expérimentales. De plus, la méthode peut être utilisée directement pour prédire diverses techniques de titrage. Une simple généralisation de l'approche proposée permettra d'étudier l'efficacité d'adsorption réelle du procédé de séparation solide-liquide. Le second système modèle concerne l'étude du procédé d'extraction liquide-liquide et il comprend trois parties distinctes. Les trois parties ont été consacrées aux cas des extractants non ioniques, puis acides (échangeurs d'ions), et enfin aux mélanges synergiques d'extractants. Un modèle simple de thermodynamique statistique, dans lequel nous avons incorporé certains des concepts bien établis en chimie colloïdale, a fourni une approche de type matière molle pour calculer le processus à l'échelle de l'ingénieur. Nous avons développé une approche classique d'équilibres simples pour une compréhension plus large et plus intuitive de la formation des agrégats polydisperses dans l'extraction liquide-liquide. La principale conclusion présentée est que l'on doit proposer un nouveau paradigme pour la chimie : à l'équilibre, de nombreux agrégats de composition très différente mais similaires en énergie libre, coexistent. Avec la polydispersité obtenue, nous avons ainsi proposé un outil pour étudier un comportement plus "global" de l'extraction liquide-liquide. Cela nous a poussés à passer des considérations classiques d'isothermes d'extraction à celles plus précises des " cartes " d'extraction. Un grand

soin a été apporté à l'étude de la synergie puisqu'il s'agit d'une important question depuis 60 ans dans la communauté scientifique et industrielle de la séparation. A notre connaissance, la première rationalisation quantitative de la synergie d'extraction a été proposée dans le cadre de cette thèse. Les effets sous-jacents des contrôles enthalpique et entropique sur la structuration des phases organiques ont été découplés et étudiés en détail. Nous espérons que cette thèse a démontré l'importance de la modélisation mésoscopique sur des exemples pratiques utilisés à la fois par les chimistes et les ingénieurs.

Contents

List of Figures

Chapter 1

General Introduction

Sustainability of chemical industry is important, and ongoing issue for the science community [1]. While chemical industry is the link between industrial growth and fundamental research, its sustainability has different manifestations which involve entire branches of chemistry. Cur-

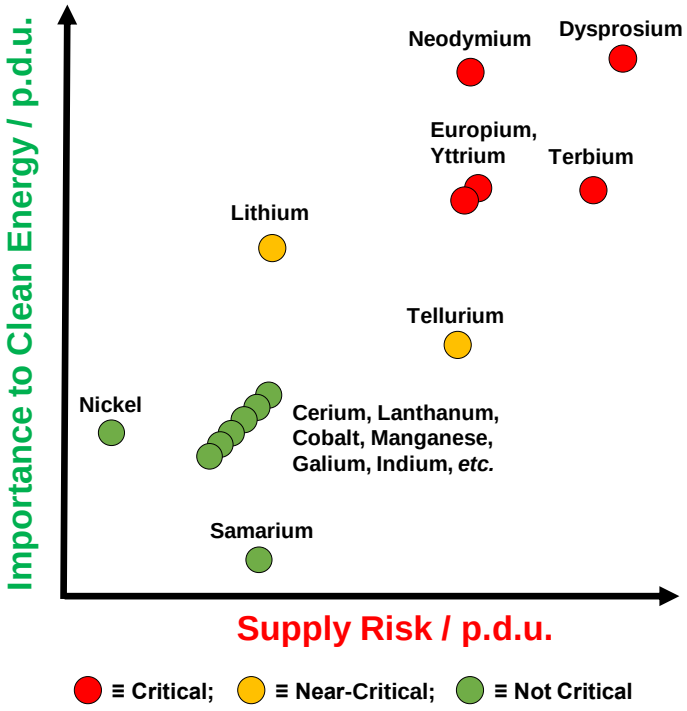

Figure 1.1 – Criticality graph illustrating the importance of some REEs relative to other common metals currently in intensive usage worldwide. Figure is replotted and adjusted from reference [2].

rently, one of the key manifestation is the selective chemical separation of rare earth metals (REEs) from aqueous solutions, especially in dilute cases [3]. This strongly emerging field of hydrometallurgy is the consequence of the fact that REEs have a major role in sustaining

the green, low carbon economy. Their numerous applications involve production of permanent magnets, lamp phosphors, batteries for hybrid cars, *etc* [4, 5, 6]. Application of REEs, in the opposite way, means also a potential for recycling from production scraps and end-of-life products [7, 5, 2, 6]. It must be emphasized that only small part of annually created waste is recycled in order to recover REEs [6]. Huge demand, constrained market, and lack of recycling place some of REEs metals into the critical group of elements in terms of importance to the clean energy and the supply risk. This is demonstrated in Figure 1.1. Therefore, the improvements of separation methods are in the core of sustainability of chemical industry. Indeed, the necessity was also recognized by European Union in the form of grant: European Research Council (ERC) REE-CYCLE (2013-2018)[1].

Out of numerous already established methods, the solid-liquid (adsorption) and liquid-liquid extractions (solvent extraction), along with flotation are still considered as a reference techniques. Although mature technologies in terms of predicted usage and improvements already applied in practical cases, their simplicity and scale-up potential urges the need for further development [8]. Within the scope of this thesis, cases of solid-liquid and liquid-liquid extraction methods will be addressed.

Indeed, it can be recognized that ions and their solvation properties are reflected on the overall process efficiency. Now the subject of this thesis comes into play, since we will model the properties of ions in these complex media that will unable us, with respect to used theory, to rationalize the effects responsible for the transfer of ions between domains. Two examples will be made: 1) the transfer of ion from bulk aqueous solution to the organic phase in a form of weak aggregate, 2) transfer of ion from bulk aqueous solution to the interior of solid adsorbent cavity under influence of the electric field. Knowledge concerning the behavior of ions and their solvation is thus in the core of sustainability of chemical industry.

1.1 Liquid-Liquid Extraction of Metals from Aqueous Solution

In metal ions separation, liquid-liquid (or solvent) extraction involves two non-miscible phases in contact, namely the aqueous phase with dissolved salts and the organic (solvent) phase with dissolved extractant molecules [9, 10]. The principle is schematically presented in Figure 1.2, as a simple representation of actual process in the mixer-settler device. The aqueous

[1]ERC REE-CYCLE (2013-2018) grant funded this thesis.

solution containing target salts is sometimes referred as 'feed', and it is pumped in the mixing chamber along with the fresh organic solvent with dissolved extractant. After certain mixing time, heterogeneous mixture is left separate in settling chamber. After settling, aqueous phase, now called the raffinate, and the loaded organic phase are separated. Organic phase is now saturated (loaded) with target salts and is transferred to striping chamber. Depending on the nature target metal, different classes of extractants[2] can be utilized, such as: chelating, solvating, or ion exchangers [4, 11].

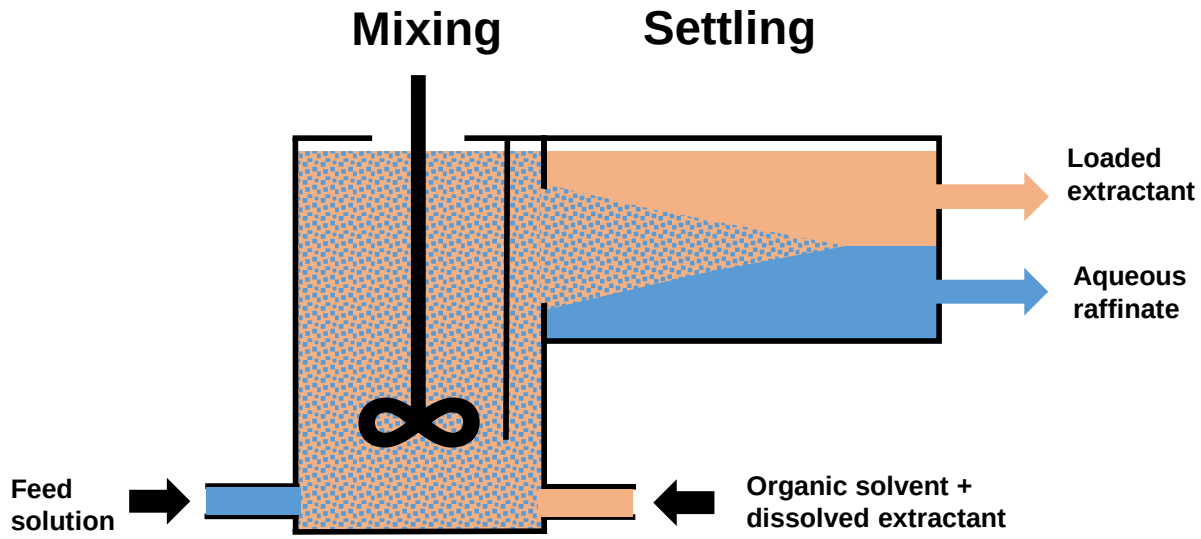

Figure 1.2 – Schematic representation of a mixer-settler for continuous operation of solvent extraction.

Beside in hydrometallurgy, liquid-liquid extraction is also a reference technique in nuclear industry, where it is utilized to separate minor actinides from REEs in used nuclear fuels [12, 13, 14, 15, 16]. Practical scheme involves the PUREX (Plutonium Uranium Extraction) process, followed by the DIAMEX-SANEX (Diamide Extraction – Selective Actinide Extraction) process, just to mention a few [17, 18, 19].

Typical extractants related to hydrometallurgy and nuclear industry of spent fuel reprocessing are *N,N´*-dimethyl-*N,N´*-dioctyl-2-(2-hexyloxyethyl)-malonamide (DMDOHEMA), and (2-ethyl-hexyl) phosphoric acid (HDEHP) [17, 20, 21, 5, 7, 16]. DMDOHEMA corresponds to the class of solvating non-ionic extractants, whereas HDEHP is a part of a class of acidic ion-

[2]Note that distinction between classes is somewhat unclear and that is why we will point out only few of them.

exchange extractants, since they dissociate upon binding of the target cation[3]. The mixture of DMDOHEMA and HDEHP is particularly interesting since at certain conditions it exhibits synergistic behavior.

We have stated that sustainability requires improvements of current liquid-liquid extraction processes. In fact, improvements are possible to achieve by utilizing the phenomenon of synergy in case of mixtures of extractants which exhibit non-linear effects. The existence of strong non-linearities in solvent extraction is actually known since more than fifty years. Up to now, the diversity of behavior has never been predicted, and separation industry relies on robust fitting procedure which generated a large number of adjusted constants [9].

Within the ERC REE-CYCLE project, green chemistry aspects in the solvent extraction are considered as lowering the amount of effluents used by almost one order of magnitude. A way to overcome this consists in combining the supramolecular complexation and the solvent reorganization, as in "ienaics" approach which is described in the reference [22].

1.2 Current Modelling State-of-the-Art: Solvent Extraction

The efficiency of the liquid-liquid extraction process is influenced by many different parameters. For example, it was shown that the type of extracted solutes, the type of extractant head group, the branching and the chain length of extractants used, the type of solvent as well as the mole ratio of the two extractants (in the case of the synergistic mixtures) have a strong impact on the efficiency [9, 23, 24, 25]. This high complexity governs the cost of employing newly developed types of extractant molecules. In addition, it makes the optimization of system conditions robust. Therefore, there is an urgent need to develop a predictive theory to assist the chemical engineering to reduce experimental plans. Here we present a short overview of the currently employed theories in liquid-liquid extraction.

1.2.1 Quantum Chemistry Calculations

The advantage of quantum chemistry calculations in liquid-liquid extraction modelling is the accurate description of the first coordination sphere between target cation and the particular extractant head group in form of optimized geometries [27, 28]. This is particularly useful in

[3]HDEHP extractant is often referred under other names such as D2EHPA, DEHPA or P204, depending on the field of the application.

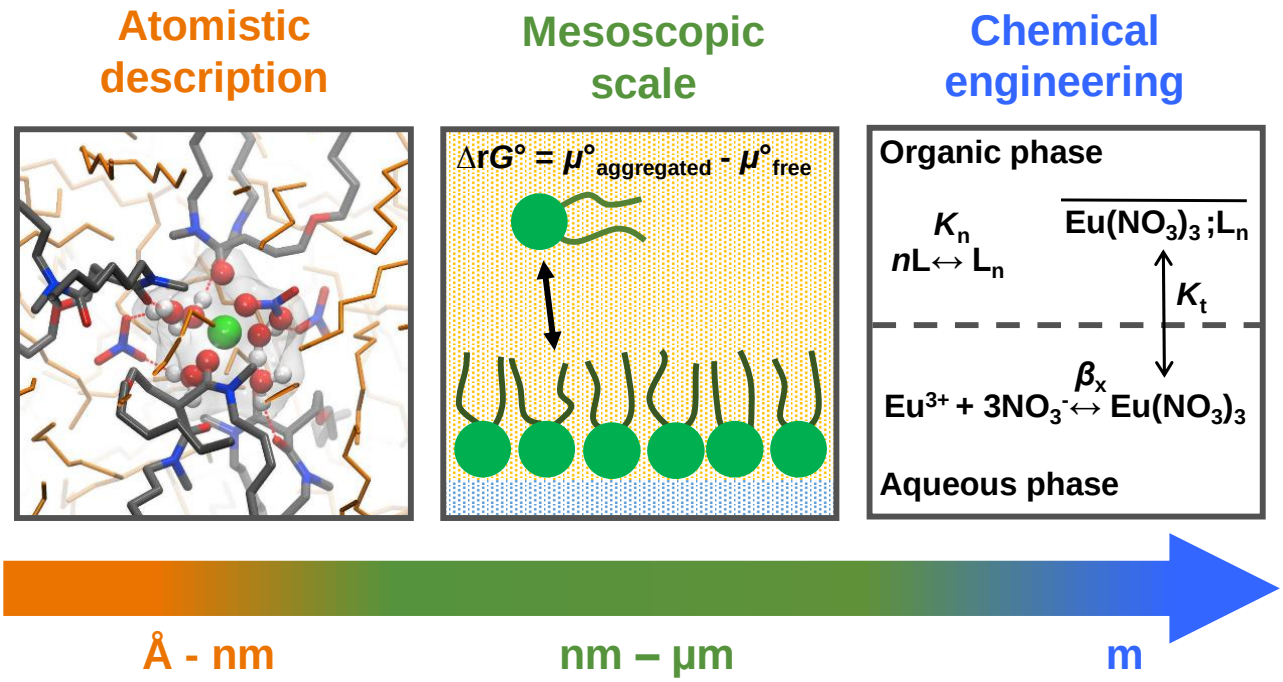

Figure 1.3 – Schematic representation of levels of theory that are currently employed in solvent extraction. Figure on the left represents atomistic studies of phenomenon underlying the solvent extraction. Snapshot obtained from MD simulations has been reprinted by the permission of authors and it corresponds to reference [26]. Sketch in the middle represents the mesoscopic models *e.g.* pseudo-phase model. Figure to the right is simplified representation of multiple equilibria approach utilized by chemical engineers. It corresponds to simple extraction of europium nitrate.

order to establish the trend in selectivity of series of metals *e.g.* lanthanide series [27, 29]. Density Functional Theory (DFT) calculations show that there is maximum occupancy of the first coordination sphere [19, 30, 31, 32, 33]. In the case of DMDOHEMA extractant, characterized by robust malonamide head group, due to the steric constraints complexed lanthanide can accommodate two DMDOHEMA molecules in its first coordination sphere. To complete the octahedron (or similar geometry) coextracted nitrate anions and water molecules fill remaining sites. This was hinted also by experimental Extended X-Ray Absorption Fine Structure (EXAFS) study [34]. Diglycolamide types of extractants show simmilar behavior as malonamides, and octahedral coordination structre is usually preferred [35]. In the case of HDEHP, similar composition of the first coordination sphere was obtained [36, 29]. Seven-coordinate lanthanide structure was also predicted, but energy difference compared to six-coordinate structure is not large. This is a consequence of smaller HDEHP phosphate head group. Furthermore, the conservation of six-to-seven coordination number was also reported when dealing with synergistic

mixtures of extractants [37]. We have stressed this since the usual coordination number of lanthanides in the bulk aqueous solution is more than that [38, 39, 40]. This fundamental difference suggests that there is an excess enthalpy contribution associated with complexing the cation with extractant head groups compared to the case in bulk aqueous solution. An attempt is often made to establish the relation between overall extraction efficiency and the free energy of the complex [11, 41]. It must be noted that these considerations can only provide the trend, but fail completely in quantitative assessment. For example, unrealistic 1:1 cation/extractant couples are reported as a reference chemical reaction describing the overall extraction efficiency[4]. We will address this important question at the end of every chapter devoted to liquid-liquid extraction.

To sum up: Quantum chemistry calculations have shown that complexation is important. Moreover, it is the leading force that governs the transfer of the target ion between aqueous and organic phases. Still, calculations are limited to small number of atoms in the system. For example, even the extractant chains are not included, and truncated analogues are used for calculations. Therefore, to study the influence of solvent effect we need another description at higher length scales.

1.2.2 Molecular Dynamics Simulations

Molecular Dynamics (MD) simulations have proven extremely useful when studying liquid-liquid extraction systems. Simulations have shown that extractant molecules in the organic phase self-assemble into structures that resemble reverse micelles [42, 43, 44]. In the case of DMDOHEMA the core of this weak aggregate retains character of general complex, as predicted by DFT calculations, but also resembles a 'small pool' filled with ions and water molecules [26]. This finding has been schematically demonstrated in Figure 1.3. Furthermore, some of water molecules present in the core of the aggregate are labile and constitute a second coordination sphere along with the residue of DMDOHEMA which are non involved in the direct complexation with the central cation. The minimum number of self-assembled extractants also called aggregation number is around four [42, 26, 45]. Also, it was demonstrated that coextracted acid can benefit the stability of DMDOHEMA aggregate [46]. Studies concerning HDEHP showed that minimum aggregation number is six [44]. It must be noted that these findings are consistent with experiment data. In the case of very 'bulky' extractants, such as

[4]Every colloidal aspect is therefore neglected. Luckily, we know that this reaction is probably only possible for highly concentrated systems, where additional cation/extractant couple is incorporated into higher-order pseudo-domain *e.g.* lamellar structure.

N,N,N,N-tetra(n-octyl)diglycolamide the aggregation numbers can be as low as three (3). It must be noted that accompanying counterions and water molecules are needed to stabilize the cation in the apolar environment[35].

MD simulations are convenient and very accurate when studying the solvent and extractant effects. Calculations in explicit n-heptane penetrating solvent have shown that DMDOHEMA extractant mean chain length in aggregated form is constant on average [47]. This is an important finding, which we will exploit when constructing our model for the micelle aggregation. Solvent effects on the shape of the aggregate can be further studied simply by running calculations for different solvents (if the force fields are known)[35]. Furthermore, HDEHP dimerization can be estimated [48]. Moreover, for larger calculation boxes used, it is possible also to obtain a proper structure (*e.g.* transition from small spherical to worm like or cylindrical aggregates) and the hierarchical organization of the solvent phase (*e.g.* superclusters of small aggregates, as recently reported) [49, 44, 33].

Still, MD simulations cannot yet be used to calculate extraction isotherms, especially the overall phase diagram.

1.2.3 Mesoscopic and Thermodynamic Models

Mesoscopic models operate on the verge of macroscopic world. Their advantage is the fact that they retain some degree of microscopic picture underlying the phenomenon of interest, but are manageable to be used for prediction of a real experiment[5].

Pseudo-phase model

Probably the most widely used model is so-called 'pseudo-phase model'. It was first proposed by Charles Tanford and became the cornerstone in colloidal self-assembly of surfactants [50]. The model assumes that individual aggregates are distinct phases. Aggregated extractants are in equilibrium with free extractants dispersed in the solvent, as demonstrated schematically in Figure 1.3. The aggregated extractant exists at and above the Critical Aggregate Concentration (CAC). It can be written as

$$\mu_{\mathrm{A}}^{0} = \mu_{\mathrm{L}}^{0} + kT \ln \mathrm{CAC} \tag{1.1}$$

μ_{L}^{0} is the standard chemical potential of the free ligands, and μ_{A}^{0} is the chemical potential of L in the pseudo-phase. The model was originally introduced for cases of direct micelles in aqueous solution. Within the free energy approach, it was possible to include additional effects and

[5] Along with all model approximations and adjusted parameters.

generalize pseudo-phase model for various morphologies [51, 52]. In the case of liquid-liquid extraction and reverse aggregates in the organic solvent, the model was used to establish the relation between electrolyte activity and the experimental CAC [53]. Another example was the relation between head groups interactions in extractant film composed of dissociated and undissociated HDEHP molecules [54]. The strength of this model is the fact that in the free energy approach, the calculation of standard chemical potential of the particular aggregate can be made if the relation of some energetic contribution as a function of the composition is known *e.g.* the energy of curved extractant interface, or the lateral head groups interactions [55, 56]. Still, pseudo-phase model was not yet ripe to predict overall extraction efficiency since it assumes already created aggregate with certain aggregation number. Moreover, it gives a sharp transition in aggregation after CAC, which states that addition of extractant in the system must be incorporated in aggregates.

Langmuir-like model

At the very borderline with models based on chemical equilibria are Langmuir-like adsorption models [57, 58]. The relation is given as

$$K = V_{\mathrm{a}} e^{-\beta \Delta G^0} \tag{1.2}$$

for which V_{a} is the accessible volume of one site and $\beta = 1/k_{\mathrm{B}}T$. Thus the constant K has the dimension of volume. ΔG^0 can be defined as the change of Gibbs free energy from the aqueous phase to the organic phase. In a way, Langmuir-like models are offspring of pseudophase model since it is needed to consider the aggregates in the organic phase as either: 1) single accessible sites to accommodate (or bind) the cation, or 2) or set of sites in extractant film. In either case it is assumed that aggregates already exist. The difference between aggregated and free extractant would correspond to mostly enthalpic contribution due to the binding of cation to accessible site [59]. To conclude, Langmuir-like models can be used to predict the extractant saturation. At high concentrations of target electrolyte in the aqueous solution, extraction isotherms show asymptotic behavior towards saturation limit.

1.2.4 Modelling Based on Establishing Possible Chemical Equilibria

So far, we have covered atomic description and mesoscopic-to-macroscopic models. Very important, and the only approach that can predict extraction process, is based on establishing every possible chemical equilibria [60]. Example of non-ionic extractants equilibria is usually

written[6] as

$$\mathrm{Eu^{3+}} + 3\mathrm{NO_3^-} + x\mathrm{H_2O} + y\overline{\mathrm{L}} \rightleftharpoons \overline{\mathrm{Eu\,(NO_3)_3\,L}_y\,\mathrm{(H_2O)}_x} \tag{1.3}$$

where L denotes ligand (or the extractant) and y is the particular aggregation number, and $\overline{\mathrm{Eu\,(NO_3)_3\,L}_y\,\mathrm{(H_2O)}_x}$ denotes the aggregate of the particular composition. Eq. 1.3 can be written in terms of equilibrium constant K° as

$$K^\circ = \frac{\overline{[\mathrm{Eu\,(NO_3)_3\,L_4\,(H_2O)}_x]}}{\left[\mathrm{La^{3+}}\right]\left[\mathrm{NO_3^-}\right]^3[\mathrm{H_2O}]^x\,[\overline{\mathrm{L}}]^y} \quad . \tag{1.4}$$

This chemical reaction is a part of larger system of possible equilibria that are simultaneously solved within the minimisation procedure (see Figure 1.3). The closure of the Mass Action Law (MAL) along with the method to minimize it then provides directly the extraction isotherms, as is readily done in chemical engineering [61]. The procedure works and provides a cornerstone for the actual plant process design *e.g.* implemented PAREX code for PUREX process [62]. In the case of HDEHP and its synergistic mixtures with additional extractant, modelling based on multiple equilibria provided acceptable description of solutes speciation in the organic phase. In the case of mixture of extractants, a synergistic peak in extraction isotherm was obtained [63, 64, 65].

Even though the method works, there are few issues with the approach. The minimization procedure requires large amount of experimental data and yields high number of adjusted constants [9, 10, 61, 66]. From Eq. 1.4 it can be seen that every composition yields additional constant. Sometimes, constants cannot be justified from molecular simulations. Moreover, the solvent interactions are idealized and the water coextraction effects are often neglected [31]. Synergistic mixtures are especially difficult to model. Strong non-linearities observed in Job's plots are often impossible to predict. To overcome the issue, the chemical engineering utilizes procedures for extra parametrization [9]. Therefore, there is a room to improve and to bridge the two approaches (molecular simulations and chemical engineering).

1.2.5 Our Approach

In order to propose a model that can be used by chemists as well as chemical engineers, we need to be able to calculate actual extraction isotherms. Therefore, multiple equilibria approach is useful. Still, we want to avoid fitting the large number of constants. Furthermore, we wish to account for a colloidal aspect of liquid-liquid extraction. Best tactics is to take befits of both extremes (atomistic descriptions and multiple equilibria modelling), while minimizing

[6] Example is given on the extraction of europium.

their drawbacks. From atomistic descriptions we can take structures and particular solvent effects, whereas from chemical equilibria approach we take the MAL closure and minimization procedures. The only way to do that is to take approach similar, but not equal, to pseudo-phase model, as was done by Leontidis and coworkers in a series of papers dealing with the extraction of amino acids [67, 68, 69, 70]. Our approach is similar because we need to calculate the free energy of the particular aggregate in the organic solvent. Difference is the fact that we want to create different possible aggregates at equilibrium, as defined by MAL. The free energy of the particular aggregate is the sum of different energy contributions (terms), which will be described in Chapter 4, 5, and 6. The free energy of an individual aggregate is by definition its standard chemical potential. When standard chemical potential is known, it allows us to complete MAL, but now not only one: if we know functionality of energy terms we can calculate every possible aggregate. This is the key idea of this part of the thesis and it can be written in more general colloidal chemistry vocabulary: every aggregate is possible and can coexist at equilibrium with its probability being determined by its composition.

Yet, it must be added that the idea is not original, only the way we put it to use. It was demonstrated on a series of papers[7] that the methodology is intuitive in its core and that can predict overall extraction isotherms [71, 72, 73].

To conclude, this mesoscopic model is between the two extremes: quantum chemistry and molecular simulations at one end, and the chemical equilibria-based engineering approaches at the other [32, 44, 64, 65]. The approach consists in calculating the free energy of all the possible aggregates. This route is opposite to the traditional approach of establishing a few chemical equilibria, since we do not fit the reaction constants: constants are among the output of the model. The systematic calculation of the Gibbs energy of self-assembly in liquid-liquid extraction is the path to understand these systems and the path to an efficient chemical engineering. Another advantage is that the system can be studied as function of any independent variable. It is possible to explore the complex two-phase multicomponent system as a function of all the thermodynamic variables.

1.3 Solid-liquid separation

The simplest case of the solid-liquid cations separation is the dispersion of the solid adsorbent in the aqueous matrix containing target solutes. The procedure describing a typical laboratory experiment is presented as a sketch in Figure 1.5. Suspended solid adsorbent interacts with

[7] Although papers dealt with much simpler systems.

aqueous solution. As a result, solutes adsorb to it[8]. In the context of metals separation, the relevant chemical process is the cation exchange which occurs at the exposed surface of the solid adsorbent. After the system reaches the equilibrium, the supernatant and the solid residue are separated. It must be noted that this now again disrupts the equilibrium between (mostly) ions adsorbed to the solid and ions in the aqueous solution in contact.

In order to have efficient exchange of ions between aqueous phase and solid adsorbent, two conditions must be met: 1) the surface of adsorbent exposed to the aqueous solution needs to be highly hydrophilic, 2) the specific surface area of adsorbent needs to be large. If two conditions

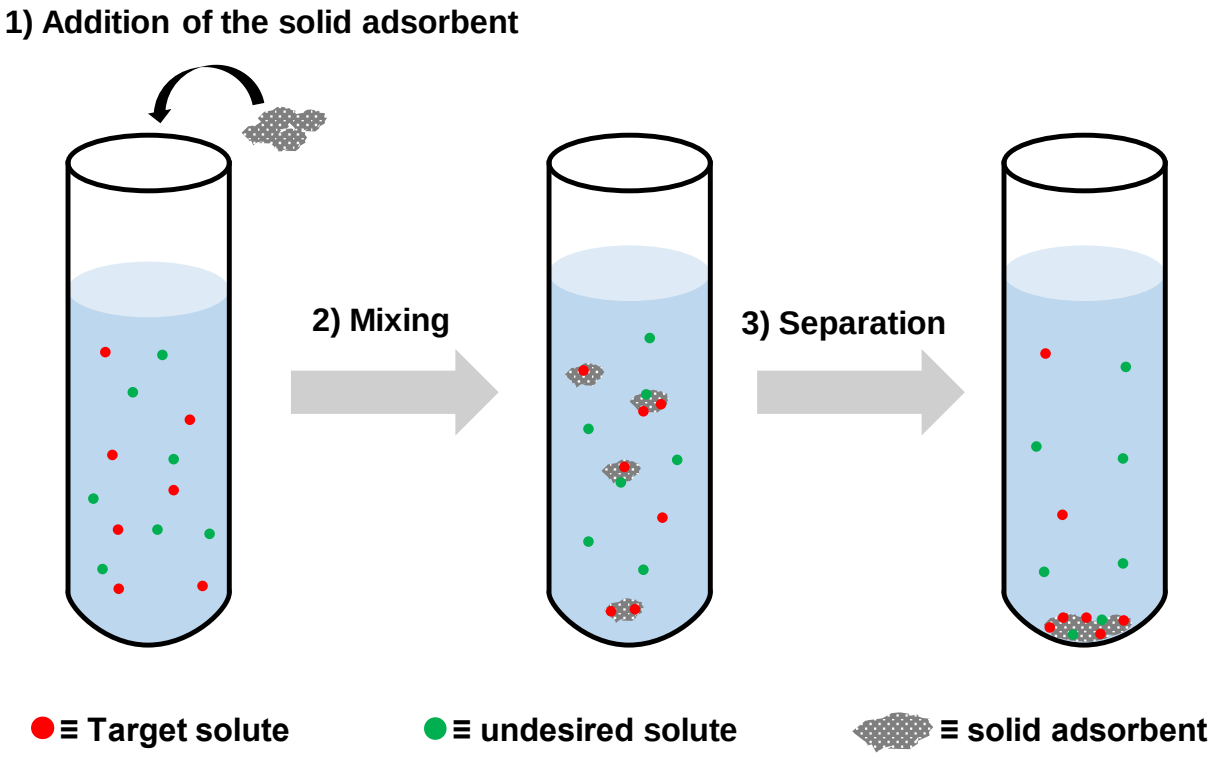

Figure 1.4 – Schematic representation of selective laboratory scale solid-liquid separation.

are met, then large accessible surface can sustain high rate of ion-exchange reactions. Currently, numerous materials display desired properties. Class of efficient solid adsorbents of metal cation is not only restricted to historical metal-oxides [74, 75, 76, 77]. Nowadays, mentioned metal-oxides are also available as highly ordered structures at nano-scale and are characterized with high degree of porosity. These nanomaterials readily synthesized, and already at use. Silica nanoparticles, titanates nanoparticles (or various morphologies, some of which we are interested in!), carbon nanotubes, various oxide nanorods, and many more fall into category of efficient adsorbents [78, 79, 41, 80, 81]. Not directly connected with subject of this thesis, but still

[8] Adsorption can be of chemical nature (chemisorption), or mediated by weaker forces (physisorption).

important solid adsorbents already used for decontamination applications, are metal-organic frameworks (MOFs), composite MOFs/ligand materials, porous aromatic frameworks (PAFs), polymer nano-traps, *etc.* [82, 83, 84, 85, 86].

Within French Alternative Energies and Atomic Energy Commission (CEA) the main application of solid-liquid separation corresponds to both selective and non-selective decontamination of wastewater from radioactive contaminants. It was identified that the wastewater can contain up to 40 radioactive species after the fission. Materials like zeolites, titanates, silicotitanates, and hexacyanoferrates have already been used as efficient ion-exchangers and thus as a tool for the decontamination of wastewater containing radioactive cations of Cs^{+}, Sr^{2+}, Ru^{3+} *etc.* [87, 88, 89, 90, 79, 91, 92, 93]. The advantage of the solid adsorbents for decontamination of radioactive wastewater is the fact that only aqueous phase is needed. Avoiding the usage of organic solvents (as in liquid-liquid extraction) is in the core of the green chemistry of industrial processes [1]. Another advantage is enhanced resistance to radiolytic cleavage of the used material, compared to extractants used in liquid-liquid extraction, or compared to soft membranes[9].

Solid-liquid separation of metal is conducted in the aqueous medium. Therefore, it is understandable that charge properties of materials have a large impact on the efficiency of separation. It must be emphasized that the expression 'charge properties' is somewhat ambiguous. In context of materials which surface groups build up charge upon dissociation when contacted with aqueous solution, the charge properties in fact assume two main contributions: the bare surface charge of material and the non-uniform cloud of ions surrounding it. The two contributions are mutually dependent since ions organize to counter the electric field exhibited by the charged surface, and surface charge in most cases depends on ion concentration at the interface[10]. Therefore, to predict efficiency of the solid-liquid separation, we need to have a proper description of charge properties. The situation is of twofold importance:

1) Study of ions in confined media and its surface charge density are important questions in colloidal chemistry of porous materials. Processes like ions association, or water diffusion (and many other) are not completely understood in complex medium, such as charged cavity of porous nanomaterials.

2) Increasing employment of nanomaterials for adsorption applications lacks a proper modelling which can distinguish what happens at the outer surface of nanoma-

[9]This is a major drawback of soft-matter applications in nuclear industry.

[10]Note that this is the case for pH-dependent surface charge densities. Some materials like clays have constant charge so the statement is not true.

terials exposed to medium, and what happens inside the nanopores. Theoretical modelling should address this issue in order to provide chemical engineering with tools for more efficient process design.

Issues mentioned above will be addressed within this thesis from theoretical point of view, and to some extent (quite modest extent) experimental point of view. The following section provides a short overview of the current theories employed to study the solid-liquid interface and separation processes. Note that we will consider only the case of charged interfaces since it is relevant to the separation of cations.

1.4 Current Modelling State-of-the-Art: Adsorption of Ions by Solid Adsorbents

The simplest system we can imagine to represent the suspension of solid nanoparticles adsorbent is a single macroion (nanoparticle) immersed into aqueous solution. This simplest system is still not 'simple' enough for chemical engineering considerations. Why is that? In fact, we can immediately notice that described simple system is already quite difficult to model and numerous effects need to be understood and quantified.

Within the scope of multi-scale modelling it is possible to obtain a proper description of the phenomena occurring at the interface, which can then combine with mesoscopic theories to recover global behavior of macroions in suspension [94, 95, 96]. As a result, thermodynamic models can be derived that can in principle bridge with chemical engineering. The schematic representation of the multi-scale modelling employed for the systems of solid-adsorbents is presented in Figure 1.5. It can be seen how description of the ions, water molecules and surface groups of the nanomaterial can be transferred to meso-scale. Theories of inhomogenous liquids can then be used to correct MAL crucial for chemical engineering. As a result separation efficiency can be predicted. Here we present a short overview of the levels of theory used in the field of charging phenomenon in cavities of complex porous materials.

1.4.1 Quantum chemistry calculations

Usage of quantum chemistry calculations is limited to systems made of small number of atoms. In context of nanomaterials, quantum chemistry calculations are mostly Density Functional Theory (DFT). Furthermore, DFT is usually used to obtain the structure of material at the

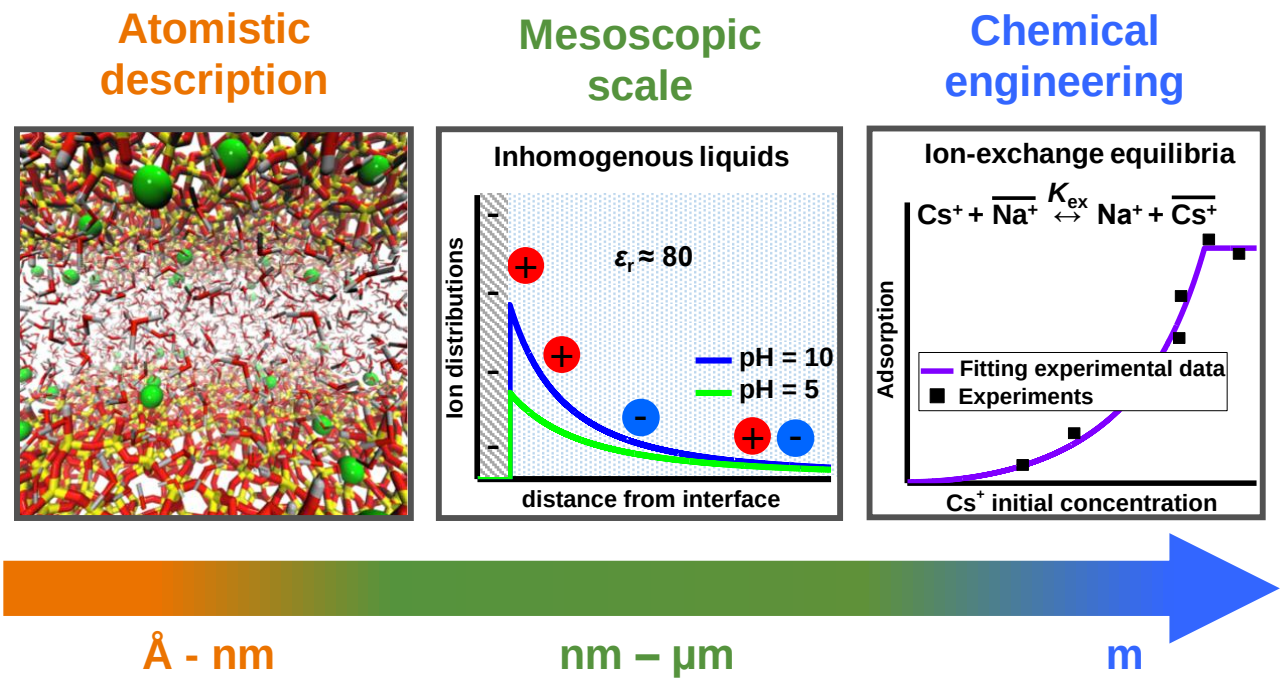

Figure 1.5 – Schematic representation of levels of theory that are currently employed in solid-liquid separation. Figure on the left represents atomistic studies of ions association phenomenon at the interface. Snapshot obtained from MD simulations has been reprinted by the permission of authors and it corresponds to reference [97]. Sketch in the middle represents the mesoscopic models *e.g.* Poisson-Boltzmann theory. Figure to the right is simplified representation of equilibria approach utilized by chemical engineers. Example is made on hypothetical Cs^+ and Na^+ exchange equilibria decontamination applications.

interface *i.e.* to recover the proper chemical structure of exposed atoms at phase boundary [98]. A well described structure of exposed surface atoms can be used to create the concept of surface site which is one of key-ingredients for surface site models. Site models are can be used to regulate the charge of the surface. Furthermore, quantum chemistry calculations can be used to study the structure of species at interface, or the adsorption with the clear distinction between created covalent and coordinate bonds.

1.4.2 MD simulations

MD simulations are powerful tool to study interfacial phenomena, and behavior of ions and water molecules inside the cavity of porous materials [99]. The schematic representation of typically study of ion in confined medium via MD simulations is given as a snapshot on the left in Figure 1.5. Some of key prospects/advantages for using MD simulations are:

a) Association of counterion and the surface group *i.e.* explicit charge regulation.

b) Ion pair formation (counterion and coion association) in the cavity of porous material can be identified (if association occurs).

c) Explicit solvent simulations can elucidate behavior of water molecules confined inside the cavity.

d) Mesoscopic models can be validated by MD simulations for certain conditions of the system.

The association of counterion and the charged surface group can be understood as typical ion association, as proposed by Bjerrum [97]. The constant of association K_0 can be written as

$$K_0 = \int_0^d \mathrm{d}r 4\pi r^2 \exp\left[-\beta V_{\mathrm{int}}(r)\right] \tag{1.5}$$

where r is the distance, V_{int} is the interaction potential, d is the arbitrary defined limit of integration. K_0 depends on the choice of d. In most cases it is sufficient to account the contact ion pair (CIP) and solvent separated ion pair (SSIP) with K_0. CIP and SSIP correspond to two minima in calculated V_{int}. A properly calculated K_0 is important because it can be used in charge regulation method within continuum theories of liquids, but can also be used to represent one of competing reactions to establish multiple MAL in chemical engineering.

We have mentioned that some mesoscopic models can be validated via MD. Indeed, it was shown that Poisson-Boltzmann theory is valid once the description of counterion/surface site association is properly accounted for [100, 101]. After the first layer (the Stern layer) the aqoueous solution behaves as predicted by Poisson-Boltzmann theory. With some advantages described, one can imagine how to now use benefits of simulations as apart of multi-scale approach, and incorporate them into continuum solvent models to even further close the gap towards chemical engineering.

Before proceeding, it is important to stress the limits of MD simulations. A major drawback of MD simulations is the proton exchange and surface regulation governed by ambient pH. Proton is a small ion and its surface charge density is quite large which makes it difficult to model. A big portion of MD-based studies therefore assume constant charge and pH influence is neglected. Furthermore, low electrolyte concentration aqueous systems with immersed macroion are in most cases not possible to calculate. The reason is the fact that long-range electrostatic interactions are not fully screened [102]. The relevant measure of electrostatic interactions is so-called Debye length, which is defined as

$$\lambda_{\mathrm{D}} = \left(4\pi l_{\mathrm{B}} \sum_{\alpha} z_\alpha^2 c_\alpha^0\right)^{-1/2} \tag{1.6}$$

where c_α^0 and z_α are respectively the reservoir concentration and the charge number of ion z. l_B is the Bjerrum length defined as $l_\mathrm{B} = e^2/4\pi k_\mathrm{B} T \epsilon_0 \epsilon_\mathrm{r}$. In the case of low concentration of 1:1 electrolyte, λ_D has the magnitude of tens of nanometers. This means that in order to guarantee the electroneutrality, a huge simulation boxes need to be used, which is in most cases undesired.

1.4.3 Monte Carlo simulations

To describe the interaction between the colloids (in our case nanomaterial particles) useful method is Monte Carlo (MC) simulation. Accurate description of multivalent ion distribution can be obtained, even in the case of small cavities. Additional degree of freedom, such as angular dependency on free energy of rod-like ions [103], is easily incorporated[11]. Additional benefit is the fact that MC gives insights into structure of the suspensions in terms of mean distance and orientations between macroions [104, 105]. This is then allows to draw the conclusions concerning properties of real macroscopic systems such as cohesion of cements[106]. Still, MC simulations cannot be used to predict efficiency of metal cations removal from suspension due to the robustness of the procedure. MC simulations are often used to validate predictions by classical Density Functional Theory (cDFT)[12][107].

1.4.4 Classical Density Functional Theory

At the beginning, we need to emphasize that the level of theory that we used for the study of solid nanomaterials in aqueous solution corresponds to cDFT. For that reason, in the next chapter we will go in details of derivation and its approximations. Here we present only short overview on examples employed and the main findings. We are in the domain of continuous solvent models (but not necessarily). cDFT (DFT in general) is convenient since it gives energy of the overall system. If we can construct the system functional as a function of particle, or in our case ion distributions, then by finding its minimum value by variational procedure we can recover description of the system at equilibrium. The description comes in the form of particle distribution functions that can be integrated over volume of the system to obtain the free energy [108]. It has been showed that ion distribution functions can be obtained in the case of nanochannels, dense layered clay, and other porous materials [109, 110]. Advantage of the cDFT is that is is compatible with the surface charge regulation method (which will be

[11] This increases computational time but the benefit of inclusion of additional degree of freedom increases prediction power of the method.

[12] DFT explained at the beginning of the chapter was in the field of quantum chemistry. To avoid possible confusing we denote mesoscopic theories of inhomogenous liquids by cDFT.

further expanded within the scope of this thesis). This opens the route for the modelling of pH-governed process.

cDFT is in between MD and MC simulations, and ion-exchange equilibria approach. It preserves the properties of inhomogenous liquids and yields acceptable description of ion distributions in confined medium, but also corrects the ions concentrations at interface. Surface complexation then takes hold in form of established exchange equilibria (cation exchange MAL) and we can predict the efficiency of adsorption or decontamination. Furthermore, surface complexation can be justified either through cDFT or MD simulations as Bjerrum contact ion pair.

Probably the most widely used example of cDFT is the Poisson-Boltzmann (PB) theory. Minimization of the grand potential functional (solvent as dielectric continuum) when ion-ion correlations are neglected, yields the ion distributions that depend only on electrostatics. Inducing them into relevant electrostatics relations yields PB level of description. The big advantage is the fact that it is easily solved numerically of even in some cases analytically. The example of this level of theory is given as the sketch in the middle of Figure 1.5. In order to understand the behavior of charged colloids in aqueous electrolyte solution Poisson-Boltzmann theory is often used since in low salt condition, it provides satisfying explanations [111]. Poisson-Boltzmann theory is often coupled with charge regulation method to explain various phenomena in colloidal chemistry [112]. Advancements towards more realistic descriptions of colloidal systems include interactions between dissimilar surfaces, rod-like polyions, mobile surface groups and even the interactions between soft multi-layered particles [113, 114, 115, 116]. Another advantage is the fact that PB can be easily improved by including additional potentials in the variational procedure. The modifications that have the largest impact are in the form of size of ions. Those can be included if we divide the accessible volume for ions into cells of finite size. Mean-field approximation then yields ideal gas-like entropic part of free energy functional which does not allow oversaturation of the interface with ions [117, 118]. In principle, one can go beyond single macroion considerations and achieve a description of the overall behavior of the suspension [96, 119, 120].

Advanced classical Density Functional Theory simulations made considerable progress about the description of ion density profiles inside confined media and about the evaluation of surface charge of porous materials [109, 110].

Yet, to our knowledge, there is no model that can quantitatively describe the charge difference between the inner and outer surfaces of porous materials, and quantify the extent of ion-exchange at each surface. Currently, it is not clear where does the adsorption of ions takes

place. As stated before, we will address such problems further in the thesis.

1.4.5 Ion-exchange equilibria approach

The usual approach in modelling of solid-liquid separation that chemical engineers use is the fitting of the free energy of transfer of ion from aqueous bulk solution to solid phase. From the free energy of transfer the constant of transfer is obtained [88]. The procedure is demonstrated schematically in the sketch to the right in Figure 1.5. If we imagine a simple hypothetical decontamination of wastewater from Cs^+ by some solid (based on the exchange Na^+) then associated equilibria can be written as

$$Cs^+ + \overline{Na^+} \rightleftharpoons Na^+ + \overline{Cs^+} \tag{1.7}$$

which can be written in form constant of the ion exchange

$$K^0_{\text{exchange}} = \frac{a_{Na^+}\overline{a_{Cs^+}}}{a_{Cs^+}\overline{a_{Na^+}}} = \frac{\left[Na^+\right]\overline{\left[Cs^+\right]}}{\left[Cs^+\right]\overline{\left[Na^+\right]}}\frac{\gamma_{Na^+}}{\gamma_{Cs^+}}\frac{\overline{\gamma_{Cs^+}}}{\overline{\gamma_{Na^+}}}. \tag{1.8}$$

Now is the question how to obtain K^0_{exchange}? It is usually done by taking the logarithm of Eq. 1.8 [92]. The experimental data can be plotted in a linear form. Then by identification, we can recover K^0_{exchange}. There are multiple issues with dealing with logarithmic form of Eq. 1.8:

1) The calculation of activity coefficients in solid phase can be troublesome (note that at this point we are not even concerned with activity coefficients in the concentrated aqueous phase, even though that itself is a huge issue). Practically what is done is stating that $\overline{\gamma_{Cs^+}} = \overline{\gamma_{Na^+}} = 1$ *i.e.* activity coefficients in the solid phase are neglected. If the exchange includes monovalent cations in the same accessible volume, this is not that severe approximation [89].

2) The concentration of cation that is released in the competition exchange, in this case $\overline{\left[Na^+\right]}$ is unknown. What is practically done again is to declare $\overline{\left[Na^+\right]}$ equal to the Cation Exchange Capacity (CEC) [88]. CEC represents the maximum amount (or concentration) of cation to be exchanged within competition reactions. It is assumed to be property of the material and thus constant. The approximation of $\overline{\left[Na^+\right]}$ = CEC is often used. It must be emphasized that CEC is more of a hypothetical concept than the real scientific argument since it is only valid if the exact number of ions able to participate in the exchange is known at given pH and temperature. Instead of this concept, a site model (which we will use later) is probably more accurate since it connects surface site density and local ion association

Recently there were mesoscopic models that battled issues above. In particular, activity coefficients in solid were calculated as well as the ones in the aqueous solution. It was shown

that calculated K^0_{exchange} depends on the level of theory (description of the system) [89]. Another example on what be done is employing cDFT. This can improve the calculation of Eq. 1.8 since by differentiation of thermodynamic functional, we can obtain activity coefficients. Moreover, a surface site models are probably more adequate since it is more intuitive to understand the complexation of ions to the interface (a local phenomenon giving a cation/surface site pair). Moreover, one can estimate number of sites in the system (to more satisfactory accuracy compared to CEC) based on the combination of experimental techniques *e.g.* BET, HR-TEM, *etc.*

1.4.6 Summary and prospects of multi-scale modelling

Multi-scale modelling can in principle serve as a powerful tool for the prediction of various materials. By systematic procedure which involves atomistic modelling of the ion-surface group and ion-ion associations, the calculation of acceptable ion distributions inside the cavities of porous materials, along with the multiple equilibria ion-exchange MAL, one can predict the efficiency of the solid-liquid separation process. Then delicate effects such as stability of suspension or ion specific effects can be included to even further correct calculated constants of transfer.

Chapter 2

A Toolbox of Physical Concepts

We start with the basics of thermodynamics by defining the fundamental relation for the full description of the system in study. We will show how it is useful to transform the fundamental relation into thermodynamic potentials as a function of extensive and intensive variables. This general procedure allows for adjustments to whatever framework is needed in order to study a phenomenon at hand. Later we will introduce a famous Boltzmann relation that bridges equations of state and the statistical mechanics. This, along with a few modifications, can be used to elegantly evaluate properties of system by building a microscopic model in an appropriate ensemble. Furthermore we will expand our considerations to the concept of inhomogenous liquids in the scope of density functional theory. Finally, we will add separate sections dealing with the concepts that are used in constructions of our models.

2.1 Thermodynamics

The strength of thermodynamics comes in the form of choosing a representation which best suits our considerations. We can define a fundamental equation as the internal energy U of the system

$$U = U\left(S, V, \{N_\alpha\}\right) \tag{2.1}$$

as a function of solely extensive thermodynamic quantities namely the entropy S, the volume of the system V, and the chemical composition N (multiple species present are represented by generalized symbol $\{N_\alpha\}$). In differential form U can be written as

$$\mathrm{d}U = T\mathrm{d}S - P\mathrm{d}V + \sum_\alpha \mu_\alpha \mathrm{d}N_\alpha \quad . \tag{2.2}$$

From Eq. 2.2 we obtain the definition of equations of state[121] in the form of

$$T = \left(\frac{\partial U}{\partial S}\right)_{V,\{N_\alpha\}} \quad , \quad P = -\left(\frac{\partial U}{\partial V}\right)_{S,\{N_\alpha\}} \quad , \quad \mu_\alpha = \left(\frac{\partial U}{\partial N_\alpha}\right)_{S,V,\{N_\beta\}} \quad . \tag{2.3}$$

2.1.1 Definition of Thermodynamic Potentials

As we have stressed in the first sentence of this section, that the strength thermodynamics comes in the form of choosing a representation which best suits our considerations. This implies that we can write a fundamental relation given by Eq. 2.1 in the form of inverse relationship *i.e.* the entropic fundamental relation $S\left(U, V, \{N_\alpha\}\right)$. Both fundamental relations are functions of extensive variables and contain a full description of the system. Choosing of the representation is arbitrary, but once adopted, must be respected throughout the procedure. In fact we have presented this alternative representation in terms of entropy because this view is consistent with statistical thermodynamic, which will be presented in following sections.

Even though this is somewhat intuitive $U\left(S, V, \{N_\alpha\}\right)$ representation[1], its practical use is somewhat less appealing since it requires the measurement of S. Luckily, by utilizing Legendre transformation procedure, we can switch extensive quantities to their conjugate counterpart. This leads to the definition of thermodynamic potentials. By eliminating the entropy S from U we obtain the Helmholtz energy

$$F\left(T, V, \{N_\alpha\}\right) = U\left(S, V, \{N_\alpha\}\right) - TS \tag{2.4}$$

which can be written in differential form as

$$\mathrm{d}F = -S\mathrm{d}T - P\mathrm{d}V + \sum_\alpha \mu_\alpha \mathrm{d}N_\alpha \quad . \tag{2.5}$$

Helmholtz energy or the free energy is manageable since we need only to control measurable quantities. Thermodynamic potentials are extensive quantities *i.e.* functions of at least one extensive quantity. According to Euler's theorem for first-order homogeneous functions[2], it follows that

$$F\left(T, V, \{N_\alpha\}\right) = V\left(\frac{\partial F}{\partial V}\right)_{T,P,N_\alpha} = -PV + \sum_\alpha \mu_\alpha N \tag{2.6}$$

Another thermodynamic potential is obtained if we further replace $\{N_\alpha\}$ by its conjugate variable *i.e.* the chemical potential μ_α. This yields the Grand potential defined as

$$\Omega\left(T, V, \{\mu_\alpha\}\right) = F\left(T, V, \{N_\alpha\}\right) - \sum_\alpha \mu_\alpha N_\alpha \tag{2.7}$$

[1] Same probably follows for $S\left(U, V, \{N_\alpha\}\right)$.

[2] Let $f\left(x_1, ..., x_N, X_1, ..., X_N\right)$ be a homogeneous function of order n. x_i and X_i are respectively extensive and intensive variables, just like in thermodynamic potentials. Euler's Homogeneous Function Theorem states that $\sum_{i=1}^{N} x_i \frac{\partial f}{\partial x_i} = nf$.

and its differential form

$$\mathrm{d}\Omega = -S\mathrm{d}T - P\mathrm{d}V - \sum_{\alpha} N_{\alpha}\mathrm{d}\mu_{\alpha} \quad . \tag{2.8}$$

Euler's theorem again gives

$$\Omega = -PV \tag{2.9}$$

since the Grand potential is function of only one extensive variable, namely the volume V. Another very useful potential is semi-grand potential where one or more variables describing the compositions of the system are converted into chemical potentials[122], but the rest are kept in their extensive form (for example $\Omega\left(T, V, \mu_{\alpha}, \{N_{\beta}\}\right)$). In fact, we will use this framework in our considerations of the liquid-liquid extraction where we will fix the chemical potential of ions and water in the reservoir, while the chemical potential of organic ligands is allowed to fluctuate.

Still, probably the most used thermodynamic potential is Gibbs energy $G\left(T, P, \{N_{\alpha}\}\right)$. $G\left(T, P, \{N_{\alpha}\}\right)$ is defined as a double Legendre transformation of $U\left(S, V, \{N_{\alpha}\}\right)$

$$G\left(T, P, \{N_{\alpha}\}\right) = U\left(S, V, \{N_{\alpha}\}\right) - TS + PV \tag{2.10}$$

with its differential form given as

$$\mathrm{d}G = -S\mathrm{d}T + V\mathrm{d}P + \sum_{\alpha} \mu_{\alpha}\mathrm{d}N_{\alpha} \quad . \tag{2.11}$$

Gibbs free energy is the function of natural variables which are easily controlled in terms of laboratory experiments. Euler's theorem yields

$$G = \sum_{\alpha} \mu_{\alpha} N_{\alpha} \tag{2.12}$$

2.1.2 The Gibbs-Duhem Relation

An important and widely used application of Euler's theorem is to derive a differential form of relation among equations of state. A differential form is known as the Gibbs-Duhem relation. By taking a infinitesimal variation of Eq. 2.12 and identifying with Eq. 2.11 we obtain

$$S\mathrm{d}T - V\mathrm{d}P + \sum_{\alpha} N_{\alpha}\mathrm{d}\mu_{\alpha} = 0 \tag{2.13}$$

If T and P are constant their variations are equal to 0 ($\mathrm{d}T = \mathrm{d}P = 0$), we obtain

$$\sum_{\alpha} N_{\alpha}\mathrm{d}\mu_{\alpha} = 0 \quad . \tag{2.14}$$

Eq. 2.14 states that if we know the functional form of all chemical potentials but one, we can obtain the functional form of the last one, to a given constant.

To demonstrate the benefit of Gibbs-Duhem relation, we will derive the chemical potential of water in a mixture of water and salt *i.e.* a simple aqueous solution. This part will be used in the derivation of our model, so it is quite pleasant to have a twofold benefit at this stage: 1) demonstration of Gibbs-Duhem procedure for obtaining the functional form of the dependent equation of state, and 2) to shorten the derivation in later stages of this thesis where there will be enough equations already. We consider ideal aqueous solution where activity coefficients γ are equal 1. In that case the chemical potential of ions j in aqueous solution can be written as

$$\mu_j = \mu_j^\circ + k_\mathrm{B}T \ln\left(\frac{m_j}{m_j^\circ}\right) \tag{2.15}$$

where μ_j is the chemical potential of ion j, μ_j° is the standard chemical potential of ion j, m_j° is the molality at standard state, and m_j is the molality of j. m_j is defined as

$$m_j = \frac{n_j}{n_\mathrm{w} M_\mathrm{w}} \tag{2.16}$$

where n_j, n_w, and M_w are respectively the amount of ions j, the amount and the molar mass of water molecules. We can now employ Eq. 2.14 for the case of a simple mixture of water and ions. We write

$$\sum_j n_j \mathrm{d}\mu_j + n_\mathrm{w}\mathrm{d}\mu_\mathrm{w} = 0 \tag{2.17}$$

where μ_w is the chemical potential of water molecules. Variation of Eq. 2.15 (for the given definition of molality) with respect to n_j yields

$$\mathrm{d}\mu_j = RT\,\mathrm{d}\ln n_j = RT\,\frac{\mathrm{d}n_j}{n_j} \quad . \tag{2.18}$$

R is the gas constant. After inserting Eq. 2.18 into Eq. 2.17 we obtain

$$\mathrm{d}\mu_\mathrm{w} = -\frac{RT}{n_\mathrm{w}} \sum_j \mathrm{d}n_j. \tag{2.19}$$

Integration yields

$$\mu_\mathrm{w} = -\sum_j RT\frac{n_j}{n_\mathrm{w}} + C(n_j) \tag{2.20}$$

where $C(n_j)$ is integration constant. If we consider a pure water, then first term in the expression for chemical potential of water goes to 0 and we can identify the integration constant with the standard chemical potential of water $C(n_j) = \mu_\mathrm{w}^\circ$. Finally we have

$$\mu_\mathrm{w} = \mu_\mathrm{w}^\circ - RT\frac{\sum_j n_j}{n_\mathrm{w}} \tag{2.21}$$

which is the a consequence of Gibbs-Duhem procedure. If μ_w is defined in terms of Gibbs free energy $\mu_j = \left.\frac{\partial G}{\partial N_j}\right|_{T,P,N_{i\neq j}} = \left.\frac{1}{N_\mathrm{A}}\frac{\partial G}{\partial n_j}\right|_{T,P,n_{i\neq j}}$ we have

$$\mu_\mathrm{w} = \mu_\mathrm{w}^\circ - \frac{RT\sum_j x_j}{x_\mathrm{w}} \tag{2.22}$$

where N_A is the Avogadro constant.

2.2 Basic Principles of Classical Statistical Thermodynamics

Statistical mechanics, a branch of physics, provides a link between the macroscopic level of phenomenological thermodynamics, and a microscopic level of description. With macroscopic state of the system at equilibrium uniquely defined by a (small) number of experimentally controlled state variables (as described in previous section), the microscopic level of description in principle includes specification of a point Γ_N in $6N$-dimensional space, where N denotes the total number of particles in the system. The coordinates of Γ_N are generalized position vectors $\mathbf{r}_i$, and momenta $\mathbf{p}_i$ of N particles. Statistical averaging reduces the detailed microscopic description involving an untractable number of rapidly varying degrees of freedom. According to Gibbs ensemble theory, the probability of occurrence of such a state is given by a phase space probability density $P(\Gamma_N)$. It is in fact the ratio of the particular state of the system and all possible states. All possible states represent a normalization factor called the partition function[3]. Once the partition is known the link to the calculation of thermodynamic potentials is straightforward, as we will see in the following text. Here we shortly present and describe some of widely used ensembles and corresponding relations between partition functions and thermodynamic potentials. Note that for the sake of simplicity we will deal with one-component systems, but generalization to mixtures is straightforward.

Micro-Canonical ensemble

Micro-Canonical ensemble is used to describe the closed isolated systems, where the energy E, chemical composition N_α, and volume V are fixed. The differences within states originate only from different $\mathbf{r}_i$, and $\mathbf{p}_i$ of particles. Since energies of the states are equal we can write the probability density as

$$P(\Gamma_N) = \begin{cases} \text{constant} & \text{if } H_N = E \\ 0 & \text{otherwise} \end{cases} \tag{2.23}$$

where H_N is the Hamiltonian defined as

$$H_N = K_N + V_N + \Phi \tag{2.24}$$

[3]The example of calculation of the partition function will be provided in the following section.

K_N is the kinetic energy, V_N is the interaction energy between particles, and Φ is the arbitrary potential exhibited by the external generator. In this case there is no external potential, thus $\Phi = 0$. We can write micro-canonical partition function W accounting for all possible microstates as[4]

$$W = \frac{1}{N!h^{3N}} \int \mathrm{d}\Gamma \delta(H_N - E) \tag{2.25}$$

where h^{3N} is a measure of the accessible phase space 'volume' (makes a partition function dimensionless), factor $1/N!$ accounts for indistinguishability of particles. Finally, the link between thermodynamics and statistical mechanics is given by Boltzmann relation as

$$S(U, V, N) = k_\mathrm{B} \ln W \quad . \tag{2.26}$$

The relation is a direct link between number of possible microstates of the system and the macroscopic entropy. As described in previous section, if the fundamental relation is known, we can derive equations of state. In the case of Micro-Canonical ensemble we have

$$\begin{aligned} \mathrm{d}S &= \frac{1}{T}\mathrm{d}E + \frac{P}{T}\mathrm{d}V - \frac{\mu}{T}\mathrm{d}N \\ \frac{1}{k_\mathrm{B}T} &= \left(\frac{\partial \ln W}{\partial E}\right)_{N,V}, \frac{P}{k_\mathrm{B}T} = \left(\frac{\partial \ln W}{\partial V}\right)_{E,N}, \frac{\mu}{k_\mathrm{B}T} = \left(\frac{\partial \ln W}{\partial N}\right)_{E,V} \end{aligned} \tag{2.27}$$

Even though intuitively simple, a Micro-Canonical ensemble is in fact difficult to manage since it involves computing the every possible microstate. To overcome this difficulty, the macroscopical constraints are either established or removed which generates various Gibbs ensembles corresponding to various thermodynamic potentials. The choice of ensemble can be thus made so it simplifies the comparison with the reference experimental setup.

Canonical ensemble

We have described an ensemble for description of an isolated closed system. We can now imagine that thermal insulator is removed and the energy can fluctuate between different systems, each one characterized by corresponding $P(\Gamma_N)$. They are in contact with a thermostat which fixes the temperature T. Volume and the number of particles remain fixed. In Canonical ensemble the probability distribution represents the number of ways the total energy of the system can be distributed among microstates. A way of obtaining the expression for $P(\Gamma_N)$ is by using the Lagrange method of undetermined multiplier with respect to constraint of the system. In the

[4] The Dirac delta function $\delta(x)$ is used to give functionality to probability density in the case of equal energies of different microstates.

case of Canonical ensemble, the Lagrange multiplier is $\beta = 1/k_{\mathrm{B}}T$. The probability distribution follows Boltzmann distribution and can be written as

$$P\left(\Gamma_N\right) = \frac{1}{N!h^{3N}} \frac{\exp\left(-\beta H_N\right)}{Z} \tag{2.28}$$

where Z is canonical partition function defined as

$$Z = \frac{1}{N!h^{3N}} \int_{\Gamma_N} \exp\left(-\beta H_N\right) \mathrm{d}\Gamma_N \tag{2.29}$$

Z will be derived in the following sections for the case of the ideal gas mixtures. The link with thermodynamics is given by the statistical definition of the Helmholtz potential (recall Eq. 2.4) as

$$F(T, V, N) = -k_{\mathrm{B}}\, T \ln Z \tag{2.30}$$

Grand-Canonical Ensemble

Grand-Canonical ensemble is very useful since it simplifies description of various common phenomena in chemistry. For example the adsorption of particles to a surface can be simply understood if the we consider the medium containing the free particles as a infinite reservoir in contact to the surface. Another example can be aqueous solution of ions in contact to plane describing the immersed electrode. Grand-Canonical ensemble can be generated if we open a closed systems (described by Canonical ensemble) to exchange particles with the reservoir. To account for the most probable distribution of the particles among systems we need to employ Lagrange method once again. As will be seen in following section on a practical example, the multiplier is equal to the chemical potential of the particular particle in the reservoir μ. The probability distribution is again given as a Boltzmann distribution and has form of

$$P\left(\Gamma_N\right) = \frac{1}{N!h^{3N}} \frac{\exp\left(-\beta H_N + N\mu\right)}{\Xi} \tag{2.31}$$

where grand-canonical partition function Ξ is given as

$$\Xi = \sum_N \frac{1}{N!} \frac{e^{N\beta\mu}}{h^{3N}} \int \mathrm{d}\Gamma e^{-\beta H(\Gamma)} \quad . \tag{2.32}$$

Later we will see that factorization will yield the activity (or fugacity) of the particle. Finally, the link with thermodynamics is given through relation

$$\Omega(T, V, \mu) = -k_{\mathrm{B}} T \ln \Xi \tag{2.33}$$

2.3 Classical Density Functional Theory - cDFT

The complexity of dense fluids increases if there is an external potential source present. An external potential affects molecules in liquid and therefore induces inhomogeneity of it. So called non-uniform fluids are defined as fluids which number density exhibits spatial variation. External potential can be, for example a Earth's gravitational field that creates variation by height, or the source can be an electrode immersed in the aqueous solution that affects ion distribution near electrode surface. To acquire description of macroscopic system, we divide it into so called mesoscopic subsystems which are much smaller than the original system. Yet, its size is enough for thermodynamics to apply.

Classical Density Functional Theory (cDFT), as a branch of statistical thermodynamics has proven very convenient method of choice for description of inhomogeneous fluids. Not only that it is computationally a lot less demanding and available to study larger systems compared to for example Molecular Dynamics or Monte Carlo simulations, but it also directly provides values of thermodynamic quantities of system in study, since functionals typically represent the free energy. Canonical and Grand canonical ensemble are convenient, and frequently used in cDFT, which will be demonstrated throughout this section.

2.3.1 General cDFT Framework

Let us begin with a fluid where there is no external potential source to create a fluid inhomogeneties. Influence of one particle to another can be expressed as a pair interaction which in turn can be separated into repulsive short-ranged and mostly attractive long-ranged interactions. Former could be understood as excluded volume (finite size) effects, while the latter interactions can be introduced as Coulombic and van der Waals forces[5], *etc.* We can decouple the potential energy between species in the system $U(\{\mathbf{r_i}\}$ as

$$U(\{\mathbf{r_i}\}) = V^0(\{\mathbf{r_i}\}) + W(\{\mathbf{r_i}\}) \tag{2.34}$$

where $V^0(\{\mathbf{r_i}\})$ denotes short-ranged interactions, while $W(\{\mathbf{r_i}\})$ corresponds to long-ranged interactions. In the absence of the external potential, the fluid density is uniform (ρ is constant), and therefore we have bulk behavior. Density is then defined as

$$\rho = \frac{N}{V} \tag{2.35}$$

[5]Note that the method is not restrained to small ions and molecules only. In principle, one can study the suspension of macroions as a complex inhomogenous fluid[96].

where V and N are again volume and total number of particles of the system.

Now let us impose arbitrary external potential $\Phi_{\text{ext}}(\mathbf{r})$. Since there is spatial difference in densities a convenient way of description is by the functional[6] of one-particle density function. If we name the functional $F[\rho(\mathbf{r})]$ where $\rho(\mathbf{r})$ is the one-particle density then we consider it as a 'intrinsic' functional. Term 'intrinsic' will be far better understood later in the text. For now, maybe it would be better to refer it as a Helmholtz free energy functional $F[\rho(\mathbf{r})]$.

Generally $F[\rho(\mathbf{r})]$ depends on $U(\{\mathbf{r_i}\})$ which is the total interaction energy among particles of fluid. $F[\rho(\mathbf{r})]$ is a property of many-body interactions, therefore it is difficult to obtain its functional form. By definition of $U(\{\mathbf{r_i}\})$, even in simplest cases where no long-ranged interactions ($W(\{\mathbf{r_i}\}) = 0$) are included, the $F[\rho(\mathbf{r})]$ is hard to acquire. The only exactly known form of $F[\rho(\mathbf{r})]$ is the one for a ideal atomic gas, where only kinetic part of Hamiltonian operator is taken into account. Few approximations can be useful such as the quadratic and square gradient approximation. In following paragraphs we derive exact solution for ideal gas from canonical ensemble.

Canonical partition function of the one-component ideal gas

Ideal gas hypothetical assumption is that there are no many-body interactions among particles so even $V^0(\{\mathbf{r_i}\}) = 0$ (then of course $U(\{\mathbf{r_i}\})$ is 0 also). The canonical partition function when there is no potential energy among particles is given as

$$Z = \frac{1}{N!} \int \frac{\mathrm{d}\mathbf{r}^N \mathrm{d}\mathbf{p}^N}{h^{3N}} \, e^{-\beta \sum_i \frac{\mathbf{p}_i^2}{2m}} \tag{2.37}$$

which further yields

$$Z = \frac{1}{h^{3N} N!} \int \mathrm{d}\mathbf{r}^N \int \mathrm{d}\mathbf{p}^N \, e^{-\beta \sum_i \frac{\mathbf{p}_i^2}{2m}} \tag{2.38}$$

where β is Lagrange multiplier that corresponds to $k_{\mathrm{B}}T$, p_i is momenta, h is Planck constant and m is mass of the particle. The equation above is valid for single-component systems. Since there is no potential energy among particles we can factorize the partition function. The configuration integral is equal to the volume of the system V. We have

$$Z = \frac{V^N}{h^{3N} N!} \left(\int_{-\infty}^{+\infty} \mathrm{d}\mathbf{p} \, e^{-\beta \sum_i \frac{\mathbf{p}_i^2}{2m}} \right)^{3N} . \tag{2.39}$$

[6] Functional is defined as real-valued function on a vector space V, usually of functions.

$$f \to I[f] = \int f(x, y, y') dx \tag{2.36}$$

where f is element of V and $y = y(x)$. Functional is conventionally denoted by square brackets.

To solve integral of this type, we used Gauss integral[7] given in footnote. After integration we have

$$Z = \frac{1}{\Lambda^{3N}} \frac{V^N}{N!} \tag{2.41}$$

where

$$\Lambda = \frac{h}{\sqrt{2\pi m k_{\mathrm{B}} T}} \tag{2.42}$$

is de Broglie thermal length. Λ is a measure whether gas (ideal gas) can be treated within classical mechanics. If an average spacing between particles is approximately given by $\left(\frac{V}{N}\right)^{\frac{1}{3}}$ then condition for applicability of classical mechanics is

$$\left(\frac{V}{N}\right)^{\frac{1}{3}} >> \Lambda.$$

Keeping this condition in mind, we proceed to evaluation of Helmholtz free energy from relation $F = -k_{\mathrm{b}} T \ln Z$ in which we insert canonical partition function. Now we have

$$F = -k_{\mathrm{B}} T \ln \left(\frac{1}{\Lambda^{3N}} \frac{V^N}{N!} \right). \tag{2.43}$$

Since factorials are usually difficult to compute, in order to 'clear the path' from natural logarithm of $N!$ we use so called Stirling's approximation[8]. Problems which require small number of particles can be addressed with model developed by Robert Evans and co-workers and can be found in the reference [109].

Reorganization of the expression Eq. 2.43 yields Helmholtz energy in the following form

$$\frac{F}{k_{\mathrm{B}} T} = 3N \ln \Lambda + N \ln \frac{N}{V} - N. \tag{2.45}$$

It is clear that F is extensive. Rearranging and dividing both side of equation by volume V we obtain

$$\frac{F}{V k_{\mathrm{B}} T} = \rho \ln(\Lambda^3 \rho) - \rho \tag{2.46}$$

which after integration over volume yields familiar form

$$F = k_{\mathrm{B}} T \int_V \mathrm{d}v \, \rho(\ln(\Lambda^3 \rho) - 1) \tag{2.47}$$

[7] Gauss integral defined as

$$I = \int_{-\infty}^{+\infty} \mathrm{d}x \, e^{-\frac{x^2}{\alpha}} = \sqrt{\pi} \tag{2.40}$$

for $\alpha = 1$.

[8] Stirling's approximation for large N

$$\ln N! \simeq N \ln N - N. \tag{2.44}$$

whereas for a mixture generalization is straightforward:

$$F = k_{\mathrm{B}}T \sum_{\alpha} \int_{V} \mathrm{d}v \, \rho_{\alpha}(\ln(\Lambda^3 \rho_{\alpha}) - 1). \tag{2.48}$$

which is valid when the interaction between different particles is negligible.

Introducing the external potential to induce inhomogeneity of the fluid

By now we considered bulk, a region of fluid with no external potential present, or the region very far form it. ρ_i are just number concentrations of species present in a fluid. From above expression one can calculate thermodynamic property of interest. Not to get confused, this derivation was made in canonical ensemble, or system in contact with far larger reservoir of constant temperature, yet on the beginning of section we claimed that Grand-Canonical ensemble is more convenient. The latter is still the case. Moreover, we will see later that Helmholtz energy or 'intrinsic' energy of the fluid corresponds to one term of Grand potential.

Let us now consider case where we have a reservoir of constant temperature and chemical potential. In such case, the uniform fluid from above is determined by the chemical potential of species μ_i fixed in the reservoir. At this point we complicate system by adding an external potential $\Phi_{ext}(\mathbf{r})$ in a fluid (a simple example of this is rigid polyion in electrolyte solution).

Fluid can no longer be considered as uniform. The inhomogeneity induced by $\Phi_{ext}(\mathbf{r})$ can be described by non-uniform local density $\rho(\mathbf{r})$. Comparing notation for particle densities with or without $\Phi_{ext}(\mathbf{r})$, it is immediately clear that there is a spatial variation in $\rho(\mathbf{r})$ compared to ρ_i in bulk. Particles near walls of polyion have different chemical potential. The so called 'local' chemical potential $\Theta(\mathbf{r})$ of species differs form the one in the bulk as shown below. In the case of one-component fluid, the 'local' chemical potential is defined as

$$\Theta(\mathbf{r}) = \mu - \Phi_{ext}(\mathbf{r}). \tag{2.49}$$

Unlike in the equation that describes Helmholtz energy of ideal gas in absence of external potential, which is function of concentrations, now we are considering functionals. Local densities are now functions of distance from polyion. Grand potential and Helmholtz free energy are functionals (or functions of higher order) of local densities. Moreover, by same analogy local densities are functionals of $\Phi_{ext}(\mathbf{r})$ because it is also function of distance from surface of polyion. Helmholtz and Grand potential are uniquely described by external potential[9].

It follows that slight perturbation in $\Phi_{\mathrm{ext}}(\mathbf{r})$ will result in slight change in $\Theta(\mathbf{r})$. To be more accurate, if there is an infinitesimal change $\delta\Phi_{\mathrm{ext}}(\mathbf{r})$ in external potential, then for a fixed

[9]Proof can be found in Appendix I of paper by R. Evans *Advances in Physics*, **28**, 143 – 200 (1979).

μ there is an infinitesimal change $\delta\Theta(\mathbf{r})$ in 'local' chemical potential. Above we stated that functional is uniquely defined by the external potential, so after infinitesimal change a linear response yields a new functional defined at $\Theta(\mathbf{r}) + \delta\Theta(\mathbf{r})$. In a case infinitesimal change of Grand potential functional can be written as

$$\delta\Omega = \Omega\left[\Theta(\mathbf{r}) + \delta\Theta(\mathbf{r})\right] - \Omega[\Theta(\mathbf{r})] = -\int \mathrm{d}\mathbf{r}\rho(\mathbf{r})\delta\Theta(\mathbf{r}). \tag{2.50}$$

If we now take functional derivative of with respective to 'local' chemical potential, e.g. to variate the Grand potential functional for a small change in $\Theta(\mathbf{r})$, we obtain local density function $\rho(\mathbf{r})$. We have

$$\frac{\delta\Omega\left[\Theta(\mathbf{r})\right]}{\delta\Theta(\mathbf{r})} = -\rho(\mathbf{r}). \tag{2.51}$$

Easiest way to understand it is to imagine how small perturbation in external potential influences energy functional (of course mediated by change in local' densities). In previous section we stated that Grand potential is Legendre transform of Helmholtz energy, following Eq. 2.7. Just like N and μ are conjugate variables, same applies for $\rho(\mathbf{r})$ and $\Theta(\mathbf{r})$. A general form of Grand potential functional expressed as a Legendre transform of Helmholtz free energy functional, is

$$\Omega\left[\Theta(\mathbf{r})\right] = F\left[\rho(\mathbf{r})\right] - \int \mathrm{d}\mathbf{r}\rho(\mathbf{r})\Theta(\mathbf{r}) \tag{2.52}$$

where $F\left[\rho(\mathbf{r})\right]$ is 'intrinsic' property of the fluid, and $\Theta(\mathbf{r})$ is 'local' chemical potential in presence of external potential $\Phi_{ext}(\mathbf{r})$. The Grand potential functional is now completely formulated. Next task is to find most stable state described by such functional. If this was the case with functions, we would simply make a derivative with respect to variable of interest and equate it with 0 to find extremum. For minimisation of functional, the calculus of variation techniques are required [10]. Minimising(or maximising) the Grand potential functional with respect to local densities(slight variation in local density) can be expressed in following way:

$$\frac{\delta}{\delta\rho(\mathbf{r})}\left\{F\left[\rho(\mathbf{r})\right] - \int \mathrm{d}\mathbf{r}\rho(\mathbf{r})\Theta(\mathbf{r})\right\} = 0. \tag{2.54}$$

Equation above represents condition for local density to minimise Grand potential. After variation of functional we obtain

$$\frac{\delta F\left[\rho(\mathbf{r})\right]}{\delta\rho(\mathbf{r})} - \Theta(\mathbf{r}) = 0. \tag{2.55}$$

[10] The condition for y, where $y = y(x)$ is function which minimizes functional $I[y]$ is given by Euler-Lagrange equation.

$$\frac{\partial f}{\partial y} - \frac{\mathrm{d}}{\mathrm{d}x}\left(\frac{\partial f}{\partial y'}\right) = 0. \tag{2.53}$$

where f is integrand of functional $I[y]$. More on variational principle can be found in work by P.C. Hohenbeg and W. Khon, *Phys. Rev. B* **136**, 864 (1964).

Inserting definition for 'local' chemical potential yields

$$\frac{\delta F\left[\rho(\mathbf{r})\right]}{\delta\rho(\mathbf{r})} - \mu + \Phi_{\text{ext}}(\mathbf{r}) = 0 \tag{2.56}$$

which rearranges to

$$\frac{\delta F\left[\rho(\mathbf{r})\right]}{\delta\rho(\mathbf{r})} - \Phi_{ext}(\mathbf{r}) = \mu. \tag{2.57}$$

Acquired expression is the fundamental equation in theory of non-uniform fluids. Chemical potential μ, or any other parameter, can be found as a Lagrange multiplier in terms of constraints. Such constraints are for example total number of particles in the Canonical ensemble, or sum of probabilities in the Micro-Canonical ensemble. Besides being calculated as Lagrange multiplier, chemical potential μ can be fixed to some value which seems either logical or convenient.

Just one more thing to add at this point. In order to make equations more general[119], we split Helmholtz free energy functional into

$$F[\rho] = F_{\text{ideal}} + F_{\text{excess}} \tag{2.58}$$

The ideal term for mixtures was derived in the previous section and is given as

$$F_{\text{ideal}}[\rho] = k_{\text{b}}T \sum_{\alpha} \int_{V} \mathrm{d}\mathbf{r}\, \rho_{\alpha}(\mathbf{r})(\ln(\Lambda^3\rho_{\alpha}(\mathbf{r})) - 1) \tag{2.59}$$

and excess term is sum of various contributions, namely Coulombic but other contributions may arise such as hard sphere repulsions, Leonnard-Jonnes attractions, MSA short-ranged attractions, dispersion interactions, *etc.* Commonly it is written as

$$F_{\text{excess}} = F_{\text{Coulomb}} + F_{\text{correlations}}. \tag{2.60}$$

Such generalization represents powerful approach because all the contributions to total energy of fluid are just summed up. Of course, it should be always kept in mind that such form of decoupled interactions is far from realistic, but since this is still an example of classical mechanics, it has proven reliable and working approach. Minimization of $F[\rho]$ yields Boltzmann distributions of non-interacting particles in the presence of external potential.

Minimization of grand potential functional

We are interested in the free energy of ions arranged in an electric field exhibited by polyion. We consider a continuous solvent model for which only solutes are specifically described. This polyion will later be assumed as TiO_2 nanotube, which is the subject of the next chapter. Solutes densities are denoted as ρ_{α}. At the end of the calculation we will express results in generalized form adequate for the study of mixtures.

For convenience we make derivation in Grand canonical ensemble. In such case, Grand potential functional $\Omega(\mathbf{r})$ is given by Eq. 2.52. After inserting the definition for the local chemical potential given by Eq. 2.49 we obtain

$$\Omega[\rho_\alpha(\mathbf{r})] = F[\rho_\alpha(\mathbf{r})] + \int \rho_\alpha(\mathbf{r})\Phi_{\text{ext}}\mathrm{d}\mathbf{r} - \mu_\alpha \int \rho_\alpha(\mathbf{r})\mathrm{d}\mathbf{r} \tag{2.61}$$

We can now introduce the expression for the Helmholtz functional for ideal gas, as well as replacing the arbitrary external potential Φ_{ext} with electrostatic potential energy equal $z_\alpha e\psi(\mathbf{r})$. We have

$$\Omega[\rho_\alpha(\mathbf{r})] = k_\mathrm{B}T \int \mathrm{d}\mathbf{r}\, \rho_\alpha(\mathbf{r})(\ln(\Lambda_\alpha^3\rho_\alpha(\mathbf{r})) - 1) + \int \rho_\alpha(\mathbf{r}) z_\alpha e\psi(\mathbf{r})\mathrm{d}\mathbf{r} \; - \; \mu_\alpha \int \rho_\alpha(\mathbf{r})\mathrm{d}\mathbf{r}. \tag{2.62}$$

where α denotes type of ion considered, z_α its valency, μ_α is its chemical potential in the bulk, and $\psi(\mathbf{r})$ is electrostatic potential $\psi(\mathbf{r}) = \frac{1}{4\pi\epsilon_0\epsilon_\mathrm{r}} \int \rho_\alpha(\mathbf{r}') \frac{z_\alpha e}{|\mathbf{r}-\mathbf{r}'|}$. $\psi(\mathbf{r})$ is the Coulomb potential. Minimization procedure with respect to $\rho(\mathbf{r})$, results in

$$\frac{\delta\Omega[\rho_\alpha(\mathbf{r})]}{\delta\rho_\alpha(\mathbf{r})} = k_\mathrm{B}T\ln(\Lambda_\alpha^3\rho_\alpha(\mathbf{r})) + z_\alpha e\psi(\mathbf{r}) - \mu_\alpha = 0. \tag{2.63}$$

Rearranging we obtain

$$k_\mathrm{B}T\ln(\Lambda_\alpha^3\rho_\alpha(\mathbf{r})) = \mu_\alpha - z_\alpha e\psi(\mathbf{r}) \tag{2.64}$$

which after dividing by $k_\mathrm{B}T$ and exponentiating yields

$$e^{\ln(\Lambda_\alpha^3\rho_\alpha(\mathbf{r}))} = e^{\frac{\mu_\alpha - z_\alpha e\psi(\mathbf{r})}{k_\mathrm{B}T}} \tag{2.65}$$

where we can now apply rules of logarithmic functions to obtain

$$\Lambda_\alpha^3\rho_\alpha(\mathbf{r}) = e^{\mu_\alpha}\, e^{-z_\alpha e\psi(\mathbf{r})}. \tag{2.66}$$

Finally, after dividing by Λ_α^3 the α-ion distribution take form of

$$\rho_\alpha(\mathbf{r}) = \frac{e^{\frac{\mu_\alpha}{k_\mathrm{B}T}}}{\Lambda_\alpha^3}\, e^{\frac{-z_\alpha e\psi(\mathbf{r})}{k_\mathrm{B}T}}. \tag{2.67}$$

Factor $\frac{e^{\frac{\mu_\alpha}{k_\mathrm{B}T}}}{\Lambda_\alpha^3}$ can be understood as fugacity of species[111]. At this point we need to define value of μ_α. Lagrange multiplier method with the Canonical ensemble constraint of the constant total number of particles $\int \rho_\alpha(\mathbf{r}) = N_\alpha$ yields

$$\mu_\alpha = k_\mathrm{B}T\ln\left(\rho_\alpha^0\Lambda_\alpha^3\right) \tag{2.68}$$

where ρ_α^0 is bulk ion density. Typically it is a concentration of ion in the reservoir. After insertion of chemical potential into 'local' ion density, we recover Boltzmann ion density.

$$\rho_\alpha(\mathbf{r}) = \rho_\alpha^0\, e^{\frac{-z_\alpha e\psi(\mathbf{r})}{k_\mathrm{B}T}}. \tag{2.69}$$

We can now plug expression given by Eq. 2.69 into Eq. 2.62 which yields a full form of Grand potential functional here, but now generalized for any mixture of electrolyte (not only for one species α).

$$\Omega[\rho_\alpha(\mathbf{r})] = k_\mathrm{B}T \sum_\alpha \int \mathrm{d}\mathbf{r}\, \rho_\alpha(\mathbf{r})(\ln(\Lambda_\alpha^3 \rho_\alpha(\mathbf{r})) - 1) + \int \varrho_{el}(\mathbf{r})\psi(\mathbf{r})\mathrm{d}\mathbf{r} \; - \sum_\alpha \mu_\alpha \int \rho_\alpha(\mathbf{r})\mathrm{d}\mathbf{r}. \quad (2.70)$$

where sum goes over all species, and $\varrho_{el}(\mathbf{r}) = \sum_\alpha z_\alpha e \rho_\alpha(\mathbf{r})$ is volume charge density. This functional can be written in a more neat form. By rearranging the terms and keeping in mind definition of μ_α we obtain:

$$\Omega[\rho_\alpha(\mathbf{r})] = k_\mathrm{B}T \sum_\alpha \int \mathrm{d}\mathbf{r}\, \rho_\alpha(\mathbf{r}) \left(\ln\left(\frac{\rho_\alpha(\mathbf{r})}{\rho_\alpha^0}\right) - 1 \right) + \int \varrho_{el}(\mathbf{r})\psi(\mathbf{r})\mathrm{d}\mathbf{r}. \quad (2.71)$$

Calculation of energy can be conducted as a numerical integration of functional integrand over the whole volume. A simple rectangle rule or a composite rule method which is slightly more accurate[11] can be used, depending on the mesh.

[11] Mentioned numerical integration techniques are basically sum of interpolating functions which are easy to integrate. The rectangle rule follows

$$\int_a^b f(x)\mathrm{d}x \approx \; (b-a) f\left(\frac{a+b}{2}\right) \quad ; \quad x \in [a,b] \quad (2.72)$$

whereas for composite rule, the difference is only that interval $[a,b]$ is divided by some integer and the results are summed.

2.3.2 Poisson-Boltzmann Theory

In previous section we have obtained the generalized expression for ion distributions in the presence of the external field, typically originating form charged polyion. As a result after variational calculus on Grand potential functional, or better to say after the minimisation of Grand potential functional, Boltzmann ion (microion) distributions were acquired. We consider this electrostatics problem as one-dimensional along the normal from the surface. Therefore Eq. 2.69 is simplified to

$$\rho_\alpha(r) = \rho_\alpha^0 \exp\left(\frac{-z_\alpha e\psi(r)}{k_\mathrm{B}T}\right) \tag{2.73}$$

where $\rho(r)_\alpha$ describes equilibrium ion density of species α, ρ_α^0 ion number density of species α in the bulk (reservoir). The charge density ϱ is given as

$$\varrho(r) = e\sum_{\alpha=1}^{N} z_\alpha \rho_\alpha(r) \tag{2.74}$$

where N is number of different species (ions) in a solution. The potential $\psi(r)$ is given by Coulomb law or equivalently by Poisson equation:

$$\nabla \cdot \mathbf{E}(r) = \frac{\varrho(r)}{\epsilon_0\epsilon_\mathrm{r}} \tag{2.75}$$

with vacuum dielectric permittivity ϵ_0 and permittivity of medium ϵ_r. If $\mathbf{E}(r) = -\nabla\psi(r)\hat{r}$ is inserted Eq. 2.75, we get

$$\nabla^2\psi(r) = -\frac{\varrho(r)}{\epsilon_0\epsilon_\mathrm{r}}. \tag{2.76}$$

We can now insert charge density relation along with ion distributions into the Poisson equation to get

$$\nabla^2\psi(r) = -\frac{e}{\epsilon_0\epsilon_\mathrm{r}}\sum_{\alpha=1}^{N} z_\alpha \rho_\alpha^0 \exp\left(\frac{-z_\alpha e\psi(r)}{k_\mathrm{B}T}\right). \tag{2.77}$$

which is the Poisson-Boltzmann equation. SI units are understood throughout. Ion densities are given in particle per cubic meter (particle/m^3). Eq. 2.77 is a second order non-linear function which solution requires knowledge of two boundary conditions.

2.4 Additional Concepts in Physical and Colloid Chemistry

This section is devoted to the concepts that are needed for the reader, to simplify later understanding of our models derivation. Some concepts are readily found in graduate-oriented textbooks, whereas some are not. To make sure that the reader is equipped with appropriate knowledge, here we present few of those concepts.

2.4.1 Regular Solution Theory

This section deals with the simple model that can explain the excess free energy associated with mixing of different chemical species. We will provide a short derivation, which is enough to capture a physical interpretation of interactions governed by the contact of species.

To represent a dense fluid made of two-component, we can imagine a finite total volume V divided into cells *i.e.* a lattice model. The schematic representation of lattice model is given in Figure 2.1. Framework of choice is definitely the canonical ensemble where only temperature

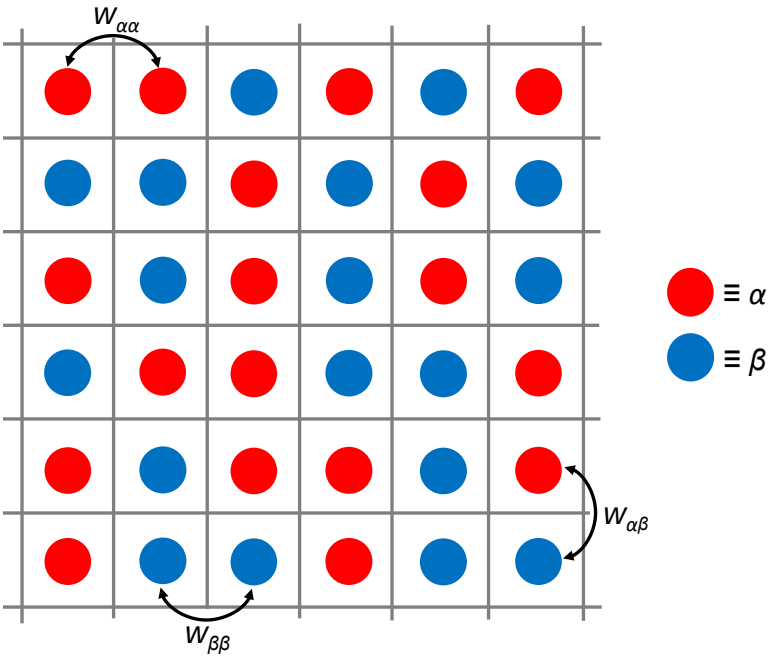

Figure 2.1 – Schematic representation of the lattice model. The red circles denote the particle α, whereas blue circles denote the particle β. $w_{\alpha,\alpha}, w_{\beta,\beta}$, and $w_{\alpha,\beta}$ are respectively the contact energies, as described in the text.

is fixed by the reservoir. For for two-component mixture, the total number of particles reads:

$$N = N_\alpha + N_\beta \tag{2.78}$$

where N_α and N_β are respectively numbers (or amounts) of species α and β. Since we are dealing with the dense fluid, the total volume V is filled in a manner described by Eq. 2.78. The total number of possible α and β arrangements in V (or the number of microstates in entropy vocabulary) is then given as

$$W = \frac{N!}{N_\alpha! N_\beta!} \quad . \tag{2.79}$$

We can now use previously defined relation to obtain the entropy of mixing the two components S_{mix}. We have[12]

$$S_{\text{mix}} = k_{\text{B}}(N_\alpha \ln N + N_\beta \ln N - N_\alpha \ln N_\alpha - N_\beta \ln N_\beta) \quad . \tag{2.80}$$

By introducing the mole fractions x_α and x_β into the above expression, we recover

$$S_{\text{mix}} = N k_{\text{B}} \left(x_\alpha \ln x_\alpha + x_\beta \ln x_\beta\right) \tag{2.81}$$

which clearly has maximum value at $x_\alpha = x_\beta = 0.5$.

To derive the Helmholtz potential, we need the internal energy contribution U_{mix}. We can imagine that U_{mix} is the sum of all contact energies between species α and β arranged in the lattice which represents volume of the system. In this simple representation, we have

$$U_{\text{mix}} = n_{\alpha,\alpha} w_{\alpha,\alpha} + n_{\beta,\beta} w_{\beta,\beta} + n_{\alpha,\beta} w_{\alpha,\beta} \tag{2.82}$$

where $n_{\alpha,\alpha}$, $n_{\beta,\beta}$, and $n_{\alpha,\beta}$ are respectively the total numbers of particular contacts, whereas $w_{\alpha,\alpha}$, $w_{\beta,\beta}$, and $w_{\alpha,\beta}$ are associated contact energies. At this point we can simply count the total number of cell 'walls' of particular contact as an product of the number of particular species *i.e.* cells (N_α or N_β) and the maximum number of accessible walls z *i.e.* first neighbours constrained by geometry of the cell. This yields expressions

$$n_{\alpha,\alpha} = \frac{z N_\alpha x_\alpha}{2} \tag{2.83}$$

and

$$n_{\beta,\beta} = \frac{z N_\beta x_\beta}{2} \quad . \tag{2.84}$$

Still, $n_{\alpha,\beta}$ is unknown. The factor $1/2$ is inserted to avoid double counting of contacts. To obtain an approximate expression, we employ the mean-field approximation, where we have assumed the completely random mixing of cells, irrespective of the magnitude of the interaction energies. The procedure is described in detail in reference [123]. Reported $n_{\alpha,\beta}$ can be written as

$$n_{\alpha,\beta} = \frac{z x_\alpha N_\beta}{N} \quad . \tag{2.85}$$

Finally we can insert expressions given by Eq. 2.83 - 2.85 into Eq. 2.82 to obtain

$$U_{\text{mix}} = \left(\frac{z w_{\alpha,\alpha}}{2}\right) N_\alpha + \left(\frac{z w_{\beta,\beta}}{2}\right) N_\beta + k_{\text{B}} T \chi_{\alpha,\beta} \frac{N_\alpha N_\beta}{N} \quad . \tag{2.86}$$

where $\chi_{\alpha,\beta}$ is the exchange parameter defined as

$$\chi_{\alpha,\beta} = \frac{z}{k_{\text{B}} T} \left(w_{\alpha,\beta} - \frac{w_{\alpha,\alpha} + w_{\beta,\beta}}{2}\right) \quad . \tag{2.87}$$

$\chi_{\alpha,\beta}$ is a dimensionless quantity and is adjusted parameter. The physical meaning of $\chi_{\alpha,\beta}$ can be understood the measure of interactions between particles:

[12] Again with the use of Stirling's approximation.

1. When $\chi_{\alpha,\beta} < 0$ the interactions between species are favorable.

2. When $\chi_{\alpha,\beta} > 0$ the interactions between species are unfavorable.

If we now wish to obtain the expression for the difference between mixture and pure phases we combine Eq. 2.81 and Eq. 2.86. By subtracting the pure phases internal energy terms, we obtain a familiar expression

$$\Delta F_{\text{mix}} = Nk_{\text{B}}T\left(x_\alpha \ln x_\alpha + x_\beta \ln x_\beta\right) + Nk_{\text{B}}T\chi_{\alpha,\beta}x_\alpha x_\beta \quad . \tag{2.88}$$

where ΔF_{mix} is the free energy difference. From this expression one can further derive many interesting properties, such as the activity coefficients by differentiating with respect to the number of species, *etc.*.

We have used the described concept when we needed to account for interactions between different extractant head groups in mixed film. As will be explained in later chapters, we simply generalized Regular Solution Theory to 2D plane.

2.4.2 The Free Energy of Curved Amphiphile-Filled Water/Oil Interface

Effects of packing the amphiphilic molecules onto the water/oil interface are some of dominant contributions in the free energy of the colloid self-assembly. The curvature of the interface matters and based on it, some generality among the occurring shapes and associated free energy was introduced[124, 56]. Still, approximating the interface simply as the infinitely thin film could not capture the effect entirely, which lead to improvements that included a geometrical properties of amphiphilic molecules.

A useful and manageable concept came in the form of defining the preferred, optimum, or the spontaneous packing properties of the amphiphile in the film[125]. The spontaneous packing parameter p_0 is defined as

$$p_0 = \frac{V_{\text{chain}}}{a_0 l_{\text{chain}}} \tag{2.89}$$

where V_{chain} is the partial molar volume of the hydrophobic chains, a_0 is area per head group, and l_{chain} is the average length of chains in a given solvent. p_0 is sort of equation of state since it depends on system variables such as temperature, chemical potentials of salts in the system, *etc.* Important is also the choice of organic solvent since it affects the value of both V_{chain} and l_{chain}. Based on this concept the value of p_0 sets:

1) The preferred curvature of the extractant film towards the water. By convention the curvature towards the water is positive, whereas negative towards the oil.

2) An approximate morphology of the self-assembled aggregate.

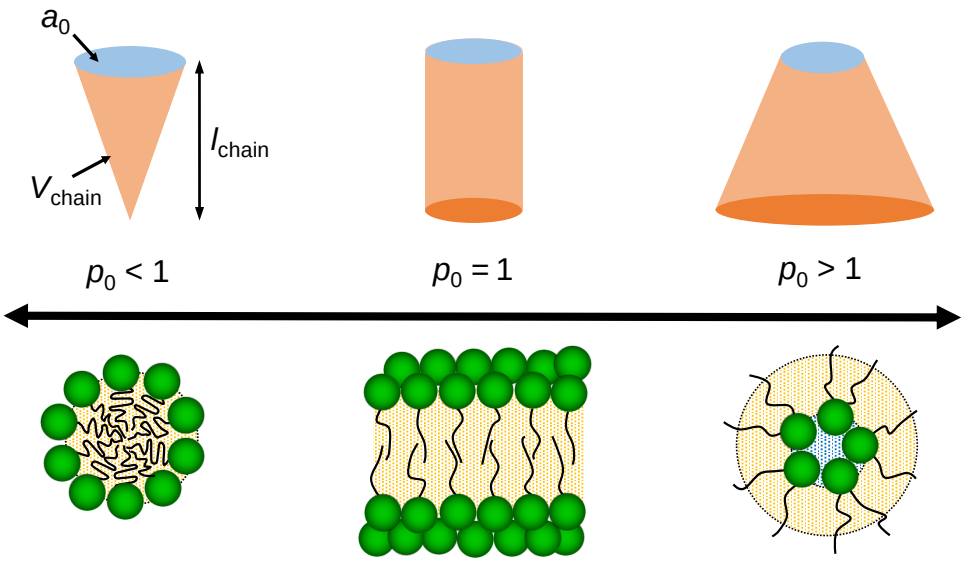

Figure 2.2 – Schematic representation the spontaneous packing parameter p_0 and preferential geometry of aggregates.

The concept is illustrated in Figure 2.2 (quite simplified representation). We can see that on opposite regions of p_0 scale (black arrow), the two distinct morphologies are identified. For the case of $p_0 \leq 1$, spherical direct micelles (oil-in-water) are preferred, whereas $p_0 > 1$ the reverse micelles (water in-oil) are preferred. Between the two extremes, a myriad of structures is predicted to exists. In the context of this thesis, those structures are not required, and are therefore excluded from further considerations. As will be demonstrated, we will deal with the reverse micelles characterized by $p_0 > 1$.

So far, we have defined p_0, but definition itself is inadequate to calculate the associate free energy of the bent extractant film *i.e.* we do not have a functionality to compose a thermodynamic potential. To overcome this difficulty the following idea was proposed. Each amphiphile molecule for each distinct morphology at given conditions of the system, has associated equilibrium state defined by p_0. In practical case the extractant is in a similar but not exactly the same 'ideal' state. The current, practical state is described as the packing parameter p. We can study this departure from 'ideal' state in a form of harmonic approximation, which is quadratic by nature. If we furthermore multiply this factor by a number of such extractants in the film

and the proportionality constant of energy units[126], we obtain the following expression

$$F = \frac{N_{\mathrm{Agg}}\kappa^{\star}}{2}\left(p - p_0\right)^2 \tag{2.90}$$

where N_{Agg} is the number of amphiphiles is the film, and $\kappa^{\star}$ is generalized bending constant *i.e.* the proportionality constant. The analytical expression for p will be given in later in this thesis manuscript, along with appropriate references where full derivation can be found.

Chapter 3

Charge Properties of Nanotubular Adsorbents in an Aqueous Solution: an example of TiO_2 Nanotubes

We have studied the charge properties of TiO_2 NTs from both experimental and theoretical aspect. The surface charge properties of titania nanotubes in $NaNO_3$ solution were investigated through electrophoretic mobility and polyelectrolyte colloid titration measuring techniques. In addition, we used HR-TEM imaging to determine the morphology of TiO_2 NTs. A theoretical model based on the classical Density Functional Theory coupled with the charge regulation method in terms of mass action law was developed in order to understand the experimental data and to provide insights into charge properties at different physical conditions, namely pH and $NaNO_3$ concentration. Rationalization of the pH, the reservoir salt concentration and the inner nanotube radius influences was discussed. At low reservoir salt concentrations our calculations reported surprising result of accumulation of the charge at the outer surface of nanotube, which was attributed to the inefficient screening of the inner surface charge by ions confined inside the pore.

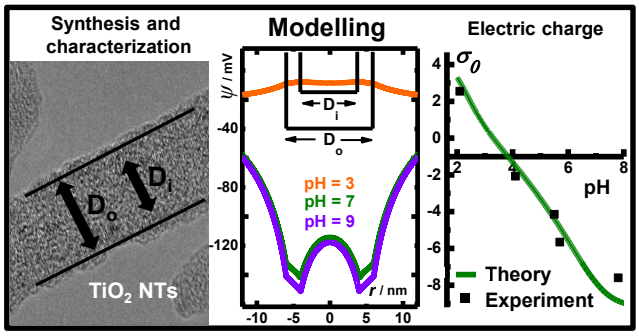

Figure 3.1 – Approach to study charge properties of porous materials

3.1 Proposition of new type of material: TiO_2 nanotubes

Over the past few decades, titanate nanomaterials and their application in adsorption and separation nanotechnology constitute a fast-growing field of interest[127, 128, 129, 130, 131, 132]. Among a variety of possible titanate morphologies, we focus on the one-dimensional (1D) titanate nanoparticle morphologies, namely titanium dioxide nanotubes (TiO_2 NTs) do to their enhanced properties. TiO_2 NTs represent a versatile material with already well-established applications[133]. TiO_2 NTs are possibly an efficient adsorbent for separation (decontamination) of radioactive cations from wastewater. There few aspect that come into play. For example, economical aspect and industrial scale-up potential of TiO_2 NTs is due to the fact that the material is synthesized via inexpensive optimized hydrothermal method[134]. Conveniently, the method provides mostly anatase phase solid which is suitable for the study of decontamination efficiency due to the well-exposed surface groups (towards the aqueous media). Furthermore TiO_2 NTs are multilayered structures with the radius up to a few tens of nanometers, characterized by very high specific surface (from 200-300 m^2 g^{-1}), synthesis-tuneable number of walls and radius lengths, high electrical conductivity, hydrophilicity which governs a stability (ageing) of suspensions, pH tuneable adsorption of heavy ions, one-step functionalization with organic amphiphilic molecules. The above-mentioned properties make TiO_2 NTs extremely efficient ion-exchangers which also makes them the ideal tool in the context of decontamination sciences and industrial processes.

But before any application for separation or decontamination, we need to properly describe the charge properties of TiO_2 NTs. Electrostatics of the system impact the efficiency of applied processes in the aqueous solution. To describe charge properties, we have made a study which involved experimental and theoretical part, as will be presented within this chapter. The benefit of doing so is twofold. First, the fundamental science of ions behavior inside cavities of porous materials will be studied. Second, in the attempt to clarify the phenomenon at hand with simple and manageable theories, we simultaneously provide chemical engineering with the framework for more accurate separation process design. Here we focus on a simple case of TiO_2 NTs suspended in a dilute $NaNO_3$ aqueous solution.

3.2 Experimental support: ingredients for the development of the mesoscopic model

We start by presenting the results of the experimental support, made within the scope of the project. The experimental measurements were, based on our planning, conducted by collaborators, which were appropriately acknowledged in the Acknowledgments section. For the purpose of the completeness of the work, we have provided a details of conducted experiments in Appendix A. Details are left to the reader, and not described in the main body of the thesis manuscript.

HR-TEM imaging

From HR-TEM images presented in Figures 3.2a-d, it was concluded that TiO_2 NTs were few hundreds nanometer long and around 12 nm thick. Structures were double walled and showed faint and diffuse electron diffraction pattern indicating very poor crystallinity. After the synthesis the analyzed TiO_2 NTs were not annealed at high temperature, therefore a substantial amount of the amorphous mass present within the raw TiO_2 NTs sample. Two visible circles in diffraction pattern could be indexed as (101) and (200) planes of anatase (inset Figure 3.2b). Still, other lines are missing which is characteristic of incomplete crystallinity. The same could be concluded from EELS spectrum (inset Figure 3.2a) where Ti L3 and L2 edges were observed without crystal splitting, characteristic for fully crystalline material with +4 valence state of titanium (like in anatase, rutile or brookite). Evidence that we successfully functionalized the TiO_2 NT surface with polyelectrolyte is seen in Figure 3.2d where 1 - 2 nm thick layer of organic material with different contrast could be observed (inset is showing the surface at higher magnification). The sample of polyelectrolyte functionalized TiO_2 NT corresponds to residue after charge determination in Mutek-PCD05. Non-functionalized TiO_2 NT has a clean and smooth surface as shown in Figure 3.2c.

Electrophoretic mobility as a function of bulk pH

Figure 3.3 represents the electrophoretic mobility of the TiO_2 NTs as a function of pH with $c(NaNO_3)$=0.001 mol dm^{-3} as a supporting electrolyte. Results of electrophoretic mobility measurements are given for a qualitative purpose only and only the correlation between the mobility and surface charge is considered[74, 135, 136]. The reason is in the fact that we have investigated a hollow cylindrical particles of various sizes for which the evaluation of ζ-potential

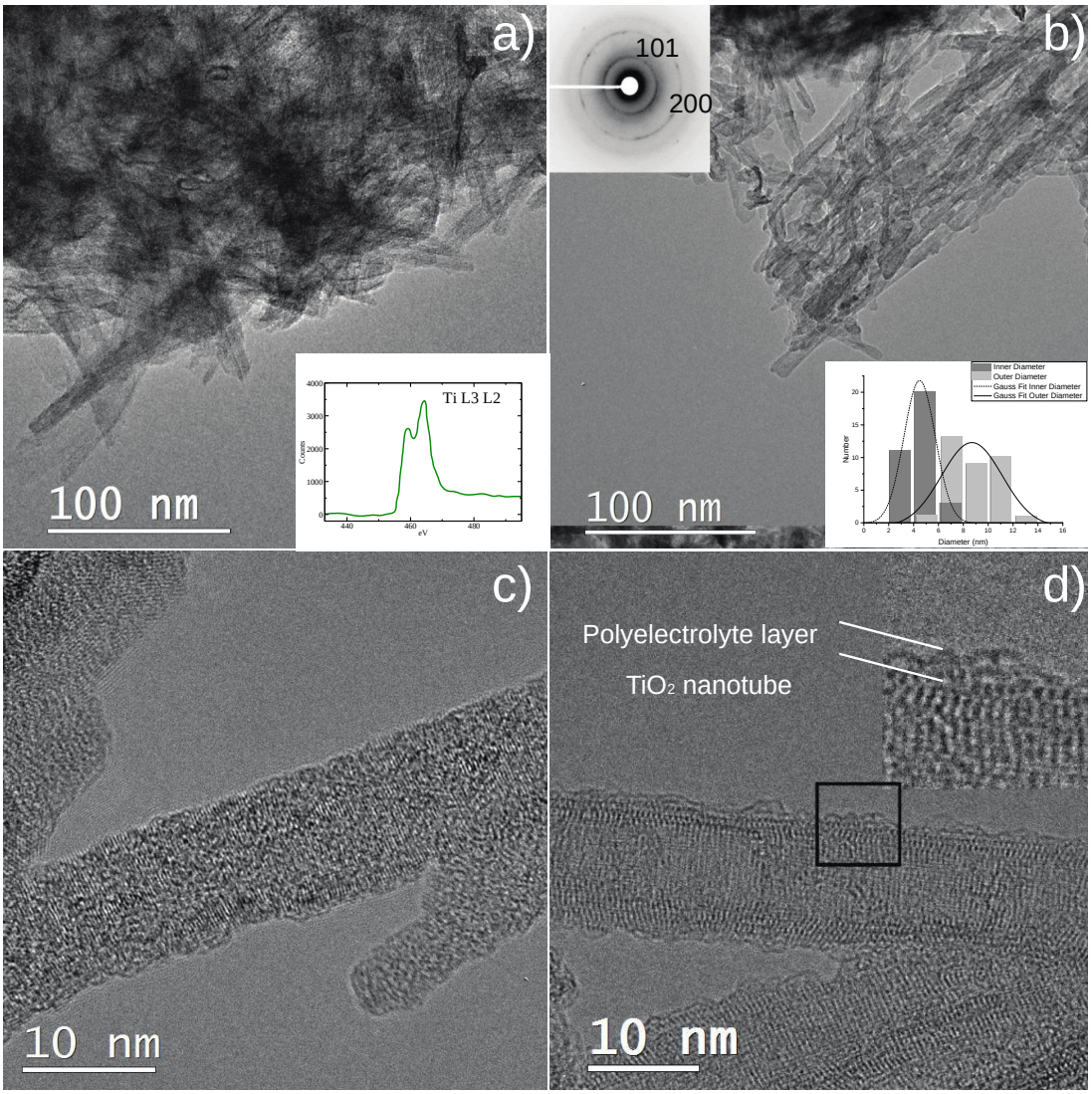

Figure 3.2 – HR-TEM micrographs of TiO_2 NTs sample. a) few hundreds nanometer sized TiO_2 NTs with characteristic EELS spectrum of poorly crystalized titania (inset), b) TEM image of functionalized nanotubes with selected area electron diffraction pattern in upper-left and distribution curve in terms of the inner and outer radii of TiO_2 NTs in the lower right corner inset. Two visible circles were indexed as 101 and 200 anatase planes, c) pure TiO_2 NT with clean and flat surface and d) functionalized TiO_2 NT surface with polyelectrolyte where rough 1-2 nm sized layer could be observed at the surface (inset).

through Smoluchowski equation is not valid. Therefore no quantitative conclusion about the surface charge properties can be drawn. Yet, few things can be noted. First, the shape of the mobility μ as a function of pH reveals the asymmetry with respect to the isoelectric point, pH_{iep}, which is probably a consequence of the asymmetric charges of anatase phase surface groups. The isoelectric point pH_{iep} is around pH = 3.6. When pH is higher than pH_{iep} the outer surface of the TiO_2 NTs is negatively charged. When pH is below pH_{iep} the surface is positively

charged. This is a consequence of the proton exchange equilibria, which is governed by the change in pH. One more thing to add here is the plateau of measured μ at pH values higher than 9. Such regime is a consequence of high surface charge of TiO_2 NTs, which is typical for fully deprotonated surface sites. High electric field at the interface causes an efficient screening by counterions, so far from the surface, the apparent charge remains constant[137]. Further increase of bulk pH does not increase electrophoretic mobility.

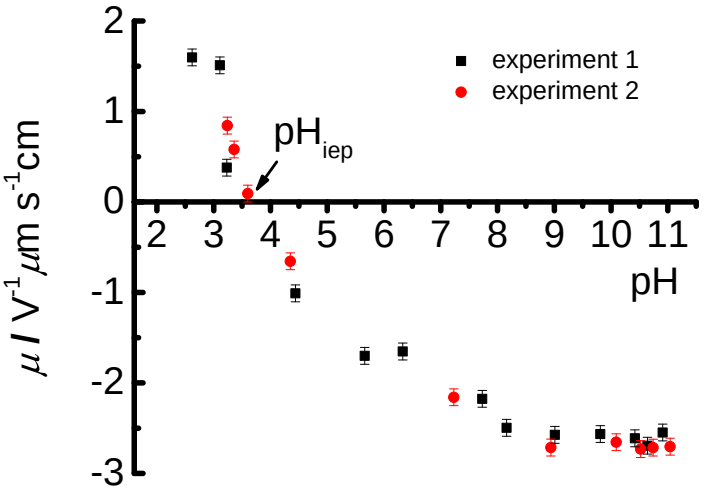

Figure 3.3 – Electrophoretic mobility of the TiO_2 NTs in $NaNO_3$ aqueous electrolyte solution as a function of pH at $\gamma = 0.1$ g dm^{-3}, $c(NaNO_3) = 0.001$ M, and $T = 298$ K. The results of the two independent measurements are presented.

Surface charge as a function of bulk pH

TiO_2 NTs bare charge was measured by the titration with strong (fully dissociated) polyelectrolyte as a function of pH[138, 129]. This method is especially accurate at low salt concentrations[139, 140]. Results presented in Figure 3.4. Data show continuous increase in positive charge of TiO_2 NTs when pH is decreased (left of point of zero charge), while negative charge builds up with increasing pH (right of the point of zero charge). The increase in TiO_2 NTs charge (for pH higher than the point of zero charge) is a consequence of the deprotonation of surface groups. Compared to electrophoretic mobility measurements presented in Figure 3.3, there is no leveling-off of the surface charge. This distinction will be further addressed in the following section, in Figure 3.6. It is the wish of the authors to provide a reasonable explanation for the experimental chemists who often try to recover protonation constants, but

rarely succeed in providing consistent data. It is convenient to summarize the experimental

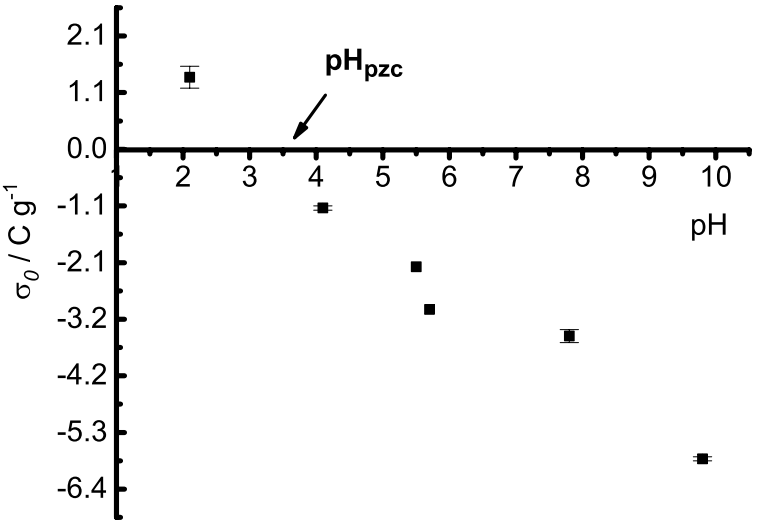

Figure 3.4 – Determination of TiO_2 NTs total charge by polyelectrolyte titration. The data are expressed in charge per unit of mass of the sample as a function of pH at $\gamma = 0.1$ g dm^{-3}, and $c(NaNO_3) = 0.001$ M, $T = 298$ K.

indications and ingredients on which we based our model.

Ingredients for the model: a summary of experimental support

1. Diffraction patterns indicated anatase phase (along with amorphous material) in the sample: we can use protonation reactions for the charge regulations depicted by eq 3.14 and 3.15 (Figure 3.2b).

2. Geometrical parameters: the inner and the outer TiO_2 NTs radii we taken as an average obtained form polydispersity curves of the analyzed sample, hence $R_i = 4$ nm and $R_o = 6$ nm (Figure 3.2b).

3. Asymmetries in electrophoretic mobility and surface charge density versus suspension pH indicated asymmetry of surface site charge upon protonation/deprotonation reaction (Figures 3.3 and 3.4).

4. Assumed 1:1 stoichiometry of the surface site/polyelectrolyte monomer unit charge compensation upon colloids condensation, is based on the HR-TEM micrograph showing a monolayer of polyelectrolyte backbone attached to the nanotube surface(Figure 3.2d).

3.3 Theoretical Section

The TiO_2 NTs are modeled as infinitely long cylinders so the electric field edge effects are neglected, as presented in Figure 3.5. Based on the structural characterization presented in the inset of Figure 3.2b, the inner cylinder radius is taken as $R_\mathrm{i} = 4$ nm and the outer radius as $R_\mathrm{o} = 6$ nm. Both the inner and outer cylinder surfaces are in contact with an aqueous solution of univalent electrolyte. The origin of a cylindrical coordinate system is placed at the center of the cylinder with the abscissa axis being radial coordinate r and ordinate axis being along the cylinder axis. Both electrolyte solution and TiO_2 layer are considered as dielectric continua with dielectric constants being respectively $\epsilon_{\mathrm{r},1}$ and $\epsilon_{\mathrm{r},2}$. The schematic representation of our model is provided in Figure 3.5.

The inner cylinder surface is characterized by the uniform surface charge density σ_i and the outer surface with the uniform surface charge density σ_o.

3.3.1 Bulk Model for Electrostatics of Cylindrical System

Within the framework of classical Density Functional theory, described in previous chapter, we can construct the grand-canonical functional. For the case of ions considered as point-like charges with only electrostatic interactions and no additional correlations taken into account, the grand canonical potential for the change in only radial component can be written as[119]

$$\Omega[\rho_\alpha(r)] = k_\mathrm{b}T \sum_\alpha \int \mathrm{d}^3 r\ \rho_\alpha(r) \left(\ln\left(\frac{\rho_\alpha(r)}{\rho_\alpha^0} \right) - 1 \right) \ + \ k_\mathrm{B}T \int \sum_\alpha z_\alpha \rho_\alpha(r) \Phi(r) \mathrm{d}^3 r \tag{3.1}$$

where $\rho_\alpha(r)$, z_α are respectively one-body ion densities and the charge (or the valency) of the ions α. ρ_α^0 is reservoir ion concentration while $\Phi(r) = e\Psi(r)/k_\mathrm{B}T$ is the 'dimensionless' potential calculated from the Coulomb law. $\Psi(r)$ is the electrostatic potential, e is the elementary charge, k_B is the Boltzmann constant and T is the thermodynamic temperature. The only difference between Eq. 3.1 and 2.71 is the fact that 3.1 is defined through the 'dimensionless' potential. Minimization of grand canonical functional yields usual Boltzmann distributions:

$$\rho_\alpha(r) = \rho_\alpha^0 \exp\left(-z_\alpha \Phi(r)\right) \tag{3.2}$$

The system satisfies Poisson equation. Note that experiments made for this study are with 0.001 mol dm^{-3} concentration of $NaNO_3$ therefore the validity of this approach is assured. Inserting Eq. 3.2 into Poisson equation (introduced in previous chapter by Eq. 2.76) leads to Poisson-Boltzmann equation which can be solved for any mixture of electrolyte. In the

cylindrical coordinate system with respect to symmetry the Poisson-Boltzmann equation reads

$$\frac{\mathrm{d}^2\Phi(r)}{\mathrm{d}r^2} + \frac{1}{r}\frac{\mathrm{d}\Phi(r)}{\mathrm{d}r} = -4\pi l_\mathrm{B} \sum_\alpha z_\alpha \rho_\alpha^0 \exp\left(-z_\alpha \Phi(r)\right) \tag{3.3}$$

where $\frac{\mathrm{d}^2}{\mathrm{d}r^2} + \frac{1}{r}\frac{\mathrm{d}}{\mathrm{d}r}$ being radial component of the Laplace operator[1], $l_\mathrm{B} = e^2/4\pi k_\mathrm{B} T \epsilon_0 \epsilon_{\mathrm{r},1}$ is the Bjerrum length and ϵ_0 is the vacuum permittivity. $\kappa = \left(4\pi l_\mathrm{B} \sum_\alpha z_\alpha^2 \rho_\alpha^0\right)^{1/2}$ is the inverse Debye length ($\lambda_\mathrm{D} = 1/\kappa$). Since both inner and outer cylinder surfaces are in contact with an electrolyte solution the problem of finding an electrostatic profile consists in solving two coupled nonlinear second-order differential equations with two sets of boundary conditions. The boundary conditions are given by Gauss's Law[141, 142]. Due to the symmetry, in the center of cylinder the electric field goes to zero. The first boundary condition for the dimensionless potential is therefore

$$\left.\frac{\mathrm{d}\Phi(r)}{\mathrm{d}r}\right|_{r=0} = 0 \tag{3.4}$$

Note that even though the electric field along the cylinder axis is zero, the ions can still diffuse inside TiO_2 NTs due to the gradient of concentrations. Even if we consider the length of TiO_2 NTs on micrometer scale, the system is fully equilibriated within few milliseconds. If the Gauss surface encloses volume very close to inner cylinder surface ($r \to R_\mathrm{i}$) then second boundary condition states

$$\left.\frac{\mathrm{d}\Phi(r)}{\mathrm{d}r}\right|_{R_\mathrm{i}} = -\frac{e\int_0^{R_\mathrm{i}} \varrho_{\mathrm{el},1}\, r}{\epsilon_0 \epsilon_{\mathrm{r},1} k_\mathrm{B} T R_\mathrm{i}} \tag{3.5}$$

where $\varrho_{\mathrm{el},1}$ is the electrolyte charge density inside of cylinder. Factor $1/k_\mathrm{B}T$ in denominator of Eq. 3.5 is a consequence of the fact that we are dealing with dimensionless potential $\Phi(r)$. The electrolyte charge density is defined by

$$\varrho_{\mathrm{el,j}}(r) = e\sum_{\alpha=1}^{N} z_\alpha \rho_\alpha(r) \tag{3.6}$$

where index j defines inner or outer cylinder cases. Consequently, $\varrho_{\mathrm{el},1}(r)$ denotes the electrolyte charge density of confined aqueous solution, whereas $\varrho_{\mathrm{el},2}(r)$ denotes the aqueous solution outside the outer nanotube surface. Throughout the text the charge per unit length will be discussed, as was earlier mentioned by stating that edge effects are neglected. Consequently, there is no $2\pi L$ factor in Eq. 3.5 (and in following equations), where L is the length of the

[1]Laplace operator applied on arbitrary function f in cylindrical coordinates reads $\Delta f = \frac{1}{r}\frac{\partial}{\partial r}\left(r\frac{\partial f}{\partial r}\right) + \frac{1}{r^2}\frac{\partial^2 f}{\partial \theta^2} + \frac{\partial^2 f}{\partial z^2}$ where r, θ, and z are respectively the distance from the cylinder axis, the azimuthal angle, and the height (or the length) describing the cylinder. For our practical case, only radial component is necessary, since we consider an infinitely long cylinder.

cylinder. The dimensionless electrostatic potential through neutral TiO_2 layer is obtained by applying the integral form of the Gauss Law

$$\frac{\mathrm{d}\Phi(r)}{\mathrm{d}r} = -\frac{e\int_0^{R_\mathrm{i}} \varrho_{\mathrm{el},1}\, r}{\epsilon_0\epsilon_{\mathrm{r},2}k_\mathrm{B}Tr} - \frac{e\sigma_\mathrm{i}R_\mathrm{i}}{\epsilon_0\epsilon_{\mathrm{r},2}k_\mathrm{B}Tr} \quad . \tag{3.7}$$

We can now use separation of variables method to obtain

$$\mathrm{d}\Phi(r) = -\frac{e\int_0^{R_\mathrm{i}} \varrho_{\mathrm{el},1}\, r\,\mathrm{d}r}{\epsilon_0\epsilon_{\mathrm{r},2}k_\mathrm{B}Tr} - \frac{e\sigma_\mathrm{i}R_\mathrm{i}\mathrm{d}r}{\epsilon_0\epsilon_{\mathrm{r},2}k_\mathrm{B}Tr} \quad . \tag{3.8}$$

The integration of Eq. 3.8 gives[2]

$$\Phi(r) = -\frac{e\int_0^{R_\mathrm{i}} \varrho_{\mathrm{el},1}\, r}{\epsilon_0\epsilon_{\mathrm{r},2}k_\mathrm{B}T}\ln(r) - \frac{e\sigma_\mathrm{i}R_\mathrm{i}}{\epsilon_0\epsilon_{\mathrm{r},2}k_\mathrm{B}T}\ln(r) + A \tag{3.9}$$

where A is the undetermined integration constant. But A can be calculated such that $\Phi(r)$ is continuous at $r = R_\mathrm{i}$. It follows

$$A = \Phi(R_\mathrm{i}) + \frac{e\int_0^{R_\mathrm{i}} \varrho_{\mathrm{el},1}\, r}{\epsilon_0\epsilon_{\mathrm{r},2}k_\mathrm{B}T}\ln(R_\mathrm{i}) + \frac{e\sigma_\mathrm{i}R_\mathrm{i}}{\epsilon_0\epsilon_{\mathrm{r},2}k_\mathrm{B}T}\ln(R_\mathrm{i}) \quad . \tag{3.10}$$

We can now insert Eq. 3.10 into Eq. 3.9 and rearrange the expression to obtain

$$\Phi(r) = \Phi(R_\mathrm{i}) + \frac{e\int_0^{R_\mathrm{i}} \varrho_{\mathrm{el},1}\, r\,\mathrm{d}r}{\epsilon_0\epsilon_{\mathrm{r},2}k_\mathrm{B}T}\ln\left(\frac{R_\mathrm{i}}{r}\right) + \frac{e\sigma_\mathrm{i}R_\mathrm{i}}{\epsilon_0\epsilon_{\mathrm{r},2}k_\mathrm{B}T}\ln\left(\frac{R_\mathrm{i}}{r}\right) \tag{3.11}$$

for $R_\mathrm{i} \leq r \leq R_\mathrm{o}$. Note that in TiO_2 NT layer we have neglected the polarization field $\mathbf{P}$ part of the displacement field $\mathbf{D}$. TiO_2 NT layer is assumed as a material without additional polarization.

Up to this point, the dimensionless potential inside the cylinder and through its walls is obtained. Next thing is to set boundary conditions for the outer surface which is in contact with the outer electrolyte solution. At the outer cylinder surface ($r \to R_o$) the Gauss theorem expresses the electric field as a function of the total charge. The latter is a sum of volume integral of the inner cylinder electrolyte charge density $\varrho_{\mathrm{el},1}(r)$, the charge on the inner and outer surfaces. Consequently, the boundary condition for the potential outside the cylinder reads

$$\left.\frac{\mathrm{d}\Phi(r)}{\mathrm{d}r}\right|_{R_\mathrm{o}} = -\frac{e\int_0^{R_\mathrm{i}} \varrho_{\mathrm{el},1}\, r\, dr}{\epsilon_0\epsilon_{\mathrm{r},1}k_\mathrm{B}TR_\mathrm{o}} - \frac{e\sigma_\mathrm{i}R_\mathrm{i}}{\epsilon_0\epsilon_{\mathrm{r},1}k_\mathrm{B}TR_\mathrm{o}} - \frac{e\sigma_\mathrm{o}}{\epsilon_0\epsilon_{\mathrm{r},1}k_\mathrm{B}T} \tag{3.12}$$

Far from the cylinder's outer surface the potential goes to zero, which guaranties that the overall system is electroneutral (confined aqueous solution + nanotube + aqueous solution in contact to the outer surface of nanotube). The boundary condition is thus

$$\Phi(r >> \kappa^{-1}) = 0 \quad . \tag{3.13}$$

[2] $\int \frac{1}{r}dr = \ln|r|$

The solution of Eq. 3.3 for both cases (inside and outside) with respect to four boundary conditions yields the dimensionless potential which is at the end converted to the electrostatic potential $\Psi(r) = k_{\mathrm{B}}T\,\Phi(r)/e$. For the purpose of easier reproducing of the model results, the summary of four boundary conditions are provided in the following text.

Boundary conditions summary.

1. At the cylinder axis of symmetry:

$$\left.\frac{\mathrm{d}\Phi(r)}{\mathrm{d}r}\right|_{r=0} = 0.$$

2. At the inner surface:

$$\left.\frac{\mathrm{d}\Phi(r)}{\mathrm{d}r}\right|_{R_{\mathrm{i}}} = -\frac{e\int_0^{R_{\mathrm{i}}}\varrho_{\mathrm{el},1}\,r\,\mathrm{d}r}{\epsilon_0\epsilon_{\mathrm{r},1}k_{\mathrm{B}}TR_{\mathrm{i}}}.$$

3. At the outer surface::

$$\left.\frac{\mathrm{d}\Phi(r)}{\mathrm{d}r}\right|_{R_{\mathrm{o}}} = -\frac{e\int_0^{R_{\mathrm{i}}}\varrho_{\mathrm{el},1}\,r\,dr}{\epsilon_0\epsilon_{\mathrm{r},1}k_{\mathrm{B}}TR_{\mathrm{o}}} - \frac{e\sigma_{\mathrm{i}}R_{\mathrm{i}}}{\epsilon_0\epsilon_{\mathrm{r},1}k_{\mathrm{B}}TR_{\mathrm{o}}} - \frac{e\sigma_{\mathrm{o}}}{\epsilon_0\epsilon_{\mathrm{r},1}k_{\mathrm{B}}T}.$$

4. Far from cylinder's outer surface:

$$\Phi(r >> \kappa^{-1}) = 0.$$

The procedure of finding a solution of a system of two coupled non-linear PB equations with regulated surface charge densities are described in detail further in the text as a separate section.

3.3.2 Surface Charge Regulation

In order to obtain boundary conditions, the charging phenomenon was taken into account through charge regulation method which assumes ion exchange equilibira between local sites and ions at the interface.

The charge of TiO_2 NTs is pH-dependent which means that there is an equilibrium between amphoteric surface groups and ions in the solution. The surface charge density is regulated via mass action law[143]. Figure 3.5 shows the schematic representation of the charging processes that take place at both TiO_2 NT surfaces. According to the experimental data the anatase planes were identified in the sample. In anatase phase the Ti^{4+} is coordinated in octahedra with six oxygen atoms. As a surface site we have chosen to consider only singly coordinated sites. By using Pauling concept to estimate bond valence we can estimate the charge of ions consituting the surface sites[144]. Fully deprotonated surface oxygen atom bonded to one Ti^{4+}

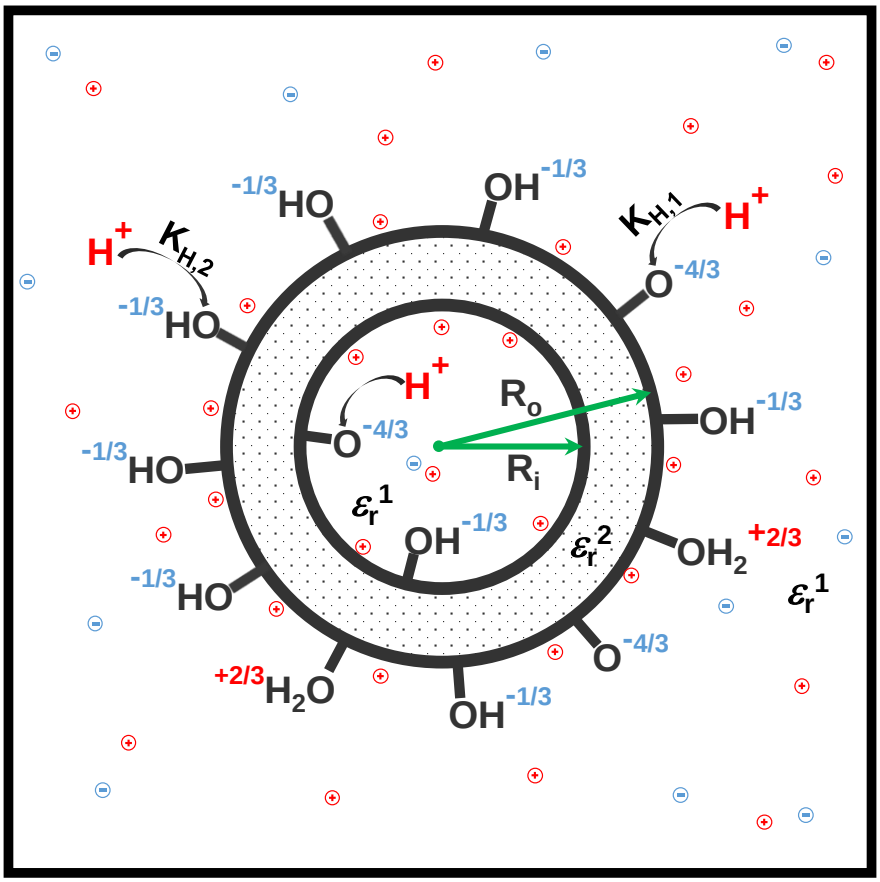

Figure 3.5 – Schematic cross section of TiO_2 NTs. The cross section is perpendicular to cylinder axis of symmetry. R_i and R_o respectively correspond to the inner and outer cylinder radii. $\epsilon_{r,1}$ and $\epsilon_{r,2}$ correspond respectively to electrolyte solution and TiO_2 layer dielectric constants. Surface groups $\equiv TiO^{-\frac{4}{3}}$, $\equiv TiOH^{-\frac{1}{3}}$ and $\equiv TiOH_2^{+\frac{2}{3}}$ are in equilibrium with surrounding electrolyte solution. $K_{H,1}$ and $K_{H,2}$ are surface reactions constants. Proton ions H^+ are distinguished from other ions only because of surface equilibria and autoprotolysis of water. Within the model all ions are point-like charges.

has $-4/3$ e charge in anatase[145], where e is the elementary charge. For such surface groups the following equilibrium protonation reactions are obtained[146]

$$\equiv \mathrm{TiO}^{-\frac{4}{3}} + \mathrm{H}^{+} \rightleftharpoons \equiv \mathrm{TiOH}^{-\frac{1}{3}} \tag{3.14}$$

and

$$\equiv \mathrm{TiOH}^{-\frac{1}{3}} + \mathrm{H}^{+} \rightleftharpoons \equiv \mathrm{TiOH}_2^{+\frac{2}{3}} \tag{3.15}$$

The two equations can be expressed through intrinsic equilibrium constants $K_{\mathrm{H},1}$

$$K_{\mathrm{H},1} = \frac{\{\equiv \mathrm{TiOH}^{-\frac{1}{3}}\}}{\{\equiv \mathrm{TiO}^{-\frac{4}{3}}\}[\mathrm{H}^{+}]_{\mathrm{loc}}} \tag{3.16}$$

and $K_{\mathrm{H},2}$

$$K_{\mathrm{H},2} = \frac{\{\equiv \mathrm{TiOH}_2^{+\frac{2}{3}}\}}{\{\equiv \mathrm{TiOH}^{-\frac{1}{3}}\}[\mathrm{H}^{+}]_{\mathrm{loc}}} \tag{3.17}$$

where $[\mathrm{H}^{+}]_{\mathrm{loc}}$ is the local proton concentration at surfaces, $\{\equiv \mathrm{TiOH}_2^{+\frac{2}{3}}\}$, $\{\equiv \mathrm{TiOH}^{-\frac{1}{3}}\}$, and $\{\equiv \mathrm{TiO}^{-\frac{4}{3}}\}$ are surface site concentrations[147]. The influence of surface groups is taken into account indirectly through mean field approximation[115].

The autoprotolysis of water has been taken into account in order to adjust the reservoir proton and hydroxide ion concentrations. The reaction

$$\mathrm{H_2O} \rightleftharpoons \mathrm{H}^{+} + \mathrm{OH}^{-} \tag{3.18}$$

can be expressed in the form of the chemical equilibrium constant

$$K_{\mathrm{w}} = [\mathrm{H}^{+}]_0[\mathrm{OH}^{-}]_0 \tag{3.19}$$

where the subscript 0 denotes the bulk equilibrium concentrations, K_{w} is the autoprotolysis constant for water[148].

Since our experimental salt concentrations are around 0.001 mol dm^{-3} while molar concentrations of surface groups is around 0.0001 mol dm^{-3} it is safe to assume the ideality of the solution and all its species. Throughout the model the activity coefficients γ are chosen to be 1[149]. With such formulation the surface site density Γ is the sum of all equilibrium surface site concentrations[150].

$$\Gamma = \{\equiv \mathrm{TiO}^{-\frac{4}{3}}\} + \{\equiv \mathrm{TiOH}^{-\frac{1}{3}}\} + \{\equiv \mathrm{TiOH}_2^{+\frac{2}{3}}\} \tag{3.20}$$

Combining equations 3.16, 3.17 and 3.20 yields expressions for equilibrium surface concentrations of each group. Eq. 3.20 is typical Langmuir-like competitive adsorption equation[76]. For

the convenience, it is desirable to write the equilibrium surface concentrations as a product of total site density and the factor called the fractional coverage f_l. The fractional coverage f_l defines the ratio of the particular charged group l in the total number of sites on the surface for a given conditions T, pH, *etc.* In our case, for three types of surface groups (sites) we obtain

$$f_1 = \frac{1}{1 + K_{\mathrm{H},1}[\mathrm{H}^+]_{\mathrm{loc}} + K_{\mathrm{H},1}K_{\mathrm{H},2}[\mathrm{H}^+]^2_{\mathrm{loc}}} \tag{3.21}$$

$$f_2 = \frac{K_{\mathrm{H},1}[H^+]_{\mathrm{loc}}}{1 + K_{\mathrm{H},1}[\mathrm{H}^+]_{\mathrm{loc}} + K_{\mathrm{H},1}K_{\mathrm{H},2}[\mathrm{H}^+]^2_{\mathrm{loc}}} \tag{3.22}$$

$$f_3 = \frac{K_{\mathrm{H},1}K_{\mathrm{H},2}[\mathrm{H}^+]^2_{\mathrm{loc}}}{1 + K_{\mathrm{H},1}[\mathrm{H}^+]_{\mathrm{loc}} + K_{\mathrm{H},1}K_{\mathrm{H},2}[\mathrm{H}^+]^2_{\mathrm{loc}}} \tag{3.23}$$

where f_1, f_2, and f_3 are respectively fractional coverages of the $\equiv\mathrm{TiO}^{-\frac{4}{3}}$, $\equiv\mathrm{TiOH}^{-\frac{1}{3}}$, and $\equiv\mathrm{TiOH}_2^{+\frac{2}{3}}$ surface groups. Sum of f_{l}-s is always 1. This fact can be used as a indicator of accuracy within calculations. If sum of f_l is not equal to 1, there is an error in calculations or there is severe numerical noise. In either case, it is convenient to preform this control. Surface charge density expressed through f_l reads

$$\sigma_{\mathrm{j}} = e\Gamma \sum_{l=1}^{3} z_l f_l \tag{3.24}$$

where index $j = i$ or o defines inner or outer surface, z_l is the charge of the surface group l. σ_i and σ_o are functions of electrostatic potentials at the two solid/electrolyte solution interfaces. We can write the full expression of the surface charge density (for our case of anatase-based surface groups) of individual surfaces as

$$\begin{aligned}\sigma_{\mathrm{j}} = e\Gamma \Bigg[& \frac{z_1}{1 + K_{\mathrm{H},1}[\mathrm{H}^+]_{\mathrm{loc}} + K_{\mathrm{H},1}K_{\mathrm{H},2}[\mathrm{H}^+]^2_{\mathrm{loc}}} + \\ & \frac{z_2 K_{\mathrm{H},1}[H^+]_{\mathrm{loc}}}{1 + K_{\mathrm{H},1}[\mathrm{H}^+]_{\mathrm{loc}} + K_{\mathrm{H},1}K_{\mathrm{H},2}[\mathrm{H}^+]^2_{\mathrm{loc}}} + \\ & \frac{z_3 K_{\mathrm{H},1}K_{\mathrm{H},2}[\mathrm{H}^+]^2_{\mathrm{loc}}}{1 + K_{\mathrm{H},1}[\mathrm{H}^+]_{\mathrm{loc}} + K_{\mathrm{H},1}K_{\mathrm{H},2}[\mathrm{H}^+]^2_{\mathrm{loc}}} \Bigg]\end{aligned} \tag{3.25}$$

3.3.3 Autoprotolysis of Water

The autoprotolysis of water (Eq. 3.19) occurs everywhere in space. In the present algorithm it is assumed only in the reservoir. Nevertheless, considering the mathematical form of the equation it is in fact valid anywhere in space, as can be understood from the following argument.

When the potential Ψ is not zero, the generalization of the mass action law is:

$$\mu_{\mathrm{w}} = \mu_{\mathrm{H}^+} + \mu_{\mathrm{OH}^-} = \mu^\circ_{\mathrm{H}^+} + k_{\mathrm{B}}T \ln \frac{\rho_{\mathrm{H}^+}}{\rho^\circ} + e\Psi + \mu^\circ_{\mathrm{OH}^-} + k_{\mathrm{B}}T \ln \frac{\rho_{\mathrm{OH}^-}}{\rho^\circ} - e\Psi \tag{3.26}$$

where μ_{w}, $\mu_{\mathrm{H^+}}$, $\mu_{\mathrm{OH^-}}$ are respectively the chemical potentials of water, H^+ and OH^-. $\mu^{\circ}_{\mathrm{H^+}}$ and $\mu^{\circ}_{\mathrm{OH^-}}$ are standard chemical potentials of H^+ and OH^-, while ρ° is the concentration of the standard state. Consequently, because H^+ and OH^- have an opposite charge, the mass action law (Eq. 3.19) is not modified. The autoprotolysis of water is valid if the equality

$$\rho_{\mathrm{H^+}}\rho_{\mathrm{OH^-}} = K_{\mathrm{w}} \tag{3.27}$$

is true everywhere in the system. The latter equality is automatically satisfied by the Poisson-Boltzmann equation because

$$\rho_{\mathrm{H^+}}(r) = [\mathrm{H^+}]_0 \exp\left(-e\Psi(r)/k_{\mathrm{B}}T\right) \tag{3.28}$$

while the local hydroxide concentrations are equal to

$$\rho_{\mathrm{OH^-}}(r) = [\mathrm{OH^-}]_0 \exp\left(e\Psi(r)/k_{\mathrm{B}}T\right) \tag{3.29}$$

so that we recover the same equilibria as the one in the reservoir.

3.3.4 Algorithm for Finding a Solution of Coupled Non-linear PB equations system

After establishing appropriate boundary conditions, next step is to solve the system of non-linear equations. The solution of system was obtained by numerical integration. The length of the system, or the interval of concern was discretized. The interval was considered starting from the cylinder's axis of symmetry (the center of the coordinate system) and ranging to a value for which boundary condition in Eq 3.13 is fulfilled. For r being the distance from the center of the coordinate system, we define Δr as step in numerical propagation. In our work, Δr was taken as a quantity 1000 times smaller than the smallest physical lengths in the system (cylinder radii R_{i} and R_{o}, Bjeruum length l_{B}, and Debye length λ_{D}. On a discretized interval, the next thing is to define potential derivatives. If Δr is sufficiently small ($\Delta r \to 0$), then the derivative of the potential Φ_n around a given point n in discretized interval is defined as:

$$\left.\frac{\mathrm{d}\Phi}{\mathrm{d}r}\right|_{\mathrm{n}} = \frac{\Phi_{n+1} - \Phi_{n-1}}{2\Delta r} \tag{3.30}$$

where Φ_{n-1} and Φ_{n+1} are respectively potentials at positions n-1 and n+1. In similar fashion the second derivative around point n is derived and expression is

$$\left.\frac{\mathrm{d}^2\Phi(r)}{\mathrm{d}r^2}\right|_{\mathrm{n}} = \frac{\Phi_{n+1} + \Phi_{n-1} - 2\Phi_n}{\Delta r^2}. \tag{3.31}$$

Note that derivatives could be derived from expansion by Taylor series. In that case we would obtain following expression for the first derivative.

$$\left.\frac{\mathrm{d}\Phi}{\mathrm{d}r}\right|_{\mathrm{n}} = \frac{4\Phi_{n+1} - \Phi_{n+2} - 3\Phi_n}{\Delta r} \tag{3.32}$$

We must emphasize that for sufficiently small Δr, there are almost no differences in calculated electrostatic potential profiles, therefore, we adopt former, simpler definition of derivatives on discretized interval. We can now insert Eq 3.30 and 3.31 in Laplace operator. Again, considering only radial component $\frac{\mathrm{d}^2}{\mathrm{d}r^2} + \frac{1}{r}\frac{\mathrm{d}}{\mathrm{d}r}$, we recover

$$\Delta\Phi_n = \frac{\Phi_{n+1} + \Phi_{n-1} - 2\Phi_n}{\Delta r^2} + \frac{1}{r_n}\frac{\Phi_{n+1} - \Phi_{n-1}}{2\Delta r} \tag{3.33}$$

where r_n is the distance at point n on discretized interval. From this stage finding a solution to Poisson-Boltzmann equation is straightforward. Combining Eq 3.3 and Eq 3.33 yields

$$\frac{\Phi_{n+1} + \Phi_{n-1} - 2\Phi_n}{\Delta r^2} + \frac{1}{r_n}\frac{\Phi_{n+1} - \Phi_{n-1}}{2\Delta r} = -4\pi l_{\mathrm{B}} \sum_{\alpha} z_\alpha \rho_\alpha^0 \exp\left(-z_\alpha \Phi(r)\right). \tag{3.34}$$

In order to isolate Φ_{n+1}, which represents every subsequent point in the propagation, we rearrange Eq 3.34 to obtain

$$\Phi_{n+1} = \frac{\left(-\Delta r^2 4\pi l_{\mathrm{B}} \sum_\alpha z_\alpha \rho_\alpha^0 \exp\left(-z_\alpha \Phi(r)\right) - \Phi_{n-1} + 2\Phi_n + \frac{\Delta r\, \Phi_{n-1}}{2r_n}\right)}{\left(1 + \frac{\Delta r}{2r_n}\right)}. \tag{3.35}$$

As can be seen from Eq 3.35, a new Φ_{n+1} value is estimated from last previous two values. To start a propagation, the initial guess of potential at the center of the coordinate system is given arbitrary and the rejection method is utilized until all boundary conditions are fulfilled. We must emphasize that in our model, we have regulated surface charge densities as a function of bulk pH. The charge regulation was explained in detail in the previous section. In terms of finding a solution of our system means that potentials at the inner and the outer surface depend on surface charge density, and *vice versa*. Due to that fact the developed rejection algorithm of finding a solution of two coupled second order nonlinear second-order differential equations (Eq. 3.3) is based on self-consistent approach. The calculations have been made on pH-scale in order to decrease the numerical noise which can be severe when dealing with proton concentrations. The rejection algorithm is the following:

1. Calculate $\sigma_{\mathrm{i}}(\Phi_{\mathrm{i}})$ and $\sigma_{\mathrm{o}}(\Phi_{\mathrm{o}})$ for inner surface potential $\Phi_{\mathrm{i}}(R_{\mathrm{i}}) = 0$ and outer surface potential $\Phi_{\mathrm{o}}(R_{\mathrm{o}}) = 0$ (for the first three points only).
2. Find $\Phi_{\mathrm{i}}(R_{\mathrm{i}})$ and $\Phi_{\mathrm{o}}(R_{\mathrm{o}})$ with propagation method described by eq 3.35, where boundary conditions are previously calculated $\sigma_{\mathrm{i}}(\Phi_{\mathrm{i}})$ and $\sigma_{\mathrm{o}}(\Phi_{\mathrm{o}})$.

3. Calculate again $\sigma_{\mathrm{i}}(\Phi_{\mathrm{i}})$ and $\sigma_o(\Phi_o)$ but now with newly acquired values of surface potentials $\Phi_{\mathrm{i}}(R_{\mathrm{i}})$ and $\Phi_{\mathrm{o}}(R_{\mathrm{o}})$.

4. Repeat the procedure until two consecutive calculations do not provide different σ_{i} and σ_{o} (up to the convergence limit).

5. When the convergence is achieved calculate again the electrostatic potential.

It must be noted that even on pH scale, the numerical noise is severe when system is dilute in terms of bulk salt concentrations. The numerical noise can be observed as large number of cycles within convergence loop are generated before the unique solution of potentials is found. Moreover, the subsequently calculated $\sigma_{\mathrm{i}}(\Phi_{\mathrm{i}})$ and $\sigma_{\mathrm{o}}(\Phi_{\mathrm{o}})$ showed a sort of alternating series sequence trend, which interfered with convergence loop performance. In order to guarantee and accelerate the convergence of the calculated surface charge densities, the Aitken's δ^2 numerical accelerator was used[151].

The problem of numerical noise was even more pronounced when titration curve, and its accompanying electrostatic properties were needed to be calculated for pH values approaching the point of zero charge. Detailed analysis of the problem showed that the initial guess of the surface charge density also matters. To overcome this difficulty, the initial guess for surface charge densities at given pH was predicted as extrapolated value, based on previously calculated correct values of surface charge density at given pH. The second-order Lagrange polynomial was constructed on previously calculated surface charge densities. It must be clarified that even though Lagrange polynomial is usually used to interpolate data, in our case it provided a satisfying guess for the surface charge density of subsequent calculation.

This concluded the framework for the calculation of electrostatic potentials and ion distributions in confined media. In the following sections, the experimental work made by our collaborators is described, as well as the results of various techniques are discussed in detail. Moreover, the model was compared with the experimental data and the insights into behavior of ions in confined charged media were obtained.

3.4 Model Predictions and Discussion

3.4.1 Comparison of the Model and Experimental Data

Results of polyelectrolyte titration (Figure 3.4) have been replotted and presented in Figure 3.6. The propagation of the experimental error was not taken into account. The experimental

data of total charge per unit of mass are transformed to charge per unit of length. In this way, we avoided dealing with polydispersity in terms of length of TiO_2 NTs, which is substantial for this type of the materials. Similar considerations have already been reported[152]. The multiplication of charge per length (ordinate axis) and the average length of TiO_2 NTs provides the total average charge. The charge per unit of length can also be converted to surface charge density, if the polydispersity is taken into account. The order of magnitude for measured charge at pH= 10 is only around 30 mC m^{-2} or 0.18 e nm^{-2}. TiO_2 NTs are therefore weakly charged. Figure 3.6 shows transformed titration data along with the predictions of the model for three different sets of adjusted parameters: Γ, $\log K_{H,1}$, and $\log K_{H,2}$.

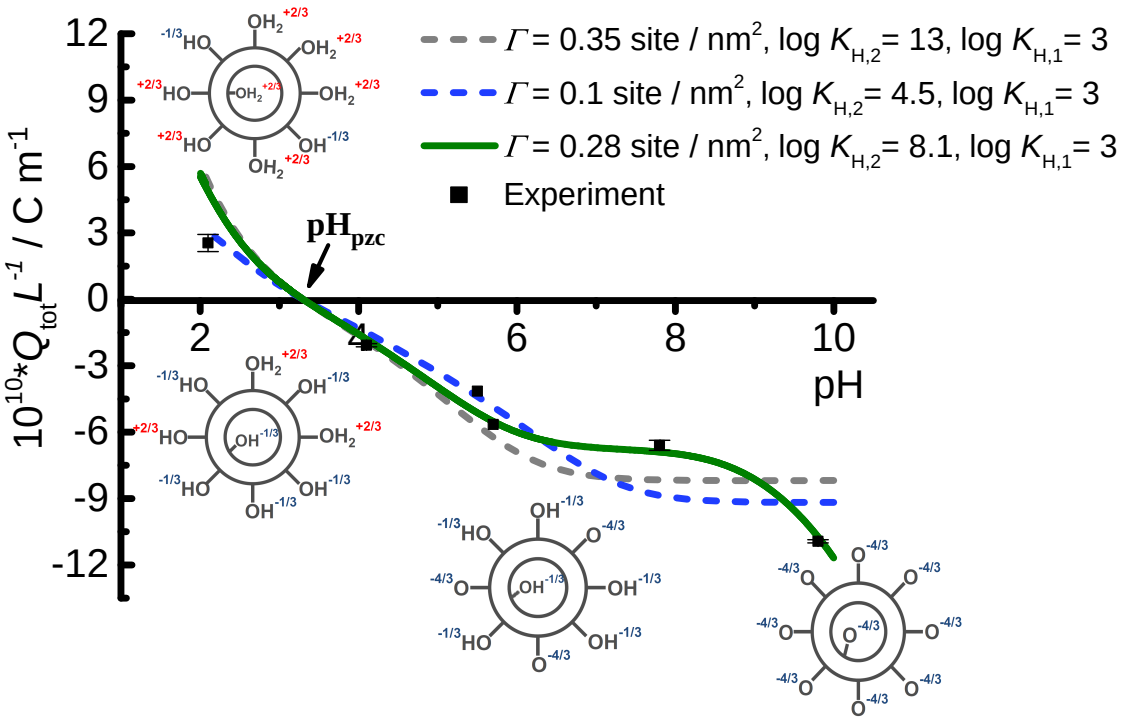

Figure 3.6 – Determination of TiO_2 NTs total charge by polyelectrolyte titration. The data are expressed in charge per unit of length as a function of pH. Black squares denote experimental data whereas solid and dashed curves present possible fits. Schemes representing charging process are added for intuitive purpose. Both experimental data and model calculations are made at/with $T = 298$ K and $c(NaNO_3) = 0.001$ M.

The choice of the protonation constant value

Before proceeding, it must be emphasized that experimental data obtained by polyelectrolyte titration, ζ-potential, potentiometric acid-base, and mass titration measurements provide an

average total charge of examined samples. In the case of porous materials (including TiO_2 NTs), besides the total charge, no other conclusion can be accurately drown about the fractions of charge in the pores. It follows that the results of these methods can be safely interpreted for charge determination of nonporous materials only *i.e.* the ones that have a simple shape and well-defined surface planes (*e.g.* a single crystal). For all other cases, a theoretical description of charging is needed to elucidate the charge distribution in the entire system.

In the special case of dispersed cylinders, like TiO_2 NTs, the total compensated charge during the polyelectrolyte titration is the sum of three terms: the charge of electrolyte solution confined inside of TiO_2 NT, the charge at the inner surface and the charge at the outer surface of the TiO_2 NT (recall Gauss Law). We have

$$Q_{\mathrm{tot}} = 2\pi L \int_0^{R_{\mathrm{i}}} \varrho_{\mathrm{el},1}\, r\, \mathrm{d}r + \sigma_{\mathrm{i}} 2\pi L R_{\mathrm{i}} + \sigma_{\mathrm{o}} 2\pi L R_{\mathrm{o}} \tag{3.36}$$

with L being the average length of TiO_2 NTs, σ_{i} and σ_{o} being the inner and outer surface charge densities. The first term is volume integral of electrolyte charge density inside of TiO_2 NTs. The second and the third terms are the charge on the inner and the outer TiO_2 NTs surfaces and are obtained by multiplying surface charge densities with appropriate surface areas. The first term is always of opposite sign compared to the surface charge densities and it lowers total charge that is compensated during the titration. If we divide both sides of Eq. 3.36 by L the total compensated charge per unit of length is obtained.

$$Q_{\mathrm{tot}} L^{-1} = 2\pi \int_0^{R_{\mathrm{i}}} \varrho_{\mathrm{el},1}\, r\, \mathrm{d}r + \sigma_{\mathrm{i}} 2\pi R_{\mathrm{i}} + \sigma_{\mathrm{o}} 2\pi R_{\mathrm{o}} \tag{3.37}$$

A charge per unit length is plotted in Figure 3.6 as a function of pH. It is crucial to emphasize that interpretation of data we report here is specific to the experimental setup, as should be always done when dealing with complex porous systems. During the titration inside of Mütec-PCD03 titration cell the polyelectrolyte binds to the outer surface of TiO_2 NTs under the influence of moving piston creting the pressure and strong electrostatic forces between these colloids[153, 154]. The polyelectrolyte is under the influence of the electric field created by the total charge Q_{tot} enveloped by Gauss surface (Eq. 3.36 and 3.37). The schematic representation of the polyelectrolyte condensation onto the nanotube, and the total charge compensation is given in Figure 3.7.

In measurements, we used high molar mass polyelectrolyte at 0.001 mol dm^{-3} $NaNO_3$ solution. In this way, we are sure that the polyelectrolyte cannot penetrate inside the TiO_2 NTs thus violating Eq. 3.36. Moreover, at 0.001 mol dm^{-3} salt concentrations (which are the physical conditions of our system), the polyelectrolyte has fully stretched conformation

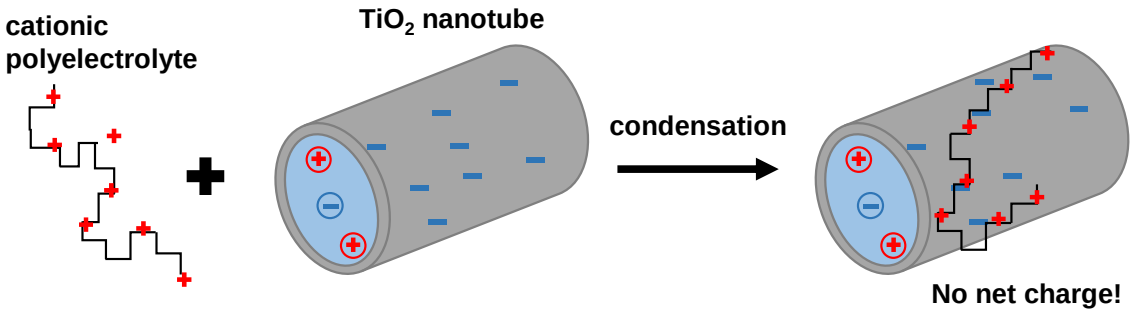

Figure 3.7 – The schematic representation of the phenomenon underlying the polyelectrolyte titration of solid colloids. The charged nanotube along with the ions confined in its interior and charged cationic polyelectrolyte interact via electric force, which governs the condensation thus the charge neutralization.

so it is safe to assume the accuracy of the method. It is worth to mention that HR-TEM measurements of titrated sample show that polyelectrolyte binds to TiO_2 NTs outer surface in monolayer. This finding is important to justify the assumed 1:1 stoichiometry of the charge compensation during the titration experiment. Results can be found in Figure 3.2. Results presented here (the point of zero charge and low charge per length values) are in accordance with those obtained by previous studies of TiO_2 NTs system[80]. Interestingly, in both present and past studies, the charge of TiO_2 NTs is typically one order of magnitude smaller compared to other TiO_2 nanomaterials, namely nanowires or nanosheets[80].

Fitting the experimental data with the model can provide different sets of parameters. Using obtained sets of parameters can lead to different explanations of the system behavior. Yet, a prior knowledge of similar systems points to the fact that only few explanations physically make sense. To ensure that we made a proper choice of parameters, we have identified and described three distinct cases and presented them in Figure 3.6. The calculated point of zero charge, pH_{pzc}, is in our model determined by the second intrinsic protonation constant $\log K_{H,2} = 3$. Therefore, according to the experiment we fixed this value for all three possible fits. This reduces the number of simultaneously fitted parameters to two, namely the surface site density Γ and the first intrinsic protonation constant $\log K_{H,1}$. In the literature, the variety of fitted protonation constants were reported and the differences between them (the difference between $\log K_{H,1}$ and $\log K_{H,2}$) were ranging from 1 up to 20[155, 75]. This inconsistency urged the study to make a clear distinction on how experimental data can be interpreted. Therefore, we have decided to describe three distinct sets of fitted parameters separately. The first case is when $\log K_{H,1}$ and $\log K_{H,2}$ are close and it corresponds to the blue dashed curve in Figure 3.6. If one assumes such parameters then the interpretation of data would be that already at pH= 7 there

is a saturation of surface charge since all surface groups are in fact fully deprotonated $\equiv TiO^{-\frac{4}{3}}$ groups. f_1 dominates the sum in Eq. 3.24. The charge of TiO_2 NTs is constant throughout all higher pH values. Although interesting, this way of fitting cannot properly account the measured values of charge at high pH. The opposite case is presented as a gray dashed curve. Now the $\log K_{H,1}$ equals 13. Even if the $\log K_{H,1}$ is much higher, results are globally the same. If this set of parameters is used, then there is again the plateau after pH= 6.5, but now it does not represent the population of $\equiv TiO^{-\frac{4}{3}}$ but $\equiv TiOH^{-\frac{1}{3}}$ surface groups. Now f_2 dominates in the sum in Eq. 3.24. Since $\log K_{H,1}$ is high, an extremely high pH (unreachable by an experiment) is needed in order to deprotonate $\equiv TiOH^{-\frac{1}{3}}$ surface groups. As in the previous case, it can be seen that the grey dashed curve cannot properly describe experimental data at high pH.

The third case is the green solid curve in Figure 3.6 which corresponds to $\log K_{H,1} = 8.1$. As can be seen, the green curve predicts a steep increase of the TiO_2 NTs charge with increasing pH. When pH is little less, but still near 8, the population of $\equiv TiO^{-\frac{4}{3}}$ increases and so the overall charge of TiO_2 NTs increases. The small plateau in the region between pH= 6 and 8, corresponds to the region where $\equiv TiOH^{-\frac{1}{3}}$ surface groups dominate in the expression for surface charge density (Eq. 3.24).

Protonation constant with MUSIC-like model

Since the green curve provided the best fit of the experimental data, we considered that $\Gamma = 0.28$ site/nm^2 and $\log K_{H,1} = 8.1$ is the most accurate (*i.e.* realistic) set of parameters that uniquely describe the experimental data. Furthermore, this choice of $\log K_{H,1}$ has been justified from a small theoretical argument. If the association of ions at the site is driven mainly by electrostatic force, *e.g.* as in Born model or the MUSIC approach, we can estimate the difference $\log K_{H,2} - \log K_{H,1}$[75]. Indeed within the framework of McMillian-Mayer theory the protonation constants can be written as a typical Bjerrum association constants[156, 157, 97]. In section Theory, we identified surface groups made of oxygen (O−atom) covalently bonded to titanium atom. The O−atom can associate with the proton from the reservoir. The maximum number of protons that can be associated with O−atom (adsorbed to surface site in terminology of colloid chemistry) is determined by the accessible volume for protons. Allowing the successive two-step protonation of site written as

$$\equiv TiO^{-\frac{4}{3}} + H^+ \rightleftharpoons \equiv TiOH^{-\frac{1}{3}}$$

and

$$\equiv TiOH^{-\frac{1}{3}} + H^+ \rightleftharpoons \equiv TiOH_2^{+\frac{2}{3}}$$

the fully deprotonated O−atom (corresponding to the $\equiv TiO^{-\frac{4}{3}}$ surface group) therefore has accessible volume two times the O−atom with already bonded one proton (corresponding to the $\equiv TiOH^{-\frac{1}{3}}$ surface group). The statistical mechanics derivation already reported by our group justifies the use of following expression for the definition of association constant $K^{\circ}_{\mathrm{H},l}$ between ions[156]

$$K^{\circ}_{\mathrm{H},l} = \int_{V_{\mathrm{site},l}} e^{-\beta U(\mathbf{r})}\, \mathrm{d}^3 r \tag{3.38}$$

where $K^{\circ}_{\mathrm{H},l}$ represents protonation constants, $V_{\mathrm{site},l}$ volume of sites accessible to protons, index l again denotes type of surface group, $\beta = 1/k_{\mathrm{B}}T$, and $U(\mathbf{r})$ is interaction potential for a paired anion and cation (O–H). We treat protonated surface groups like a contact ion pairs. The center of O−atom has been chosen as a center of coordination system, with $R_{\mathrm{O-H}}$ being the distance between O−atom and associated proton. For simplicity, we ignore any change of Ti–O and O–H bond lengths upon the association of proton (or any other structural change). This is important to emphasize since it simplifies the calculation. Upon division of two protonation constants, the short-ranged part of potential cancel out and only Coulomb part remains (all the equal terms cancel upon division of the partition functions of two successive reactions). This works because we are only interested in O–H bond. Therefore the interaction potential $U(\mathbf{r})$ between the pair is by nature considered as Coulombic only, and can be written as

$$U(\mathbf{r}) = \frac{z_{\mathrm{site,l}}\, e^2}{4\pi\epsilon_0\epsilon_{\mathrm{r},1} R_{\mathrm{O-H}}} \tag{3.39}$$

where $z_{\mathrm{site,l}}$ is the charge of site l. Dividing the two protonation constants yields

$$\frac{K^{\circ}_{\mathrm{H},1}}{K^{\circ}_{\mathrm{H},2}} = \frac{\int_{V_{\mathrm{site},1}} e^{-\beta U(\mathbf{r})}\, \mathrm{d}^3 r}{\int_{V_{\mathrm{site},2}} e^{-\beta U(\mathbf{r})}\, \mathrm{d}^3 r} \tag{3.40}$$

We have already stated that $R_{\mathrm{O-H}}$ does not change, so the two integrals on the right side can be factorised. We obtain

$$\frac{K^{\circ}_{\mathrm{H},1}}{K^{\circ}_{\mathrm{H},2}} = \frac{e^{-\beta \frac{z_{\mathrm{site,l}}\, e^2}{4\pi\epsilon_0\epsilon_{\mathrm{r},1} R_{\mathrm{O-H}}}}}{e^{-\beta \frac{z_{\mathrm{site},2}\, e^2}{4\pi\epsilon_0\epsilon_{\mathrm{r},1} R_{\mathrm{O-H}}}}} \frac{\int_{V_{\mathrm{site},1}} \mathrm{d}^3 r}{\int_{V_{\mathrm{site},2}} \mathrm{d}^3 r}. \tag{3.41}$$

Writing the $U(\mathbf{r})$ in terms of Bjerrum length l_{B} we have

$$\frac{K^{\circ}_{\mathrm{H},1}}{K^{\circ}_{\mathrm{H},2}} = \frac{e^{-\beta \frac{z_{\mathrm{site,1}}\, l_{\mathrm{B}}}{R_{\mathrm{O-H}}}}}{e^{-\beta \frac{z_{\mathrm{site},2}\, l_{\mathrm{B}}}{R_{\mathrm{O-H}}}}} \frac{\int_{V_{\mathrm{site},1}} \mathrm{d}^3 r}{\int_{V_{\mathrm{site},2}} \mathrm{d}^3 r}. \tag{3.42}$$

Note that we did not specify the type of coordinate system. The important fact is that radii vectors describing positions of both particles have the same origin. Taking the natural logarithm of the expression above yields

$$\ln\left(\frac{K^{\circ}_{\mathrm{H},1}}{K^{\circ}_{\mathrm{H},2}}\right) = \frac{l_{\mathrm{B}}\left(z_{\mathrm{site},2} - z_{\mathrm{site},1}\right)}{R_{\mathrm{O-H}}} + \ln\left(\frac{\int_{V_{\mathrm{site},1}} \mathrm{d}^3 r}{\int_{V_{\mathrm{site},2}} \mathrm{d}^3 r}\right) \tag{3.43}$$

The second term is a ratio of accessible volumes for proton. It is assumed to be equal to $\ln 2$, since we are investigating the two successive protonations (the fully deprotonated surface group $\equiv TiO^{-\frac{4}{3}}$ has twice as much volume for proton, compared to the $\equiv TiOH^{-\frac{1}{3}}$ group). After rearrangement of the former expression, we obtain the value of O–H bond.

$$R_{O-H} = \frac{l_B \left(z_{site,2} - z_{site,1}\right)}{\ln\left(\frac{K^{\circ}_{H,1}}{K^{\circ}_{H,2}}\right) - \ln 2} \tag{3.44}$$

Preforming a simple calculation to determine the R_{O-H} values for the sets of intrinsic protonation constants obtained from the fitting procedure yields:

a) $R_{O-H}(\log K_{H,1} = 4.5, \log K_{H,2} = 3) = 2.5$ Å

b) $R_{O-H}(\log K_{H,1} = 8.1, \log K_{H,2} = 3) = 0.63$ Å

c) $R_{O-H}(\log K_{H,1} = 13, \log K_{H,2} = 3) = 0.31$ Å

The set of intrinsic protonation constants $\log K_{H,1} = 8.1$ and $\log K_{H,2} = 3$ yields the length of O–H bond equal to 0.63 Å. This is a reasonable bond length and it does justify the use of $\log K_{H,1} = 8.1$ and $\log K_{H,2} = 3$ for further calculations and exploration of charge properties of TiO_2 NTs. It must be noted that constants are obtained with the mean-field approximation for surface sites, which guaranties smeared, uniform charge of polyion (nanotube).

Surface site density in semi-amorphous materials

Before passing our considerations to the study of TiO_2 NTs electrostatics, there is another thing worth addressing. Within the fitting procedure, the obtained surface site density Γ was rather low. In fact, in every possible fit, the value of Γ was always below 1 site/nm^2. In case of anatase phase colloid particles, a majority of previous work reported surface site densities larger than 1 site/nm^2[77]. It must be noted that these studies were made for the materials with flat surfaces and well defined crystalline structure. In our study, we examined materials characterized by highly curved interface on nanometer scale and high degree of amorphous solid within the samples. Conveniently, the low site density results in values of normalized surface charge densities that are usually used in classical Density Function Theory calcuations, Molecular Dynamics simulations, *etc.*[101, 158, 159].

In fact, in order to predict experimental data one may take a few possible routes. One route is to fix the point of zero charge according to the experimental data and to assume a priori high surface site density and then to fit the intrinsic protonation constants for one or more surface groups. This approach has proven useful in predicting ζ-potential of colloids. Still, we argue

that it is not a proper way of fitting, since Γ, $\log K_{H,1}$ and $\log K_{H,2}$ are mutually dependent[149]. Sometimes, in order to achieve the steep increase of charge the additional type of surface groups is introduced. This way imposes additional two parameters, namely new intrinsic protonation constant and the site density of new surface group. The third approach consists in allowing the association of supporting electrolyte with charged surface groups as usual competition reactions. Higher association constant of metal cations (compared to anions) causes decrease of the total charge and thus higher surface site densities Γ can be obtained in the fitting process. Note that this approach also adds two additional adjusted parameters.

Results obtained by this study arose from the intent of authors to make a model with the lowest possible number of parameters. A shape of the titration curve, values of total charge and the point of zero charge are the consequence of solution of two coupled nonlinear Poisson-Boltzmann equations along with charge regulated boundary conditions with $\log K_{H,2} = 3$ fixed accordingly to experimental data and two adjustable parameters $\Gamma = 0.28$ site/nm^2, $\log K_{H,1} = 8.1$.

It must be noted that from the practical point of view the preparation of samples for charge determinations in case of TiO_2 NTs is a difficult task. Apart by study made by our group, the mechanical damage of TiO_2 NTs upon the ultrasonic treatment was previously reported by other authors[80, 160]. The breakage of TiO_2 NTs was reflected on their properties in an aqueous solution *i.e.* ion-exchange kinetics. However, it is not completely clear if the mechanism is associated with the cleavage of nanotubes, or simple fragmentation of larger agglomerates causes a release of various particles, besides nanotubes themselves. In order to overcome that difficulty, the ultrasound was applied during short intervals (the procedure can be found in the Experimental data section). Within such procedure it is intuitive that a large portion of TiO_2 NTs remains attached into a larger agglomerate. This can be seen from topography graph obtained from Atomic Force Microscopy measurments (AFM) of our post-dispersion sample (Figure 3.8). Topography images show that our short ultrasound treatment did not cause a mechanical breakage of nanotubes, but in turn also enabled a large portion of nanotubes to remain agglomerated. Still, the extent of agglomeration was not quantified, since it demands a robust investigation in order to obtain consistent statistics. Note that DLS measurements also suggested that large agglomerate exist, if ultrasound treatment is to short (see Figure 3.17d). This issue will be mentioned again in the Conclusion and Prospects section (Figure 3.17). Agglomeration caused decrease of specific surface exposed to aqueous solution results in lower total charge measured. In this manner the Γ values obtained through fitting procedure are lower. These results are consistent with finding known from literature[160]. Also, it was

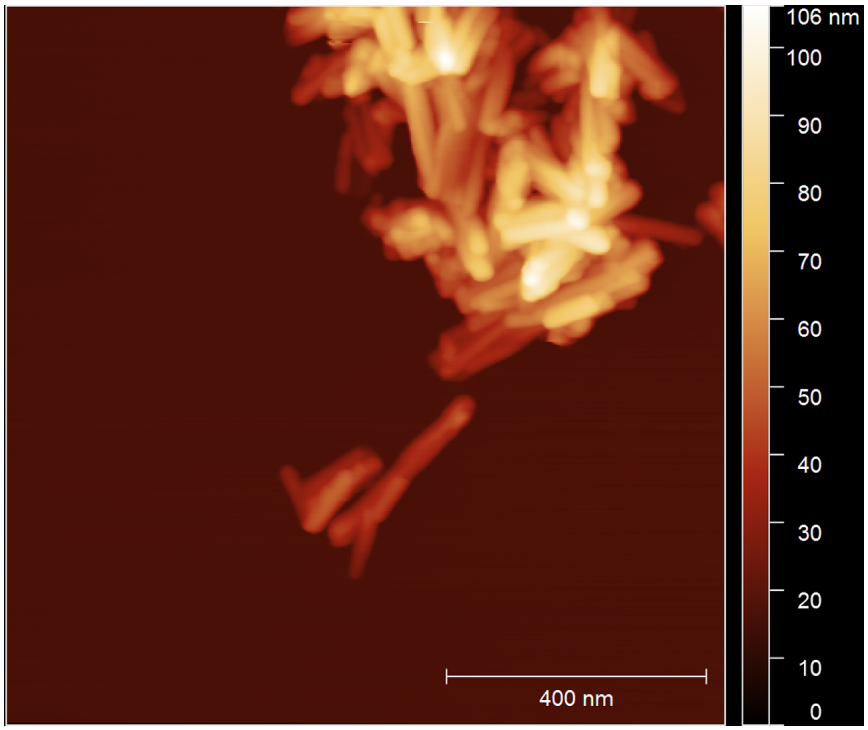

Figure 3.8 – AFM topography of TiO_2 NTs sample taken from suspension after three minute sonication treatment by bath sonicator.

noted at the beginning of this section that the sample analyzed by HR-TEM has shown a high degree of an amorphous phase. With such an experimental evidence we understand that the value of Γ cannot be predetermined and it has to be somewhat adjusted. Moreover, the choice we made (not to fix Γ) has another advantage. If the intrinsic protonation constants are known and their values can be assumed to be reliable, then the model can predict a surface site densities for porous materials. A *vice-versa* deduction also applies. A predictive method is crucial for the study of any ion behavior in confined media.

The main objective of this work was to exploit the utility of the set of nonlinear Poisson-Boltzmann equations in order to understand the charge properties of TiO_2 NTs. Therefore, in the following subsection, we present results of calculations for the system of infinitely long cylinder immersed in the aqueous solution for various physical conditions (pH, reservoir salt concentrations). All subsequent calculations were made with values of parameters Γ =0.28 site / nm^2, $\log K_{\mathrm{H},1} = 8.1$ and $\log K_{\mathrm{H},2} = 3$ at $T = 298$ K. Once again we must emphasize that using other two sets of parameters would greatly influence the interpretation of charge properties.

3.4.2 Ions in Confined Medium Under the Influence of the Electric Field

The solution of the system of coupled nonlinear Poisson-Boltzmann equations (Eq. 3.3) is presented in Figure 3.9. The electrostatic potentials, counterion and coion profiles are plotted for five different pH values. The supporting electrolyte concentration is 0.001 M. In the experiment we used $NaNO_3$, but within the model, no ion specificity is taken into the account. Debye length κ^{-1}, for such conditions is around 96 Å.

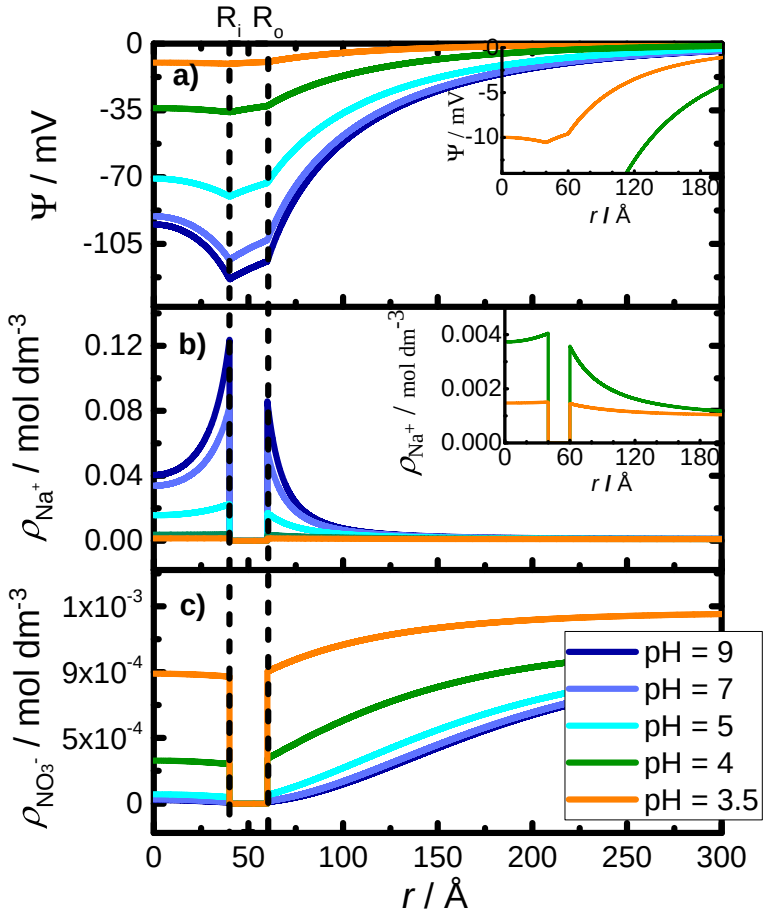

Figure 3.9 – Results of the calculation: a) electrostatic potential profiles; b) equilibrium counterion profiles; c) equilibrium coion profiles; $T = 298$ K, $c_0 = 0.001$ M, $\Gamma = 0.28$ site/nm^2, $\log K_{H,1} = 8.1$, $\log K_{H,2} = 3$. The inner radius is $R_i = 40$, while the outer radius is $R_o = 60$

Electrostatic potential and ion distributions

Figure 3.9a shows the electrostatic potentials from the center of the cylinder up to some point away from the outer surface. The calculations have shown that there is a non-zero electrostatic potential along the cylinder axis but the electric field is equal to 0. Therefore, the boundary

conditions are satisfied. The region from 40 Å to 60 Å represents the electrostatic potential through TiO_2 layer and is described by a monotonic increasing function (Eq. 3.11). The difference in surface electrostatic potentials at the inner and outer surfaces causes asymmetry in ion distributions (as shown in Figure 3.9b). The Figure 3.9c shows the equilibrium concentrations of coions inside of the cylinder. At high pH, the negatively charged TiO_2 NTs exhibit an electric field which attracts counterions (Na^+) near the surface and repels coions (NO_3^-). Since Debye length is more than twice the inner radius of TiO_2 NTs, it is understandable that at high pH calculated coion concentrations are negligible. At lower pH values, closer to the point of zero charge, the counterion concentrations near the surface are still higher compared to the bulk, but now the coion concentrations are greatly increased. Such results are expected since with lowering of surface charge, the electric field diminishes and NO_3^- coions can approach the interface. In order to solve Poisson-Boltzmann equation the overall electroneutrality condition must be fulfilled.

$$2\pi L \int_0^{R_\mathrm{i}} r\varrho_{el,1}\,\mathrm{dr} + 2\pi R_\mathrm{i} L\sigma_\mathrm{i} + 2\pi R_\mathrm{o} L\sigma_\mathrm{o} + 2\pi L \int_{R_\mathrm{i}}^{\infty} r\varrho_{el,2}\,\mathrm{dr} = 0 \tag{3.45}$$

At 0.001 mol dm^{-3}reservoir salt concentration, the electroneutrality is not fulfilled inside of the cylinder. Similar results have already been obtained reported[161]. The excess charge is then compensated at the outer surface by electrolyte solution and overall the system in neutral. We made calculations with the higher value of the inner TiO_2 NTs radius R_i. The thickness of the TiO_2 layer was kept constant at 2 nm and reservoir salt concentration at 0.001 M. As the inner radius is increased, the asymmetry in terms of electrostatic potential and ion distributions is lost and the system starts to behave like a charged plate immersed in the electrolyte solution. Note also that the asymmetries in ion distributions are lost in the limit of zero-thickness of TiO_2 layer.

3.4.3 Donnan Effect in the Case of Charge-Regulated Nanotubular Structures

We have mentioned the effect of the pH and the electric field on the ions distributions inside nanotubes. But the system is more complex than that, since there is the effect of the curvature expressed through the inner radius, R_i. In this sense, it is suitable to study the Donnan effect. The study of the Donnan effect, presented in Figure 3.10 enabled us to rationalize the conditions of the inner radius and the reservoir salt, as well as pH for which the NO_3^- can fill the interior of nanotubes. We have plotted the ratio of the mean concentration of nitrate coions

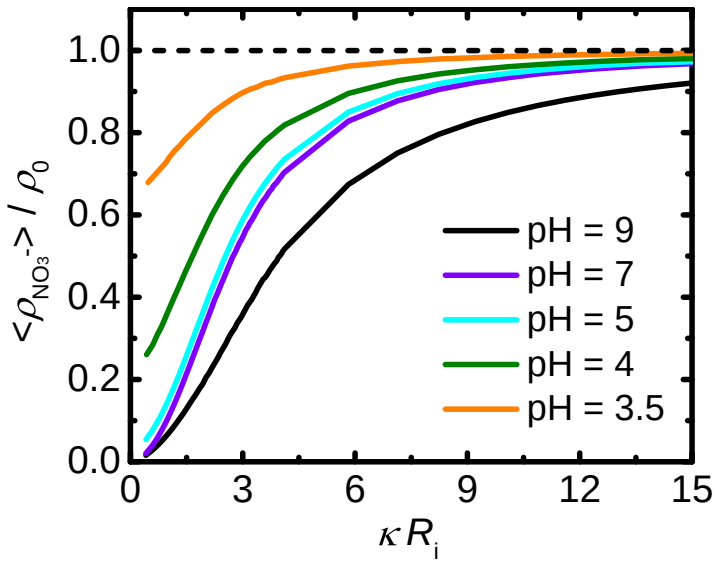

Figure 3.10 – Study of Donnan effect. $<\rho_{NO_3^-}>/\rho_0$ is the ratio of mean coion (NO_3^-) concentration inside TiO_2 NTs and the reservoir coion concentration. The results are shown for various reservoir pH values.

$<\rho_{NO_3^-}>$ inside the cylinder and the reservoir salt concentration as a function of κR_i. The mean concentration of NO_3^- is defined as

$$<\rho_{NO_3^-}>=\frac{2\int_0^{R_i}\rho_{NO_3^-}(r)\,r\,dr}{R_i^2}. \tag{3.46}$$

κR_i parameter varies either when the reservoir salt concentration is modified (the inverse Debye length κ is proportional to $\rho_0^{1/2}$), or when inner radius R_i is greatly increased. Results show that at high pH and low R_i, the electric field does not permit the penetration of NO_3^- ions inside the nanotube. Moreover, the reservoir salt concentrations need to be very high in order to have mean coion concentration $<\rho_{NO_3^-}>$ equal to the reservoir salt concentration. It is the case when the surface charge is completely screened by counterions, namely Na^+. With a decrease of reservoir pH, surface charge density also decreases. When the electric field at TiO_2 NTs inner surface is diminished (near the point of zero charge) NO_3^- ions can more easily penetrate inside. Just to emphasize how the strength of electric field effect the ion distributions, let us once again study the two extreme cases of pH. For pH = 9 in 0.001 M $NaNO_3$ system, there are almost no NO_3^- ions inside of the TiO_2 NTs at $T = 298$ K, whereas at pH = 3.5 for the same conditions around 35% of the total amount of NO_3^- ions is already inside. Briefly, there are three major conditions for which the mean coion concentration $<\rho_{NO_3^-}>$ is equal to the reservoir salt concentration are: 1) high reservoir salt concentration that guaranties an efficient inner charge screening, 2) very high R_i for lower reservoir salt concentrations, 3) pH close to the pH_{pzc}. Variations and combinations of mentioned conditions are possible, but the global

behavior of nanotubes (nanochanels in general) predicted by PB theory is summarized within the three noted cases.

3.4.4 Predicting the Polyeletrolyte Titration Curve for Different System Conditions

Simulation of the titration curve: a salt effect

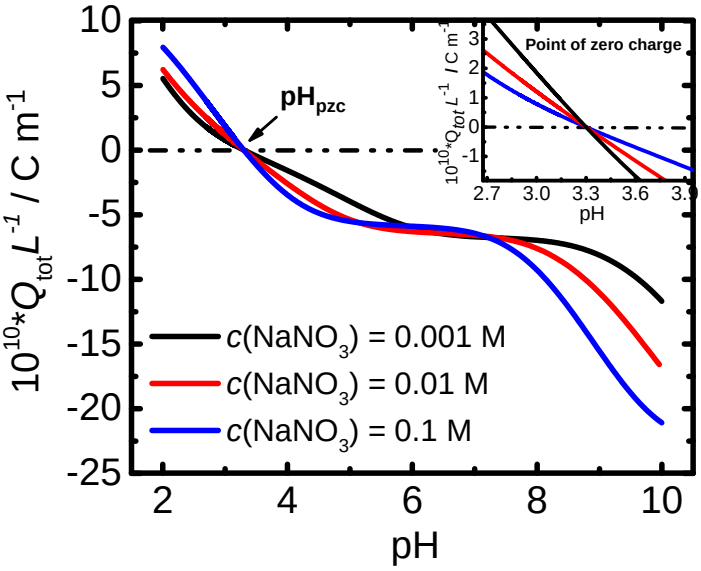

Figure 3.11 – Calculated titration curves for three different reservoir salt concentrations: black line corresponds to $c(NaNO_3) = 0.001$ M, red line to $c(NaNO_3) = 0.01$ mol dm^{-3} and blue line to $c(NaNO_3) = 0.1$ mol dm^{-3}. The inset shows the enlarged pH region near the point of zero charge.

Besides reproducing the experimental data, the model was used to give insights into charge properties at different conditions. The titration curves were calculated for different reservoir salt concentrations. The results are shown in Figure 3.11. The shape of the curves does not change considerably with the increase of the bulk salt concentrations. As known from the literature, the increase in reservoir salt concentration is followed by the increase in charge of colloids[162]. Our calculations have shown the same trend. The origin of such increase in charge is just a question of more efficient screening of the surface charge. For higher salt concentrations the calculated surface potentials Ψ_i and Ψ_o are less negative (when discussing only the case where TiO_2 NTs are negatively charged). In this manner, the proton concentrations at the surface are decreased and most of the surface groups remains deprotonated *e.g.* more charge is

detected. Practically, it means that within the titration experiment (polyelectrolyte titration or some other technique) the consumption of titrans increases when more salt is added into the system. From Figure 3.11 it can be seen that inflection points that describe the shape of charging curve are at different positions (pH values) for different salt concentrations. The origin for such phenomena is the same as written previously. The change in calculated surface potentials governs the ratio of the population of charged surface groups and thus determines the value of charge at particular pH value.

The inset in Figure 3.11 shows that all three curves have the same point of zero charge. In real systems, pH_{pzc} depends on reservoir salt concentrations and on the type of salt, as was found experimentally [80]. Our calculations showed no such difference. The explanation for such phenomena is rather simple. In section Theory, we assumed the ideality of the solution. The (electro)chemical potential of ion H^+ is defined as: $\mu_{H^+} = \mu^o_{H^+} + k_B T \ln\left(\gamma_{H^+}\ c_{H^+}/c^o\right) + e\Psi$. At the point of zero charge Ψ is equal to zero so the last term disappears. Since coefficients of activity are equal to 1 the intrinsic protonation constants are independent bulk salt concentrations and thus the point of zero charge does not change.

Simulation of acid-base titrations

Within this study, we did not simulate the charge versus pH-curve in the case of acid-base titration experiment due to the fact that we did not have experimental support. Still, it must be noted that the procedure for the simulation of acid-base titration is straightforward and quite simple. Instead of using Eq. 3.37, which is valid when polyelectrolyte is condensed onto the outer nanotube surface, in the case of direct acid-base titration for the 1:1 charge compensation of surface sites we have following expression for the total charge per unit length:

$$Q_{tot} L^{-1} = \sigma_i 2\pi R_i + \ \sigma_o 2\pi R_o. \tag{3.47}$$

It is clear that the acid-base titration is sensitive only to the charge on surface, when compared to the polyelectrolyte titration. The H^{-1} and OH^- ions penetrate inside the nanotube interior.

Influence of $\epsilon_{r,2}$ through TiO_2 layer

Even though we have neglected arising of the displacement field P (recall Theory section), it is still needed to justify the usage of the dielectric constant $\epsilon_{r,2}$ through TiO_2 layer. The influence of $\epsilon_{r,2}$ on the overall simulated titration curve has been studied so that calculations were made with $\epsilon_{r,2}$ values 40, 80 and 120 for entire pH region. Results are presented in Figure 3.12. The choice of dielectric constant trough TiO_2 layer does not provide significant

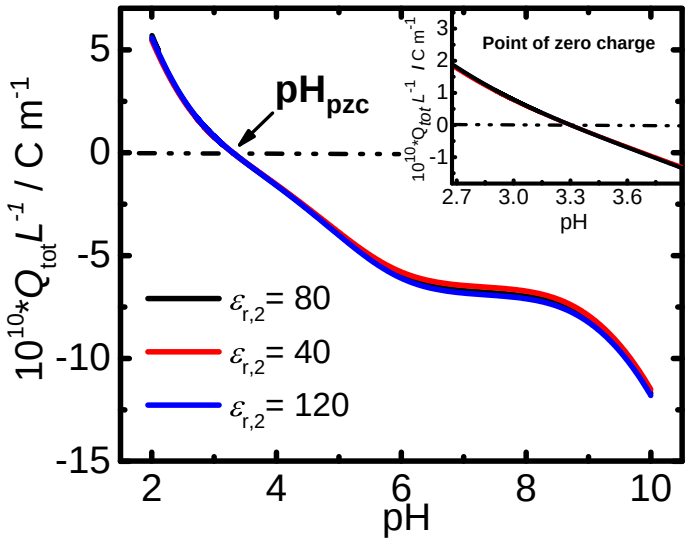

Figure 3.12 – Influence of a dielectric constant of TiO_2 layer on the titration curve.

change in overall titration curves. The differences in total charge per unit length as a function of pH for those three values were very small and namely in the region of high pH. A better knowledge of crystal structure of TiO_2 NT layer would motivate further investigations about the influence of the dielectric constant on overall system charge properties. A possibility is to use the Clausius–Mossotti relation to estimate $\epsilon_{r,2}$, but again, this is a macroscopic level of estimation. In our case of the high degree of amorphous mass within the examined sample, the attempt to correct this this effect is useless. Still it needs to be emphasized that further lowering $\epsilon_{r,2}$ bellow 40 would definitely influence the charge behavior. In this domain the solvent averaged Coulombic interactions would be very strong. Luckily, within this study we haven't dealt with such system, although it might be important for biological systems such as lipid bilayers or vesicles.

3.4.5 Charge Dissimilarities Between Surfaces Exposed of the Aqueous Solution

One of the major motivation of this work was to quantify the charge on both surfaces of tubular porous materials in contact with an aqueous solution. To address this, we have calculated the absolute value of σ_o and σ_i and plotted them as a function of pH. Results are presented in Figure 3.13. At first glance, the surface charge curves are globally similar and no major difference can be observed. Yet, closer look reveals that there is always more charge on the outer surface compared to the inner surface. This finding is a consequence of the differences

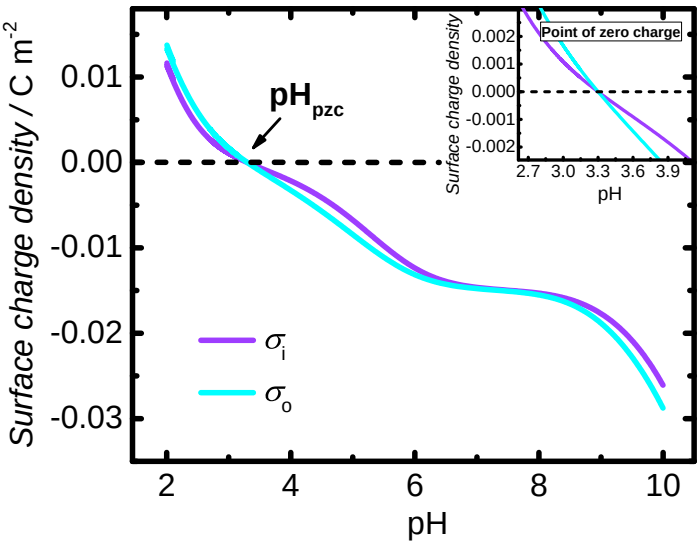

Figure 3.13 – Calculated inner and outer TiO_2 NTs surface charge densities, σ_i and σ_o at $c(NaNO_3) = 0.001$ M, $T = 298$ K. The average length of TiO_2 NTs assumed to be 100 nm (Figure 2b and S3).

in the curvatures of the two surfaces ($R_o > R_i$). The surface charge density scales with the radius of TiO_2 NTs: there are always more charges on the outer surface because the area is larger. Also, our calculations have shown that proton concentrations at the inner surface are higher when compared to the outer surface *i.e.* the higher proton adsorption/desorption at the inner surface. This means that there are less deprotonated surface groups, and therefore, less amount of charges. The two effect account for the differences in the amount of charge between the surfaces. But, as we have mentioned earlier, differences globally seem small. To properly demonstrate and elucidate the difference in charging phenomenon between the two surfaces, we have replotted the data from Figure 3.13 in a more informative way. The ratio between two surfaces is plotted as a function of pH. The charge at the surface is understood as the sum of charges from the surface groups only, since we did not consider the association of supporting electrolyte.

$$\frac{2\pi L R_o \sigma_o}{2\pi L R_i \sigma_i} = \frac{\sigma_o R_o}{\sigma_i R_i} \tag{3.48}$$

The ratio of charge between the outer and the inner cylinder surface (Eq. 3.48) plotted as a function of pH in Figure 3.14, shows that there is a pronounced increase of the charge at the outer TiO_2 NTs surface near the point of zero charge, pH_{pzc}. The factor is around 2.4. A smaller increase can be seen also in the region above pH = 8. Besides the increase of the charge at the outer surface, there is also the leveling of charge regime, as can be seen in the inset of Figure

3.14. It is in the region of pH between 6 an 8, depending on the reservoir salt concentrations. This leveling has a value 1.5 (roughly) and corresponds to the ratio of inner and outer TiO_2 NTs radius. It is the region where $\equiv TiOH^{-\frac{1}{3}}$ surface groups are most populated ones for both inner and outer surface (fractional coverage f_2 dominates the sum in Eq. 3.24). In fact, Figure

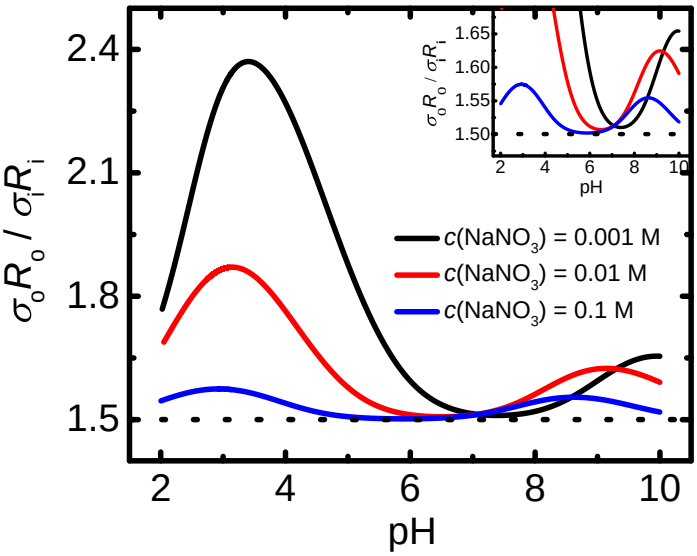

Figure 3.14 – Fraction of the charge between the outer and the inner surface as a function of pH. The results are given for three different reservoir salt concentrations: the black line corresponds to $c(NaNO_3) = 0.001$ M, the red line to $c(NaNO_3) = 0.01$ M, and the blue line to $c(NaNO_3) = 0.1$ M.

3.14 is the central finding of this study and requires more care to dismantle the phenomenon.

First, we examine the curve calculated for reservoir salt concentration equal to 0.001 M. The accumulation of charge at the outer surface when pH is close to values of intrinsic protonation constants can be understood from the following argument. We have already stated that surface charge density depends exponentially on the Ψ_i and Ψ_o (Eq. 3.28). The pronounced change in the population of particular surface groups occurs in the case when pH is near the value of intrinsic protonation constants. In those conditions even small differences between calculated Ψ_i and Ψ_o cause pronounced differences in surface charge densities, which can be simply understood since the functionality is exponential. Practically, this phenomenon means that the asymmetry in proton adsorption between the two surfaces is even more pronounced when pH is close to the value of intrinsic protonation constants. The largest difference is found for pH near pH_{pzc} (or $\log K_{H,2}$). The explanation of the phenomena is simple. At high pH the surface groups are already mostly deprotonated and therefore less sensitive to the changes in surface potentials.

This is reflected in small differences of charge between the inner and the outer surfaces. When pH approaches pH_{pzc}, we are comparing almost no charge on the inner surface, and more charge (more than twice) on the outer surface. This in turn generates such a pronounced differences in charge. On more thing to notice in Figure 3.14 are the charge ratio curves for 0.01 mol dm^{-3} and 0.1 mol dm^{-3} reservoir salt concentrations. The increase of reservoir salt concentrations reduces differences between the amount of charge on the inner and the outer surface due to the more efficient screening (Eq. 3.11). The case of $c(NaNO_3) = 0.1$ mol dm^{-3} in large pH intervals collapses to the dashed black line *i.e.* the ratio of surface areas (or the ratio of the outer and the inner nanotube radius). An efficient screening of both surfaces by high salt concentrations provides similar surfaces groups populations, thus the only difference in charge between two surfaces is naturally given by the surface area.

Convenience of our model is the fact that we can quantify fraction of the compensated charge. The amount of charge confined inside the nanotube and normalized of the inner surface area can be written as

$$\sigma_{\mathrm{el,i}} = \frac{\int_0^{R_\mathrm{i}} \varrho_{\mathrm{el},1}\, r \,\mathrm{d}r}{\epsilon_0 \epsilon_\mathrm{r}^1 k_\mathrm{B} T R_\mathrm{i}} \tag{3.49}$$

where $\sigma_{\mathrm{el,i}}$ in the normalized charge. The ratio $\sigma_{\mathrm{el,i}}/\sigma_\mathrm{i}$ is plotted in Figure 3.15 as a function of pH for three salt contractions. In low reservoir salt regime the calculation has shown that around point of zero charge, only 30% of inner surface charge is screened by the inner cylinder electrolyte solution (black line). This is in accordance with previous discussion that electric field (or the pH since it fixes boundary conditions) plays important role in the screening efficiency. An increase in reservoir salt concentrations induces screening, which can be seen as the increase of $\sigma_{\mathrm{el,i}}/\sigma_\mathrm{i}$ for $c(NaNO_3) = 0.01$ mol dm^{-3} (red line). After a certain threshold (not shown here) the screening no longer depends on pH and it is always roughly around 95 %. This can be noticed if the case of $c(NaNO_3) = 0.1$ mol dm^{-3} is examined (blue line).

To sum up, the phenomena of the asymmetry in accumulation of charge between two surfaces predicted by our model can be decoupled to two major contributions: 1) trivial ratio of surface areas, 2) excess population of surface groups governed by screening of the supporting electrolyte. Still, the question arises: is this intriguing result a consequence of the intrinsic default by PB theory where ions are point-like charges? Moreover, can this finding be confirmed by some experimental technique? It must be noted again that due to the relatively large radius of the cylinder, and low salt concentration in the system, Molecular Dynamics simulations are not applicable to study this effect. We will address this core question for ions in confined media in the prospects discussed in the next section.

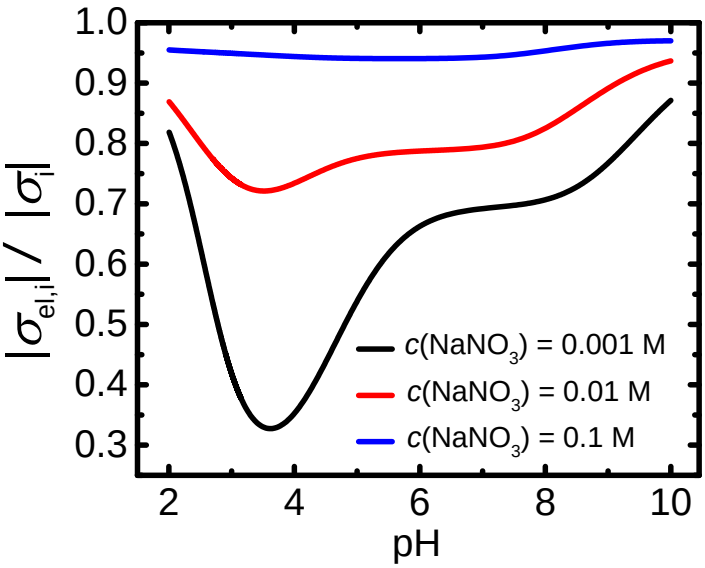

Figure 3.15 – Screening of inner surface charge as a function of pH for different reservoir salt concentrations.

3.5 Conclusion and Prospects

Chapter Conclusion

Within this chapter, we addressed on of the core questions concerning ions in confined media under influence of the electric field. Within this study we have presented a framework for quantifying a charge properties of TiO_2 NTs and other porous material in low salt aqueous solution.

With the HR-TEM we have obtained the distributions of the inner and the outer TiO_2 NTs radii. The electrophoretic mobility measurements at 0.001 mol dm^{-3} $NaNO_3$ showed that pH_{iep} of TiO_2 NTs is around 3.6. With the particle charge detector we have measured the charge of TiO_2 NTs in 0.001 mol dm^{-3} $NaNO_3$. The measurements showed that TiO_2 NTs are weakly charged and pH_{pzc} is around 3.2. Polyelectrolyte condensation onto TiO_2 NTs in a monolayer supported an assumption of 1:1 stoichiometry of surface site/PDDA monomer unit charge compensation.

The theoretical model was developed in order to understand and interpret the experimental data. The basis of the theoretical model includes Poisson-Boltzmann equation (which is the simplest case of classical Density Functional Theory for electrolyte solutions) and surface charge regulation method via the law of mass action. A system of two coupled nonlinear second-order differential equations was solved numerically in a self-consistent manner with respect

to four coupled boundary conditions. The proposed algorithm involves the prediction of the initial guess of the pH-dependent surface charge by extrapolation using Lagrange second-order polynomial, and rejection methods for calculation of both $\sigma_{o,i}$ and $\Psi_{i,o}$.

Fitting of experimental results with theoretical model yielded the surface site density Γ and intrinsic protonation constants $\log K_{H,1}$ and $\log K_{H,2}$. The three possible fits were addressed and discussed separately. As the best fit we considered the one obtained for $\Gamma = 0.28$ site/nm^2, $\log K_{H,1} = 8.1$ and $\log K_{H,2} = 3$ (note that $\log K_{H,2}$ was fixed by the surface charge density measurements and not simultaneously fitted). Plausibility of using this set of parameters was justified with a theoretical calculation based on Bjerrum-like contact ion pair formation model where only a solvent-averaged Coulombic interaction is considered. Obtained constants are only valid when mean-field approximation for sites and smeared charge is assumed.

The calculation of total TiO_2 NT charge with fitted values of Γ, $\log K_{H,1}$ and $\log K_{H,2}$, predicts continuous increase of the charge as a function of reservoir pH. A steep increase of the surface charge is predicted after pH= 8. At low salt concentrations in the system (*e.g.* $c(NaNO_3)$=0.001 mol dm^{-3}) the inner TiO_2 NTs surface charge is not fully compensated by the electrolyte solution confined inside TiO_2 NT. The overall electroneutrality of TiO_2 NTs system for those conditions is achieved by the electrolyte solution outside of TiO_2 NTs. The story is slightly more complicated than simple salt screening effect since the pH determines the surface charge density. The surface charge density sets the slope at the interface (recall boundary conditions), and thus the screening by ions. The screening of both TiO_2 NTs surfaces is more efficient at high reservoir pH. The total charge of TiO_2 NTs increases with the increase of the reservoir $NaNO_3$ concentration. Within the study of Donnan effect, it was found that the influence of NO_3^- coions on TiO_2 NT surfaces is negligible at high pH since strong electric field repels them from TiO_2 NT surface. When the pH is close to the pH_{pzc}, the screening becomes inefficient and there is a pronounced penetration of NO_3^- coions into the interior of the TiO_2 NTs. Furthermore, our calculations show that the difference in charge between the inner and outer surfaces is also pH-dependent and is not always equal to the ratio of TiO_2 NT radii. The difference in charge between the two surfaces is diminished by an increase of the reservoir $NaNO_3$ concentration. With this being the central finding of this chapter, we ask ourselves is this the consequence of the fact the PB approach treats ions as a point-like charges?

Prospects

If the size of the ions is accounted, like in Modified PB approach one obtains smaller concentrations of ions at the interfaces and in confined media[161]. This consequently changes the calculated surface charge densities as the accessible volume for ions reduces upon the increase of the lattice parameter a which defines the length of the unit cell. Here we will only provide a final expression for ions distributions in Modified PB approach in the case of 1:1 electrolyte.

$$\rho_\alpha(r) = \frac{\rho_{\text{cell}}\rho_\alpha^0 \exp\left(-\frac{e\psi(r)}{k_\text{B}T}\right)}{\rho_\text{w}^0 + 2\rho_\alpha^0 \cosh\left(\frac{e\psi(r)}{k_\text{B}T}\right)} \tag{3.50}$$

where $\rho_\alpha(r)$, ρ_α^0, ρ_w^0, and ρ_{cell} are respectively local, and reservoir ion number density, water molecules number density, and density of cells equal $\rho_{\text{cell}} = 1/a^3$ with a being lattice parameter[141]. Furthermore, it was demonstrated that classical Density Functional Theory can be used instead of Molecular Dynamics or Monte Carlo simulation to obtain satisfying distributions of confined ion distributions[108, 109, 107]. Since surface complexation of an ion to the surface site can be justified form first principles, just as an ion-pair analogue in the solution, there is a hope that our methodology can be improved for more accurate quantification of the charge properties of porous materials. Also, one of the possible improvements is to couple Mean Spherical Approximation (MSA) with the PB in order to obtain semi-empirical McMillian-Mayer framework in Grand Ensemble which takes into account ion-ion correlations via activity coefficients. Coupling between MSA and PB, as proposed by Prof. Dufrêche, results in the following expression

$$\rho_\alpha(r)\gamma_\alpha\left(\rho_\alpha(r)\right) = \rho_\alpha^0\gamma_\alpha\left(\rho_\alpha^0\right)\exp\left(-\frac{e\psi(r)}{k_\text{B}T} - V_\text{wall}\right) \tag{3.51}$$

where $\gamma_\alpha\left(\rho_\alpha(r)\right)$ is the local spatial activity coefficient distribution as a function of ion distributions, and V_wall is infinite well potential to ensure ions cannot penetrate inside the rigid interface.

At the end it is worth a while to shortly focus on the prospects and current open questions. As stated in previous sections, the literature is filled with different values of dissociation constants $K_{\text{H,x}}$ obtained though fitting procedures on apparently similar materials. Through our work, we have noticed that the bare charge or the electrophoretic mobility in fact varies from measurement to measurement. Depending on the synthesis, suspension preparation in terms of type of devices used to apply ultrasound, and the length and the frequency of applied ultrasound all exhibit influence onto the overall charge measurement. If this is so, then fitting the experimental data with the same model yields different values of $K_{\text{H,x}}$. The concept of this

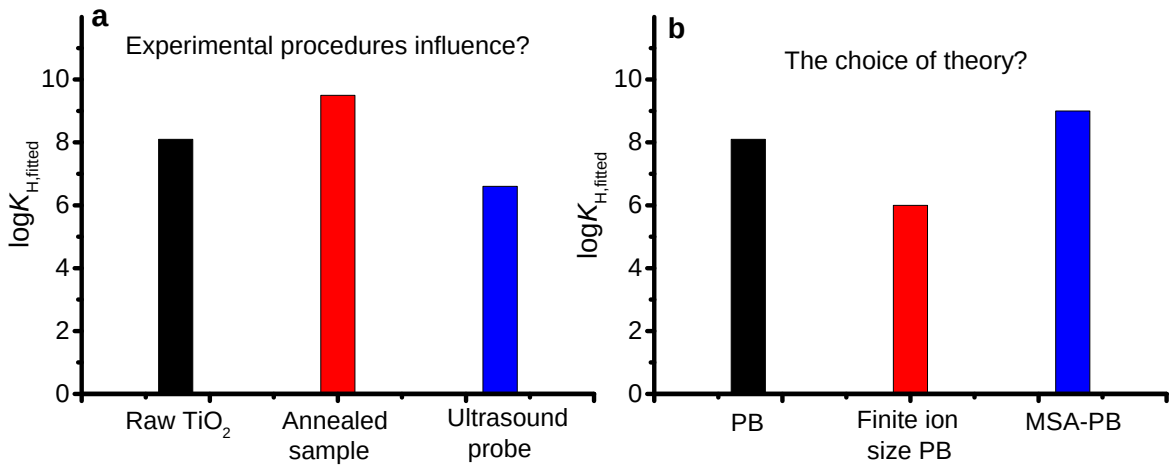

Figure 3.16 – Concept graphs: a) Influence of the experimental procedures on the total measured charge of solid sample dispersed in the aqueous solution. b) Influence of the level of theory used create a model and to fir the experimental charging data.

is illustrated in Figure 3.16a, where for example the raw TiO_2 NTs sample, annealed sample, and the change in dispersion procedure are fitted with the same model and different $K_{\mathrm{H,x}}$ are obtained. The consequence of this ambiguity is severe in terms of fundamental science, but losses its relevance when one goes to the chemical engineering level, where details sometimes get lost or are counterbalanced by other effects. As long as for the material in focus fitted protonation constants are able to reproduce reference data and to accurately predict process beyond that, it is credible to use them. If the experiment affect the outcome of the fitting procedure, could the same thing happen if the different level of theory is used *e.g.* differences between PB and Modified PB. This scenario is illustrated in Figure 3.16b, where PB, Modified PB, or the MSA-PB theory is used to fit the experimental charging data.

It must be added that in beside the extension of our model to account size and ion correlations, the greater care is devoted to purifying the crude sample by annealing, as well as to optimize the extent of dispersion by ultrasound treatment, as presented in Figure 3.17.

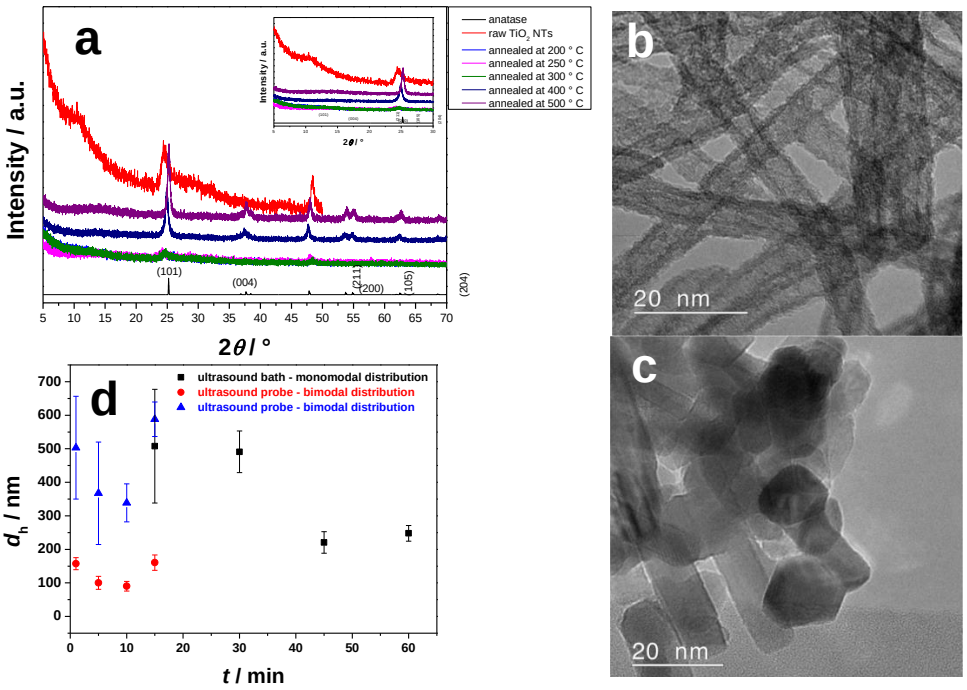

Figure 3.17 – a) PXRD patterns of nanotubes after post-synthesis treatment for different annealing temperatures. b) HR-TEM micrograph of raw TiO_2 NTs sample. c) HR-TEM micrograph of raw TiO_2 NTs sample annealed at 500 °C. d) Hydrodynamic radius of TiO_2 NTs suspension as a function of time, for different suspension preparation techniques *e.g.* ultrasound probe or ultrasound bath.

Chapter 4

Modelling of Liquid-Liquid Extraction: a Case of Non-Ionic DMDOHEMA Extractant

We develop a minimal model for the prediction of solvent extraction. It accounts for spherical micelles and takes into account competition complexation, mixing entropy of complexed species, differences of salt concentrations between the two phases, and the surfactant nature of extractant molecules. We consider the practical case where rare earths are extracted from iron nitrates in the presence of acids with a common neutral complexing extractant. The solvent wetting of the reverse aggregates is taken into account via the spontaneous packing. All the water-in-oil reverse aggregates are supposed to be spherical on average. The minimal model captures several features observed in practice: reverse aggregates with different water and extractant content coexist dynamically with monomeric extractant molecules at and above a critical aggregate concentration (CAC). We will demonstrate that the free energy of the transfer of an ion to the organic phase is lower than the driving complexation.

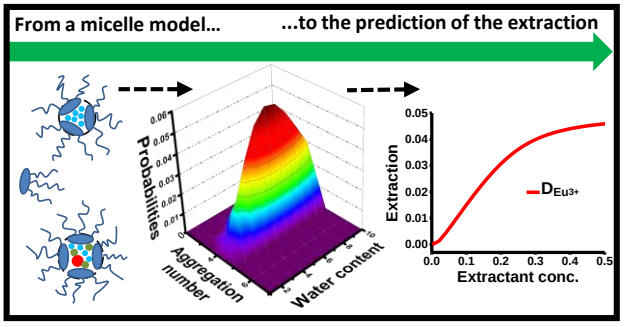

Figure 4.1 – Modelling liquid-liquid extraction: DMDOHEMA case

4.1 How to Interpret a Laboratory-Scale Experiment?

In the light of the concept of this thesis, we ought to show how derived model can be used to interpret both laboratory and engineering experiments.

In this chapter we will present the full derivation of the minimal thermodynamic model for the prediction of extraction efficiency. The model is first of its kind, and will be expanded and generalized in next two chapters. Therefore, here we will present a bottom-up derivation, starting from partition function, and so forth. Moreover, in this chapter we will be dealing with the 'simplest' extractant system *i.e.* non-ionic extractants. Also it is useful to make a clear distinction between laboratory and engineering scale experiments since both require appropriate way of modelling. If we imagine the simple experiment in the laboratory, as described in Figure

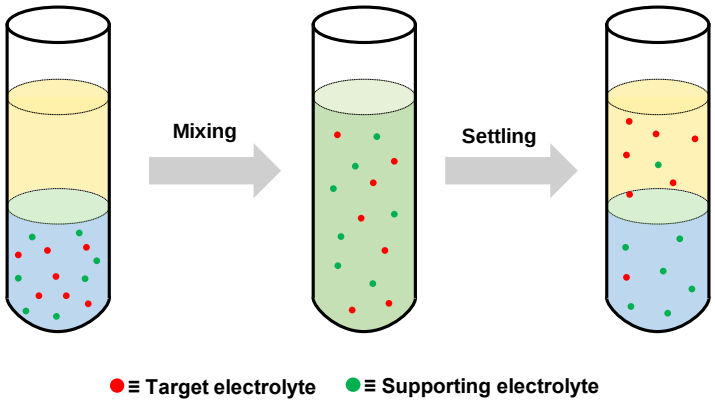

Figure 4.2 – Schematic representation of selective laboratory-scale solvent extraction experiment. The system is made of two non-miscible liquids, namely organic solvent (pale yellow color), and aqueous phase (pale blue color). Red circles represent target solutes *e.g.* $Eu(NO_3)_3$, whereas green circles represent background solutes *e.g.* $Fe(NO_3)_3$

4.2, the fact the we have small vessel urges the need to make calculations in canonical ensemble. Practically, what we need to do is to minimize Mass Action Law for every component in the system. On the laboratory scale, the extent of reaction, and thus the difference between the final and the initial state of the system are transparent. The total number of particles is fixed in the vessel. This is not the case when there is for example a pump which forces a constant flux of concentrated brine into mixer-settler device, as presented in Figure 1.2. In that case, we can consider a fixed chemical potentials of ions by infinite reservoir.

To demonstrate how we can battle the situation at hand (to mimic the laboratory experiment), we will describe a multicomponent system: a non-ionic extractant is dissolved in the organic phase, whereas the aqueous phase contains namely HNO_3, $Eu(NO_3)_3$, and $Fe(NO_3)_3$.

It must be noted that in the case of non-ionic solvating extractants, achieving the equilibrium assumes only the transfer of solutes from the aqueous to the organic phase. There is no release of solutes in opposite direction like in the case of ion-exchanger extractants (the subject of the next chapter). This is convenient from the aspect of the program code development, since it simplifies convergence of the multicomponent Mass Action Law. Furthermore, it is this convenience that enabled us to study the system involving three salts. Two salts, HNO_3 and $Eu(NO_3)_3$ (red circles in Figure 4.2), are readily extracted, while $Fe(NO_3)_3$ serves as a background (green circles in Figure 4.2), just like in a typical experiment.

4.2 Theoretical Section: Deriving the Droplet Model

4.2.1 Establishing the Model System for Liquid-Liquid Extraction

To study the liquid-liquid extraction by the non-ionic extractant dissolved in the organic solvent, we constructed the model system made of two phases in contact. The two phases are namely the aqueous and the organic phase (*i.e.* the solvent). We consider a bulk model for the formation of reverse micelles *i.e.* aggregates responsible for the transfer of ions between two phases. Aggregates are considered as a gas of spherical droplet-like particles of different compositions present in equilibrium, hence the name the Droplet model. The schematic representation of the model is presented in Figure 4.4. Spherical reverse micelles are adequate approximation in dilute regime, especially in the case when constituting extractants have more than one chain and when chains are branched[163, 164]. The combined study of X-ray reflectivity at the n-dodecane/ aqueous solution (containing REEs), MD simulations and mesoscopic modelling showed that initially, the spherical micelles are preferred in the case of bulky extractants[163]. The extractant considered in this chapter is *N,N´*-dimethyl-*N,N´*-dioctyl-2-(2-hexyloxyethyl)-malonamide (DMDOHEMA). DMDOHEMA chemical structure is presented in Figure 4.3. This is the type of extractant that has three chains. The branched extractant is the subject of the next chapter. The aqueous solution contains multiple ion species, whereas the organic phase is made of monomeric DMDOHEMA extractants, and self-assembled water-in-oil (w/o) 'reverse micelles' (shortly aggregates). In our approach, the aggregates are only a solute-filled self-assembled structures in the organic phase. All species are in the thermodynamic equilibrium. The aqueous solution represents the brine whereas the organic phase is the solvent phase in some industrial process *e.g.* DIAMEX process. A model system is applicable to any hydrometallurgical recovery or nuclear fuel reprocessing which utilize non-ionic solvating

extractants. We have neglected the solubility (*i.e.* the aqueous partitioning) of DMDOHEMA in water[165, 166]. The dimerization of DMDOHEMA is neglected[167].

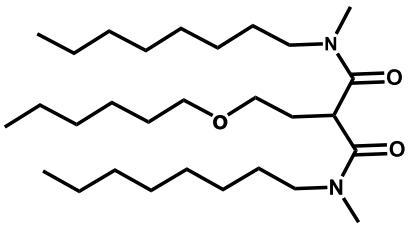

Figure 4.3 – DMDOHEMA extractant chemical structure.

4.2.2 Free Energy of the Spherical DMDOHEMA Aggregate

Aggregates are considered as spheres with two distinct parts. The outer part is assumed as a layer of extractant molecules chains (resembling a corona) with the average length, $l_{\text{chain,D}}$. The inner part, or the core of the aggregate, consists of extractant polar head groups immersed in the pool of an aqueous solution. The core is characterized by the volume, V_{core}. The free energy of such aggregate of particular composition, $F_{\text{Agg},x}$, can be written as

$$F_{\text{Agg},x} = F_{\text{chain}} + F_{\text{core}} \tag{4.1}$$

where F_{chain} is the free energy associated with the layer (or a highly curved film) of extractant molecules (shortly the chain term) and F_{core} is the free energy of the core of the aggregate. F_{core} is defined as

$$F_{\text{core}} = F_{\text{droplet}} + F_{\text{complex}} \tag{4.2}$$

where F_{droplet} is free energy of a droplet of aqueous electrolyte solution and F_{complex} is the complexation term which describes interactions between cations and extractant head groups.

We start by deriving the expression for the free energy of a single droplet of aqueous solution, F_{droplet}, immersed in the medium characterized with low dielectric constant. The partition function $\tilde{Z}$ in canonical ensemble for a single droplet of the aqueous solution can be written as[168, 169]

$$\tilde{Z} = \frac{1}{N_{\text{H}_2\text{O}}! \prod_j N_j!} \cdot \frac{1}{h_{\text{H}_2\text{O}}^{3N_{\text{H}_2\text{O}}} \prod_{\text{j}} h_j^{3N_j}} \int \cdots \int \mathrm{d}\mathbf{r}^{N_{\text{H}_2\text{O}}}\, \mathrm{d}\mathbf{r}^{N_j} \mathrm{d}\mathbf{p}^{N_{\text{H}_2\text{O}}}\, \mathrm{d}\mathbf{p}^{N_j}\, e^{-\beta\left(V + \sum_k \frac{\mathbf{p}_k^2}{2m_k}\right)} \tag{4.3}$$

where index j accounts for all ions present in the core of the aggregate, k accounts for all ions and water molecules present in the core, h is the Planck's constant, $\mathbf{r}_{\text{k}}$ and $\mathbf{p}_{\text{k}}$ are respectively the position and momenta of each particle in the droplet, β is defined as $\beta = 1/k_{\text{B}}T$, k_{B} is

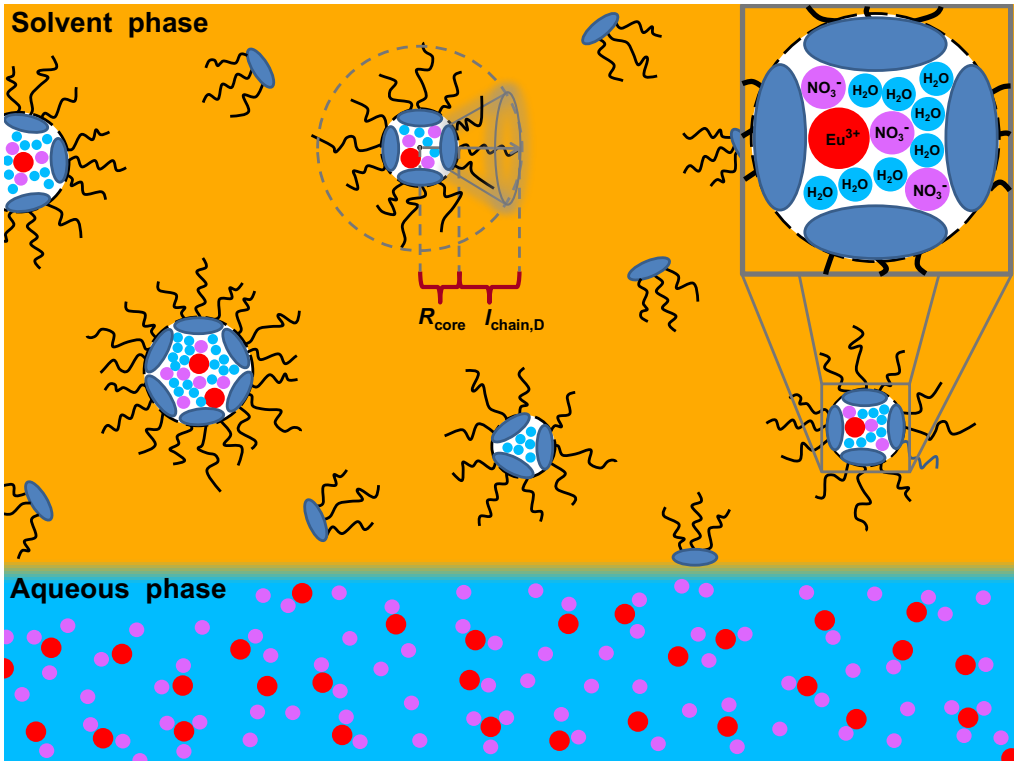

Figure 4.4 – Schematic representation of the bulk model for the liquid-liquid extraction using non-ionic extractant. Various types of aggregates are present in the organic phase (solvent phase), and their probability at equilibrium is determined by the composition of their cores and extractant film. Considering the surfactant nature of the extractant, the interface is at least partially covered by the extractant molecules (not shown here). The zoomed region shows the core of the aggregate with the europium cation (red), the nitrate anion (pink), water molecules (pale blue), and DMDOHEMA malonamide extractant head groups (dark blue). Extractant hydrophobic chains are presented in black.

the Boltzmann constant, T is the thermodynamic temperature, m_k is the mass of k-th particle and V is the interacting potential among particles. The factorials in the denominator of Eq. 4.3 account for the indistinguishability of particles. In such formulation the integral of Eq. 4.3 over momenta of the particles gives

$$\tilde{Z} = \frac{1}{N_{\mathrm{H_2O}}! \prod_j N_j!} \cdot \frac{1}{\Lambda_{\mathrm{H_2O}}^{3N_{\mathrm{H_2O}}} \prod_j \Lambda_j^{3N_j}} \int \cdots \int \mathrm{d}\mathbf{r}^{N_{\mathrm{H_2O}}} \, \mathrm{d}\mathbf{r}^{N_j} \, e^{-\beta V} \tag{4.4}$$

where $\Lambda_{\mathrm{H_2O}}$ and Λ_j are the effective de Broglie thermal wavelengths of water molecules and ions. Eq. 4.4 holds for large number of particles. In contrast to such conditions, our droplet is composed of typically up to 10 particles, with small variation depending on the composition of polar core. Therefore $\tilde{Z}$ needs to be corrected for such a small number of particles. If Stirling's

approximation is written as $N! \simeq N^N e^{-N}$ then

$$\tilde{Z}_{\text{approx}} = \frac{N_{\text{H}_2\text{O}}^{N_{\text{H}_2\text{O}}} e^{-N_{\text{H}_2\text{O}}} \prod_j N_j^{N_j} e^{-N_j}}{N_{\text{H}_2\text{O}}! \prod_j N_j!} \tilde{Z} \tag{4.5}$$

where $\tilde{Z}_{\text{approx}}$ is the canonical partition function for a droplet of aqueous electrolyte solution, corrected for the small number of particles. By taking a negative logarithm of the Eq. 4.5 and multiplying with $k_{\text{B}}T$ we obtain

$$-k_{\text{B}}T \ln \tilde{Z}_{\text{approx}} = -k_{\text{B}}T \ln \frac{N_{\text{H}_2\text{O}}^{N_{\text{H}_2\text{O}}} e^{-N_{\text{H}_2\text{O}}} \prod_j N_j^{N_{\text{j}}} e^{-N_j}}{N_{\text{H}_2\text{O}}! \prod_j N_j!} - k_{\text{B}}T \ln \tilde{Z}. \tag{4.6}$$

By identification we have $F_{\text{droplet}} = -k_{\text{B}}T \ln \tilde{Z}$ which is the free energy of the macroscopic droplet in the bulk, and the correction term $F_{\text{correction}}$, due to the small number of particles has following expression

$$F_{\text{correction}} = k_{\text{B}}T \ln \left(N_{\text{H}_2\text{O}}! \prod_j N_j! \right) - k_{\text{B}}T \left(N_{\text{H}_2\text{O}} \ln N_{\text{H}_2\text{O}} + \sum_j N_j \ln N_j - N_{\text{H}_2\text{O}} - \sum_j N_j \right) \tag{4.7}$$

F_{droplet} is considered as equivalent system in the bulk. It follows that ions and water molecules inside the core of the aggregate have the same standard state defined as the ones in the aqueous phase in contact[170]. In the case of the liquids, where PV-term is negligible we can equalize $F_{\text{droplet}} \simeq G_{\text{droplet}}$. G_{droplet} can be written as

$$G_{\text{droplet}} = N_{\text{H}_2\text{O}} \mu_{\text{H}_2\text{O}}^{\text{org}} + \sum_j N_j \mu_j^{\text{org}} \tag{4.8}$$

where G_{droplet} is the Gibbs energy of the droplet of the aqueous solution, $\mu_{\text{H}_2\text{O}}^{\text{org}}$ and μ_j^{org} are respectively chemical potentials of water molecules and ions present in the core of the aggregate. Both aqueous solutions inside the core of the aggregate and in the aqueous phase are considered as ideal, thus ion activity coefficients and the osmotic coefficient are equal to 1 ($\gamma_j^{\text{org}} = \phi^{\text{org}} = 1$)[67]. We have

$$\mu_j^{\text{org}} = \mu_j^{\circ} + k_{\text{B}}T \ln \left(\frac{m_j^{\text{org}}}{m_j^{\circ}} \right) \tag{4.9}$$

and

$$\mu_{\text{H}_2\text{O}}^{\text{org}} = \mu_{\text{H}_2\text{O}}^{\circ} - k_{\text{B}}T \frac{\sum_j x_j^{\text{org}}}{x_{\text{H}_2\text{O}}^{\text{org}}} \tag{4.10}$$

where μ_j°, $\mu_{\text{H}_2\text{O}}^{\circ}$, m_j^{org}, m_j°, x_j^{org}, $x_{\text{H}_2\text{O}}^{\text{org}}$ are respectively the standard chemical potentials of ions and water molecules in the core of the aggregate, molalities and mole fraction of ions of species j and of water molecules in the core, and $m^{\circ} = 1$ mol kg^{-1} is the standard molality. The Eq. 4.10 is the consequence of Eq. 4.9 when Gibbs-Duhem relation is used (recall derivation

of Gibbs-Duhem relation and the integration of the differential form presented in the second chapter of this manuscript). By taking into account the ideal behavior of the ions and water molecules, we are only dealing with entropic part of the free energy *i.e.* the accessible volume in the aggregate polar core.

In our approach the excess energy contribution to account for non-ideality of the aqueous solution inside the core of the aggregate, is given as a complexation energy F_{complex}. For example, we can imagine this as the energy difference between the state that lanthanide would have in weak association by extractant molecules while retaining partiality its hydration sphere and the state with its full hydration sphere in the bulk aqueous solution. F_{complex} is the energy term which describes interaction between complexed ion and extractant head groups. In our formulation it is taken into account as a primitive general description of the complex between cation and electron donor atoms, which is sometimes referred as a basis of the extraction[11] and it typically represents the bond energy measured in the EXAFS measurement. In our approach F_{complex} is a quantity independent to the accessible volume of monolayer of the extractant head groups and is assumed to be additive by nature[171, 172]. It reads

$$F_{\text{complex}} = -k_{\text{B}}T \ln N_{\text{complex}} - \sum_i N_{i,\text{D}} N_{\text{bond},i,\text{D}} E_{i,\text{D}} \tag{4.11}$$

where subscript D depicts DMDOHEMA extractant, N_{complex} is the number of microstates associated with the binding of cations to the 2D array of sites (a monolayer of extractant head groups), $N_{i,\text{D}}$ is the number of particular cations i in the core bonded to extractant film, $N_{\text{bond},i,\text{D}}$ is the number of sites of type D (or the number of DMDOHEMA extractants) occupied by a particular cation i (created a bond), $E_{i,\text{D}}$ is the internal energy parameter and represents the energy contribution for each bond created between particular cation i and extractant head groups. It is adjusted parameter (fitting procedure is described in later in the text). In the case of Eu^{3+} or Fe^{3+}, we have the number of DMDOHEMA sites bonded per one cation $N_{\text{bond},\text{Eu}^{3+},\text{D}} \in [1, 2]$. This practically means that there can be maximum of two DMDOHEMA in the first coordination sphere of metal cation. For the acid (the proton), we have occupancy of only one site, $N_{\text{bond},\text{H}^{+},\text{D}} = 1$[34, 43]. There is a often neglected 'hidden' entropy associated with the binding of the cation to 2D array of sites, but it needs to be derived in a proper way. It must be noted that this effect is intrinsically included in molecular simulations, but in these kind of modelling it needs to be included by hand.

A general formula for N_{complex} can be derived from basic combinatorics[172]. We approximate a spherical film of extractant molecules as a 2D array of sites. The schematic representation of this process is given in Figure 4.5. Sites corresponding to non-ionic extractant

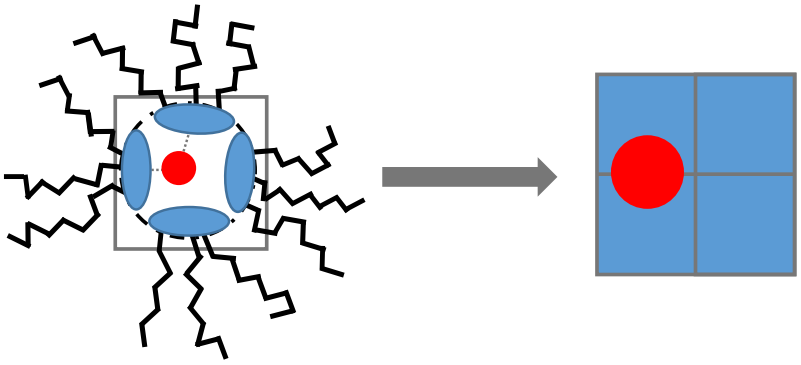

Figure 4.5 – Schematic representation of the calculation of the number of microstates (the entropy) associated with the binding of mixed extractant head group film N_{complex}. The extractant head groups film is approximated with 2D array of sites - an expanded lattice model. Eu^{3+} cation (red), and DMDOHEMA malonamide extractant head groups (dark blue). Gray dashed lines connecting the cation with the head groups serve as guideline for bonding. It can be seen that Eu^{3+} can be bonded to on or two extractant head group.

DMDOHEMA remain unchanged upon binding of any cation. Sites that bind the cation are mutually indistinguishable, but are distinguishable from empty sites (no cations bound), and the one that bind the extracted acid. Acid can take up only one site. The number of microstates associated with binding of different cations to extractant film N_{complex} has a form of

$$N_{\text{complex}} = \frac{N_{\text{D}}!}{\prod_i N_{i,\text{D}}! \, (N_{\text{D}} - \sum_i N_{i,\text{D}} N_{\text{bond},i,\text{D}})!} \cdot \frac{1}{\prod_i N_{\text{bond},i,\text{D}}!^{N_{i,\text{D}}}} \tag{4.12}$$

where factor $1/\prod_{\text{i}} N_{\text{bond},i,\text{D}}!^{N_i}$ accounts for intra-indistinguishability of DMDOHEMA sites that bind a particle[26, 172]. Note that $1/\prod_i N_{i,\text{D}}!$ is omitted form the calculation since the factor is already intrinsically included within the calculation of F_{droplet} (in order to recover Eq 4.8, we need to take negative value of the natural logarithm of the partition function for the droplet of the aqueous solution).

In the perspective of the statistical thermodynamics in order to justify the usage of F_{complex} we can write the corrected partition function given in Eq. 4.13 with the additional potential independent to the accessible volume of the extractant film. We have

$$\tilde{Z}_{\text{approx}} = \frac{N_{\text{H}_2\text{O}}^{N_{\text{H}_2\text{O}}} e^{-N_{\text{H}_2\text{O}}} \prod_j N_j^{N_j} e^{-N_j}}{N_{\text{H}_2\text{O}}! \prod_j N_j!} \cdot$$

$$\frac{1}{N_{\text{H}_2\text{O}}! \prod_j N_j!} \cdot \frac{1}{\Lambda_{\text{H}_2\text{O}}^{3N_{\text{H}_2\text{O}}} \prod_j \Lambda_j^{3N_j}} \int \cdots \int \mathrm{d}\mathbf{r}^{N_{\text{H}_2\text{O}}} \, \mathrm{d}\mathbf{r}^{N_j} \mathrm{d}\mathbf{p}^{N_{\text{H}_2\text{O}}} \, \mathrm{d}\mathbf{p}^{N_j} \, e^{-\beta(V - N_{i,\text{D}} N_{\text{bond,D},i} E_{i,\text{D}})} \tag{4.13}$$

At this point we need to multiply Eq. 4.13 with the number of microstates when we have

complexed ion in the system N_{complex}. We obtain

$$\tilde{Z}_{\text{approx,tot}} = \frac{N_{\text{H}_2\text{O}}^{N_{\text{H}_2\text{O}}} e^{-N_{\text{H}_2\text{O}}} \prod_{\text{j}} N_{\text{j}}^{N_{\text{j}}} e^{-N_{\text{j}}}}{N_{\text{H}_2\text{O}}! \prod_{\text{j}} N_{\text{j}}!} \cdot N_{\text{complex}} \cdot \frac{1}{N_{\text{H}_2\text{O}}! \prod_{\text{j}} N_{\text{j}}!} \cdot \frac{1}{\Lambda_{\text{H}_2\text{O}}^{3N_{\text{H}_2\text{O}}} \prod_{\text{j}} \Lambda_{\text{j}}^{3N_{\text{j}}}} \int \cdots \int_{V_{\text{droplet}}} \mathrm{d}\mathbf{r}^{N_{\text{H}_2\text{O}}} \, \mathrm{d}\mathbf{r}^{N_{\text{j}}} \, e^{-\beta(V - N_{i,\text{D}} N_{\text{bond,D},i} E_{i,\text{D}})} \tag{4.14}$$

If the additional potential is independent of the accessible volume, we now factorize expression in Eq. 4.14 and we recover

$$\tilde{Z}_{\text{approx}} = N_{\text{complex}} \cdot e^{-N_{i,\text{D}} N_{\text{bond,D},i} E_{i,\text{D}}} \cdot \frac{N_{\text{H}_2\text{O}}^{N_{\text{H}_2\text{O}}} e^{-N_{\text{H}_2\text{O}}} \prod_{j} N_{j}^{N_{j}} e^{-N_{j}}}{N_{\text{H}_2\text{O}}! \prod_{j} N_{j}!} \tilde{Z} \tag{4.15}$$

Finally, by taking a natural logarithm of the Eq. 4.15, multiplying by $-k_{\text{B}}T$, and identifying already defined terms, we obtain

$$F_{\text{core}} = F_{\text{droplet}} + F_{\text{complex}} + F_{\text{correction}} \ . \tag{4.16}$$

Indeed, this was a desired outcome when we defined F_{core} since it ensures the generality of the method.

Next thing is to calculate the free energy of the highly curved film of the extractant molecules. We adopt already established formulation where F_{chain} has a form of a harmonic approximation and can be written as[47, 173]

$$F_{\text{chain}} = \frac{\kappa_{\text{D}}^{\star}}{2} \left(\sum_{i} N_{i,\text{D}} N_{\text{bond},i,\text{D}} \left(p - p_{0,i,\text{D}}\right)^2 + \left(N_{\text{D}} - \sum_{i} N_{i,\text{D}} N_{\text{bond},i,\text{D}}\right) \left(p - p_{0,\text{H}_2\text{O},\text{D}}\right)^2 \right) \tag{4.17}$$

where $\kappa_{\text{D}}^{\star}$ represents the generalized bending constant of DMDOHEMA extractant film in a particular solvent, p is the packing parameter of the particular aggregate, $p_{0,i,\text{D}}$ is the spontaneous packing parameter for a certain type of DMDOHEMA extractant/cation pair in a particular solvent (*e.g.* Eu^{3+} to DMDOHEMA in *n*-heptane), $p_{0,\text{H}_2\text{O},z}$ is the spontaneous packing parameter of DMDOHEMA extractant when no cations are bound to it *i.e.* in contact to pure water[126, 174, 175]. Upon a binding of the acid (the proton) the spontaneous packing parameter is the same as for the water in contact ($p_{0,\text{H}^+,\text{D}} = p_{0,\text{H}_2\text{O},\text{D}}$). This approximation is based on the argument that binding of the proton does not impose severe structural changes of the malonamide polar head groups. The same property is not met when multivalent (Eu^{3+} or Fe^{3+}) is bound to the extractant head groups, thus we have a different values of spontaneous packing parameter. It must be noted, that generalized bending constant of DMDOHEMA $\kappa_{\text{D}}^{\star}$, is kept constant with respect to binding of different cations. We assume that $\kappa_{\text{D}}^{\star}$ reflects the property of the organic solvent used. It was shown that on average, conformations of chains are

mostly dominated by the interactions with the organic solvent[47]. In our study $\kappa^{\star}_{\mathrm{D}}$, $p_{0,\mathrm{H_2O},\mathrm{D}}$ and $p_{0,i,\mathrm{D}}$ are adjusted parameters.

If we assume the fixed chain length $l_{\mathrm{chain,D}}$ in the case of spherical reverse micelles, the packing parameter can be written in the explicit form as [47]

$$p = 1 + \frac{l_{\mathrm{chain,D}}}{R_{\mathrm{core}}} + \frac{1}{3}\frac{l^2_{\mathrm{chain,D}}}{R^2_{\mathrm{core}}}. \tag{4.18}$$

The full derivation of the expression above can be found in references [176, 177]. The radius of the core R_{core} is

$$R_{\mathrm{core}} = \sqrt[3]{\frac{3V_{\mathrm{core}}}{4\pi}} \tag{4.19}$$

with

$$V_{\mathrm{core}} = \sum_j N_j V_{\mathrm{m},j} + N_{\mathrm{H_2O}} V_{\mathrm{m,H_2O}} + N_{\mathrm{D}} V_{\mathrm{m,D}} \tag{4.20}$$

where N_j, $V_{\mathrm{m},j}$, $N_{\mathrm{m,H_2O}}$, $V_{\mathrm{m,H_2O}}$, N_{D} and $V_{\mathrm{m,D}}$ are respectively stoichiometry numbers and partial molar volumes of ions, water molecules, and DMDOHEMA head groups that constitute the core of the aggregate. Partial molar volumes that appear in Eq. 4.20 are measured quantities and are taken form the literature[178, 47].

When all terms from expressions for F_{core} and F_{chain} are summed (Eq. 4.1), the free energy of the aggregate of particular composition $F_{\mathrm{Agg},x}$ at infinite dilution is obtained. It follows that $F_{\mathrm{Agg},x}$ is by definition the standard chemical potential, $\mu^{\circ}_{\mathrm{Agg},x}$ of the reverse micelle in the particular organic solvent (recall that the partition function was written for a single droplet of an aqueous solution with complexation)[26]. We obtained a key equation of the model:

$$\mu^{\circ}_{\mathrm{Agg},x} = F_{\mathrm{Agg},x} \tag{4.21}$$

4.2.3 Analytical Expression of Standard Chemical Potential of the Particular Pure DMDOHEMA Aggregate

Here we summarize the derivation form previous section. A full expression for the standard chemical potential of the particular aggregate self-assembled from DMDOHEMA extractant molecules reads

$$\begin{aligned}\mu^{\circ}_{\mathrm{Agg},x} = F_{\mathrm{Agg},x} = F_{\mathrm{complex}} + F_{\mathrm{correction}} + F_{\mathrm{droplet}} + F_{\mathrm{chain}} = \\ -k_{\mathrm{B}}T\,\ln N_{\mathrm{complex}} - \sum_i N_{i,\mathrm{D}} N_{\mathrm{bond},i,\mathrm{D}} E_{i,\mathrm{D}} + \\ k_{\mathrm{B}}T\ln\left(N_{\mathrm{H_2O}}!\prod_j N_j!\right) - k_{\mathrm{B}}T\left(N_{\mathrm{H_2O}}\ln N_{\mathrm{H_2O}} + \sum_j N_j \ln N_j - N_{\mathrm{H_2O}} - \sum_j N_j\right) + \\ N_{\mathrm{H_2O}}\mu^{\circ}_{\mathrm{H_2O}} - k_{\mathrm{B}}T N_{\mathrm{H_2O}}\,\frac{\sum_j x_j^{\mathrm{org}}}{x^{\mathrm{org}}_{\mathrm{H_2O}}} + \sum_j N_j\mu^{\circ}_j + k_{\mathrm{B}}T\sum_j N_j \ln\left(\frac{m_j^{\mathrm{org}}}{m^{\circ}_j}\right) + \\ \frac{\kappa^{\star}_{\mathrm{D}}}{2}\left(\sum_i N_{i,\mathrm{D}} N_{\mathrm{bond},i,\mathrm{D}}\left(p - p_{0,i,\mathrm{D}}\right)^2 + \left(N_{\mathrm{D}} - \sum_i N_{i,\mathrm{D}} N_{\mathrm{bond},i,\mathrm{D}}\right)\left(p - p_{0,\mathrm{H_2O},\mathrm{D}}\right)^2\right)\end{aligned} \tag{4.22}$$

The expression is valid for any composition of an aggregate, under the condition that the electroneutrality is preserved since Born energy of maintaining charged species in the low dielectric medium is too high.

4.2.4 Global Equilibrium: Establishing a General Mass Action Law

To represent ensemble of all possible chemical reactions in $HNO_3/Eu(NO_3)_3/Fe(NO_3)_3$ liquid-liquid extraction system utilizing DMDOHEMA extractant, we establish the following relation[53, 9]:

$$N_{\mathrm{H_2O}}\cdot \mathrm{H_2O} + N_{\mathrm{M^{3+}}}\cdot \mathrm{M^{3+}} + N_{\mathrm{H^+}}\cdot \mathrm{H^+} + N_{\mathrm{NO_3^-}}\cdot \mathrm{NO_3^-} + N_{\mathrm{D}}\cdot \overline{\mathrm{D}} \rightleftharpoons \overline{\mathrm{A}_{N_{\mathrm{H_2O}};N_{\mathrm{M^{3+}}};N_{\mathrm{H^+}};N_{\mathrm{NO_3^-}};N_{\mathrm{D}}}} \tag{4.23}$$

where H_2O, M^{3+}, H^+, NO_3^-, $\overline{D}$, $N_{H_2O}, N_{M^{3+}}, N_{H^+}, N_{NO_3^-}$, and N_D are respectively symbols and stoichiometry numbers for the water molecules, the multivalent cations (Eu^{3+} or Fe^{3+}), the proton, the nitrate anion, and DMDOHEMA. $\overline{\mathrm{A}_{N_{\mathrm{H_2O}};N_{\mathrm{M^{3+}}};N_{\mathrm{H^+}};N_{\mathrm{NO_3^-}};N_{\mathrm{D}}}}$ is the general symbol for any type of the aggregate. Species present in the organic solvent are denoted by overlined symbols. Note that DMDOHEMA is neutral extractant which means that the cation is always transferred from aqueous phase to solvent along with appropriate number of nitrate anions (NO_3^-) to balance the charge. The chemical potentials of species involved in the chemical reaction described by Eq. 4.23, can be written as

$$\mu_{\mathrm{Agg},x} = \mu^{\circ}_{\mathrm{Agg},x} + k_{\mathrm{B}}T\ln\left(\frac{c_{\mathrm{Agg},x}}{c^{\circ}}\right) \tag{4.24}$$

$$\mu_{\mathrm{D}} = \mu^{\circ}_{\mathrm{D}} + k_{\mathrm{B}}T\ln\left(\frac{c_{\mathrm{D}}}{c^{\circ}}\right) \tag{4.25}$$

$$\mu^{\mathrm{aq}}_j = \mu^{\circ}_j + k_{\mathrm{B}}T\ln\left(\frac{m^{\mathrm{aq}}_j}{m^{\circ}_j}\right) \tag{4.26}$$

and

$$\mu^{\mathrm{aq}}_{\mathrm{H_2O}} = \mu^{\circ}_{\mathrm{H_2O}} - k_{\mathrm{B}}T\,\frac{\sum_j x^{\mathrm{aq}}_j}{x^{\mathrm{aq}}_{\mathrm{H_2O}}} \tag{4.27}$$

where $\mu_{\mathrm{Agg},x}$, μ_{D}, μ°_{D}, $c_{\mathrm{Agg},x}$, c_{D}, and c° are respectively the chemical potential of aggregate of the particular composition in the solvent, the chemical potential of monomer DMDOHEMA in the solvent, the standard chemical potential of monomer of DMDOHEMA in the solvent, the equilibrium molar concentrations of aggregates, molar concentration of DMDOHEMA extractants in the solvent. Concentration at standard state is: $c^{\circ} = 1$ mol dm^{-3}. It can be seen that we have neglected the activity coefficients in the organic phase. This is a consequence of our bulk model for the dilute regimes in aggregation. Therefore, we dealt with the ideal gas of dispersed aggregates in the organic phase. Supramolecular aspect of the self-assembly is neglected. μ^{aq}_j, m^{aq}_j, $\mu^{\mathrm{aq}}_{\mathrm{H_2O}}$, x^{aq}_j, and $x^{\mathrm{aq}}_{\mathrm{H_2O}}$ are respectively the chemical potentials and the molalities of ions, the chemical potential of water molecules, and mole fractions of ions and water molecules in the aqueous phase. To complete the calculation we need to write the chemical reactions (Eq. 4.23) in terms of chemical potentials of all involved species. We have

$$\mu_{\mathrm{Agg},x} = N_{\mathrm{D}} \cdot \mu_{\mathrm{D}} + N_{\mathrm{H_2O}} \cdot \mu^{\mathrm{aq}}_{\mathrm{H_2O}} + \sum_j N_j \cdot \mu^{\mathrm{aq}}_j \tag{4.28}$$

which is equal to

$$\mu^{\circ}_{\mathrm{Agg},x} + k_{\mathrm{B}}T \ln\left(\frac{c_{\mathrm{Agg},x}}{c^{\circ}}\right) = N_{\mathrm{H_2O}}\mu^{\circ}_{\mathrm{H_2O}} - N_{\mathrm{H_2O}}k_{\mathrm{B}}T\,\frac{\sum_j x^{\mathrm{aq}}_j}{x^{\mathrm{aq}}_{\mathrm{H_2O}}} + \sum_j N_j\mu^{\circ}_j + \tag{4.29}$$
$$k_{\mathrm{B}}T \sum_j N_j \ln\left(\frac{m^{\mathrm{aq}}_j}{m^{\circ}_j}\right) + N_{\mathrm{LH}} + N_{\mathrm{D}}\mu^{\circ}_{\mathrm{D}} + N_{\mathrm{D}}k_{\mathrm{B}}T \ln\left(\frac{c_{\mathrm{D}}}{c^{\circ}}\right)$$

At this point, it is convenient to define

$$\mu^{\circ''}_{\mathrm{Agg},x} = \mu^{\circ}_{\mathrm{Agg},x} - N_{\mathrm{H_2O}}\mu^{\mathrm{org}}_{\mathrm{H_2O}} - \sum_j N_j\mu^{\mathrm{org}}_j \tag{4.30}$$

where $\mu^{\circ''}_{\mathrm{Agg},x}$ is reduced standard chemical potential of the aggregate, obtained by subtracting the chemical potentials of ions and water molecules confined in the aggregate's core form $\mu^{\circ}_{\mathrm{Agg},x}$. $\mu^{\circ''}_{\mathrm{Agg},x}$ still contains the all other terms, namely the chain, the complexation, terms for the correction of statistics for small number of particles. After inserting Eq 4.30 into Eq 4.29, all the standard chemical potentials of ions and water molecules cancel out. We obtain

$$k_{\mathrm{B}}T \ln\left(\frac{c_{\mathrm{Agg},x}}{c^{\circ}}\right) = -\mu^{\circ''}_{\mathrm{Agg},x} + k_{\mathrm{B}}T \sum_j N_j \ln\left(\frac{m^{\mathrm{aq}}_j}{m^{\mathrm{org}}_j}\right) + N_{\mathrm{H_2O}}k_{\mathrm{B}}T \left(\frac{\sum_j x^{\mathrm{org}}_j}{x^{\mathrm{org}}_{\mathrm{H_2O}}} - \frac{\sum_j x^{\mathrm{aq}}_j}{x^{\mathrm{aq}}_{\mathrm{H_2O}}}\right)$$
$$+ N_{\mathrm{D}}\mu^{\circ}_{\mathrm{D}} + N_{\mathrm{D}}k_{\mathrm{B}}T \ln\left(\frac{c_{\mathrm{D}}}{c^{\circ}}\right) \tag{4.31}$$

Now we multiply Eq. 4.31 with β, with $\beta = 1/k_{\mathrm{B}}T$, and apply exponential function to the whole expression. We obtain

$$c_{\mathrm{Agg},x} = D_{\mathrm{Agg},x}\, c_{\mathrm{D}}^{N_{\mathrm{D}}} \tag{4.32}$$

where $D_{\mathrm{Agg},x}$ is defined as

$$D_{\mathrm{Agg},x} = \exp\left(-\beta\mu^{\circ\prime\prime}_{\mathrm{Agg},x} + \sum_j N_j \ln\left(\frac{m_j^{\mathrm{aq}}}{m_j^{\mathrm{org}}}\right) + N_{\mathrm{H_2O}}\left(\frac{\sum_j x_j^{\mathrm{org}}}{x_{\mathrm{H_2O}}^{\mathrm{org}}} - \frac{\sum_j x_j^{\mathrm{aq}}}{x_{\mathrm{H_2O}}^{\mathrm{aq}}}\right) + \beta N_{\mathrm{D}}\mu^{\circ}_{\mathrm{D}}\right)\left(\frac{1}{c^{\circ}}\right)^{N_{\mathrm{D}}-1} \tag{4.33}$$

with

$$\mu^{\circ\prime\prime}_{\mathrm{Agg},x} = F_{\mathrm{complex}} + F_{\mathrm{correction}} + F_{\mathrm{chain}} \tag{4.34}$$

Eq. 4.32 and 4.33 constitute the analytical expression for calculation of the equilibrium concentration of the particular aggregate.

4.2.5 Algorithm for Finding a Numerical Solution of Multiple Equilibrium System

The calculation were preformed in a semi-grand canonical ensemble (we only considered a reservoir of water molecules)[169]. Therefore, in order to obtain a correct equilibrium concentrations of the extractant and aggregates in solvent and ions in aqueous phase, we need to minimize MAL for all components simultaneously. Since Eq. 4.32 is a monotonic increasing function, the root of it was found using the bisection method[179]. The algorithm for finding the solution for the described system of equations was based on the self-consistent approach. Each component in the system represents additional dimension for the minimisation. The algorithm to calculate the equilibrium concentrations of all species is as follows:

1. Calculate equilibrium aggregate concentrations using initial concentrations of species which are provided as an input.
2. Find the root of Eq. 4.32 using the bisection method.
3. Calculate equilibrium aggregate concentrations again using newly calculated equilibrium extractant concentrations (the root of Eq. 4.32).
4. Use bisection method to find equilibrium concentrations of each ionic specie present in the system.
5. Repeat the procedure until the two consecutive calculations do not provide different values (up to convergence limit).
6. Calculate thermodynamic properties of the system.

Algorithm is presented as a flowchart in Figure 4.6, and developed program has been named: **DropEx**. To reduce a numerical noise, the minimization cycles were ordered in a such a way that extractant and the species with the lowest value of concentrations (such as Eu^{3+} or Fe^{3+}) were calculated until the relative difference of calculated equilibrium concentrations between two subsequent calculations was less than $1{\times}10^{-8}$. For the species with higher concentrations (such as NO_3^-) the relative difference was set to $1{\times}10^{-5}$. To satisfy MAL, the root of the polynomial of degree N_D (Eq. 4.32) needs to be solved.

Calculated $c_{\mathrm{Agg},x}$ are normalized over the sample. We state that aggregates are only species filled with solutes. Therefore, probabilities of particular aggregate $P_{\mathrm{Agg},x}$ are defined as

$$P_{\mathrm{Agg},x} = \frac{c_{\mathrm{Agg},x}}{\sum_x c_{\mathrm{Agg},x}}. \tag{4.35}$$

It must be noted that this algorithm was used for studies described later in Chapters 3 and 4. There is only a slight difference since in those studies, only extractant equilibrium concentrations are minimized.

4.3 Input for the Droplet Model

As was highlighted in previous section, there are certain measurable quantities and adjusted parameters needed as an input for the model. First for Eq. 4.20 we require: $V_{\mathrm{m},j}$, $V_{\mathrm{m,H_2O}}$, and $V_{\mathrm{m,D}}$ which are respectively molar volumes of ions, water, and DMDOHEMA extractant head groups and are taken from the literature[178, 47]. In the case of Eu^{3+}, as well in the case of many trivalent cations, the partial molar volume is close to -40 cm^3 mol^{-1}. This value is the consequence of the electrostriction phenomena[180]. In the case of very high ion concentrations, or in the confined media, this property is not valid. Therefore, due to the loss of the electrostriction in the core of the aggregate we neglect Eu^{3+} contribution.

Also, we need the length of the extractant molecule chains averaged over all conformations (shortly average length) $l_{\mathrm{chain,D}}$ to assemble the extractant film enclosing the core of aggregate. There is the choice for obtaining $l_{\mathrm{chain,D}}$. It can be assessed through a combination of Small Angle Neutron Scattering (SANS) and Small Angle X-ray Scattering (SAXS) pattern fits[181], or obtained from MD simulations as an average over time[47]. In the light of the multi-scale modelling, we have taken the value obtained from MD simulations where $l_{\mathrm{chain,D}} = 9.6$Å and it corresponds to typically 80% of fully stretched chain length. The length of the extractant molecule chains is considered not to change for different compositions of the core of the aggregate. Note that the solvent in simulations was *n*-heptane. In our bulk model, organic solvent

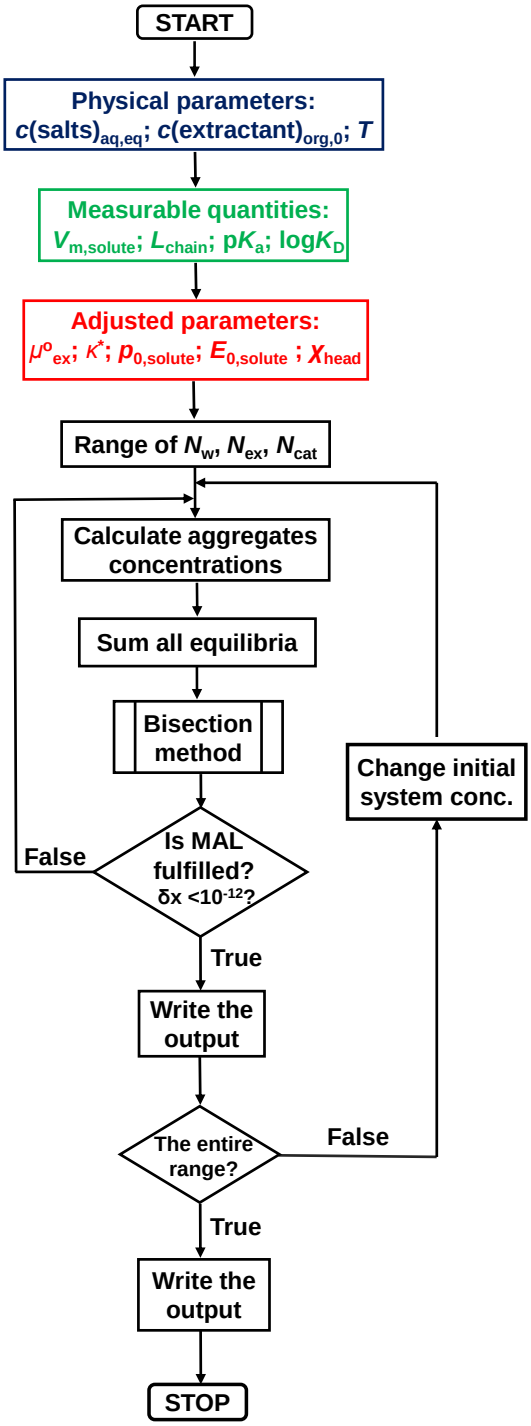

Figure 4.6 – Flowchart of the developed code

does not appear explicitly in MAL. In fact, we have taken solvent into account through $l_{\mathrm{chain,D}}$ and $\kappa_{\mathrm{D}}^{\star}$ which specific and depend on the choice of the solvent. Therefore, the influence of

penetrating and non-penetrating solvents on the overall extraction process can therefore easily be included in this model[182].

The model also requires the initial concentrations of all species in the system, namely the initial extractant concentration $c_{\mathrm{D,initial}}$, the initial nitric acid molality $m_{\mathrm{HNO_3,initial}}$, the initial europium nitrate molality $m_{\mathrm{Eu(NO_3)_3,initial}}$, and the initial iron nitrate molality $m_{\mathrm{Fe(NO_3)_3,initial}}$.

Beside measurable quantities and initial compositions of the system, our model requires a set of parameters, namely the standard chemical potential of monomeric DMDOHEMA extractant μ°_{D}, the spontaneous packing parameter $p_{0,i,\mathrm{D}}$ or particular cation/extractant couple, the rigidity constant $\kappa^{\star}_{\mathrm{D}}$ particular extractant in a given solvent, and the complexation parameter $E_{i,\mathrm{D}}$ for solutes (except water) that can be extracted to solvent phase. Among these values, only μ°_{D} is accessible by experiments. $p_{0,i,\mathrm{D}}$ and $\kappa^{\star}_{\mathrm{D}}$ can generally be assessed by fitting a whole three-component phase diagram[183]. $E_{i,\mathrm{D}}$ can be associated with the difference in first-sphere coordination sphere of complex cation in the core of the aggregate and fully hydrated cation in the aqueous phase. Fitting procedure is described in detail later in the Chapter.

Also, it is important to emphasize that our model is made entirely for the case of spherical micelles meaning that quantitative interpretation is possible for systems up to $c_{\mathrm{D,initial}} = 0.6$ mol dm^{-3} of DMDOHEMA (where worm-like micelles usually do not exist) and up to 0.5 mol dm^{-3} $Eu(NO_3)_3$ concentration (before the experimentally observed formation of the third phase occurs)[184].

4.4 Fitting of the Experimental Data

This section is deals with the procedure of adjusting the model parameters. First let us point to issue of choosing the reference data upon to base our fitting procedure. In this section we are dealing with the system of *n*-heptane solvent with dissolved DMDOHEMA extractant in contact to the aqueous solution containing respectively HNO_3, $Eu(NO_3)_3$ and $Fe(NO_3)_3$. Since the system is complex, it is difficult to find the consistent sets of data from various authors. We have chosen the work of four different working groups, materialized within available thesis manuscripts and published articles. References are given here [185, 184, 186, 54, 187]. Also, it must be noted that experimental error upon the determination of the metals extraction can be in the same order of magnitude as the value itself. The situation is especially bad for determination of the water by Karl-Fisher method. Furthermore, the measurements are done in a way that two phases are separated, which means that equilibrium is disrupted! With this in mind, the objective was to recover the trend in the extraction efficiency.

First thing to note is that the minimum aggregation number N_{D} was set to 4, with the argument that it is minimum needed to enclose a volume of confined ions and water[56].

The model parameters are: $\kappa^{\star}_{\mathrm{D}}, p_{0,\mathrm{Eu^{3+},D}}, p_{0,\mathrm{H^{+},D}}$, μ°_{D}, and $E_{i,\mathrm{D}}$. We performed fitting under constraints in order to reduce the number of possible sets of parameters that reproduce the experimental data.

Constraints for fitting procedure:

1. Experimental values of extraction of all solutes.

2. Experimentally determined Critical aggregate concentration CAC.

3. Realistic aggregate compositions based on experimental structural data.

4. Convergence of the mass integral: calculations ought to be invariant to the choice of upper limit of N_{D} and $N_{\mathrm{H_2O}}$ used as an input of the model.

These constraints are defined by authors, and their purpose is to obtain a reliable set of parameter that is able to reproduce trend of experimental data of various sources. Indeed, it was shown that these constraints help in doing so, as will be demonstrated throughout this and latter Chapters. By satisfying these three crucial conditions, we end up in the small domain of possible sets of parameters which means that the predicting power of the model is greatly enhanced. The prediction of extraction process for various species is then a consequence of satisfying those conditions. Moreover, it is crucial to start the fitting from the simplest system of pure water extraction only, and then to consider more complex systems containing respectively HNO_3, $Eu(NO_3)_3$ and $Fe(NO_3)_3$. Note that the parametrization has been made step-by-step, which means that $\kappa^{\star}_{\mathrm{D}}, p_{0,\mathrm{H_2O,D}}$ and μ°_{D} are adjusted for the extraction of water and are therefore considered fixed in later fitting of $E_{i,\mathrm{D}}$ for each solute. This is the only way to preserve reproducibility. Therefore, the first system to fit is pure water extraction[185, 184]. We have obtained $p_{0,\mathrm{H_2O,D}} = 3.5$, $\kappa^{\star}_{\mathrm{D}} = 16\ k_{\mathrm{B}}T$ per extractant molecule, and $\mu^{\circ}_{\mathrm{D}} = 2.5$ kJ mol^{-1}. $p_{0,\mathrm{H_2O,D}}$ and $\kappa^{\star}_{\mathrm{D}}$ will be discussed in detail in the next section. The value of μ°_{D} determines the transition energy between a monomeric to an aggregated state of the extractant. In our study, the aggregated state has a form of reverse micelles. It is accessible by experimental methods that can determine the mole fraction of the unbound extractant *e.g.* NMR shift techniques, scattering extrapolated to zero micelle concentration or derivatives analysis of liquid-liquid surface tension[50]. In the case of common extractants, the three techniques provided the same result[24]. The increase of μ°_{D} lowers the transition energy between the two states (Eq. 4.33)

thus favouring the micellization and the extraction of solutes. A favoured micellization is seen as lowering of CAC and increase in distribution coefficients. A notable property is that the calculated equilibrium aggregate probabilities are invariant to the change of μ_{D}° since it does not appear in the expression of the free energy of the particular aggregates, but only in the MAL. μ_{D}° was fitted accordingly to the experiments and obtained value in our study was 2.5 kJ mol^{-1}[66].

In order to obtain $E_{i,\mathrm{D}}$ for each solute, namely HNO_3, $Eu(NO_3)_3$, and $Fe(NO_3)_3$ we made a fitting based on different known studies. First, we fitted the model to the data concerning the extraction of HNO_3 alone[58, 188, 185, 184]. This yielded $E_{\mathrm{H^+,D}} = 5\ k_{\mathrm{B}}T$, which is a typical order of magnitude for the hydrogen bond formation. In order to obtain the $E_{\mathrm{Eu^{3+},D}}$ we fitted the experimental data of HNO_3 / $Eu(NO_3)_3$ system using $E_{\mathrm{Eu^{3+},D}}$[186]. Fitting resulted in $E_{\mathrm{Eu^{3+},D}} = 7.8\ k_{\mathrm{B}}T$ per Eu^{3+}/site bond. The same procedure was made for system HNO_3 and $Fe(NO_3)_3$, which in turn yielded $E_{\mathrm{Fe^{3+},D}} = 6.5\ k_{\mathrm{B}}T$ per Fe^{3+}/site bond[189]. This way of fitting was proposed in order to 'isolate' the complexation parameter of each particular cation (*i.e.* particular solute molecule). By doing this, of course, we neglected any type of interaction between different solutes in the organic phase and also, we forbid the existence of mixed-solute aggregates. Obviously, we made a very crude approximation, but this still makes a good starting point for a study of complex multicomponent systems. $E_{i,\mathrm{D}}$ in our study can be associated with the extraction free energy ΔG_0 from previous studies. ΔG_0 was defined as a difference between the free energy of an ion complexed by extractant molecules in the core of the aggregate and the ion in an aqueous phase along with its full hydration shell[71]. Such definition enabled a measurement of ΔG_0 by a combination of calorimetry and EXAFS measurements (coupled with *ab initio* calculations).

With all the parameters determined and discussed, we have preformed the calculation in attempt to quantitatively describe a properties of the extraction systems. All the following results are obtained from the calculation with $p_{0,\mathrm{H_2O,D}} = 3.5$, $\kappa_{\mathrm{D}}^{\star} = 16\ k_{\mathrm{B}}T$ per extractant molecule, $\mu_{\mathrm{D}}^{\circ} = 2.5$ kJ mol^{-1}, $E_{\mathrm{H^+,D}} = 5\ k_{\mathrm{B}}T$, $E_{\mathrm{Fe^{3+},D}} = 6.5\ k_{\mathrm{B}}T$ and $E_{\mathrm{Eu^{3+},D}} = 7.8\ k_{\mathrm{B}}T$ per bond.

4.5 Testing the Harmonic Approximation for the Calculation of the Curved Extractant Film Free Energy

Within this section we will demonstrate how to practically use the expression for the free energy of the highly curved extractant film given by Eq. 4.17. As can be seen, the expression is in fact a harmonic approximation. The minimum in free energy is obtained when packing parameter p is equal (or very close) to the spontaneous packing parameter of an extractants in the film $p_{0,i,\mathrm{D}}$. The squared difference between p and $p_{0,i,\mathrm{D}}$ guaranties that the effect of creating a highly curved extractant film is repulsive by nature and the chain free energy F_{chain} is always positive. The scaling factor $\kappa^{\star}_{\mathrm{D}}$ describes the slope of F_{chain} upon the change in packing parameter of the particular aggregate. Further in the text, we will elucidate how the choice of geometrical parameters $p_{0,i,\mathrm{D}}$ and $\kappa^{\star}_{\mathrm{D}}$ influences the formation of aggregates and we will hint their effect on the overall extraction efficiency.

4.5.1 Influence of the Spontaneous Packing Parameter $p_{0,i,\mathrm{DMDOHEMA}}$

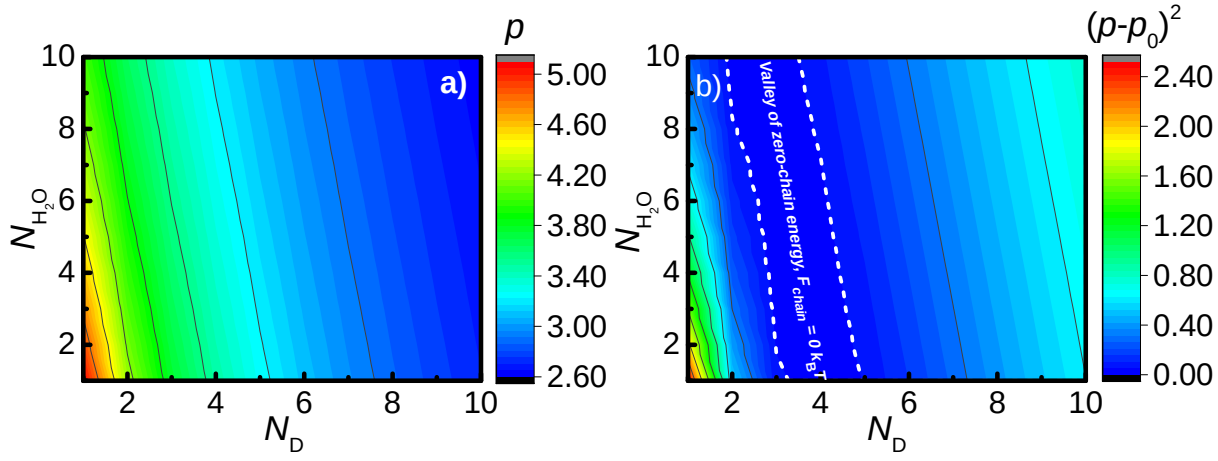

Figure 4.7 – a) Calculated packing parameter, p as a function of the composition of the core of the aggregate (*i.e.* map of packing parameter for the reverse micelle). b) Squared difference between calculated parameter p and spontaneous packing parameter $p_{0,\mathrm{Eu^{3+},D}} = 3.5$ as a function of composition of the core of the aggregate. In both figures the core contains one salt molecule, namely $\mathrm{Eu(NO_3)_3}$, N_{D} depicts number of extractant (DMDOHEMA aggregation number), whereas $N_{\mathrm{H_2O}}$ depicts number of water molecules present in the core (the water content).

In order to understand the concept of F_{chain}, it is convenient to show mapped values of p

as a function of DMDOHEMA aggregation number N_{D} and water content $N_{\mathrm{H_2O}}$. For constant $l_{\mathrm{chain,D}}$ and independent of the composition of the polar core of the aggregate, we can calculate p using Eq. 4.18. Results are presented in Figure 4.7a. Note that these values are a consequence of the assumed n-heptane solvent, since $l_{\mathrm{chain,D}}$ depends on it. p continuously decreases with lowering N_{D} and $N_{\mathrm{H_2O}}$ due to the swelling of the aggregate's core. Moreover, in Figure 4.7a it can be seen that p asymptotically approaches a value $p \approx 2.6$ for N_{D} and $N_{\mathrm{H_2O}}$. Note that if we were to calculate p for a very large number of extractant and water molecules (when $N_{\mathrm{D}}, N_{\mathrm{H_2O}} \to +\infty$), p would approach a value 1 (Eq. 4.18), which means that by huge swelling of the aggregate we would end up in the lamellar phase (plane-like structure)[190].

A map of p provides an insight into curvature effects upon swelling (or contracting) the aggregates, but to obtain quantitatively the energy cost for the departure from the equilibrium curvature, we need to study squared differences between calculated p (each p corresponds to a particular composition of the core of an aggregate) and $p_{0,i,\mathrm{D}}$, as plotted in Figure 4.7b. Results represent the case $p_{0,\mathrm{Eu^{3+},D}} = 3.5$. The choice of $p_{0,\mathrm{Eu^{3+},D}}$ positions the 'valley' of low F_{chain}, as depicted with white dashed lines in Figure 4.7b. It can be seen that the potential well is not perfectly symmetrical with respect to $p_{0,\mathrm{Eu^{3+},D}}$. At low aggregation numbers and water content $(p - p_{0,\mathrm{Eu^{3+},D}})^2$ rapidly increases, whereas a moderate increase is observed when following the diagonal. Still, the approach works fine since the borderlines of the map are of no interest since they represent unrealistic compositions of spherical aggregates that are not expected in the organic phase at equilibrium[191, 59, 52]. At low N_{D} the aggregation number is not sufficient to even create a spherical aggregate by enclosing the core (this major drawback of the approach is rarely reported!), whereas at large N_{D} and $N_{\mathrm{H_2O}}$ the aggregates are too large to maintain spherical morphology. That region would be more suitable for cylindrical shape.

The choice of $p_{0,\mathrm{Eu^{3+},D}} = 3.5$ was made based on the large number of calculations, and was found to be a good choice[72, 192, 47]. Here we present only one example of badly positioned low F_{chain} valley and its sensitivity to the choice of $p_{0,\mathrm{Eu^{3+},D}}$. In the case of $p_{0,\mathrm{Eu^{3+},D}} = 3$ graph of departures from the equilibrium curvature is presented in Figure 4.8. The radical change in the shape of F_{chain} is evident. The sensitivity is governed by quadratic nature of Eq. 4.17 which states that wrong choice of $p_{0,\mathrm{Eu^{3+},D}}$ leads to completely unrealistic aggregate compositions as is also demonstrated in Figure 4.9. The unrealistically high $N_{\mathrm{H_2O}}$ is a consequence of the fact that for $p_{0,\mathrm{Eu^{3+},D}} = 3$ the plane of calculated F_{chain} does not even have a parabolic behavior when $p \approx p_{0,\mathrm{Eu^{3+},D}}$. When $p_{0,\mathrm{Eu^{3+},D}} = 3.5$, the preferred compositions correspond to 4 extractant molecules and the number of water molecules varies between 1 and 7, depending on the type of solute present inside the core (as we will see in Figure 4.11). This outcome of the model is in

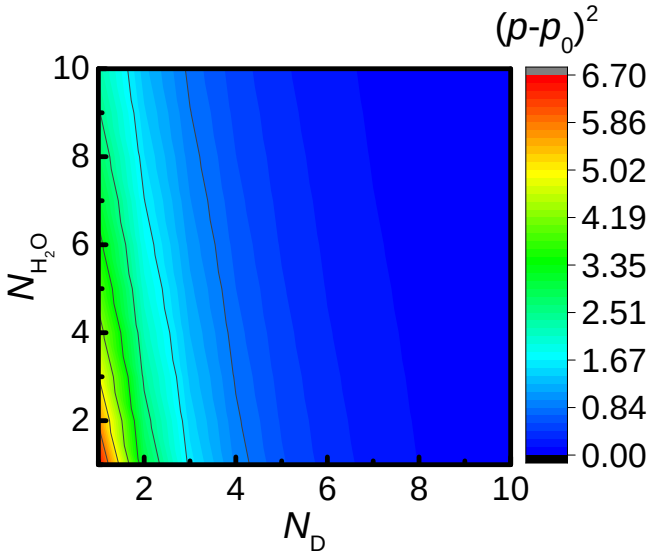

Figure 4.8 – Squared difference between calculated parameter p and spontaneous packing parameter $p_{0,Eu^{3+},D} = 3$ as a function of composition of the core of the aggregate.

the agreement with experimental reports and theoretical studies[26, 43, 167, 23, 66, 53, 47, 188]. The choice of $p_{0,Eu^{3+},D} = 3.5$ is reflected on the overall liquid-liquid extraction property in a way that allows a moderate transfer of H_2O to the organic solvent. Furthermore, there is another limitation for usage of $p_{0,Eu^{3+},D}$. For $p_0 = 2.5$ and 3, the method is not self-consistent. It means that the range of N_D and N_{H_2O} effects the prediction of overall extraction (for all solutes present in the system). The result of the calculation ought to be invariant to the upper limit of N_D and N_{H_2O}. That is another constraint which may as well be a crucial condition when deciding what $p_{0,Eu^{3+},D}$ value to take for the calculation.

The case of $p_{0,Eu^{3+},D} = 3.5$ gives a self-consistent calculation where large N_D and N_{H_2O} do not contribute to the result of the calculation and can, therefore, be neglected. This will be further addressed in section devoted to the fitting procedure.

4.5.2 Influence of the Generalized Bending Constant $\kappa^{\star}_{DMDOHEMA}$

Another geometrical parameter in our model is generalized bending constant $\kappa^{\star}_D$. We have already stated that $\kappa^{\star}_D$ represents a scaling factor to adjust the slope of F_{chain} towards (or away) from equilibrium. Therefore, we made a study of the influence of $\kappa^{\star}_D$ on the 'valley' of low F_{chain} and the equilibrium aggregate probabilities. Previously reported values of adjusted $\kappa^{\star}$ for reverse aggregates were 2.5 k_BT per DMDOHEMA molecule[176, 177]. Recently, the MD simulations study made by Duvail *et al.* reported a value of 16 k_BT per DMDOHEMA extrac-

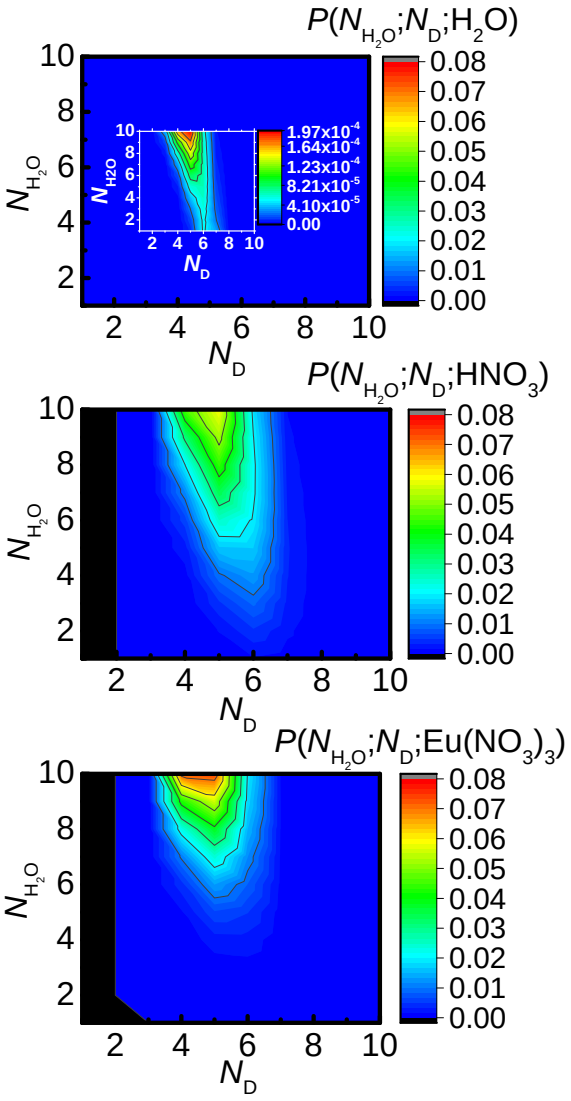

Figure 4.9 – Aggregate probabilities as a function of the composition of the core for $p_{0,\mathrm{Eu^{3+}},\mathrm{D}} = 3$. Figures show respectively the equilibrium aggregate probabilities for H_2O, HNO_3 and $Eu(NO_3)_3$ (solutes inside the core, from top to bottom). Inset shows probabilities at different scale with purpose of easier understanding for the reader.

tant molecule in *n*-heptane solvent[47]. In the work, the Potential of Mean Force (PMF) was fitted with harmonical function as a function of curvature or the packing parameter analogue. The minimum was attributed to the spontaneous packing parameter, whereas the slope was identified as a constant $\kappa_{\mathrm{D}}^{\star}$. The value of $\kappa_{\mathrm{D}}^{\star} = 16\ k_{\mathrm{B}}T$ per DMDOHEMA extractant molecule points to very high curvature towards water (in the reverse micelles) and was attributed to the strong interactions of Eu^{3+} and DMDOHEMA molecules. Indeed, the explanation they provided seems reasonable since heptane-like solvents constitute a class of penetrating solvents, which can then stabilize this high curvature needed to solubilize Eu^{3+} cation in the apolar medium. To test and to incorporate this formalism in our approach, we used the value $\kappa_{\mathrm{D}}^{\star} = 16$

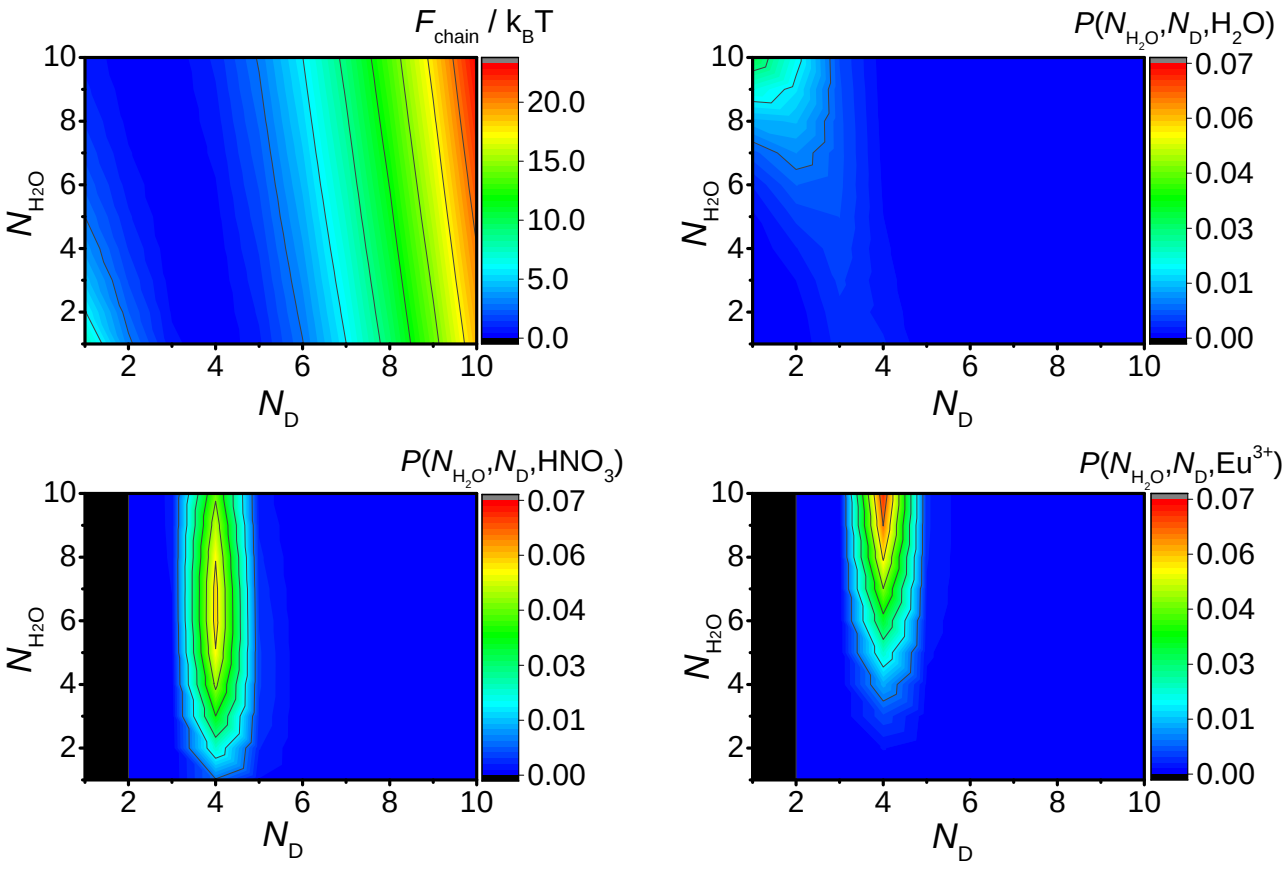

Figure 4.10 – Chain term free energy and aggregates probabilities as a function of the composition of the core for $\kappa^\star = 6\ k_\mathrm{B}T$ per extractant molecule. The upper right and the two bottom figures show respectively the equilibrium aggregate probabilities for H_2O, HNO_3 and $Eu(NO_3)_3$ (solutes inside the core).

$k_\mathrm{B}T$ per DMDOHEMA extractant molecule, and preformed calculations to obtain free energy profiles and to elucidate its influence on the compositions of the aggregates. Then we changed the value of rigidity constant to further explore its influence and to validate a choice used for the latter calculations. Contrary to the sensitivity recovered when dealing with the spontaneous packing parameter, the influence of $\kappa_\mathrm{D}^\star$ is less pronounced. In that sense the change demonstrated here is for $\pm$ 10 $k_\mathrm{B}T$ per extractant molecule. F_chain profile, as well as the probabilities at equilibrium in the case of $\kappa_\mathrm{D}^\star = 16\ k_\mathrm{B}T$ are presented in Figure 4.11, whereas lower case ($\kappa_\mathrm{D}^\star = 6$ $k_\mathrm{B}T$) and high case ($\kappa_\mathrm{D}^\star = 26\ k_\mathrm{B}T$) are respectively presented in Figures 4.10 and 4.12. The case when $\kappa_\mathrm{D}^\star = 16\ k_\mathrm{b}T$ shows that here is a optimum for the self-assembly of small spherical aggregates when aggregation number N_D is less than 6. With increasing N_D, the steep increase in F_chain blocks the formation of aggregates. Yet, there is polydispersity in the $N_{\mathrm{H_2O}}$, which is the consequence of the small molar volume of water molecules. Inclusion of the additional water molecules in the core of the aggregate induces a small energy penalty which is compensated

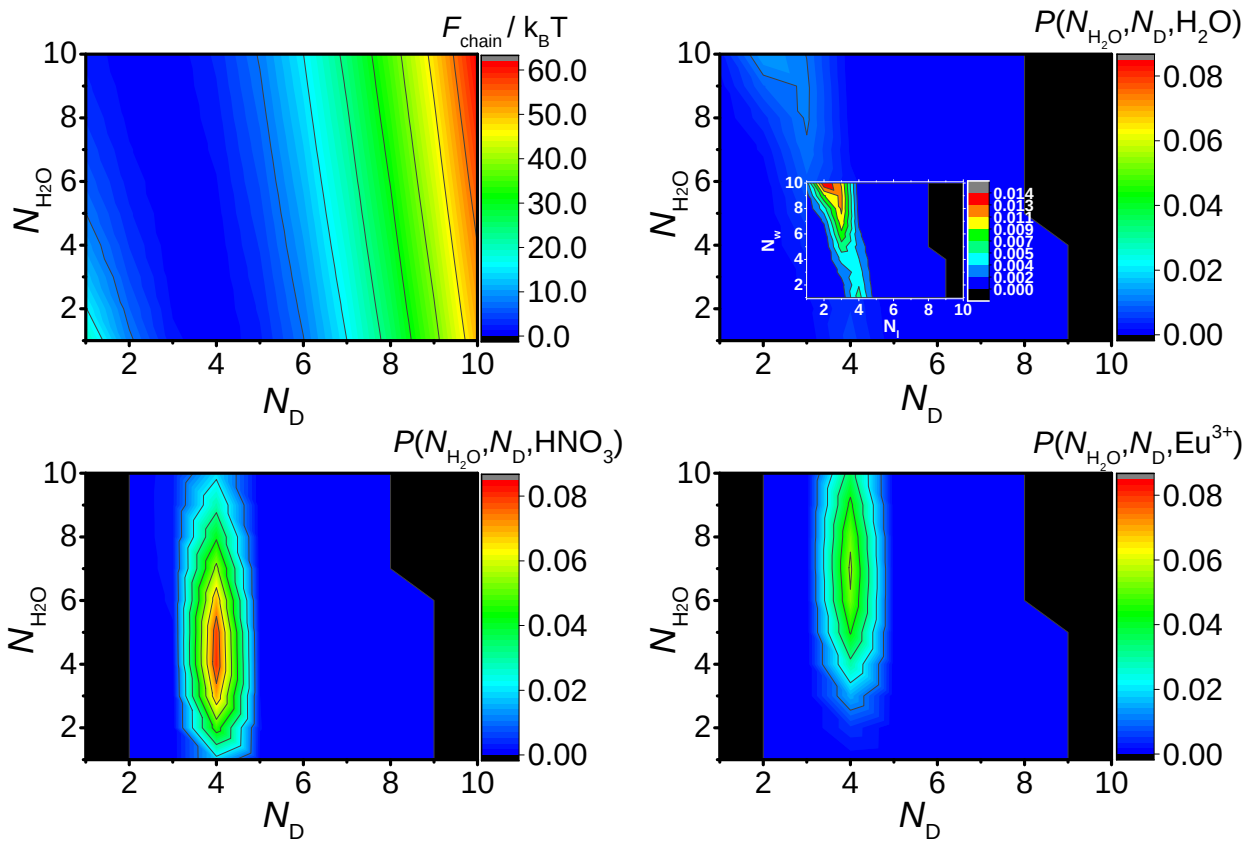

Figure 4.11 – Chain term free energy and aggregates probabilities as a function of the composition of the core for $\kappa^\star = 16\ k_\mathrm{B}T$ per extractant molecule. The upper right and the two bottom figures show respectively the equilibrium aggregate probabilities for H_2O, HNO_3 and $Eu(NO_3)_3$ (solutes inside the core).

by favourable dilution effect (dilution effect will be addressed later in the text). Increasing the rigidity constant to $\kappa_\mathrm{D}^\star = 26\ k_\mathrm{b}T$ (Figure 4.12) decreases water content polydispersity, but also reduces the overall probability of cation-filled aggregates, thus quenching the extraction below the reported values. Understandably, the case of $\kappa_\mathrm{D}^\star = 6\ k_\mathrm{b}T$ favors polydispersity and high dilution, and is thus quickly discarded form consideration. It must be emphasized that the order of magnitude of F_chain is that of the complex formation. This is indeed a desired outcome since it backs up the idea that the transfer energy difference of only few $k_\mathrm{b}T$ is in fact the residue of counterbalancing energy terms that are in mutual competition. In our approach, the energy penalty of formation of the highly curved interface is opposing a pure complexation energy of DMDOHEMA / cation couple[71, 171, 193]. At the end, we provide a sort of hint of the influence of geometrical parameters on the overall extraction efficiency. This paragraph is probably better suited later in the text, but it is the wish of the authors to constantly emphasize how the molecular scale theories are reflected on the chemical engineering aspect. By varying

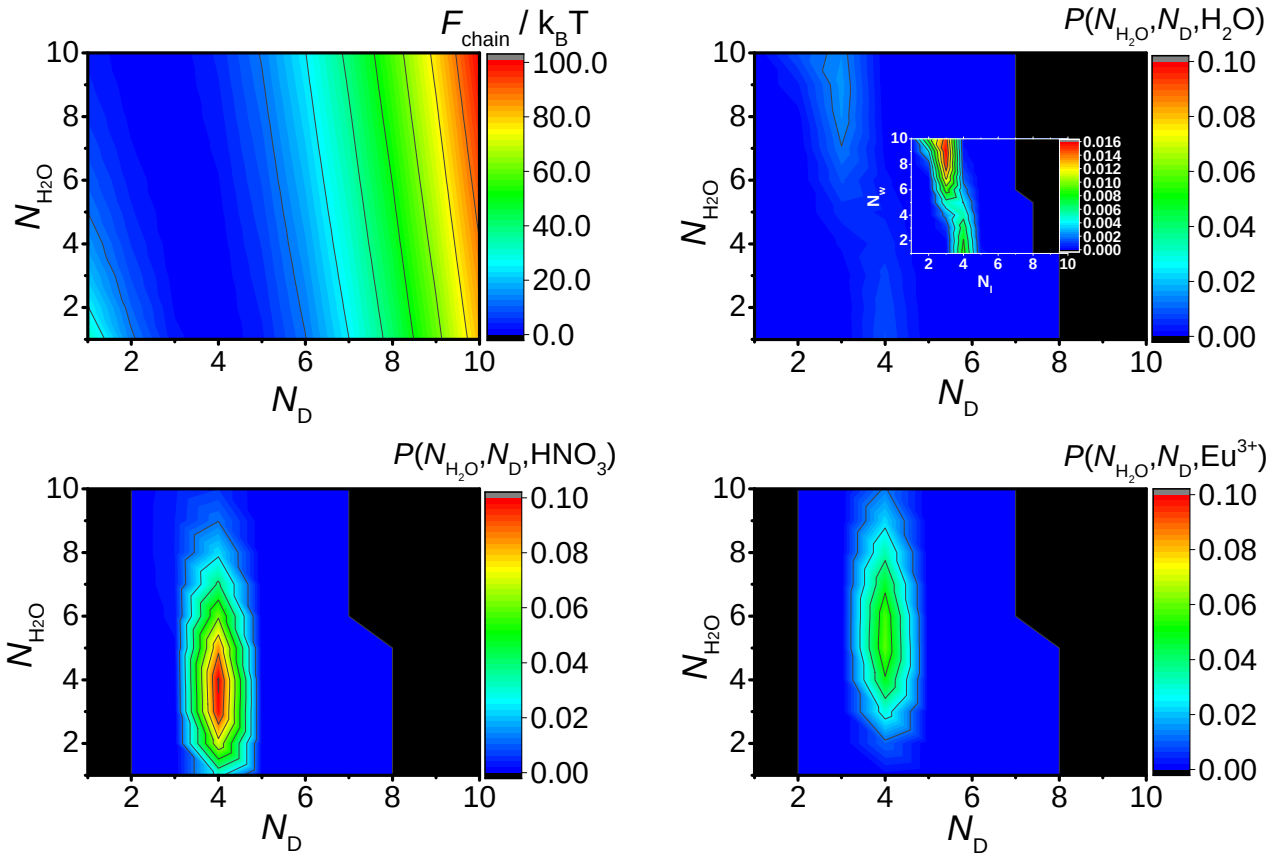

Figure 4.12 – Chain term free energy and aggregates probabilities as a function of the composition of the core for $p_0 = 3.5$, $\kappa^\star = 26\ k_\mathrm{B}T$ per extractant molecule. The upper right and the two bottom figures show respectively the equilibrium aggregate probabilities for H_2O, HNO_3 and $Eu(NO_3)_3$ (solutes inside the core).

$\kappa_\mathrm{D}^\star$ from 26 to 6 $k_\mathrm{B}T$, the calculated Eu^{3+} distribution coefficient varied from 14.6 to 5.6 i.e; for nearly a factor of 3. This counter-intuitive variation of extraction efficiency with the branching of the chains is always observed in industrial applications but has never been predicted by any model of extraction to our best knowledge[182] . The variation of $\kappa_\mathrm{D}^\star$ was also reflected in the self-assembly threshold which was decreased form 0.08 mol dm^{-3} to 0.06 mol dm^{-3} with the decrease of rigidity. It follows that the self-assembly is favored for flexible extractant films, rather than for rigid, highly curved films.

4.6 Prediction of Liquid-Liquid Extraction Properties and Self-Assembly

4.6.1 Self-Assembly Behind Liquid-Liquid Extraction: the Critical Aggregate Concentration

Definition of the Critical Aggregate Concentration - CAC

The self-assembly is the motor behind liquid-liquid extraction. To study it, means to study the conditions for which micellization occurs. The micellization threshold is often referred as the Critical Micelles Concentration (shortly CMC). The term is initially introduced for the case of the direct surfactant-made micelles in the aqueous phase. In our case, we refer to micellization threshold as the Critical Aggregate Concentration (shortly CAC). CAC is generally understood as the concentration after which some macroscopic property of the system changes, which means that in nanodomains, the change in structure occurred. Experimental chemists try to determine the change in the macroscopic property of the system, but in theoretical means, the thing is a bit mode delicate. In fact, the simplest route to take for the theoretical determination of the CAC is to first define the the aggregation phenomena, and then obtain a proper speciation of the organic phase. In the work by Bley *et al.* the two methods for calculation of the CAC in the organic phase were described[72]. Both have underling assumption that the addition of the extractant in the system is basically used to create aggregates.

The first method is to calculate the equilibrium monomeric extractant concentration as a function of the initial extractant concentration in the system, $c_{\mathrm{LH,initial}}$. Then, the beginning of the calculated curve and the end are fitted with the linear functions. The intersection of the two is defined as CAC. Beginning of the curve, at low $c_{\mathrm{LH,initial}}$ corresponds to the case where there is no self-assembly and the system behaves as a gas of monomeric extractant molecules. The case of high $c_{\mathrm{LH,initial}}$ corresponds to high self-assembly regime, for which the concentration of monomeric extractant should be constant. This method provides good results as long as the free extractant do not interact *e.g.* form dimer, trimers or adducts with different extractants in the system. We have adopted this method and to study the case of pure water extraction system and presented it in Figure 4.13. The method works since DMDOHEMA as a weak extractant remains mostly in monomeric form if there is no multivalent cations present in the aqueous phase. In the case that there is a strong dimerization of the extractant, method is not good, since it does not distinguish between the self-assembly of larges structure and dimerization.

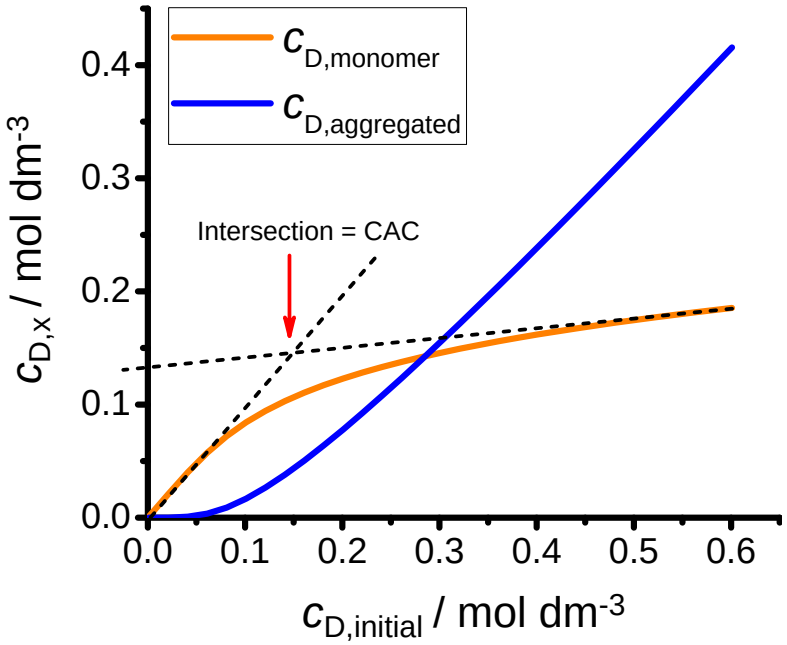

Figure 4.13 – Definition of the critical aggregate concentration (CAC) for weak extractant systems

The second method to calculate CAC is to calculate the concentration of aggregated extractant as a function of $c_{LH,initial}$ and fit it again with the linear function. Now, fitting is only in the region where aggregated concentration is in linear regime. This is useful since it guaranties that self-assembly of larger structures is dominating dimerization or adducts formation. This approach will be used in the next two chapters, where we have HDEHP extractant that readily forms dimers in the organic phase.

It is the opinion of the authors that defining CAC in organic solvents can be arbitrary, but once defined, it should be used as a reference when comparing deviations from it (comparable to the standard state in general thermodynamics).

Influence of the aqueous phase composition to DMDOHEMA self-assembly

We have already stated that one of the crucial properties of extraction system is measured CAC since it governs the transfer of solutes from the aqueous to the organic phase, but also determines the viscosity of the macroscopic system[56]. Figure 4.14 shows the calculated equilibrium concentrations of both monomeric and aggregated extractant molecules as a function of initial (or total) extractant concentration. Based on the presented speciation of the organic phase, we have calculated CAC for each system. Figure 4.14 a) shows the concentrations of the extractant for $LiNO_3$ aqueous solution in contact with a solvent, which represents a typical background non-extracted salt system. As pointed in the figure, CAC for such system is evaluated to be

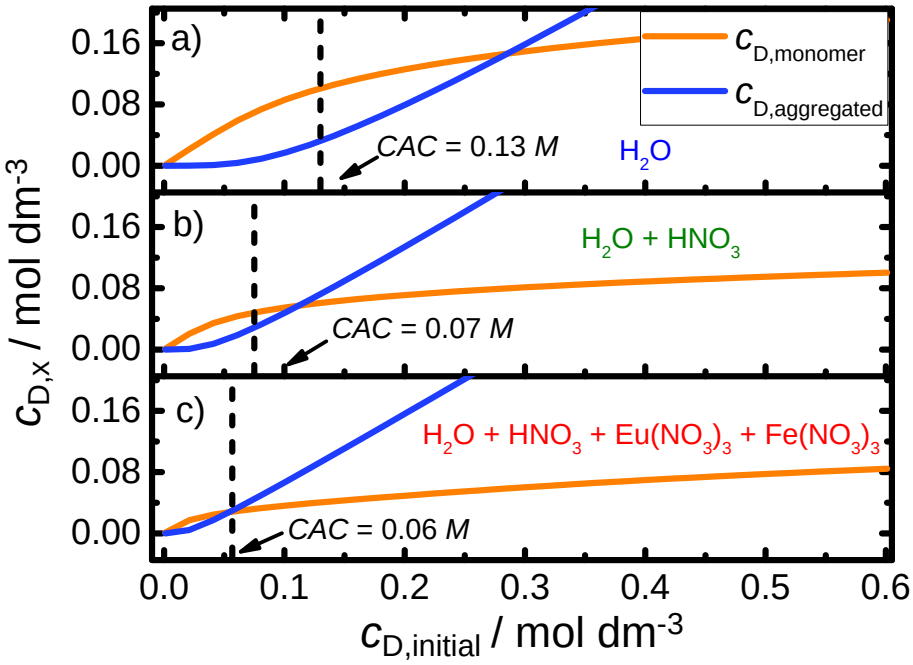

Figure 4.14 – Calculated concentrations of monomeric and aggregated extractant as a function of the initial (or total) extractant concentration $c_{D,initial}$. The self-assembly properties of DMDOHEMA system. Solvent phase in contact to: a) $m_{LiNO_3,initial} = 3$ mol kg^{-1} (non-extracted salt). b) $m_{HNO_3,initial} = 3$ mol kg^{-1}. c) $m_{HNO_3,initial} = 3$ mol kg^{-1}, $m_{Eu(NO_3)_3,initial} = m_{Fe(NO_3)_3,initial} = 0.05$ mol kg^{-1}. Intersection of the black dashed line with the abscissa axis shows the calculated critical aggregate concentration.

at 0.13 mol dm^{-3} initial extractant concentration and only water molecules are present in the aggregates. Figure 4.14 b) and c) show respectively, the system of HNO_3 aqueous solution and mixture of HNO_3, $Eu(NO_3)_3$ and $Fe(NO_3)_3$ in contact with solvent phase. The detailed concentrations of each system are written in the caption of Figure 4.14. Upon the addition of acid and cations in the system, CAC decreased to 0.07 mol dm^{-3} and 0.06 mol dm^{-3}, respectively.

Figure 4.15 demonstrates that the model captures a known decrease of CAC upon the addition of acid in the system. The results of the CAC as a function of the initial HNO_3 concentration in aqueous phase presented here are made for the system $c_{D,initial} = 0.6$ mol dm^{-3}, $m_{Eu(NO_3)_3,initial} = m_{Fe(NO_3)_3,initial} = 0.05$ mol kg^{-1}. The enhancement of the micellization is due to the two factors contributing to the free energy of the aggregates. The first and more dominant factor is the increase of the solute concentration able to make a weak complex with the extractant molecule (defined by complexation energy E_{0,HNO_3}). The second factor is an increase of NO_3^- concentrations ratio between the aqueous phase and the core of the aggregate (Eq. 4.33). The properties of the extracting systems shown in Figures 4.14 and

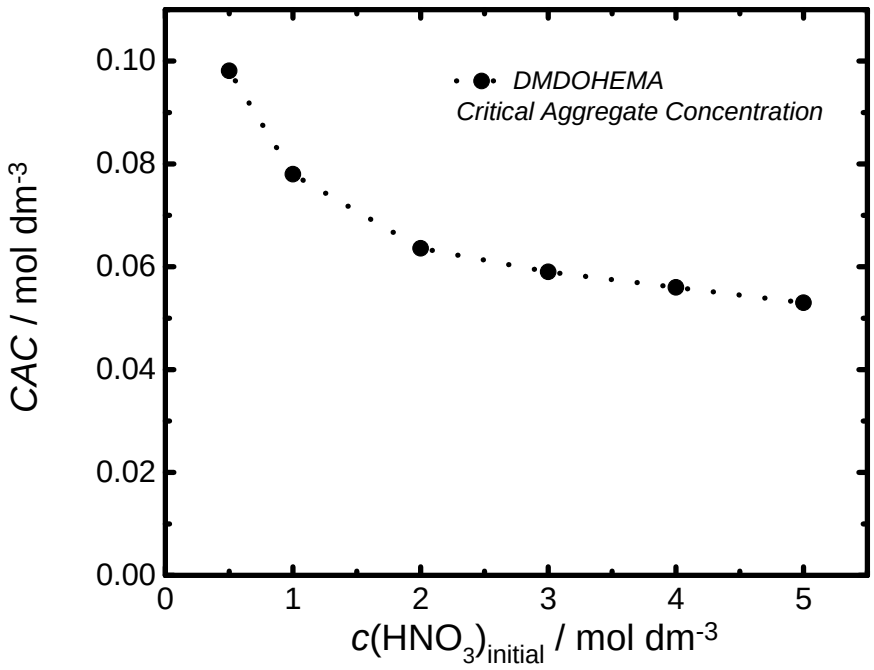

Figure 4.15 – Critical aggregate concentration as a function of HNO_3 concentration. The system in study is: $m_{Eu(NO_3)_3,initial} = m_{Fe(NO_3)_3,initial} = 0.05$ mol kg^{-1}.

4.15 correspond to experimental findings[58]. Based on the pseudo-phase model, the curve very similar to one presented in Figure 4.15 was calculated. The decrease of the CAC with increasing acid concentration in the aqueous phase was attributed to the increase of the activity of solutes. In our model, we considered the ideal solution, which explains the small differences. Note that ideality of the aqueous solution caused overestimation of the acid extraction for high acid molalities in the system. This will be addressed in the next Chapter.

4.6.2 Predicting the Transfer of Solutes Between the Organic and the Aqueous Phases: Speciation of Organic Phase and Polydispersity of Probabilities

The basis of the Droplet model is to go beyond complexation energy considerations only. The interplay of various energy contributions which are in the competition, then yields the energy of transfer of solutes to the organic phase. In this section we will demonstrate the influence of the composition of the aqueous phase to the transfer of solutes to the organic phase. Figures 4.16a-c show respectively the speciation of solutes extracted in the organic solvent as a function

of $c_{\mathrm{D,initial}}$, for the three common cases of laboratory-scale experiments: a) lower acid case, b) reference extraction from highly acidic medium, and c) the extraction from solution saturated by the non-target salt. A detailed description of the composition in three cases is given in the figure caption.

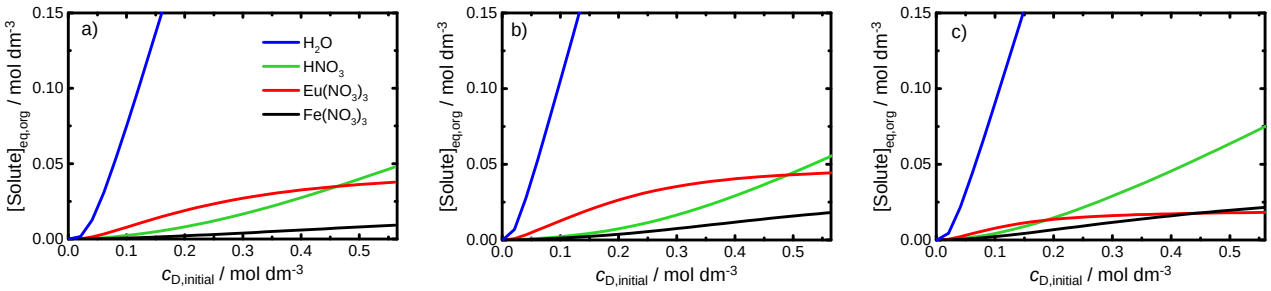

Figure 4.16 – Calculated equilibrium concentrations of all extracted solutes in the organic phase solutes as a function of the initial extractant concentration, $c_{\mathrm{D,initial}}$. The system in study is: a) $m_{\mathrm{HNO_3,initial}} = 1$ mol kg^{-1}, $m_{\mathrm{Eu(NO_3)_3,initial}} = m_{\mathrm{Fe(NO_3)_3,initial}} = 0.05$ mol kg^{-1}. b) $m_{\mathrm{HNO_3,initial}} = 3$ mol kg^{-1}, $m_{\mathrm{Eu(NO_3)_3,initial}} = m_{\mathrm{Fe(NO_3)_3,initial}} = 0.05$ mol kg^{-1}. c) $m_{\mathrm{HNO_3,initial}} = 3$ mol kg^{-1}, $m_{\mathrm{Eu(NO_3)_3,initial}} = 0.02$ mol kg^{-1} , $m_{\mathrm{Fe(NO_3)_3,initial}} = 0.05$ mol kg^{-1}. The legend describing the solutes extraction is given in figure a) and is valid for figures b) and c). The point $c_{\mathrm{D,initial}} = 0.6$ mol dm^{-3} in figure b) represents the reference experimental point by J. Rey *et al.*[54, 187].

Graphs presented in Figures 4.16a-c demonstrate a complexity of the liquid-liquid extraction systems (and this is one off the simplest systems) that appear in the industry. A display of competition reactions within the multicomponent approach demonstrates the importance of the tuning of the aqueous phase for the efficient chemical engineering. In the case of lower acid concentrations (Figure 4.16a), Eu^{3+} extraction (red line) is the dominant reaction in the system, followed by the acid extraction equilibria (green line). Fe^{3+} extraction is poor (black), due to the lack of so-called 'aqueous phase saturation effect'. Water coextraction is relatively high, and serves as stabilizing agent of the target salt by hydration. A strong initial increase of Eu^{3+} extraction reflects its complexation affinity towards DMDOHEMA. The aqueous phase saturation effect appears when acid concentration is increased by the factor 3, as in Figure 4.16b. In this case both Eu^{3+} and Fe^{3+} extraction is boosted due to the saturation of the aqueous phase, as can be understood from Eq. 4.33. Also, an abrupt increase in water coextraction occurs. Finally, for lower Eu^{3+} concentration in the system, the equilibrium is shifted towards the extraction of acid. Surprisingly, Fe^{3+} extraction dominates Eu^{3+} extraction. this practically means that even though Eu^{3+} generally forms a stronger complex with DMDOHEMA, the decrease in its concentration in the aqueous phase allows for the Fe^{3+} competition reaction to

emerge and system behaves as the dominant transfer of non-target salt.

An important feature is the low extraction of HNO_3 compared to the literature. This is a consequence of our approximation that only one type, acid or metal nitrate molecule, can occupy the aggregate. This assumption was made only for the study in this chapter. In later chapters the limit of occupancy is removed and model becomes fully general. A typical high water uptake and an increased metal nitrate extraction with an increase in $c_{\mathrm{D,initial}}$ correlate extremely well with the experiments[184]. Also, it is worth to mention that before CAC the aggregation is controlled by water extraction because of a smaller penalty in chain energy while after CAC, the aggregation is entirely controlled by complexation of metal nitrates.

In the experimental approach to liquid-liquid extraction, we can study the competition reaction by measuring the extraction efficiency of components and then drawing the conclusions about the mechanism, or we can use techniques that provide structural insights of the species involved in chemical reaction *e.g.* IR, NMR, SAXS, SANS, *etc.*. The combination of these is in the core of the multi-scale approach. With our Droplet model, we can provide the similar insights. In fact, the three cases presented in Figure 4.16a-c can be discussed in terms of probabilities of self-assembled aggregates. Probabilities in Figures 4.17, 4.18, and 4.19 correspond to $c_{\mathrm{D,initial}} = 0.6$ mol dm^{-3} and the aqueous phase composition like in the three cases in Figure 4.16a-c. It must be emphasized that results are presented for the case where only one salt molecule is inside the core of the aggregates since the calculations showed that addition of second salt molecule pays the huge penalty in terms of chain energy thus making the probabilities negligible.

Aggregates probabilities: Low acid case

The case of lower acid concentration in the aqueous phase ($m_{\mathrm{HNO_3,initial}} = 1$ mol kg^{-1})[1] corresponding to Figure 4.16a shows higher probabilities of aggregates occupied by HNO_3 and $Eu(NO_3)_3$. $Fe(NO_3)_3$ -filled aggregates have small probability. The nanoscopic picture of self-assembled aggregates elucidates the competition reactions observed in macroscopic system, or in our case, on calculated extraction isotherms. Moreover, we can dismantle the total water uptake to the organic phase by mapping the polydispersity in terms of water content $N_{\mathrm{H_2O}}$. Acid-filled aggregates are characterized by compositions from 2 to 8 water molecules per aggregate, whereas from 4 to 10 water molecules for $Eu(NO_3)_3$ and $Fe(NO_3)_3$ molecules. This is a consequence of the differences in chemical potentials of ions and water between the aqueous

[1] $m_{\mathrm{HNO_3,initial}} = 1$ mol kg^{-1} is in fact highly concentrated aqueous solution in terms of solution chemistry, but in industrial processes it is considered as low to moderate acidity in the batch.

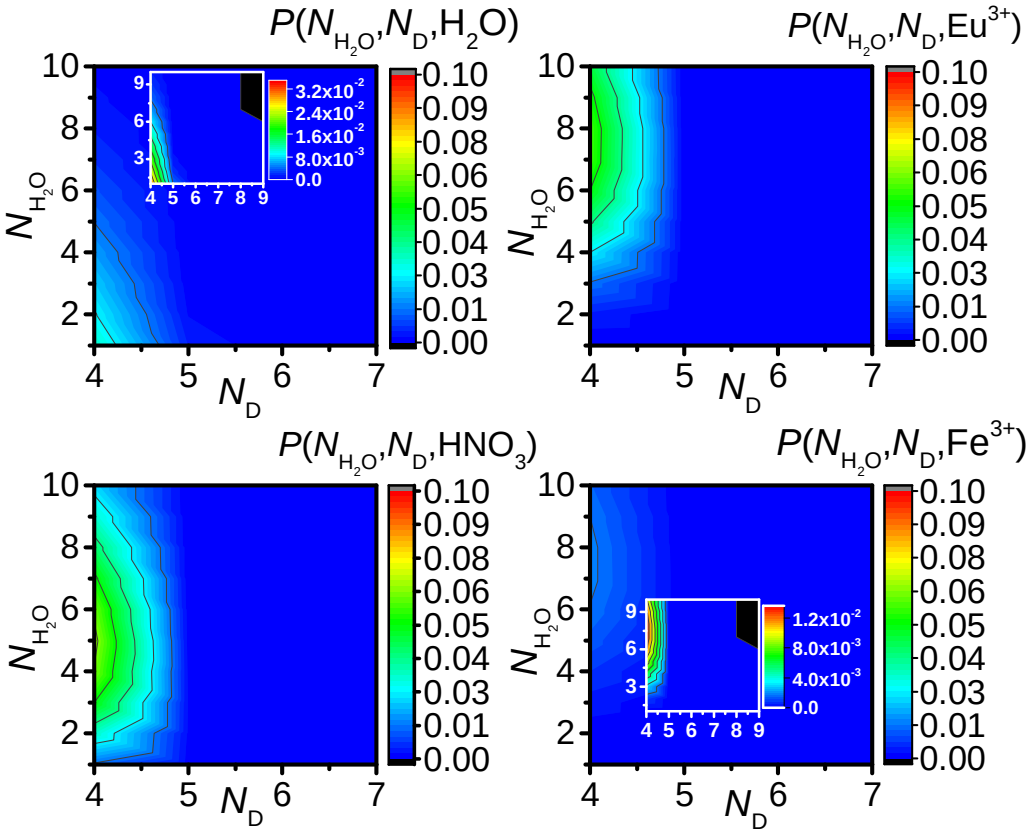

Figure 4.17 – Influence of the initial aqueous phase on calculated equilibrium aggregate probabilities as a function of the composition of the core. The system in study: $c_{\mathrm{D,initial}} = 0.6$ mol dm^{-3}, $m_{\mathrm{HNO_3,initial}} = 1$ mol kg^{-1} and $m_{\mathrm{Eu(NO_3)_3,initial}} = 0.05$ mol kg^{-1}, $m_{\mathrm{Fe(NO_3)_3,initial}} = 0.05$ mol kg^{-1}. This figure is complementary to the Figure 4.16a.

and the organic (solvent) phases. The higher water content for $\mathrm{Eu(NO_3)_3}$ and $\mathrm{Fe(NO_3)_3}$ salts is due to the higher number of particles in the core of the aggregate. The dilution of the core is a highly favorable effect that stabilizes the aggregates core, but it works in opposite way with respect to the F_{chain} because the inclusion of additional particles causes the increase in core radius (an unfavorable swelling of the reverse micelle). An interesting information that is only observable when studying this kind of probability maps is the non-negligible probability of water-filled aggregates (no salt), which formation can be represented by following chemical reaction: $N_{\mathrm{H_2O}} \cdot \mathrm{H_2O} + 4\overline{\mathrm{D}} \rightleftharpoons \overline{\mathrm{A}_{N_{\mathrm{H_2O}};4D}}$. In the absence of the aqueous phase saturation effect, the conditions are fulfilled to have competition reaction of pure water extraction only. Part of DMDOHEMA in the system is available to self-assemble around a droplet of pure water, even without excess complexation term. It follows that the isotherm depicted by blue line in Figure 4.16a, is in fact a superposition of coextracted water by acid and Eu, and by pure water extraction isotherm. Indeed, this finding shows the strength of the Droplet model, since we

can, up to our best knowledge, for the first time decouple the total extraction of solutes into contribution. The property will be further exploited in following chapters.

Aggregates probabilities: Reference case

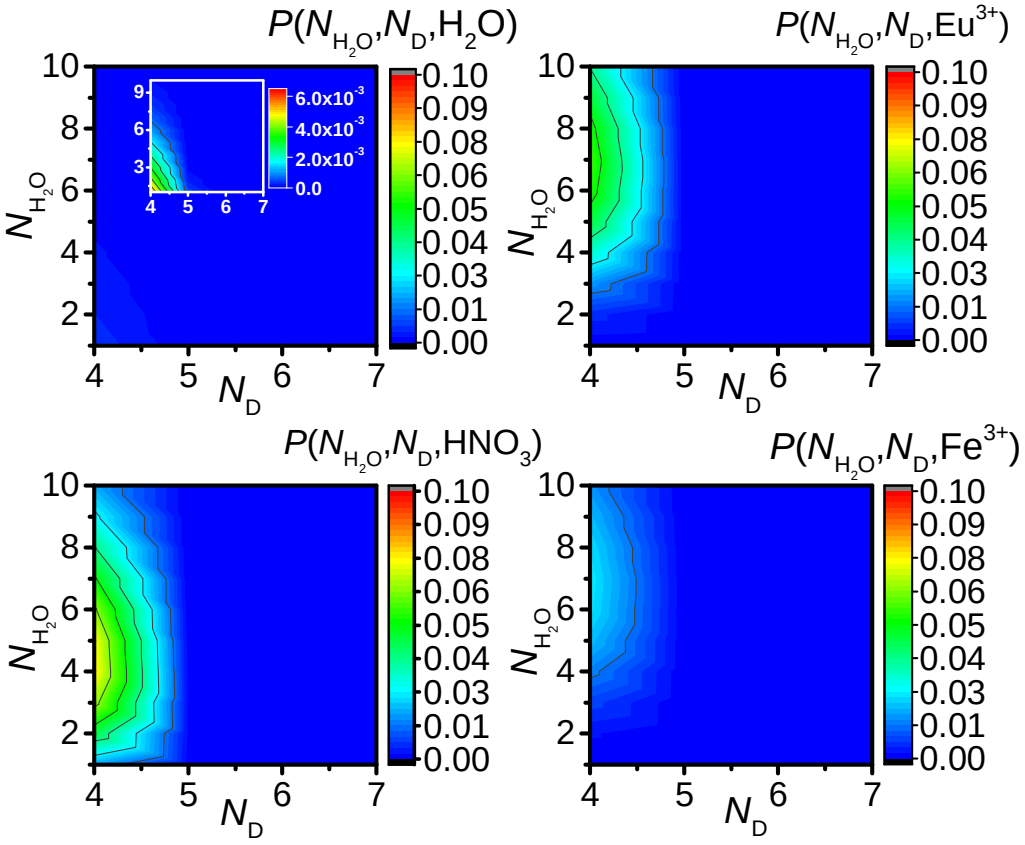

Figure 4.18 – Influence of the initial aqueous phase on calculated equilibrium aggregate probabilities as a function of the composition of the core. The system in study: $c_{\mathrm{D,initial}} = 0.6$ mol dm^{-3}, $m_{\mathrm{HNO_3,initial}} = 3$ mol kg^{-1} and $m_{\mathrm{Eu(NO_3)_3,initial}} = m_{\mathrm{Fe(NO_3)_3,initial}} = 0.05$ mol kg^{-1}. This figure is complementary to the Figure 4.16b.

The reference extraction case[2] described by Figure 4.16b, can be interpreted as the increase of $\mathrm{Eu(NO_3)_3}$ and $\mathrm{Fe(NO_3)_3}$ probabilities due to the saturation of the aqueous phase. Polydispersity of both aggregation numbers and water content is unaffected. Calculations show that now the pure water-filled aggregates have negligible probabilities. This is a consequence of the strong cation-induced aggregation. The majority of the extractant is spent, CAC lowers, and resulting water uptake to the organic phase originates form coextraction of $\mathrm{HNO_3}$, $\mathrm{Eu(NO_3)_3}$ and $\mathrm{Fe(NO_3)_3}$.

[2]It is called a reference from dual aspect: it is described in detail in the literature and it corresponds to the conditions of an actual industrial process *e.g.* DIAMEX process in nuclear fuel reprocessing cycle.

Aggregates probabilities: Low Eu^{3+} concentration

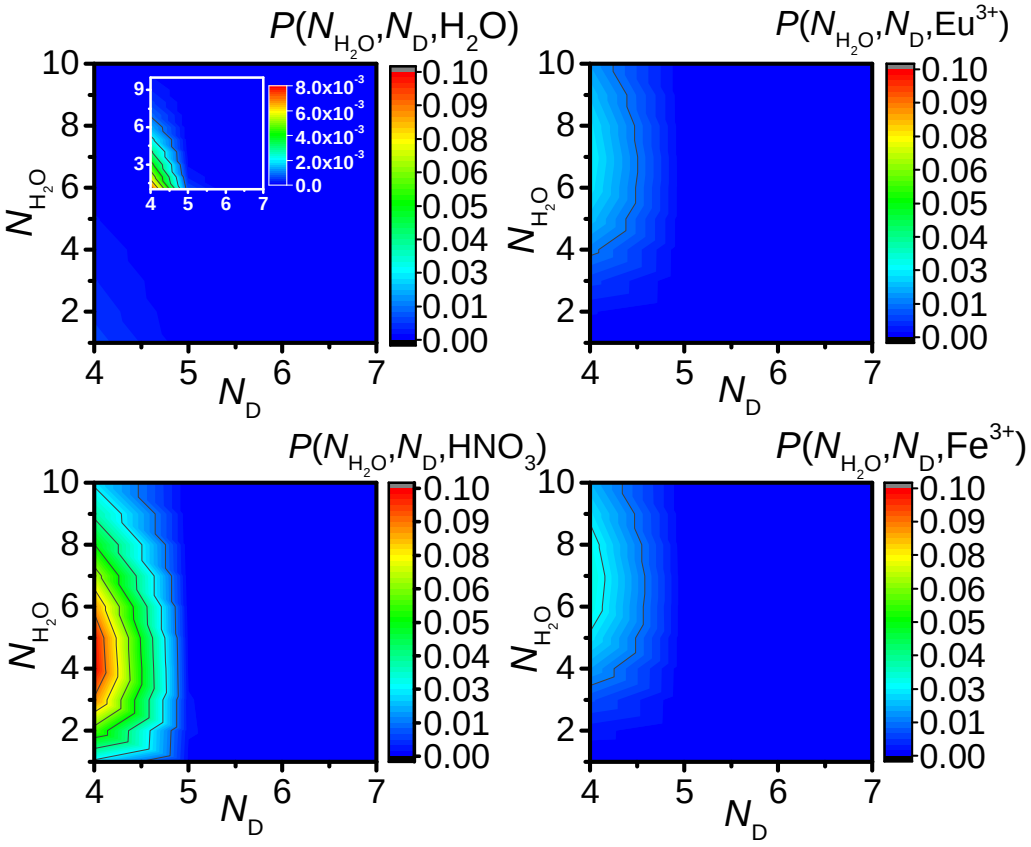

Figure 4.19 – Influence of the initial aqueous phase on calculated equilibrium aggregate probabilities as a function of the composition of the core. The system in study: $c_{\mathrm{D,initial}} = 0.6$ mol dm^{-3}, $m_{\mathrm{HNO_3,initial}} = 3$ mol kg^{-1} and $m_{\mathrm{Eu(NO_3)_3,initial}} = 0.02$ mol kg^{-1}, $m_{\mathrm{Fe(NO_3)_3,initial}} = 0.05$ mol kg^{-1}. This figure is complementary to the Figure 4.16c.

The third case of low $m_{\mathrm{Eu(NO_3)_3,initial}}$ (presented in Figure 4.19), behaves similar to the previous described system, with high acid molality favoring the assembly of aggregates containing $Eu(NO_3)_3$ and $Fe(NO_3)_3$, again at the expense of pure water filled aggregates. Since $m_{\mathrm{Eu(NO_3)_3,initial}}$ is low, HNO_3 and $Fe(NO_3)_3$ have highest probabilities.

To sum up, we have demonstrated how the self-assembly of polydisperse aggregates is responsible for the macroscopic property of the system, such as the speciation of extracted solutes in the organic phase.

4.6.3 Cation Distribution Coefficients and the Apparent Stoichiometry

Liquid-liquid extraction efficiency is usually expressed as the distribution coefficient of the target metal between the organic and the aqueous phases[9]. The extraction efficiency is then plotted

as a function of some independent system variable, for example concentration of components or temperature. We have defined the distribution coefficient as

$$D_i = \frac{\sum_x c_{\mathrm{Agg},x} N_{i,x}}{m^{\mathrm{aq}}_{\mathrm{eq},i}} = \frac{c^{\mathrm{org}}_{\mathrm{eq},i}}{m^{\mathrm{aq}}_{\mathrm{eq},i}} \tag{4.36}$$

where D_i is the distribution coefficient of target cation i between the aqueous and the solvent phases at equilibrium, $N_{i,x}$ is the number of cations i in the particular aggregate x, and $c^{\mathrm{org}}_{\mathrm{eq},i}$ is the total concentration of cation i in the organic phase. Usually, D_i is a dimensionless quantity, compared to our definition. The fact that we used our definition (Eq. 4.36) as a ratio of molar concentrations and molality does not change the result. It is strictly out of convenience to avoid additional transformation of the result. For experimental chemists, D_i can be simply converted to true, dimensionless distribution coefficient by replacing molality in denominator of Eq. 4.36 with relation: $m^{\mathrm{aq}}_{\mathrm{eq},i} = \rho^{aq}\, m^{\mathrm{aq}}_i / (1 + \sum_i m^{\mathrm{aq}}_i M_{\mathrm{i}})$, where ρ^{aq} is the density of the aqueous solution, and M_{i} is the molar mass of cation i.

Calculation of extraction isotherms

We start by establishing the extraction efficiency as a function of HNO_3 molality for different $c_{\mathrm{D,initial}}$. Figure 4.20 shows a dependency of $D_{\mathrm{Eu^{3+}}}$ as a function of HNO_3 molality for the

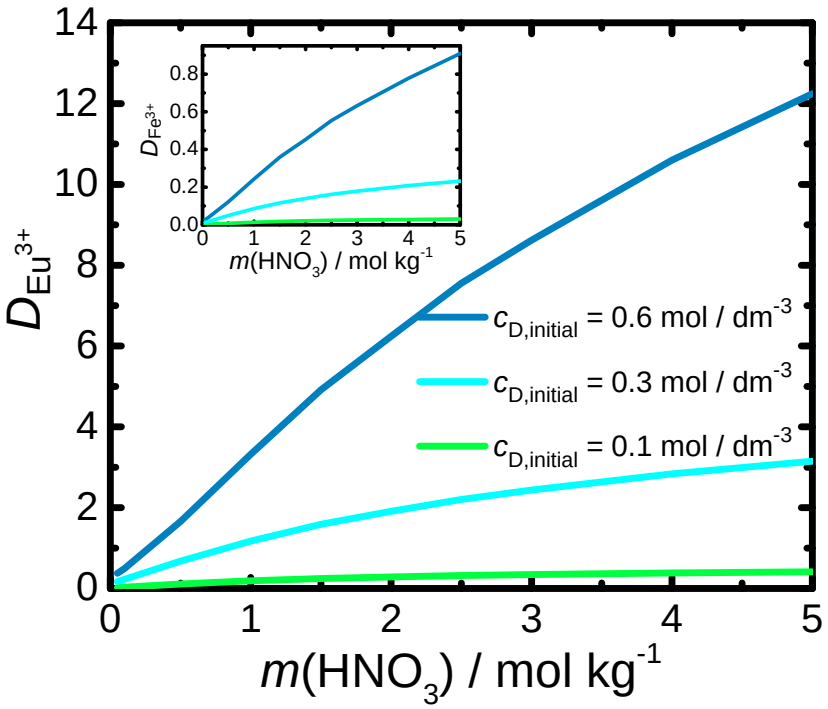

Figure 4.20 – Eu^{3+} distribution coefficient $D_{\mathrm{Eu^{3+}}}$ as a function of nitric acid molality in the aqueous phase. The system in study is: $c_{\mathrm{D,initial}} = 0.6$ mol dm^{-3}, $m_{\mathrm{Eu(NO_3)_3,initial}} = m_{\mathrm{Fe(NO_3)_3,initial}} = 0.05$ mol kg^{-1}.

mixture of salts. This represents a cut on multicomponent phase diagram along the fraction of acid in the aqueous phase. The calculations are made for the extractant concentrations after the CAC which ensures that the system is in the regime where the aggregates are dominant species in the solvent. The results show that in fact, our model recovers typical Langmuir isotherms that have already been reported by both experiments and modelling[58, 186]. For 0.1 mol dm^{-3} the extractant is entirely saturated and an additional increase of HNO_3 concentration cannot enhance the extraction. Contrary to that, when the concentration of the extractant is 0.6 mol dm^{-3} there is a sufficient amount of monomers. Adding the HNO_3 in the aqueous phase pushes the equilibrium towards Eu^{3+}-mediated self-assembly.

The extraction efficiency as a function of the initial extractant concentration in the system $c_{D,initial}$ was studied for different $m_{HNO_3,initial}$ (different acidity of aqueous phase). Results are presented in Figure 4.21 and show the nonlinear increase of distribution coefficients with increasing $c_{D,initial}$. The increase in $m_{HNO_3,initial}$ causes an increase in $D_{Eu^{3+}}$ which means that the extraction is enhanced upon addition of HNO_3 the system. This is again the consequence of an increase of NO_3^- concentrations ratio between the aqueous phase and the core of the aggregate. An important aspect is that below CAC calculated $D_{Eu^{3+}}$ is negligible[3]. Therefore, below the micellization threshold, the organic phase behaves like a gas of dispersed DMDOHEMA monomers, there is not self-assembly, and thus no transfer of solutes between the aqueous and the organic phases.

The apparent stoichiometry

Another way of plotting these results is by employing so-called 'log-log' plot, as it is traditionally made in the slope method to investigate the apparent stoichiometry of the system[194, 195]. In this manner we have transformed the data from Figure 4.21 to decimal logarithms and presented them in Figure 4.22. Figure 4.22 a) shows again the extraction for different HNO_3 concentrations. It can be noticed that depending on the region of $c_{D,initial}$ the slope of the extraction lines changes and typically three regimes are observed. Moreover, the trend in change of slope is dependent on the acidity of system *i.e.* on HNO_3 concentrations. Bellow typically $m_{HNO_3,initial} = 2$ mol kg^{-1} the calculations have shown a different behavior than for higher concentrations. In order to see the differences better, we have isolated the graphs for $m_{HNO_3,initial} = 0.5$ (black line) and 5 mol kg^{-1} (red line) and plotted them separately in Figure 4.22 b). What is striking is the fact that slope changes substantially for $m_{HNO_3,initial} = 0.5$

[3]For this system, calculated CAC was 0.06 mol dm^{-3} (Figure 4.14).

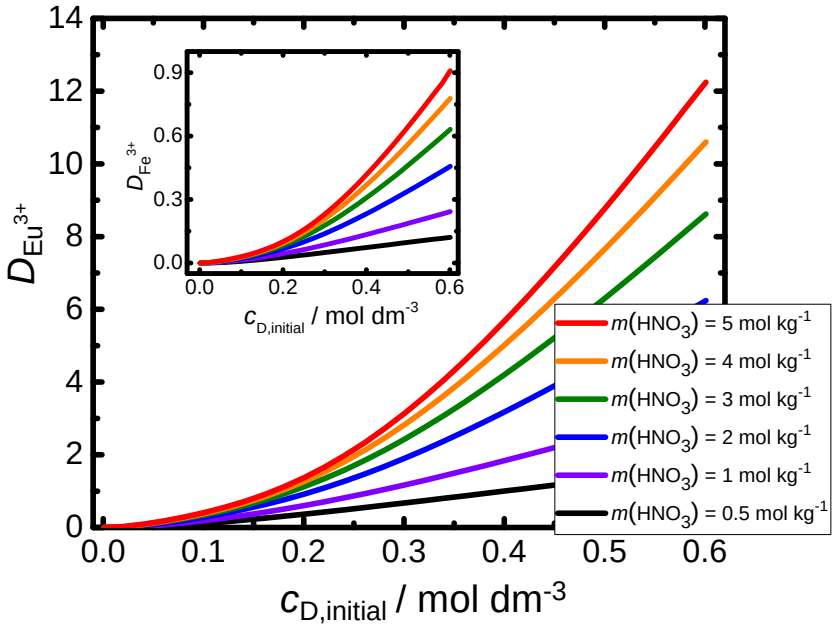

Figure 4.21 – $D_{Eu^{3+}}$ as a function of $c_{D,initial}$. The system in study is: $m_{Eu(NO_3)_3,initial} = m_{Fe(NO_3)_3,initial} = 0.05$ mol kg^{-1}, c° is the concentration at standard state. The results are presented for various initial nitric acid molalities in aqueous phase. The equivalent curve for the extraction of Fe^{3+} is presented in the inset.

mol kg^{-1}, depending on $c_{D,initial}$. A high initial slope of approximately 3.5 is followed by 1.8 and then 1.2. The case of $m_{HNO_3,initial} = 5$ mol kg^{-1} shows again the three regimes but in all regions slope is around 1.7. This observation points to the fact that high salt concentrations in aqueous phase tend to damp the fine-tuning influences on the apparent extraction stoichiometry. In practice, by considering a large concentration range the 'log-log' plots are usually not straight lines. There is a deviation at both low and high extractant concentrations. The slope value is reduced because the monomeric DMDOHEMA extractant is partially spent to extract acid and iron.

When the central slope is used, the non-integer value is said to correspond to the average effective stoichiometry. If the slope at a given range of concentrations is not an integer, several different complexes are invoked. Furthermore, the complexation at low extractant concentration is higher. Obtaining a larger aggregation number is contrary to the Le Chatelier's principle. This difficulty has been discussed in chemical engineering for different types of adducts *i.e.* molecules which participate in the aggregate but are not complexed. To overcome this difficulty, the extra parametrization is applied. Our calculations predict non-linearity on a simple explanation of competition reactions between for example, pure acid concentration in competition with metal extraction[196, 197]. This finding brings attention to the longstanding usage

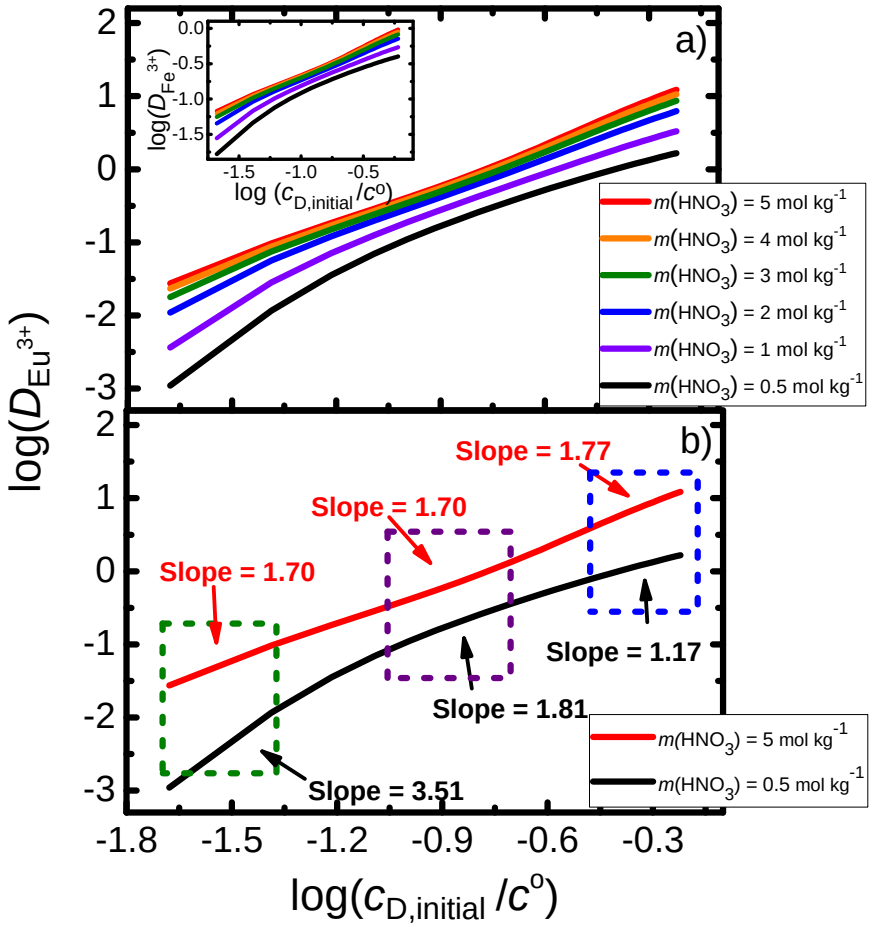

Figure 4.22 – a) Decimal logarithm of Eu^{3+} distribution coefficient as a function of decimal logarithm of $c_{\mathrm{D,initial}}$. The system in study is: $m_{\mathrm{Eu(NO_3)_3,initial}} = m_{\mathrm{Fe(NO_3)_3,initial}} = 0.05$ mol kg^{-1}. The results are presented for various concentrations of nitric acid in aqueous phase. The equivalent curve for the extraction of Fe^{3+} is presented in the inset. b) Slope method results for $m_{\mathrm{HNO_3,initial}} = 0.5$ (black line) and 5 mol kg^{-1} (red line).

of slope method in determination of the stoichiometry for various hydrometallurgical processes. We wish to emphasize that under a certain physical condition of the system, various regimes in stoichiometry can be 'masked' by experimental error, thus leading to false simplicity in an understanding of the behaviour of the system[198]. Besides the concentration of nitric acid, we have varied the concentrations of the lanthanide. As expected, the apparent stoichiometry is dependent on the initial concentration of target solutes. The results are shown in reference [171].

Determining the apparent stoichiometry is non-trivial, in the sense that meaningful value can be obtained only if the speciation of the organic phase is know and the MAL is set accordingly. Everything else is simply rounding of numbers to the closest integer. In example shown above,

the situation is somewhat simple, since DMDOHEMA does not dimerize[4]. In the next chapter, we will be dealing with HDEHP extractant for which the situation is even more complicated. There we will describe in detail how to approach the problem at hand and furthermore, how to use Droplet model to obtain proper speciation of the organic phase.

4.7 Establishing Relation Between Complexation Energy and Formulation Design: Is It Sufficient?

In hydrometallurgy, the extraction of a cation to solvent phase is often identified as the complexation of a cation by the chelating agent (the extractant molecule). In fact, the affinity to form the complex is indeed the leading force to extract the cation but it is only one of the terms in the global free energy of transfer[71]. In our model complexation is counter-balanced by a few opposing forces such as: energy cost for packing of extractant chains in ordered curved film (a curvature effect), differences in ion concentrations between the aqueous and the solvent phases (change in their configurational entropy in the scope of an ideal solution), the differences in chemical potentials of water between two phases *etc.* (see full expression in Eq. 4.22). In order to make a clear distinction between supramolecular complexation and the energy of transfer of solutes, we plotted the negative value of the natural logarithm of the $D_{\mathrm{Eu^{3+}}}$ as a function of a negative value of the complexation parameter $E_{\mathrm{Eu^{3+},D}}$. $E_{\mathrm{Eu^{3+},D}}$ represents the enthalpic (or to be more accurate: internal energy) contribution of complexation and by declaring it as a continuous variable, we mimic the strength (or affinity) of the extractant molecule/target cation couple. It follows that different types of extractants are represented by a different $E_{\mathrm{Eu^{3+},D}}$.

$-\ln D_{\mathrm{Eu^{3+}}}$ is often referred as an apparent energy of the extraction[177]. In Figures 4.23 a-c, the assumption that first neighbor complexation directly yields extraction (a green dashed line) is plotted for purpose of easier understanding of the context. Figures 4.23 a) and b) show the $-\ln D_{\mathrm{Eu^{3+}}}$ for a system $c_{\mathrm{Eu(NO_3)_3,initial}} = 0.1$ mol dm^{-3} and $c_{\mathrm{Eu(NO_3)_3,initial}} = 1$ mol dm^{-3}, respectively. The extractant concentration was fixed to $c_{\mathrm{D,initial}} = 0.6$ mol dm^{-3}. The two different initial Eu^{3+} concentrations represent the cases below and above the experimentally observed limiting organic concentration of solutes (LOC).

Two immediate conclusions can be drawn. First, the extraction cannot be solely identified with the complexation energy, since solid and dashed lines are not collinear. Second, the

[4]DMDOHEMA does not dimerize substantially, which was described in the theoretical section at the beginning of this chapter.

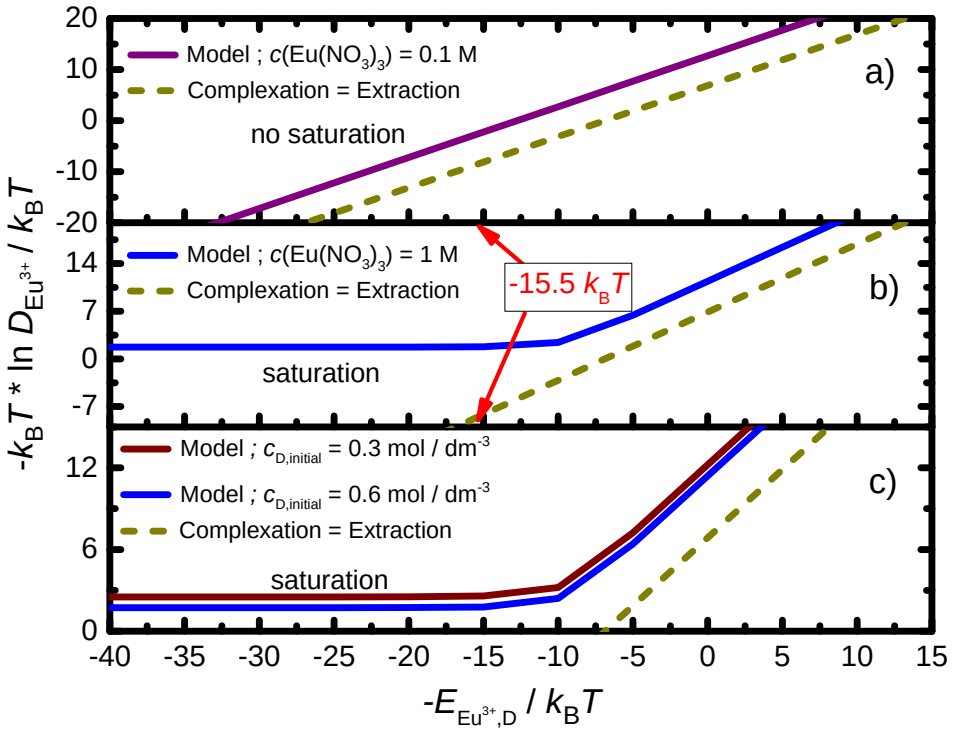

Figure 4.23 – Negative value of natural logarithm of the distribution coefficient $-\ln D_{Eu^{3+}}$, as a function of a negative value of the complexation energy parameter $E_{Eu^{3+},D}$. The negative values of $E_{Eu^{3+},D}$ are taken for the purpose of visually easier reading of the saturation limit. a) System: $c_{D,initial} = 0.6$ mol dm^{-3}, $c_{Eu(NO_3)_3,initial} = 0.1$ mol dm^{-3}. b) System: $c_{D,initial} = 0.6$ mol dm^{-3}, $c_{Eu(NO_3)_3,initial} = 1$ mol dm^{-3}. c) System: $c_{Eu(NO_3)_3,initial} = 1$ mol dm^{-3}. The calculations are shown for the two initial extractant concentrations, namely $c_{D,initial} = 0.6$ mol dm^{-3} and $c_{D,initial} = 0.3$ mol dm^{-3}.

choice of the extractant is also dependent on the concentration of the target metal cation and not only on its nature. When a concentration of metal cation is sufficiently low compared to the concentration of the extractant (Figure 4.23 a)), the $E_{Eu^{3+},D}$ can be very high (typical that of the ionic charged extractant) and saturation would still not occur. By saturation, in this context, we address the case where most of the extractant molecules are in aggregated form and the concentration of monomeric form is almost negligible. In Figure 4.23 b) for $c_{Eu(NO_3)_3,initial} = 1$ mol dm^{-3}, the saturation is achieved already for the type of the extractant described by typically $E_{Eu^{3+},D} = 10\ k_BT$ for one ion complexed to two extractant molecules, thus showing an irreversible character of the formulation. This means that in practical formulation it would be sufficient to use a lower concentration of salt or to change DMDOHEMA extractant with some less efficient one.

An important feature of this model is the usage of well defined and justified parameters.

The results presented in Figure 4.23 provide a sort of justification of $E_{Eu^{3+},D}$ in general. $E_{Eu^{3+},D}$ has a proper value if and only if, for a given definition (recall section Theory, Eq 4.15) provides the result which is in accordance with the experimental values. A value of $E_{Eu^{3+},D} = 7.8\ k_BT$ (for 2 bonds created it gives 15.6 k_BT, as pointed on the graph) is in fact a good value for the description since it corresponds to approximately $D_{Eu^{3+}} = 11$ (Figure 4.23 a)). A conclusion is that the system composed of $c_{Eu(NO_3)_3,initial} = 0.1$ mol dm^{-3} in 3 mol dm^{-3} nitric acid and DMDOHEMA extractant in a solvent represents a desirable reversible formulation.

Figure 4.23 c) shows the influence of total extractant concentration, $c_{D,initial} = 0.3$ and 0.6 mol dm^{-3}. The important feature is that saturation is achieved for the same $E_{Eu^{3+},D}$ value. The only difference between the two is the fact that formulation with the higher $c_{D,initial}$ can extract more of the target ion.

In hydrometallurgy, the supramolecular approach stipulates that the extraction free energy corresponds to the complexation of the cation by one or more chelating agents (synonym for the extractant molecules) associated to an entropy of mixing[11]. In the colloidal approach proposed here, a more general view is now possible. That is why we propose Figure 4.23 to illustrate this[71]. Since the negative value of the natural logarithm of $D_{Eu^{3+}}$ represents the apparent free energy of the electrolyte extraction, we plot this quantity related to the efficiency on y-axis, while x-axis shows the chemical motor driving the transfer towards the phase containing the extractant. The latter is specific to each lanthanide/extractant couple. Figure 4.23a shows the case where the mole ratio of the extractant to lanthanide is a factor of 6, and we see that in these conditions, the usual supramolecular approximation holds. The two lines are separated by around 7 k_BT, which corresponds to the sum of various contributions included within our model, namely differences in ion concentrations between the core of the aggregate and the aqueous phase, the differences in chemical potentials of water between two phases, steric hindrance of extractant chains *etc.* Opposite case is shown in Figure 4.23b where now the amount of the lanthanide cation is in an excess towards the amount of the extractant molecules in the system. In this case, the curves exhibit the typical Langmuir-isotherms behaviour since, after the saturation of the extractants, the extraction efficiency does not longer depend on the driving complexation energy. We show order of magnitude for our practical case of DMDOHEMA/Eu^{3+} to which the complexation parameter has been attributed (via fitting procedure). Last but not the least, in this case, monomers concentrations are negligible and this favours the danger of going in the third phase formation where oil phase becomes unstable[199].

4.8 Conclusion

In order to acquire the insight into forces that influence the aggregation process and to predict the overall extraction of solutes to solvent phase, we proposed a minimal model for which the parameters are experimentally accessible. The minimal model was derived from statistical thermodynamics within a framework of molecular self-assembly of the extractant molecules. With this colloidal approach that goes beyond supramolecular complexation considerations only, the efficiency plots can be generated for any point of Winsor II regime where the dominant aggregates are reverse spherical micelles. So-called Droplet model, in a global free energy difference approach, takes into account the dominant term called complexation free energy, which is well-known in organometallic chemistry of supramolecular self-assembly. The complexation free energy is counter-balanced by weaker quenching terms associated with the packing of extractants chains *i.e.* curvature term, differences in ion concentrations between the two phases, the activity of water, displacement of extractant from apolar solvent to the hydrophobic-hydrophilic nanodomain *etc.*

The fitting of experimental CAC and extraction curves with the respect to the imposed constraints (described in detail in Fitting of the Experimental Data section), yielded the standard chemical potential $\mu_1^\circ = 2.5$ kJ/mol, and the complexation energies namely, $E_{\mathrm{H^+,D}} = 5\ k_\mathrm{B}T$, $E_{\mathrm{Eu^{3+},D}} = 7.8\ k_\mathrm{B}T$ and $E_{\mathrm{Fe^{3+},D}} = 6.5\ k_\mathrm{B}T$ per created bond. With obtained parameters, we studied a practical system composed of HNO_3, $Eu(NO_3)_3$ and $Fe(NO_3)_3$ aqueous solution in contact with a solvent containing DMDOHEMA extractant. The calculations showed that the most probable aggregates contain typically one salt molecule, 4 extractants and from 4 to 8 water molecules inside the core (depending on the type of salt). Stable aggregates containing $Eu(NO_3)_3$ or $Fe(NO_3)_3$, are formed with an increased number of water molecules since more ions in the core require a higher dilution in order to reach a stable form. The probabilities, and thus the concentrations of the aggregates at equilibrium are dependent not only on the interaction of extractant and extracted solutes (*i.e.* on $E_{i,\mathrm{D}}$), but also on the composition of the entire system *e.g.* the initial acid and salt concentrations, temperature, *etc.*

Our model predicts a decrease of CAC upon the addition of target salts in the aqueous phase. An increase of HNO_3 concentration forces a higher water co-extraction and also enhances the extraction of metal nitrates, namely $Eu(NO_3)_3$ or $Fe(NO_3)_3$. The extractant concentration, especially above CAC for a particular system, plays a significant role in the extraction of target salts. The calculated distribution coefficient versus extractant concentration results shows nonlinear behavior which is even more pronounced upon an increase in bulk HNO_3

concentration. A slope method used to determine apparent stoichiometry complexation shows different trends that do not only depend on extractant but also on the acid and lanthanide concentration.

The central message of this chapter is presented in Figures 4.16a-c and Figures 4.17, 4.18, and 4.19. Combined, figures give an insight into polydispersity of the self-assembly for DMDOHEMA extractant system. Furthermore, it was demonstrated how the change in independent system variables affects the aggregates probabilities (or concentrations) at equilibrium. Change of the composition of the aqueous phase is then accordingly reflected in solutes extraction isotherms.

In the context of reversible and therefore desirable formulations for the extraction systems, we have performed calculations with varying $E_{3+,\mathrm{D}}$. Results show that choice of extractant is dependent, besides on nature of the target salt, also on its total concentration in the aqueous phase. The calculations show that there is a threshold of $E_{3+,\mathrm{D}}$ after which the saturation of extractant is achieved (for a defined salt concentration) thus making an unfavorable formulation. Upon an increase of the total extractant concentration, as expected, the extraction capacity of used formulation increases, but the saturation threshold remains constant. Therefore, saturation in terms of $E_{3+,\mathrm{D}}$ is invariant to the total extractant concentration, $c_{\mathrm{D,initial}}$. Also, our calculations show a clear distinction between extraction of the solute and the complexation energy term.

General behavior of DMDOHEMA

DMDOHEMA as a part of non-ionic solvating extractants favors high dilution of the core of self-assembled aggregate[11]. The overall extraction efficiency is low, but can be enhanced by concentrating the aqueous phase, preferably with the non-extracted salt, or by acids[5]. Extraction isotherms resemble Langmuir site occupancy isotherms, which means that simple Langmuir-like model proposed is not bad at all[57, 58]. Before system CAC, the extraction is low, or even negligible. Our approach thus points to the fact that colloidal self-assembly controls the transfer of solutes between aqueous and organic phases in liquid-liquid extraction process.

[5]Note that increase in acid usage in industry violates the green chemistry aspect! Luckily, Chapter 4 provides a solution.

Chapter 5

Modelling of Liquid-Liquid Extraction: a Case of Acidic HDEHP Extractant

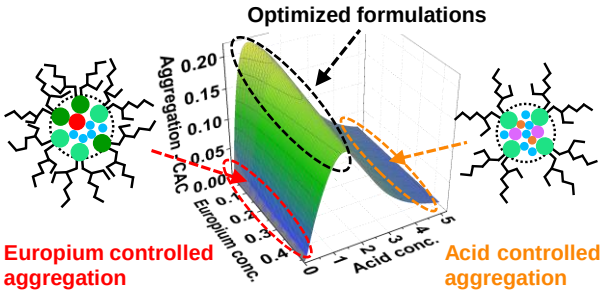

Figure 5.1 – Modelling liquid-liquid extraction: HDEHP case

We propose extension of the Droplet model for acidic extractants. Additional terms in the free energy representation are namely, lateral interactions between different extractant head groups in the film, the dimerization, and the acidity of the HDEHP extractant. With the model, we are able to establish the relation between the extraction and general complexation at any pH in the system. This further allowed us to rationalize the well-defined optimum in the extraction engineering design. Calculations show that there are multiple extraction regimes even in the case of lanthanide/acid system only. Each of these regimes is controlled by the formation of different species in the solvent phase, ranging from multiple metal cation-filled aggregates (at the low acid concentrations in the aqueous phase), to the pure acid-filled aggregates (at the high acid concentrations in the aqueous phase). These results are contrary to a long-standing opinion that liquid-liquid extraction can be modelled with only few species.

5.1 How to Interpret the Engineering-Scale Experiment?

This chapter deals with the extension of the Droplet model to the case of acidic extractants. The principal difference compared to the DMDOHEMA case, is the proton/metal cation exchange reaction[1]. Therefore, the influence of the pH needs to be accounted for.

At this point, the calculations in canonical ensemble become computationally demanding. Minimization of multiple-equilibria MAL (that assumes thousands of competition reactions) can introduce a severe numerical noise. In order to avoid this, we switch from Canonical to semi-Grand Canonical ensemble. Practically, what we do is to fix values of chemical potentials of ions and water in the aqueous phase. We consider the aqueous solution in contact to the organic phase as a infinite reservoir of ions and water molecules. Consequently, we reduce the number of variables that need to be minimized. Now the only variable is the monomer concentration of the HDEHP extractant at equilibrium.

Another major difference (compared to the previous chapter) is the fact that in this and the next chapter, we adopt more general approach in sense that different cations can fill the same aggregate. There is no more constraint on which ions can occupy particular aggregate: every composition is possible. This gives a raise to a huge number of additional competition reactions. Obviously the system is more easily managed without minimizing many variables. Furthermore the generality of the method is crucial for understanding synergistic mixtures of extractants where stoichiometry varies with the independent system variables. The generality of the model is already tested in this chapter, on much simpler pure HDEHP system. Within this chapter, the example is made on experimentally well-studied system: aqueous solution of $HNO_3/Eu(NO_3)_3$ in contact to the *n*-dodecane with dissolved HDEHP extractant.

Since we are dealing with the extension of the Droplet model, which is described in detail within previous chapter, we will only describe the modifications and novelties that are needed for HDEHP case.

[1] HDEHP dissociation reaction: $LH \rightleftharpoons L^- + H^+$

5.2 Theoretical Section: Extension of Droplet Model to Acidic Extractants

5.2.1 Model System

The extractant considered within this study is bis-(ethylhexyl) phosphoric acid (HDEHP) and its chemical structure is presented in Figure 5.2. Like in the previous chapter, the Droplet

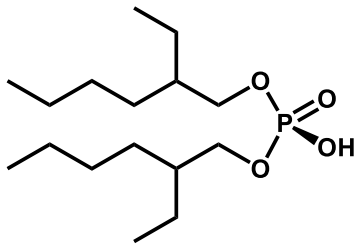

Figure 5.2 – HDEHP extractant chemical structure.

model assumes all aggregates spherical on average (but they differ in size), with aggregates being dispersed in the organic solvent, assumed as low dielectric continuum. The aqueous phase can contain multiple ionic species and is considered as an infinite reservoir which sets chemical potentials of solutes. Organic phase, at equilibrium, is made of dispersed monomers, dimers of the extractant and the self-assembled aggregates. We have neglected HDEHP aqueous partitioning since we will be dealing with a system of concentrated aqueous solutions of trivalent cations. In those conditions, it was shown that HDEHP solubility is low and the equilibrium is shifted towards the self-assembly of aggregates in the organic phase[165]. The schematic representation of HDEHP liquid-liquid extraction system at equilibrium is presented in Figure 5.3. The organic solvent considered in this study is *n*-dodecane. The initial difference of HDEHP system, compared to DMDOHEMA, is dimerization of the extractant in the system. By including dimerization as a competing chemical reaction that adjusts the equilibrium monomer HDEHP concentration. We have following set of chemical equilibria:

$$2\overline{\mathrm{LH}} \rightleftharpoons \overline{\mathrm{LH_2}} \tag{5.1}$$

$$N_{\mathrm{H_2O}} \cdot \mathrm{H_2O} + N_{\mathrm{Eu^{3+}}} \cdot \mathrm{Eu^{3+}} + N_{\mathrm{H^+}} \cdot \mathrm{H^+} + N_{\mathrm{NO_3^-}} \cdot \mathrm{NO_3^-} + N_{\mathrm{LH}} \cdot \overline{\mathrm{LH}} \rightleftharpoons \overline{\mathrm{A}_{N_{\mathrm{H_2O}};N_{\mathrm{Eu^{3+}}};N_{\mathrm{H^+}};N_{\mathrm{NO_3^-}};N_{\mathrm{L^-}};N_{\mathrm{LH,R}}}} + N_{\mathrm{L^-}} \cdot \mathrm{H^+} \tag{5.2}$$

where $\mathrm{H_2O}$, $\mathrm{Eu^{3+}}$, $\mathrm{H^+}$, $\mathrm{NO_3^-}$, $\overline{\mathrm{LH}}$, $\overline{\mathrm{LH_2}}$, and $\overline{\mathrm{A}_{N_{\mathrm{H_2O}};N_{\mathrm{Eu^{3+}}};N_{\mathrm{H^+}};N_{\mathrm{NO_3^-}};N_{\mathrm{L^-}};N_{\mathrm{LH,R}}}}$ are respectively symbols for the water, the europium cation, the proton, the nitrate anion, the monomeric

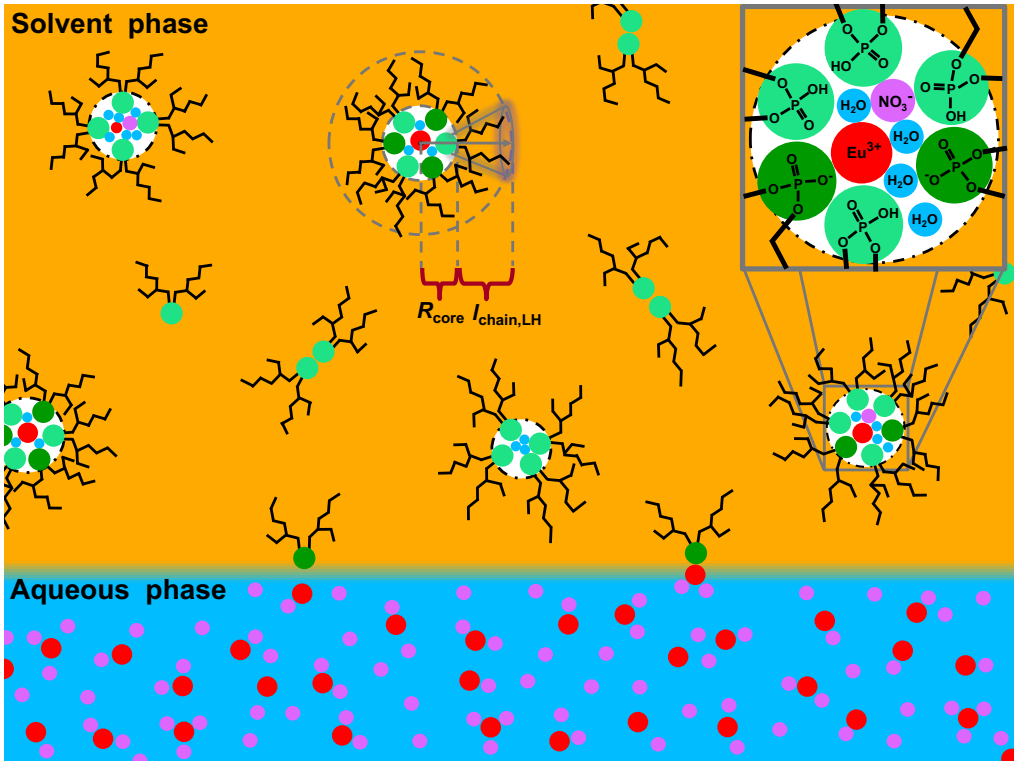

Figure 5.3 – Schematic representation of the bulk model for the liquid-liquid extraction using acidic extractant. Various types of aggregates are present in the organic phase (solvent phase), and their probability at equilibrium is determined by the composition of their cores and extractant film. Considering the surfactant nature of the extractant, the interface is at least partially covered by the extractant molecules (not shown here). The zoomed region shows the core of the aggregate with the europium cation (red), the nitrate anion (pink), water molecules (pale blue), and undissociated HDEHP head groups (dark green), and dissociated HDEHP head groups (pale green). Extractant hydrophobic chains are presented in black. Two connected HDEHP extractants denote dimer.

form of the extractant, the dimeric form of the extractant, and the aggregate of the particular composition. $N_{H_2O}, N_{Eu^{3+}}, N_{H^+}, N_{NO_3^-}, N_{LH}, N_{L^-}$ and $N_{LH,R}$ are respectively the stoichiometric numbers of extracted water molecules, europium cations, hydrogen ions (protons), nitrate anions, monomeric extractant (the aggregation number), dissociated extractant molecules in the aggregated form, and undissociated extractant in the aggregated form. Species present in the organic solvent are denoted by overlined symbols.

Note that the stoichiometry of the released proton is the same as of dissociated extractant, N_{L^-}, since it originates from it. $N_{LH,R}$ is residue, or difference between the aggregation number and dissociated extractant that forms a complex with the metal cation ($N_{LH,R} = N_{LH} - N_{L^-}$). To preserve the generality of the model, every composition of the aggregate is allowed as long as the electroneutrality of the aggregate is respected.

5.2.2 Free energy of Spherical HDEHP Aggregate

Again, like in the previous chapter, we start by deriving the analytical expression for the free energy of the particular spherical aggregate. In Eq. 4.21 we have already defined is as: $\mu^\circ_{Agg,x} = F_{Agg,x}$ for the case of non-ionic DMDOHEMA extractant. Calculation of $\mu^\circ_{Agg,x}$ for HDEHP requires an additional energy term. The term is a consequence of the dissociation of the HDEHP phosphate groups (head groups). Dissociation creates a new distinguishable site in the extractant film*i.e.* protonated and deprotonated phosphate groups. At this point, it must be noted that binding of the acid to HDEHP head group does not cause any change, therefore no additional site is created. It follows that the formation of highly curved acidic extractant film needs, beside the curvature effect, description of the interactions between different head groups. Therefore, we have

$$F_{Agg,x} = F_{extr.film} + F_{core} \tag{5.3}$$

where F_{core} is again the free energy of the aqueous solution with complexation ($F_{core} = F_{droplet} + F_{complex} + F_{correction}$), corrected for using Stirling's approximation. $F_{droplet}$ is given by Eq. 4.8, whereas $F_{complex}$ is given by Eq. 4.7. The free energy of the curved extractant film composed of extractant which can dissociate, $F_{extr.film}$ is defined as

$$F_{extr.film} = F_{chain} + F_{extr.head} \tag{5.4}$$

where F_{chain} is again the free energy of curved extractant film (similar to Eq. 4.17) and reads

$$F_{chain} = \frac{\kappa^\star_{LH}}{2}\left(\sum_i N_{i,LH} N_{bond,i,LH}\left(p - p_{0,i,LH}\right)^2 + \left(N_{LH} - \sum_i N_{i,LH} N_{bond,i,LH}\right)\left(p - p_{0,H_2O,LH}\right)^2\right) \tag{5.5}$$

where $\kappa^{\star}_{\mathrm{LH}}$ represents the generalized bending constant of HDEHP extractant film in a n-dodecane, $p_{0,i,\mathrm{LH}}$ is the spontaneous packing parameter for a certain type of HDEHP extractant/cation pair in a particular solvent, $p_{0,\mathrm{H_2O},LH}$ is the spontaneous packing parameter of HDEHP extractant when no cations are bound to it. Upon a binding of the acid (the proton) the spontaneous packing parameter is the same as for the water in contact ($p_{0,\mathrm{H^+},\mathrm{LH}} = p_{0,\mathrm{H_2O},\mathrm{LH}}$). This approximation is based on the argument that binding of the proton does not impose severe structural changes of the phosphate polar head groups. Binding of Eu^{3+} causes the change in $p_{0,i,\mathrm{LH}}$. Both bending constant $\kappa^{\star}_{\mathrm{LH}}$ and the average HDEHP chain length in the film $l_{\mathrm{chain,LH}}$ that is needed to calculate packing parameter p are assumed constant for any composition of the core of the aggregate: rigidity of film and stretching of chains are a consequence of interactions with organic solvent. Just like in the case of DMDOHEMA model, $\kappa^{\star}_{\mathrm{LH}}$, $p_{0,\mathrm{H_2O},\mathrm{LH}}$ and $p_{0,i,\mathrm{LH}}$ are adjusted parameters. Another thing to add here is the expression for calculation of the volume of the aggregate's core. We have

$$V_{\mathrm{core}} = \sum_j N_j V_{\mathrm{m},j} + N_{\mathrm{H_2O}} V_{\mathrm{m,H_2O}} + N_{\mathrm{LH,R}} V_{\mathrm{m,LH,R}} + N_{\mathrm{L^-}} V_{\mathrm{m,L^-}} \tag{5.6}$$

where the two new terms in the sum are: $V_{\mathrm{m,LH,R}}$, and $V_{\mathrm{m,L^-}}$ are respectively partial molar volumes of protonated, and deprotonated HDEHP extractant head groups.

$F_{\mathrm{extr.head}}$ is defined as the free energy of mixing two distinguishable head-groups into two-dimensional array of site[2] [123]. It reads

$$F_{\mathrm{extr.head}} = k_{\mathrm{B}}T\ \chi_{\mathrm{LH,L^-}} \frac{N_{\mathrm{LH,R}} N_{\mathrm{L^-}}}{N_{\mathrm{LH}}} - k_{\mathrm{B}}T \ln\left(\frac{N_{\mathrm{LH}}!}{N_{\mathrm{LH,R}}! N_{\mathrm{L^-}}!}\right) \tag{5.7}$$

where $\chi_{\mathrm{LH,L^-}}$ is the exchange parameter[123]. The first term in the Eq. 5.7 takes into account the enthalpic part of the free energy of mixing of two types of polar head-groups ($\overline{\mathrm{LH}}$ and $\overline{\mathrm{L^-}}$) in a monolayer. This excess energy term is derived from the regular solution theory. The approach has been shortly described in the second chapter of this manuscript. Here we deal only with the final expression. The positive values of $\chi_{\mathrm{LH,L^-}}$ describes unfavorable interaction, whereas the negative favorable interaction of the $\overline{\mathrm{LH}}$-$\overline{\mathrm{L^-}}$ contact[3]. In our model $\chi_{\mathrm{LH,L^-}}$ is adjusted parameter and we will recover its value within the fitting procedure, presented later in the text. The second term in Eq. 5.7 is entropic part and accounts for all possible arrangements of two distinguishable head groups in the film.

There is only one more issue to address at this stage. The complexation term is described

[2]We approximated the curved extractant film with 2D array of sites. Sometimes we will refer to it as: 'the plane', or as 'the monolayer', but the meaning is the same.

[3]For example fitting of the phase two-component oil and water phase diagram yielded $\chi_{\mathrm{LH,L^-}} = 5$.

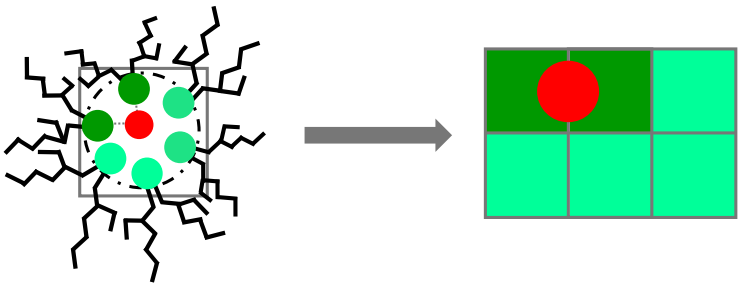

Figure 5.4 – Schematic representation of the calculation of the number of microstates (the entropy) associated with the binding of mixed extractant head group film N_{complex}. The extractant head groups film is approximated with 2D array of sites - an expanded lattice model. Eu^{3+} cation (red), dissociated HDEHP head groups (dark green), and undissociated HDEHP head groups (pale green). Gray dashed lines connecting the cation with the head groups serve as guideline for bonding. It can be seen that Eu^{3+} can be bonded to two extractant head group.

as before, and its generalized version in HDEHP notation reads

$$F_{\text{complex}} = -k_{\text{B}}T \ln N_{\text{complex}} - \sum_i N_{i,\text{LH}} N_{\text{bond},i,\text{LH}} E_{i,\text{LH}} \tag{5.8}$$

where $N_{i,\text{LH}}$, $N_{\text{bond},i,\text{LH}}$, and $E_{i,\text{LH}}$ are respectively the number of cation i complexed by HDEHP extractant, the number of extractants bonded to cation, and the complexation energy parameter per bond. N_{complex} is again the number of microstates associated with mixing of the different sites, created by binding of multivalent cations (or any other cation that causes deprotonation of phosphate group) and is defined as

$$N_{\text{complex}} = \frac{N_{\text{LH}}!}{\prod_i N_{i,\text{LH}}! \, (N_{\text{LH}} - \sum_i N_{i,\text{LH}} N_{\text{bond},i,\text{LH}})!} \cdot \frac{1}{\prod_i N_{\text{bond},i,\text{LH}}!^{N_{i,\text{LH}}}} \, . \tag{5.9}$$

N_{complex} for HDEHP case is presented schematically in Figure 5.4. From schematic representation of the complexation, it is obvious that binding the cation creates distinguishable group. It is very important to emphasize that in both definition of excess film free energy $F_{\text{extr.head}}$, and in complexation F_{complex} there is entropy term associated with arrangements, as presented in Figure 5.4. By comparing entropic parts of two expressions (Eq. 5.7 and Eq. 5.8), we notice that there is a difference. In fact, we can identify factor $N_{\text{LH,R}}$ in denominator from Eq. 5.7 with the factor $(N_{\text{LH}} - \sum_i N_{i,\text{LH}} N_{\text{bond},i,\text{LH}})$ from Eq. 5.9. It follows that entropic part of Eq. 5.7 and 5.9 differ by the factor $1/N_{\text{L}^-}!$. If we keep both expressions, we would double count the number of microstates associated with complexing the cation and creation of distinguishable site in 2D lattice. To resolve this issue, what we practically do is: we keep N_{complex} as is (given by Eq. 5.9) and multiply it by the factor $1/N_{\text{L}^-}!$. Another way of doing this would be by

replacing the entropic term in Eq. 5.7 by $-k_{\mathrm{B}}T\ln\left(1/N_{\mathrm{L}^-}!\right)$. By doing so, we guarantee that we accounted for the phenomena accordingly.

This concludes a calculation of the standard chemical potential of the aggregate of particular composition.

5.2.3 Analytical Expression of Standard Chemical Potential of the Particular Pure HDEHP Aggregate

Here we give a summary of previous derivation in a form of full expression for the standard chemical potential of the particular aggregate self-assembled from HDEHP monomers. We have

$$\begin{aligned}
\mu^{\circ}_{\mathrm{Agg},x} = F_{\mathrm{Agg},x} = F_{\mathrm{complex}} + F_{\mathrm{correction}} + F_{\mathrm{droplet}} + F_{\mathrm{chain}} + F_{\mathrm{extr.head}} = \\
-k_{\mathrm{B}}T\,\ln N_{\mathrm{complex}} - \sum_i N_{i,\mathrm{LH}} N_{\mathrm{bond},i,\mathrm{LH}} E_{i,\mathrm{LH}} + \\
k_{\mathrm{B}}T\,\ln\left(N_{\mathrm{H_2O}}!\prod_j N_j!\right) - k_{\mathrm{B}}T\left(N_{\mathrm{H_2O}}\ln N_{\mathrm{H_2O}} + \sum_j N_j \ln N_j - N_{\mathrm{H_2O}} - \sum_j N_j\right) + \\
N_{\mathrm{H_2O}}\mu^{\circ}_{\mathrm{H_2O}} - k_{\mathrm{B}}T N_{\mathrm{H_2O}}\,\frac{\sum_j x_j^{\mathrm{org}}}{x^{\mathrm{org}}_{\mathrm{H_2O}}} + \sum_j N_j\mu^{\circ}_j + k_{\mathrm{B}}T\sum_j N_j \ln\left(\frac{m_j^{\mathrm{org}}}{m^{\circ}_j}\right) + \\
\frac{\kappa^{\star}_{\mathrm{LH}}}{2}\left(\sum_i N_{i,\mathrm{LH}} N_{\mathrm{bond},i,\mathrm{LH}}\left(p - p_{0,i,\mathrm{LH}}\right)^2 + \left(N_{\mathrm{LH}} - \sum_i N_{i,\mathrm{LH}} N_{\mathrm{bond},i,\mathrm{LH}}\right)\left(p - p_{0,\mathrm{H_2O},\mathrm{LH}}\right)^2\right) + \\
k_{\mathrm{B}}T\,\chi_{\mathrm{LH,L^-}}\frac{N_{\mathrm{LH,R}}N_{\mathrm{L}^-}}{N_{\mathrm{LH}}} - k_{\mathrm{B}}T\,\ln\left(\frac{1}{N_{\mathrm{L}^-}!}\right) \quad .
\end{aligned} \tag{5.10}$$

5.2.4 Completing MAL and Calculation of Equilibrium Aggregate Concentrations: a pure HDEHP case

To derive the expression for the concentration of the particular aggregate at equilibrium, we write the MAL given by Eq. 5.2 in terms of chemical potentials of all species involved. In previous chapter, the ideal behavior of aggregates and extractants in the organic, and salts in the aqueous phase was described (Eq. 4.24 - 4.27). Therefore, MAL given by Eq. 5.2 can be written as

$$\mu_{\mathrm{Agg},x} + \mathrm{N}_{\mathrm{L}^-}\cdot\mu^{\mathrm{aq}}_{\mathrm{H}^+} = N_{\mathrm{LH}}\cdot\mu_{\mathrm{LH}} + N_{\mathrm{H_2O}}\cdot\mu^{\mathrm{aq}}_{\mathrm{H_2O}} + \sum_j N_j\cdot\mu^{\mathrm{aq}}_j \tag{5.11}$$

which is equal to

$$\mu^{\circ}_{\mathrm{Agg},x} + k_{\mathrm{B}}T \ln\left(\frac{c_{\mathrm{Agg},x}}{c^{\circ}}\right) + N_{\mathrm{L^-}}\mu^{\circ}_{\mathrm{H^+}} + \mathrm{N_{L^-}}k_{\mathrm{B}}T \ln\left(\frac{m^{\mathrm{aq}}_{\mathrm{H^+}}}{m^{\circ}_{\mathrm{H^+}}}\right) =$$
$$N_{\mathrm{H_2O}}\mu^{\circ}_{\mathrm{H_2O}} - N_{\mathrm{H_2O}}k_{\mathrm{B}}T\,\frac{\sum_j x^{\mathrm{aq}}_j}{x^{\mathrm{aq}}_{\mathrm{H_2O}}} + \sum_j N_j\mu^{\circ}_j + k_{\mathrm{B}}T\sum_j N_j \ln\left(\frac{m^{\mathrm{aq}}_j}{m^{\circ}_j}\right) + \tag{5.12}$$
$$N_{\mathrm{LH}}\mu^{\circ}_{\mathrm{LH}} + N_{\mathrm{LH}}k_{\mathrm{B}}T \ln\left(\frac{c_{\mathrm{LH}}}{c^{\circ}}\right) \quad .$$

where $\mu^{\circ}_{\mathrm{H^+}}$ is the standard chemical potential of proton in the reservoir. Following the same tactics of keeping the expressions lengths as short as possible we define

$$\mu^{\circ''}_{\mathrm{Agg},x} = \mu^{\circ}_{\mathrm{Agg},x} - N_{\mathrm{H_2O}}\mu^{\mathrm{org}}_{\mathrm{H_2O}} - \sum_j N_j\mu^{\mathrm{org}}_j - N_{\mathrm{L^-}}\mu_{\mathrm{L^-}} \tag{5.13}$$

where $\mu^{\circ''}_{\mathrm{Agg},x}$ is reduced standard chemical potential of the aggregate, obtained by subtracting the chemical potentials of ions and water confined in the aggregate's core form $\mu^{\circ}_{\mathrm{Agg},x}$. $\mu^{\circ''}_{\mathrm{Agg},x}$ still contains the all other terms, namely the chain, the complexation, terms for the correction of statistics for small number of particles, the excess internal energy of the mixed protonated/deprotonated extractant film and the factor quantifying the difference between number of N_{complex} and the number of microstates associated with arranging two distinguishable sites in the 2D array. $\mu_{\mathrm{L^-}}$ is chemical potential of dissociated extractant (or head-groups) and is defined as

$$\mu_{\mathrm{L^-}} = \mu^{\circ}_{\mathrm{L^-}} + k_{\mathrm{B}}T \ln a_{\mathrm{L^-}} \tag{5.14}$$

where $\mu^{\circ}_{\mathrm{L^-}}$ and $a_{\mathrm{L^-}}$ are respectively the standard chemical potential and the activity of dissociated extractant head-groups $\mathrm{L^-}$. After inserting Eq. 5.13 into Eq. 5.12, all the standard chemical potentials of ions and water, except the one of the proton released to aqueous phase during the chemical reaction, cancel out.

At this point we can write the aggregation number N_{LH} as the sum of the dissociated extractant with bound metal cation and the residual undissociated ones[4]. If we substitute N_{LH} in Eq. 5.12 with $N_{\mathrm{L^-}} + N_{\mathrm{LH,R}}$ (recall MAL from the beginning of the chapter), and collect standard chemical potentials multiplied by $N_{\mathrm{L^-}}$ we obtain

$$\mu^{\circ''}_{\mathrm{Agg},x} - N_{\mathrm{H_2O}}k_{\mathrm{B}}T\left(\frac{\sum_j x^{\mathrm{org}}_j}{x^{\mathrm{org}}_{\mathrm{H_2O}}}\right) + k_{\mathrm{B}}T\sum_j N_j \ln\left(\frac{m^{\mathrm{org}}_j}{m^{\circ}_j}\right) + k_{\mathrm{B}}T \ln\left(\frac{c_{\mathrm{Agg,x}}}{c^{\circ}}\right) +$$
$$\mathrm{N_{L^-}}k_{\mathrm{B}}T \ln\left(\frac{m^{\mathrm{aq}}_{\mathrm{H^+}}}{m^{\circ}_{\mathrm{H^+}}}\right) + N_{\mathrm{L^-}}k_{\mathrm{B}}T \ln a_{\mathrm{L^-}} + N_{\mathrm{L^-}}(\mu^{\circ}_{\mathrm{H^+}} + \mu^{\circ}_{\mathrm{L^-}} - \mu^{\circ}_{\mathrm{LH}}) = \tag{5.15}$$
$$-N_{\mathrm{H_2O}}k_{\mathrm{B}}T\,\frac{\sum_j x^{\mathrm{aq}}_j}{x^{\mathrm{aq}}_{\mathrm{H_2O}}} + k_{\mathrm{B}}T\sum_{\mathrm{j}} N_j \ln\left(\frac{m^{\mathrm{aq}}_j}{m^{\circ}_j}\right) + N_{\mathrm{LH,R}}\mu^{\circ}_{\mathrm{LH}} + N_{\mathrm{LH}}k_{\mathrm{B}}T \ln\left(\frac{c_{\mathrm{LH}}}{c^{\circ}}\right) \quad .$$

[4] N_{LH} account for complexed acid or simply constitute a second-sphere of metal cation. They are depicted by pale green color in Figure 5.4.

where $m^{\mathrm{aq}}_{\mathrm{H^+}}$ is the proton molality in the reservoir. We can identify the term $\mu^{\circ}_{\mathrm{H^+}} + \mu^{\circ}_{\mathrm{L^-}} - \mu^{\circ}_{\mathrm{LH}}$ as the standard reaction Gibbs energy of extractant head-group dissociation reaction $\Delta_{\mathrm{r}}G^{\circ}_{\mathrm{a}}$, which can be written as

$$\Delta_{\mathrm{r}}G^{\circ}_{\mathrm{a}} = -k_{\mathrm{B}}T\,\ln K^{\circ}_{\mathrm{a}} = k_{\mathrm{B}}T\,\ln(10)\;\mathrm{p}K^{\circ}_{\mathrm{a}} \tag{5.16}$$

where K°_{a} is the effective dissociation constant. By combining Eq. 5.15 and Eq. 5.16 we recover

$$\begin{aligned} k_{\mathrm{B}}T\,\ln\left(\frac{c_{\mathrm{Agg},x}}{c^{\circ}}\right) = -\mu^{\circ\prime\prime}_{\mathrm{Agg},x} + k_{\mathrm{B}}T\,\sum_j N_{\mathrm{i}}\,\ln\left(\frac{m^{\mathrm{aq}}_j}{m^{\mathrm{org}}_j}\right) + N_{\mathrm{H_2O}}k_{\mathrm{B}}T\,\left(\frac{\sum_j x^{\mathrm{org}}_j}{x^{\mathrm{org}}_{\mathrm{H_2O}}} - \frac{\sum_j x^{\mathrm{aq}}_j}{x^{\mathrm{aq}}_{\mathrm{H_2O}}}\right) \\ -N_{\mathrm{L^-}}k_{\mathrm{B}}T\,\ln(10)(\mathrm{p}K^{\circ}_{\mathrm{a}} - \mathrm{pH}) + N_{\mathrm{LH,R}}\mu^{\circ}_{\mathrm{LH}} + N_{\mathrm{LH}}k_{\mathrm{B}}T\,\ln\left(\frac{c_{\mathrm{LH}}}{c^{\circ}}\right) \end{aligned} \tag{5.17}$$

where pH is defined as

$$\mathrm{pH} = -\log\left(\frac{m^{\mathrm{aq}}_{\mathrm{H^+}}}{m^{\circ}}\right)\quad . \tag{5.18}$$

It must be emphasized that we have discarded the term $k_{\mathrm{B}}T\,\ln a_{\mathrm{L^-}}$ from calculation (the term is present in Eq.5.15 whereas it is not present in Eq. 5.17. In fact, it can be shown that the term is already intrinsically included within the definition of the complexation energy F_{complex} (Eq. **??**). A small phenomenological argument is provided here to support this claim.

Phenomenological Argument for Neglecting Activity of Dissociated Extractant Head Group in the Core of the Aggregate

Droplet model describes a transfer of ion from aqueous to the solvent phase on a principle of micellization. In our approach micellization is governed by self-assembly of extractant molecules in the solvent, complexation of solutes to extractant head-groups, *etc.* Now for the sake of simplicity, let us neglect various contributions that we have identified and established, and write the transfer of ions between the aqueous and the organic phases in a following way:

$$\begin{aligned} \mathrm{M^{3+}_{aq}} \rightleftharpoons \mathrm{M^{3+}_{org}} \quad ; \quad K_{\mathrm{T}} = \frac{[\mathrm{M^{3+}}]_{\mathrm{org}}}{[\mathrm{M^{3+}}]_{\mathrm{aq}}} \\ \mathrm{LH} \rightleftharpoons \mathrm{L^-} + \mathrm{H^+} \quad ; \quad K_{\mathrm{a}} = \frac{[\mathrm{L^-}][\mathrm{H^+}]}{[\mathrm{LH}]} \\ \mathrm{M^{3+}_{org}} + x\mathrm{L^-} \rightleftharpoons \mathrm{ML^{3-x}{}_{org}} \quad ; \quad K_{\mathrm{C}} = \frac{[\mathrm{ML^{3-x}}]_{\mathrm{org}}}{[\mathrm{M^{3+}}]_{\mathrm{org}}[\mathrm{L^-}]^x} \end{aligned} \tag{5.19}$$

where $K_{\mathrm{T}}, K_{\mathrm{a}}$ and K_{C} are respectively the transfer, the dissociation and the complexation constant. Brackets depict equilibrium concentrations of species. By combining these equations we can express the equilibrium concentration of formed complex as

$$[\mathrm{ML^{3-x}}]_{\mathrm{org}} = \frac{K_{\mathrm{T}}K_{\mathrm{C}}K^x_{\mathrm{a}}[\mathrm{M^{3+}}]_{\mathrm{aq}}[\mathrm{LH}]^x}{[\mathrm{H^+}]^x}$$

This expression shows that the term $k_{\mathrm{B}}T \ln a_{\mathrm{L^-}}$ from Eq. 5.15 indeed cancels out since $[\mathrm{ML}^{3-\mathrm{x}}]_{\mathrm{org}}$ does not explicitly depend on it. The term itself exists with its corresponding energy contribution but based on this phenomenological argument we avoid calculating it explicitly.

Expression of the Equilibrium Concentration of Pure HDEHP

We can now continue with the derivation. If we multiply Eq. 5.17 with β and apply exponential function to the whole expression. We obtain

$$c_{\mathrm{Agg},x} = H_{\mathrm{Agg},x}\, c_{\mathrm{LH}}^{N_{\mathrm{LH}}} \tag{5.20}$$

where $H_{\mathrm{Agg,x}}$ is defined as

$$\begin{aligned} H_{\mathrm{Agg},x} = \exp\Bigg(-\beta\mu^{\circ''}_{\mathrm{Agg},x} + \sum_j N_j \ln\left(\frac{m_j^{\mathrm{aq}}}{m_j^{\mathrm{org}}}\right) + N_{\mathrm{H_2O}}\left(\frac{\sum_j x_j^{\mathrm{org}}}{x_{\mathrm{H_2O}}^{\mathrm{org}}} - \frac{\sum_j x_j^{\mathrm{aq}}}{x_{\mathrm{H_2O}}^{\mathrm{aq}}}\right) + \\ -N_{\mathrm{L^-}}\ln(10)(\mathrm{p}K_{\mathrm{a}}^{\circ} - \mathrm{pH}) + \beta N_{\mathrm{LH,R}}\mu_{\mathrm{LH}}^{\circ}\Bigg)\left(\frac{1}{c^{\circ}}\right)^{N_{\mathrm{LH}}-1} \end{aligned} \tag{5.21}$$

with

$$\mu^{\circ''}_{\mathrm{Agg},x} = F_{\mathrm{complex}} + F_{\mathrm{correction}} + F_{\mathrm{chain}} + k_{\mathrm{B}}T\,\chi_{\mathrm{LH,L^-}}\frac{N_{\mathrm{LH,R}}N_{\mathrm{L^-}}}{N_{\mathrm{LH}}} - k_{\mathrm{B}}T\ln\left(\frac{1}{N_{\mathrm{L^-}}!}\right) \tag{5.22}$$

We have established a full framework to calculate thermodynamic properties of extraction systems by calculating the competition between different aggregates. Calculations are preformed in semi-grand canonical ensemble[169]. The adjustments of Droplet model were included in DropEx code. The same minimization procedure was used, as described in previous chapter (Figure 4.6).

5.3 Input Values for the Droplet Model

In previous section we emphasized that the derived model requires a certain set of measurable quantities and adjusted parameters to perform calculations. Here we only report extra quantities that appear within the derivation described in previous section. To assemble the core of the aggregate, besides water and ions, the partial molar volumes of HDEHP polar head groups are considered as similar partial molar volumes of phosphoric acid species. The partial molar volume of the protonated form LH is equal to the molar volume of H_3PO_4, whereas L^{-1} is equal to to the molar volume of $H_2PO_4^{-1}$[178, 200]. To calculate the packing parameter of the particular aggregate (Eq.4.18) we need the average length of HDEHP chains in the film, $l_{\mathrm{chain,LH}}$. The value used for calculations is $l_{\mathrm{chain,LH}} = 4.3$ Å, and was determined by the combination

of SAXS and SANS measurements on the system identical to our study: dodecane solvent containing HDEHP is in contact to the aqueous phase containing $Eu(NO_3)_3$ and HNO_3[24]. In previous section, for DMDOHEMA case, $l_{\mathrm{chain,D}}$ was taken as a direct result of MD simulations an explicit solvent. For HDEHP system in the explicit *n*-dodecane solvent, we did not find any MD simulation study dealing with determination of the average chain length. In section Eq. 5.17, by solving a general form of MAL, the derivation yielded the term which represents the effective dissociation constant pK_a°. For calculations, we used a value $pK_a^\circ = 2.79$, obtained from the literature[165, 201]. Note also that various sources report different pK_a° values[202, 203]. As long as the proton exchange is considered to occur ar the macroscopic oil/aqueous solution interface, we can use some of the values from the literature. Recently, an independent group reported similar approach for using deprotonation equilibria [204]. They focused coupled cDFT with proton exchange to simulate inhomogenous fluid properties in vicinity of aqueous solution/oil interface, with interface being occupied by partially dissociated extractants thus providing the electric field. But this concept is not valid if we state that proton exchange occur inside the core of the aggregate. In that case, pK_a° would be a fitted constant.

To account for the dimerization of HDEHP in the solvent (Eq. 5.1), we used $\log K_D = 4.43$, with K_D being the dimerization constant[205]. This value corresponds to the system HDEHP dissolved in pure *n*-dodecane with no aqueous phase in contact. Only this value should be used. Whenever there is a water phase in contact, there is certain aggregation which creates an error upon determination of $\log K_D$[48, 206]. Moreover, reported values of $\log K_D$ show a strong dependence on both the composition of the aqueous phase and the type of the organic solvent[207, 201].

In the next section, we will derived adjusted parameters and compare our model with experimental data reported by different group.

5.4 Fitting the Reference Data

With measured quantities described, we turn our intention to adjusted parameters of the model. The physics and the influence of each of the parameter on the properties of the extraction systems have been already described and discussed individually previous chapter. A detailed description of the influences can be also found in reference[171]. For this study we have also performed fitting under constraints in order to reduce the number of possible sets of parameters that reproduce the experimental data. Details concerning the constraints and the step-by-step fitting are described in detail in the previous chapter.

We compared our model with the experimental study which dealt with an identical system as ours. HDEHP is dissolved in the analytical grade n-dodecane and the aqueous phase is: 1) pure H_2O, 2) dissolved HNO_3, and 3) dissolved $HNO_3/Eu(NO_3)_3$[54, 187].

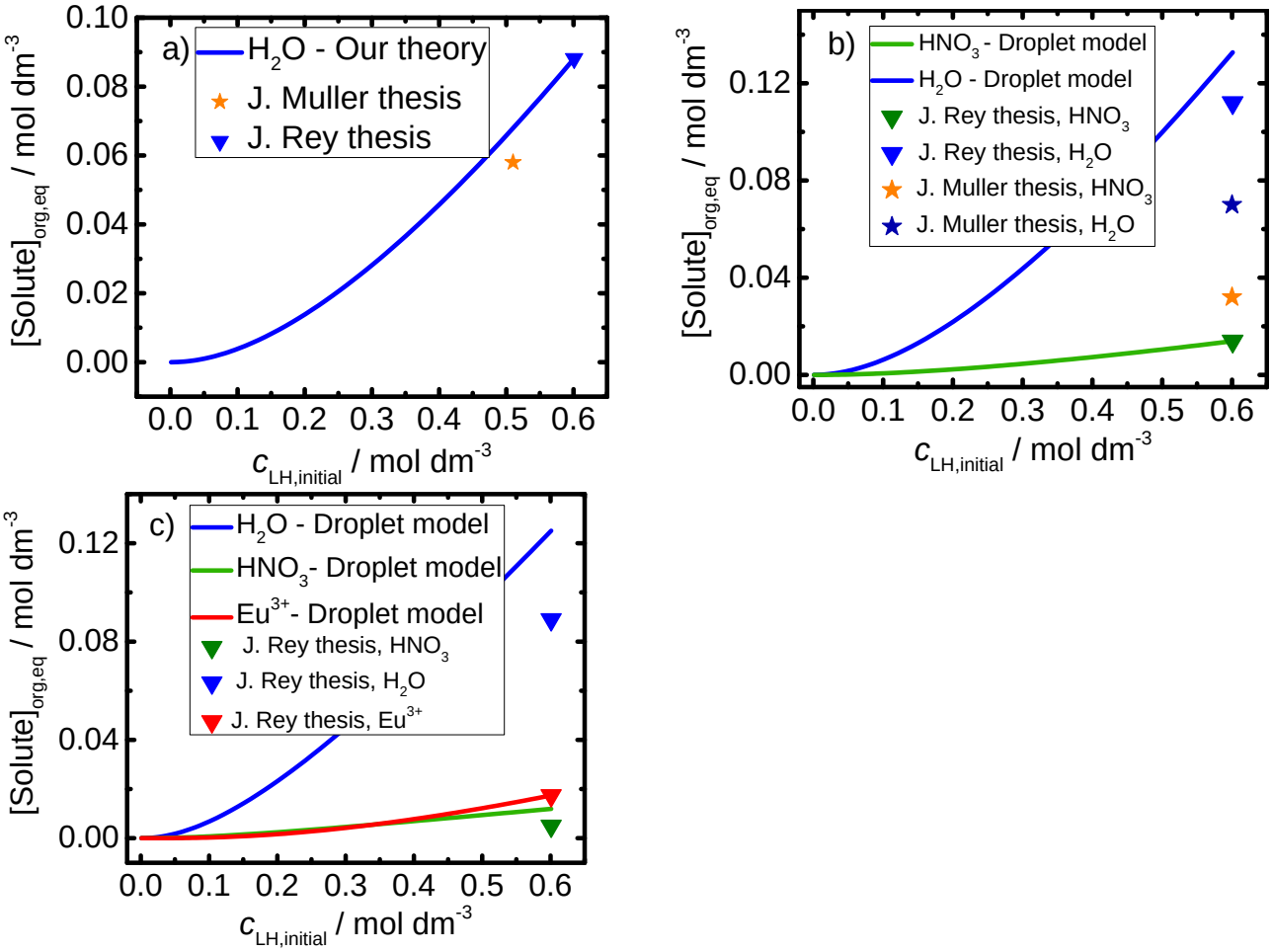

Figure 5.5 – Extraction of solutes are a function of the initial extractant concentration $c_{\mathrm{LH,initial}}$. The organic phase is in contact to: a) pure water, b) $m(HNO_3)_{aq,eq} = 1$ mol kg^{-1}, c) $m(HNO_3)_{aq,eq} = 1$ mol kg^{-1} and $m(Eu^{3+})_{aq,eq} = 0.032$ mol kg^{-1}. The comparison of the experimental data by J. Muller *et al.*[186], and J. Rey *et al.*[54, 187], and predictions of the model are presented. Symbols denote experiments while solid lines the model prediction.

First we fitted the model to the system of a pure water in contact to the solvent containing HDEHP, as can be seen from Figure 5.5a. In order to recover the experimental value we needed to adjust the HDEHP standard chemical potential to $\mu^{\circ}_{\mathrm{LH}} = 12.8$ kJ mol^{-1}, the generalized bending constant to $\kappa^{\star}_{\mathrm{LH}} = 14\ k_{\mathrm{B}}T$, and the spontaneous packing parameter to $p_{0,\mathrm{H_2O,LH}} = 2.6$ of extractant exposed to the pure water. The minimum aggregation number was set to 4. Note that $\kappa^{\star}_{\mathrm{LH}} = 14\ k_{\mathrm{B}}T$ is in the same order of magnitude as for DMDOHEMA case, but slightly

smaller ($\kappa_{\mathrm{D}}^{\star} = 16\ k_{\mathrm{B}}T$). This is expected since DMDOHEMA has three extractant chains, and the solvent was n-heptane, with pronounced penetration ability. HDEHP extractant film in n-dodecane is somewhat more flexible.

Then we fitted the model with extraction data of the system of nitric acid, $m(\mathrm{HNO_3})_{\mathrm{aq,eq}} = 1$ mol kg^{-1}, as presented in Figure 5.5b. By using already obtained parameters, we can deduce the complexation energy of the acid, $E_{\mathrm{H^+,LH}}$. We obtained $E_{\mathrm{H^+,LH}} = 4.2\ k_{\mathrm{B}}T$, which is the order of magnitude of the typical hydrogen bond. Still, compared to the DMDOHEMA, the enthalpic values is smaller, pointing to the face that nesting (bonding) of the acid to phosphate is less favorable than nesting it on larger malonamide group. In case of acid extraction, the spontaneous packing and generalized bending constants are equal to the case of pure water extraction based on an argument that additional binding of the acid to the extractant head group does not impose any severe structural change of the extractant film (the phosphate group does not dissociate). $\mu_{\mathrm{LH}}^{\circ}$ is by definition the free energy of a single HDEHP molecule in the given solvent at the infinite dilution. Therefore, $\mu_{\mathrm{LH}}^{\circ}$ is a constant for any multiphase system.

Third case of fitting is presented in Figure 5.5c. In this case we have Eu^{3+} extraction, which causes dissociation of the extractant. Naturally, there is a change in the conformation of the phosphate group attached to carbon backbone. This is reflecting the change of $p_{0,i,\mathrm{LH}}$ and we need to fit it accordingly[208]. When Eu^{3+} is bound to the extractant, $p_{0,\mathrm{Eu^{3+},LH}} = 3.5$. It can be concluded that HDEHP chains take up larger volume (the chains are more spread) when there is trivalent cation present inside the core, compared to the case of aggregates filled with acids only. As before, we deduce $E_{\mathrm{Eu^{3+},LH}} = 20.4\ k_{\mathrm{B}}T$ per bond. Note that upon the dissociation of the head groups, we create a new type of sites in the extractant film. As was described in theoretical section, the creation of distinguishable site has associated free energy contribution, $F_{\mathrm{extr.head}}$ (Eq. **??**). We have accounted for this phenomena by generalizing a regular solution theory on a 2D film. With entropic part of the associated free energy already being included within the F_{complex}, we needed to adjust the enthalpic contribution of $F_{\mathrm{extr.head}}$ which is described by $\chi_{\mathrm{LH,L^-}}$. Within the fitting procedure we obtained $\chi_{\mathrm{LH,L^-}} = 0.5\ k_{\mathrm{B}}T$ which points to the fact that there is a slight repulsive force between dissociated and undissociated extractant head groups. This contribution, along with the energy associated with dense packing of the extractant chains F_{chain}, works in the opposite direction compared to the complexation, thus quenching the extraction of solutes. The minimum aggregation number for the case of Eu^{3+} was 6. Such aggregation number is often reported in the literature (6 monomers or 3 dimers)[13, 44]. This monodispersity in terms of the aggregation number is contrary to the case of non-ionic extractants where polydispersity is severe in both the aggregation number and

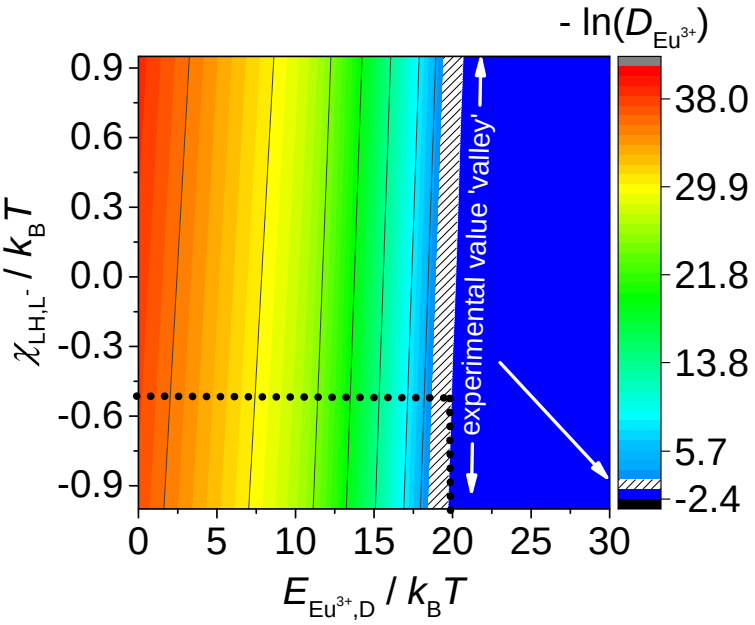

Figure 5.6 – Negative value of natural logarithm of the Eu^{3+} distribution coefficient, $-\ln D_{Eu^{3+}}$ as a function of the Eu^{3+} complexation energy parameter per bond, $E_{Eu^{3+},LH}$ and the exchange parameter, χ_{LH,L^-} used in the calculations. A white region depicts the experimental data[54, 187].

the water content[53, 26]. The difference is due to the stronger interaction between dissociated extractant groups and the trivalent cations in the case of acidic extractants.

For all subsequent calculations (the subject of the following section), we used the described set of parameters at $T = 298.15$ K.

5.4.1 Influence of Head Groups Interactions and Complexation on the Free Energy of Transfer

To derive Eq. 5.10 we needed factorize the aggregate partition function. We did this by ignoring any influence of the composition of the polar core of the aggregate on the lateral interactions between extractant head groups. The only interaction potential is given as a complexation energy and accounts for interactions of head groups and complexed multivalent cation or the acid. This is a severe simplification. Consequently it was mandatory to study the influence of χ_{LH,L^-} on the actual efficiency of the extraction. Therefore, in Figure 5.6 we plotted the negative value of natural logarithm of the Eu^{3+} distribution coefficient $-\ln D_{Eu^{3+}}$ (the scale is not prone to large variation) as a function of $E_{Eu^{3+},LH}$ and χ_{LH,L^-} used for calculations. The distribution coefficient is defined the previous chapter. A white region on the graph depicts

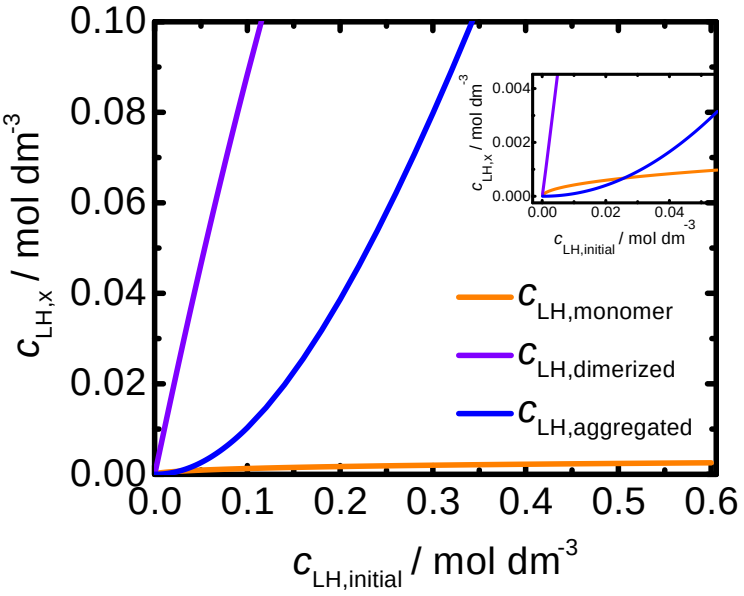

Figure 5.7 – Speciation of the extractant in the solvent as a function of the initial extractant concentration $c_{\mathrm{LH,initial}}$. The solvent phase is in contact to $m(\mathrm{HNO_3})_{\mathrm{aq,eq}} = 1$ mol kg^{-1} and $m(\mathrm{Eu^{3+}})_{\mathrm{aq,eq}} = 0.032$ mol kg^{-1}. Enlarged region at low $c_{\mathrm{LH,initial}}$ is presented in the inset.

experimental values of the Eu^{3+} extraction. It can be seen that the choice of $\chi_{\mathrm{LH,L^-}}$ on the extraction data is rather small and is easily compensated by $E_{\mathrm{Eu^{3+},LH}}$ *i.e.* complexation is dominant factor in the free energy representation. We can choose $\chi_{\mathrm{LH,L^-}}$ from slightly positive (repulsive character) to slightly negative (attractive character) value while $E_{\mathrm{Eu^{3+},LH}}$ per bond still stays globally the same. This counter-intuitive result is convenient since it enables us to omit $\chi_{\mathrm{LH,L^-}}$ from the model thus simplifying the fitting procedure.

5.4.2 Definition of the Aggregation for Dimerizing Extractants

Definition of aggregate

As suggested in previous chapter, the term 'aggregation' is somewhat ambiguous when dealing with the extractants that readily associate to form dimers, trimers, tetramers, or mixed adducts in case extractant mixtures. We have constructed our model, on the basis that HDEHP monomers self-assemble into solutes-filled aggregates. Dimerization of HDEHP is considered as competition reaction that adjusts monomeric HDEHP concentration. Therefore, in our notation, aggregates are only self-assembled structures which contain solutes extracted from the aqueous phase. With this definition, we can use our model to obtain HDEHP speciation in the organic solvent, for aqueous phase in contact same as in reference data set. In Figure 5.7

we have plotted respectively concentrations of monomers $c_{\mathrm{LH,monomer}}$, dimers $c_{\mathrm{LH,dimerized}}$, and the aggregated extractant $c_{\mathrm{LH,aggregated}}$ as a function of the initial HDEHP concentration in the system $c_{\mathrm{LH,initial}}$. In the case of $m(\mathrm{HNO_3})_{\mathrm{aq,eq}} = 1$ mol kg^{-1} and $m(\mathrm{Eu^{3+}})_{\mathrm{aq,eq}} = 0.032$ mol kg^{-1} we can see that monomeric HDEHP is globally small (orange line). This is a consequence of the strong tendency of HDEHP (and most acidic extractants) towards the dimerization and the aggregation[209, 13]. Recall that dimerization constant was quite large ($\log K_{\mathrm{D}} = 4.43$). This means that to break the HDEHP dimer, there is a penalty in energy for exposing polar head group towards oil medium. Note that before experimentally observed CAC, which is reported to be 0.21 mol dm^{-3}, the concentration of the aggregated HDEHP is moderate. The majority of extractant remains in the form of dimers. After CAC there is a pronounced increase in the concentration of the aggregated extractant. This behavior was already reported by an experimental study[210].

Definition of the micellization threshold - CAC

The inset in Figure 5.7 shows the typical self-assembly pattern where concentration of aggregated extractant increases after certain threshold. But this threshold is not really the proper micellization threshold *i.e.* CAC. In principle, we can adopt it, but there is no real connection to the macroscopic definition of CAC. This is because, in typical experiment it is not possible to distinguish between monomers, or dimers. Both can come into contact with the interface by simple diffusion. Example of such experiments are: a drop shape method for surface tension measurement or vapor pressure osmometry (VPO), *etc.*[48] As hinted in the complementary section in DMDOHEMA case, when dealing with strongly interaction extractants it is suitable to locate the region in which aggregation is linear regime. This means that globally, 'free' extractant (the sum of dimerized and monomeric extractants) upon the addition in the system, is spent to form aggregates[72]. In Figure 5.8, $c_{\mathrm{LH,aggregated}}$ was plotted as a function of $c_{\mathrm{LH,initial}}$. The red dotted line represents the linear function which was used to fit the linear aggregation regime. The intersection of the fitting function with abscissa axis corresponds to CAC. The definition is far from perfect, but it gives correct order of magnitude (like in experiments)[48]. Important features is to, once defined, interpret change in CAC only when same method for calculating it was applied[5]. From now, all the CAC calculations were made with this method.

[5]This notation resembles a convention for the standard state of species.

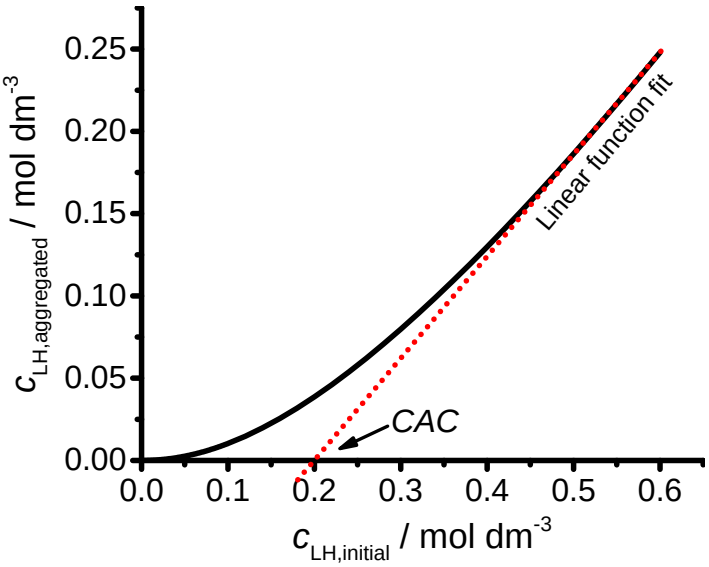

Figure 5.8 – Definition of CAC for the case of interacting extractants *e.g.* dimerization or adduct formation.

5.5 Influence of the Independent System Variables on Solutes Speciation in the Organic Phase

In this section we will demonstrate how the change in independent system variables affects the transfer of all solutes for the aqueous to the organic phase. Results are in the form of usual isotherms. In following sections, we will enlarge the study to obtain the global overview of the liquid-liquid extraction in form of maps, but first it is desirable to provide simple explanation of the system. Two usual ways to study liquid-liquid extraction using acidic extractants are: the dependence of the total extractant concentration, and the acid influence.

Influence of the initial extractant concentration

We start by analyzing results presented in Figures 5.9a-c, where the concentration of extracted solutes in the solvent phase is plotted as a function of $c_{\mathrm{LH,initial}}$. When comparing the results from Figure 5.5a and b, it can be noticed that upon the addition of HNO_3 to the system, the extraction of water slightly increases. H_2O is mandatory to stabilize the core of the aggregate by the dilution effect, *i.e.* co-extracted water solubilizes the extracted acid. Figure 5.5c shows a slight decrease in H_2O and HNO_3 extraction since now there is stronger competition reaction of Eu^{3+} extraction present in the system. The model predicts the lower H_2O uptake when multivalent cations are present in the system. In the case of the Eu^{3+} extraction, there are only few water molecules present in the core of the aggregate, whereas HNO_3 occupied cores can

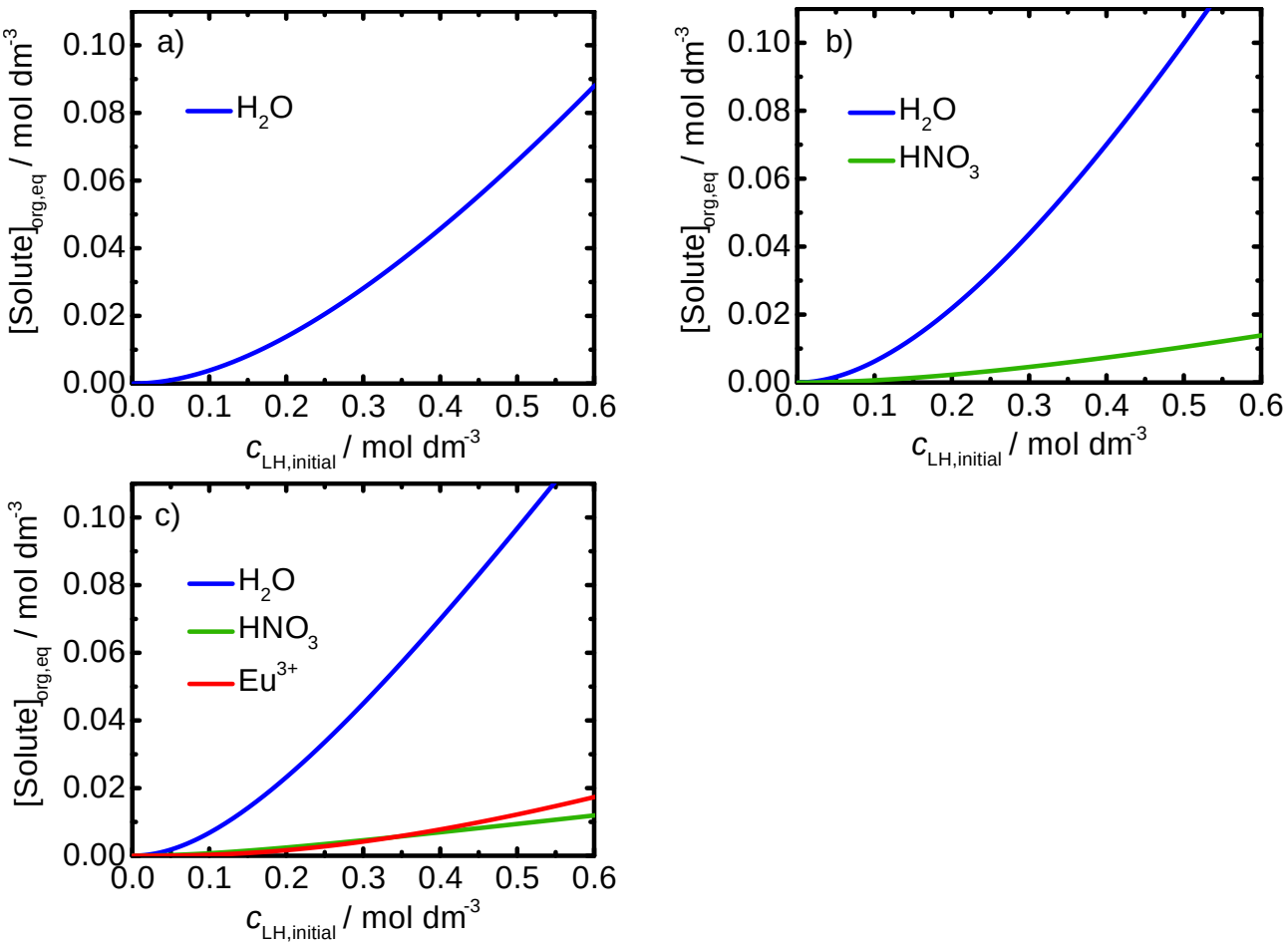

Figure 5.9 – Extraction of solutes are a function of the initial extractant concentration $c_{\mathrm{LH,initial}}$. The organic phase is in contact to: a) pure water, b) $m(\mathrm{HNO_3})_{\mathrm{aq,eq}} = 1$ mol kg^{-1}, c) $m(\mathrm{HNO_3})_{\mathrm{aq,eq}} = 1$ mol kg^{-1}, and $m(\mathrm{Eu^{3+}})_{\mathrm{aq,eq}} = 0.032$ mol kg^{-1}.

contain from 2 to 7 water molecules. The water extraction and its influence on stabilization of the aggregate core are often reported in the literature[36, 211, 212, 213, 186].

Influence of the acid molality

Figures 5.10a shows the speciation of extracted solutes as a function of $m(\mathrm{HNO_3})_{\mathrm{aq,eq}}$. Immediately, we can observe the the sharp decrease in $\mathrm{Eu^{3+}}$ extraction with the increase of $m(\mathrm{HNO_3})_{\mathrm{aq,eq}}$. The high proton molality in the reservoir causes the shift of equilibrium towards protonated form of HDEHP, thus quenching the extraction. More on this influence is provided in the following section. Initially, water content in the organic phase. It corresponds to water molecules coextracted with $\mathrm{Eu^{3+}}$. Our calculation showed that there a fraction of self-assembly is due to the pure water extraction, characterized by following chemical reaction: $N_{\mathrm{H_2O}} \cdot \mathrm{H_2O} + N_{\mathrm{LH}} \cdot \overline{\mathrm{LH}} \rightleftharpoons \overline{\mathrm{A}_{N_{\mathrm{H_2O}};N_{\mathrm{LH}}}}$. It ensures a non-negligible water content in the organic phase. $\mathrm{HNO_3}$ concentration is initially low, but increases with saturation of the aqueous phase

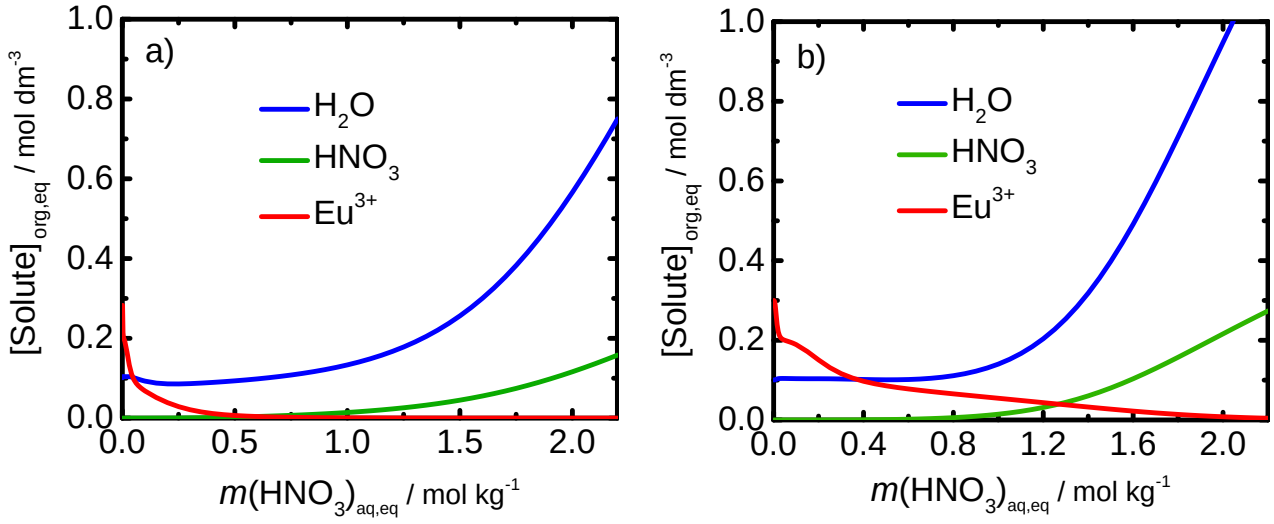

Figure 5.10 – Extracted solutes speciation in the organic phase as a function of $m(\mathrm{HNO_3})_{\mathrm{aq,eq}}$. Results are presented for the case of: a) $m(\mathrm{Eu^{3+}})_{\mathrm{aq,eq}} = 0.001$ mol kg^{-1} and $c_{\mathrm{LH,initial}} = 0.6$ mol dm^{-3} b) $m(\mathrm{Eu^{3+}})_{\mathrm{aq,eq}} = 0.05$ mol kg^{-1} and $c_{\mathrm{LH,initial}} = 0.6$ mol dm^{-3}.

(increase of $m(\mathrm{HNO_3})_{\mathrm{aq,eq}}$) and acid extraction becomes dominant competition reaction.

So far we have demonstrated the influence of the total extractant concentration and the acid influence. If we increase the $m(\mathrm{Eu^{3+}})_{\mathrm{aq,eq}}$, as is presented in Figure 5.10b, the solutes speciation changes drastically. $\mathrm{Eu^{3+}}$ extraction decay is less pronounced than in Figure 5.10a. Higher $m(\mathrm{HNO_3})_{\mathrm{aq,eq}}$ is needed to fully damp $\mathrm{Eu^{3+}}$ extraction. At very high $m(\mathrm{HNO_3})_{\mathrm{aq,eq}}$, again the dominant competition reaction is the acid extraction.

Diversity of competition reactions was observed in Figures 5.9 and 5.10. The question arises: are usual 2D extraction isotherms adequate for the proper prediction of the extraction since there is diversity of extraction regimes. Identification of these regimes is crucial for chemical engineering since it can lower the expenses of method optimization.

5.6 $\mathrm{Eu^{3+}}$ Transfer to the Organic Phase

In this section, we will validate our model by comparing its predictions with the literature. Furthermore, we will investigate the influence of $m(\mathrm{HNO_3})_{\mathrm{aq,eq}}$ and $m(\mathrm{Eu^{3+}})_{\mathrm{eq,aq}}$ on the overall extraction efficiency.

Influence of $m(\mathrm{HNO_3})_{\mathrm{aq,eq}}$

Figure 5.11 shows the dependence of $D_{\mathrm{Eu^{3+}}}$ on the acid molality in the aqueous phase, $m(\mathrm{HNO_3})_{\mathrm{aq,eq}}$. Calculations for various $c_{\mathrm{LH,initial}}$ are presented. Globally, our results are in agreement with

the literature[11, 120, 214]. At low $m(\mathrm{HNO_3})_{\mathrm{aq,eq}}$ the extraction is high, whereas it de-

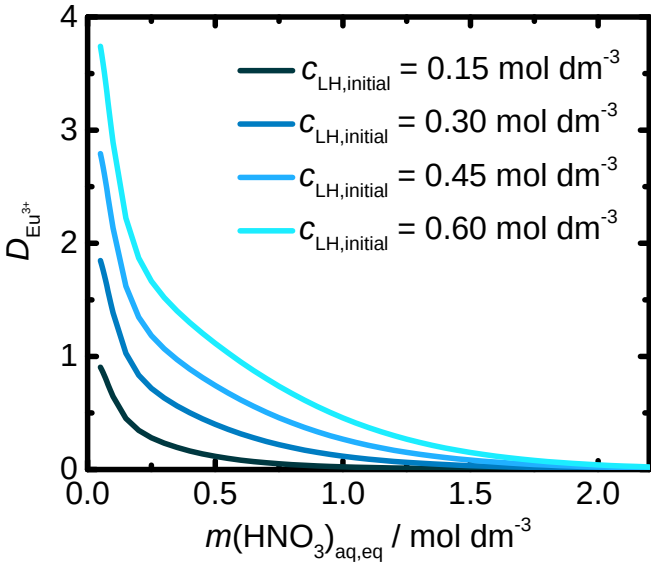

Figure 5.11 – Eu^{3+} distribution coefficient, $D_{Eu^{3+}}$ as a function of $m(\mathrm{HNO_3})_{\mathrm{aq,eq}}$. Results for various initial extractant concentrations $c_{\mathrm{LH,initial}}$ are presented. The solvent phase is in contact to $m(Eu^{3+})_{\mathrm{aq,eq}} = 0.05$ mol kg^{-1}.

creases upon an increase of $m(\mathrm{HNO_3})_{\mathrm{aq,eq}}$. Within our model, this property is reflected in $-N_{\mathrm{L}}\ln(10)(\mathrm{p}K_{\mathrm{a}}^{\circ} - \mathrm{pH})$ energy term (Eq.5.21). It clearly shows that the difference between the effective $\mathrm{p}K_{\mathrm{a}}^{\circ}$ and the pH in the reservoir governs the extraction efficiency as one of the leading terms in the free energy approach. When changing $c_{\mathrm{LH,initial}}$, from lower values up to 0.6 mol dm^{-3} isotherms shift towards higher $D_{Eu^{3+}}$. This happens due to the fact that higher extractant concentrations in the system can take up higher cation loading. Upon examination of isotherms, we can see that there is still a pronounced Eu^{3+} extraction in the case of $c_{\mathrm{LH,initial}} = 0.15$ mol dm^{-3}. Recall that experimentally observed CAC is around 0.21 mol dm^{-3}. It practically means that even below the aggregation threshold, if the acid concentration is sufficiently low, acidic extractants will still extract cations (as reported experimentally[215]). The phenomena of the extraction below CAC is contrary to the case of non-ionic extractants (*e.g.* amides, malonamides or diglycolamides)[194, 190, 216]. For non-ionic extractants, the extraction efficiency is strongly dependent on CAC[171].

Results from Figures 5.11 can be shown in the free energy representation. Instead of plotting concentrations of cations in the solvent, we have plotted a negative value of the natural logarithm of the distribution coefficient, $-\ln D_{Eu^{3+}}$ as a function of $m(\mathrm{HNO_3})_{\mathrm{aq,eq}}$. The value $-\ln D_{Eu^{3+}}$ is historically referred as the apparent energy of transfer. Results are presented in Figure 5.12. It can be seen that the apparent energy of transfer increases with $m(\mathrm{HNO_3})_{\mathrm{aq,eq}}$.

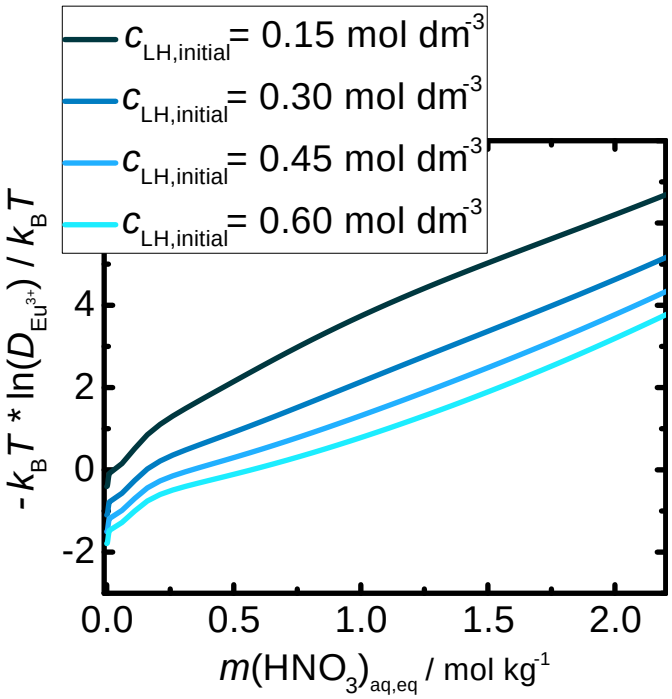

Figure 5.12 – Negative value of natural logarithm of the distribution, $-\ln D_{Eu^{3+}}$ as a function of $m(HNO_3)_{aq,eq}$ for $m(Eu^{3+})_{aq,eq} = 0.05$ mol kg^{-1}. Results are presented for various $c_{LH,initial}$. This figure is an apparent energy of transfer analogue of Figure 5.11

In order to lower the apparent energy of transfer (*i.e.* to boost the extraction of the cation) there must be a compensation in terms of an increase of either $c_{LH,initial}$ or $m(Eu^{3+})_{aq,eq}$ in the system.

Influence of $m(Eu^{3+})_{aq,eq}$

We have studied the dependence of the extracted Eu^{3+} concentration in the solvent $c\,(Eu^{3+})_{org,eq}$, on $m(Eu^{3+})_{aq,eq}$ at $c_{LH,initial} = 0.6$ mol dm^{-3}. Results are presented in Figure 5.13 for three different $m(HNO_3)_{aq,eq}$. We can see that obtained curves have the shape of Langmuir isotherms with asymptotic behavior at high $m(Eu^{3+})_{aq,eq}$. Lower $m(HNO_3)_{aq,eq}$ again favors higher extraction (pale green lines). Our calculations also show that the acid concentration (or pH) has a stronger influence on the efficiency of the extraction compared to cation concentration in the aqueous phase. This can be seen as moderate increase in $c\,(Eu^{3+})_{org,eq}$ with increasing $m(Eu^{3+})_{aq,eq}$, whereas differences in $m(HNO_3)_{aq,eq}$ impose large differences in $c\,(Eu^{3+})_{org,eq}$.

Plotting results from Figure 5.13 as $-\ln D_{Eu^{3+}}$ shows again the unfavorable influence of $m(HNO_3)_{aq,eq}$ increasing the apparent energy. Note that curves are divergent, since $D_{Eu^{3+}}$ diverges at very low $m(Eu^{3+})_{aq,eq}$. A steep decrease in the apparent energy of transfer clearly demonstrates a loss of reversibility of extraction formulations (thus making it undesirable for

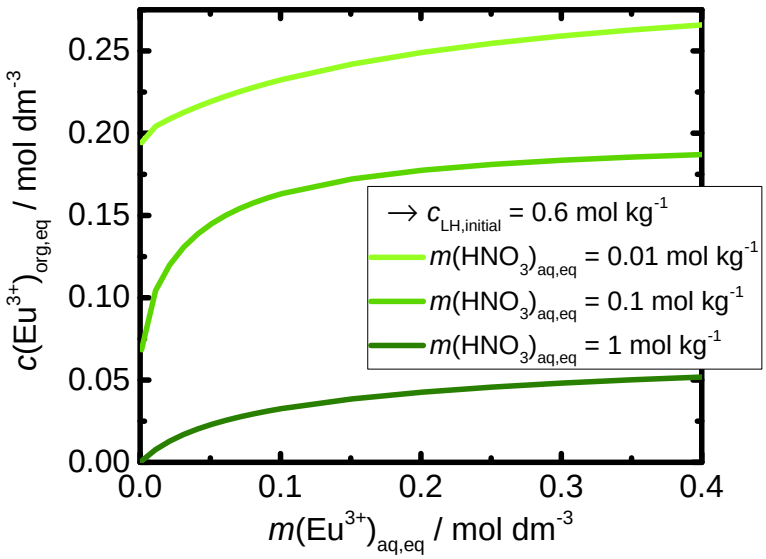

Figure 5.13 – Eu^{3+} concentration in the solvent as a function of europium concentration in the aqueous phase, $m(Eu^{3+})_{aq,eq}$. Results for various $m(HNO_3)_{aq,eq}$ and $c_{LH,initial} = 0.6$ mol dm^{-3} are presented.

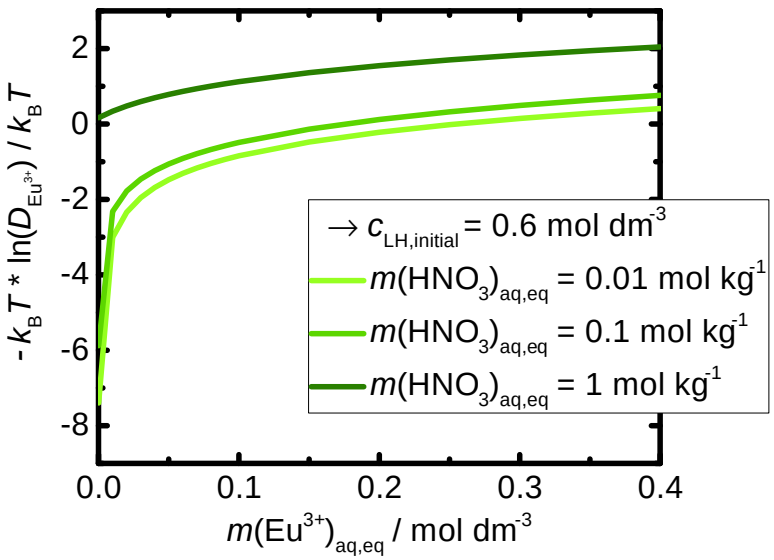

Figure 5.14 – Negative value of natural logarithm of the distribution, $-\ln D_{Eu^{3+}}$ as a function of $m(Eu^{3+})_{aq,eq}$ for $c_{LH,initial} = 0.6$ mol dm^{-3}. Results are presented for various $m(HNO_3)_{aq,eq}$.

chemical engineering) at low $m(HNO_3)_{aq,eq}$ and $m(Eu^{3+})_{aq,eq}$ and high $c_{LH,initial}$.

5.7 Slope Method and the Apparent Stoichiometry

A so-called slope method is usually employed to study the apparent stoichiometry of the extraction. The method is valid if one equilibria only is considered (no variation of aggregation number, unless it is very dilute), if activity coefficients of the species are constant and if logarithm of the distribution coefficient of target cation is plotted as a logarithm of free monomers at equilibrium. If three conditions are fulfilled the slope corresponds to the apparent stoichiometry *i.e.* to the stoichiometric ratio of average aggregation number and average number of target cation[9].

In this section, we will demonstrate the actual meaning of the slope method for determination of the apparent stoichiometry. Moreover, we will present the framework, within the Droplet model, for obtaining the proper stoichiometry of the system that experimental chemists can use.

Our model is set in a way that it takes into account dimerization of the extractant and aggregates are formed from monomers. In this case the slope method should be equal to 6. Indeed, if we plot logarithm of the europium distribution coefficient $\log D_{Eu^{3+}}$ as a function of logarithm of free monomers $\log(c_{LH,monomer}/c^\circ)$, calculated slope is 6, as can be seen form Figure 5.15d. The result is consistent with the calculations of aggregates probabilities where polydispersity in terms of water content, whereas a monodispersity in aggregation numbers were observed.

In the literature the MAL is often written such that HDEHP dimers are species that aggregate and not monomers[120]. In this case the slope should be equal to 3. This was also the result of our calculations for the plotted $\log D_{Eu^{3+}}$ as a function of logarithm of dimerized extractant concentration $\log(c_{LH,dimerized}/c^\circ)$. Results are plotted in Figure 5.15c.

In terms of experiments, it is difficult to measure dimerized and monomeric equilibrium extractant concentrations, but the sum of the two can be measured. In that sense, we can plot $\log D_{Eu^{3+}}$ as a function of the sum of the amount of monomeric and dimerized extractant at equilibrium, $\log(c_{LH,equilibrium}/c^\circ)$ with $c_{LH,equilibrium} = c_{LH,monomer} + 2c_{LH,dimerized}$. Results show different slopes depending on $\log(c_{LH,equilibrium}/c^\circ)$. The initial slope is now 4, and it corresponds an average of the slopes for monomeric and dimerized extractants. In the case that $\log(c_{LH,initial}/c^\circ)$ is plotted, then the differences in apparent stoichiometry regimes are even more pronounced and more difficult to interpret (see Figure 5.17a). Moreover, the situation

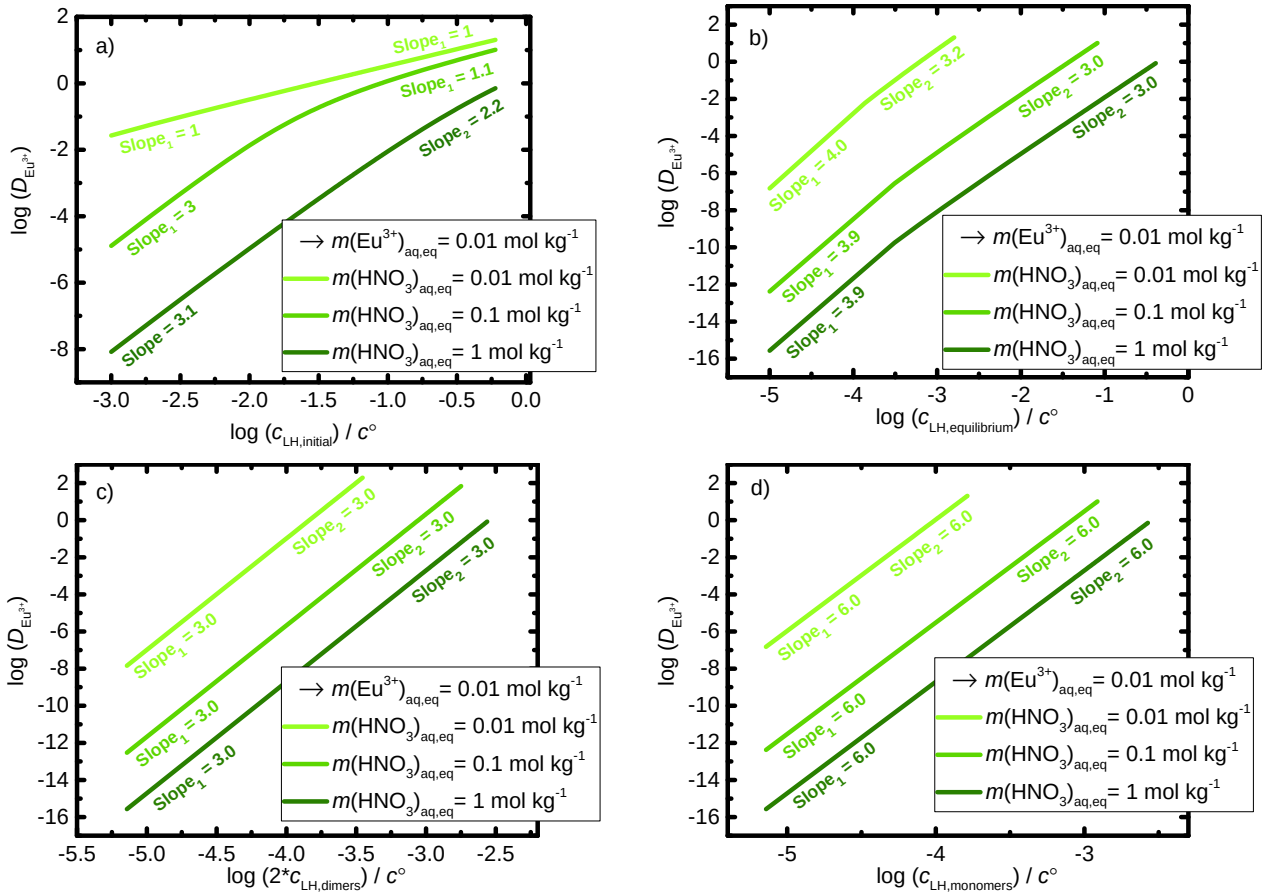

Figure 5.15 – Interpretation of the Slope Method. Decimal logarithm of Eu^{3+} distribution coefficient as a function of decimal logarithm of respectively the initial, the sum of equilibrium monomeric and dimerized extractant, the equilibrium dimerized extractant, and the equilibrium monomeric extractant. The system conditions are noted in figures of graphs.

is especially bad when the part of HDEHP (or any hydrophilic extractant) is involved in the equilibrium with HNO_3 and H_2O[193]. To treat these complicated situations, one needs a proper speciation of the organic phase for any experimental condition (Figure 5.17a and b). Our model can help get a correct apparent stoichiometry in case of non-ionic extractants and acidic extractants[193].

5.8 Overview of the Extraction and Desirable Formulations

So far in this thesis, on few occasion we have stressed the importance to study the influence of independent system variables on the liquid-liquid extraction efficiency. Because liquid-liquid extraction systems are complex, it is convenient to study extraction efficiency by simultaneously changing few independent variables. Therefore, we pass our considerations of probability plots and two- dimensional extraction isotherms to what we call: 'the extraction landscape maps'

(shortly maps). These maps will provide us with a perspective of global behavior of liquid-liquid extraction by identifying various regimes in extraction and the self-assembly behind it. By the end of the chapter, we will be able to distinguish different regime, quantify extraction of corresponding solutes, and to (at least on a primitive level) provide chemical engineering with the insights into more adequate liquid-liquid extraction formulation design.

In previous section, which was more of a -proof-of-concept that the Droplet model works for acidic extractants, we have made a solutes and HDEHP speciation study as a function of the change of one independent system variable, while other were kept constant. In this section, we we go further and will presented results of the extraction of all solutes and HDEHP speciation while changing simultaneously two independent system variables and keeping third one constant.

5.8.1 Acid and Extractant influence

We start by studying the speciation in terms of $c_{\mathrm{LH,initial}}$, and $m(\mathrm{HNO_3})_{\mathrm{aq,eq}}$ for fixed $m(\mathrm{Eu^{3+}})_{\mathrm{eq,aq}}$. When $c_{\mathrm{LH,initial}}$ is below CAC, the extraction is low. $\mathrm{Eu^{3+}}$ extraction increases while increasing $c_{\mathrm{LH,initial}}$ and keeping low acidity in the reservoir. At high $c_{\mathrm{LH,initial}}$ and very low $m(\mathrm{HNO_3})_{\mathrm{aq,eq}}$, $\mathrm{Eu^{3+}}$ extraction increases significantly. Just identifying extraction regimes, does not directly provide insight into self-assembly. A complementary graphs of extraction speciation for the same system conditions (Figures 5.17a-d) reveal that in high $\mathrm{Eu^{3+}}$ extraction the aggregation is also at maximum, and free extractant (monomers + dimers) are very low. This is understandable since we already stated that 6 HDEHP is needed to assemble $\mathrm{Eu^{3+}}$-filed aggregate.

There is another regime identified and it occurs at high $c_{\mathrm{LH,initial}}$ and $m(\mathrm{HNO_3})_{\mathrm{aq,eq}}$. $\mathrm{Eu^{3+}}$ extraction is completely diminished due to the blocking acid effect, but once $m(\mathrm{HNO_3})_{\mathrm{aq,eq}}$ is sufficiently high, $\mathrm{HNO_3}$ accompanied with $\mathrm{H_2O}$ coextraction. Even though HDEHP does not readily extract acid, when the aqueous phase is extremely saturated, the self-assembly will occur. This is also demonstrated in Figures 5.17a-d.

At two extremes of phase diagram (low and high acid molalities), there is a solutes-induced self-assembly. But what happens in the intermediate cases. The situation is especially interesting around a so-called 'working point' in industrial applications[9]. A local maximum of the dimerized and monomeric extractant concentrations (or a local minimum in terms of the aggregated HDEHP), as can be observed in Figures 5.17a-d, occurs around $m(\mathrm{HNO_3})_{\mathrm{aq,eq}} = 1.5$ mol $\mathrm{kg^{-1}}$ for high $c_{\mathrm{LH,monomeric}}$. The solutes speciation maps give information that that region and it corresponds to quenched $\mathrm{Eu^{3+}}$ extraction. There is slight pure $\mathrm{HNO_3}$ extraction but in insuf-

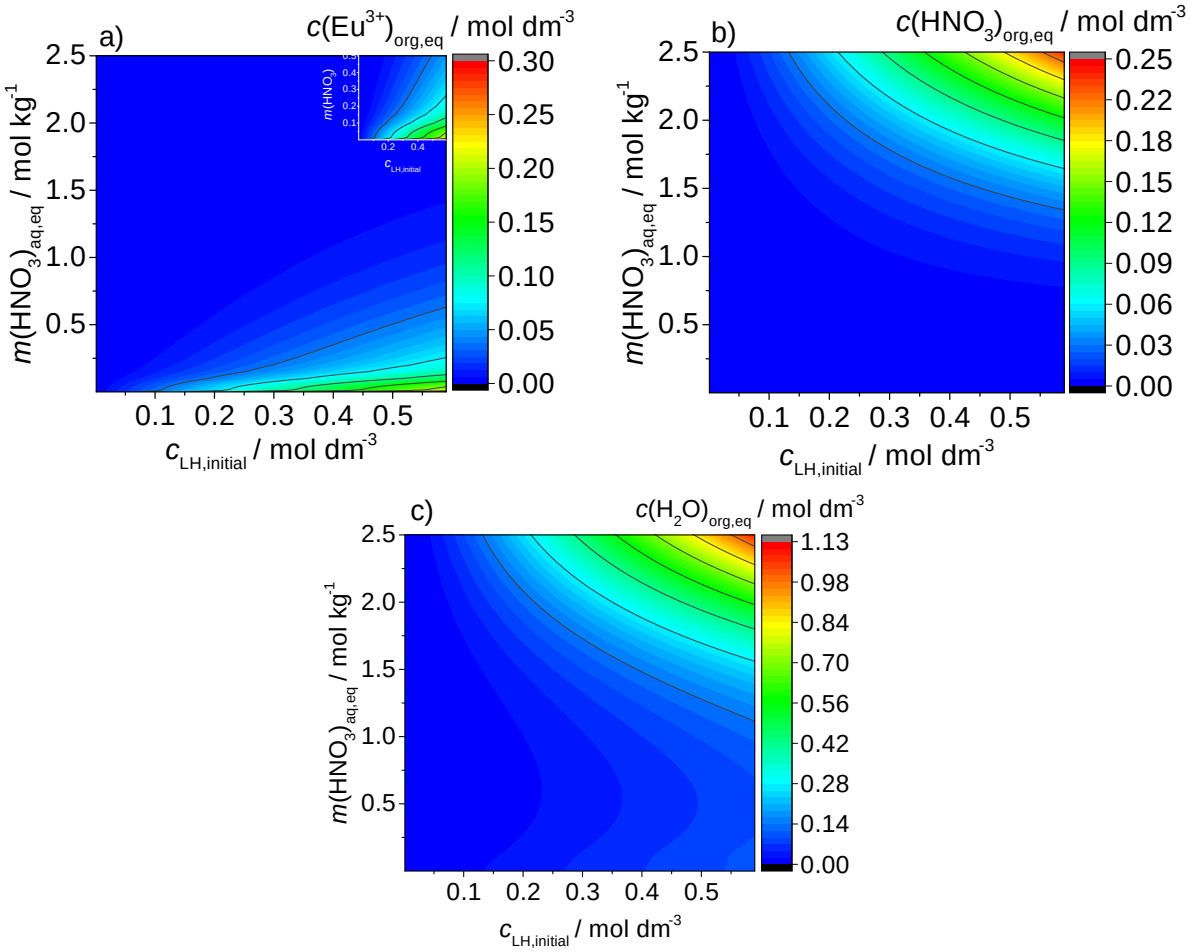

Figure 5.16 – Maps of extracted solutes concentrations in the organic phase as a function of $m(HNO_3)_{aq,eq}$ in the aqueous phase and the initial extractant concentration $c_{LH,initial}$, for $m(Eu^{3+})_{eq,aq} = 0.032$ mol kg^{-1}. a) corresponds to Eu^{3+} extraction, b) to HNO_3 extraction, and c) to H_2O extraction. The inset in figure a) shows enlarged region of the pronounced Eu^{3+} extraction.

ficient to induce the aggregation. A slight decrease of $m(HNO_3)_{aq,eq}$ increases Eu^{3+} extraction but cuts the acid uptake. The aggregation is still weak, and monomers and dimers dominate the organic phase. This is indeed a good solution for the chemical engineering since the Eu^{3+} extraction is non-negligible, but is far from irreversible character (at very low $m(HNO_3)_{aq,eq}$), and the expected viscosity of the organic phase should be modest since the self-assembly is in the weak regime and no large structures can be formed.

5.8.2 Acid and Europium Nitrate Influence

Next thing to study is the speciation in terms of $m(Eu^{3+})_{eq,aq}$, and $m(HNO_3)_{aq,eq}$ for fixed $c_{LH,initial}$. This study is far more important since for fixed $c_{LH,initial}$ we can go ahead and

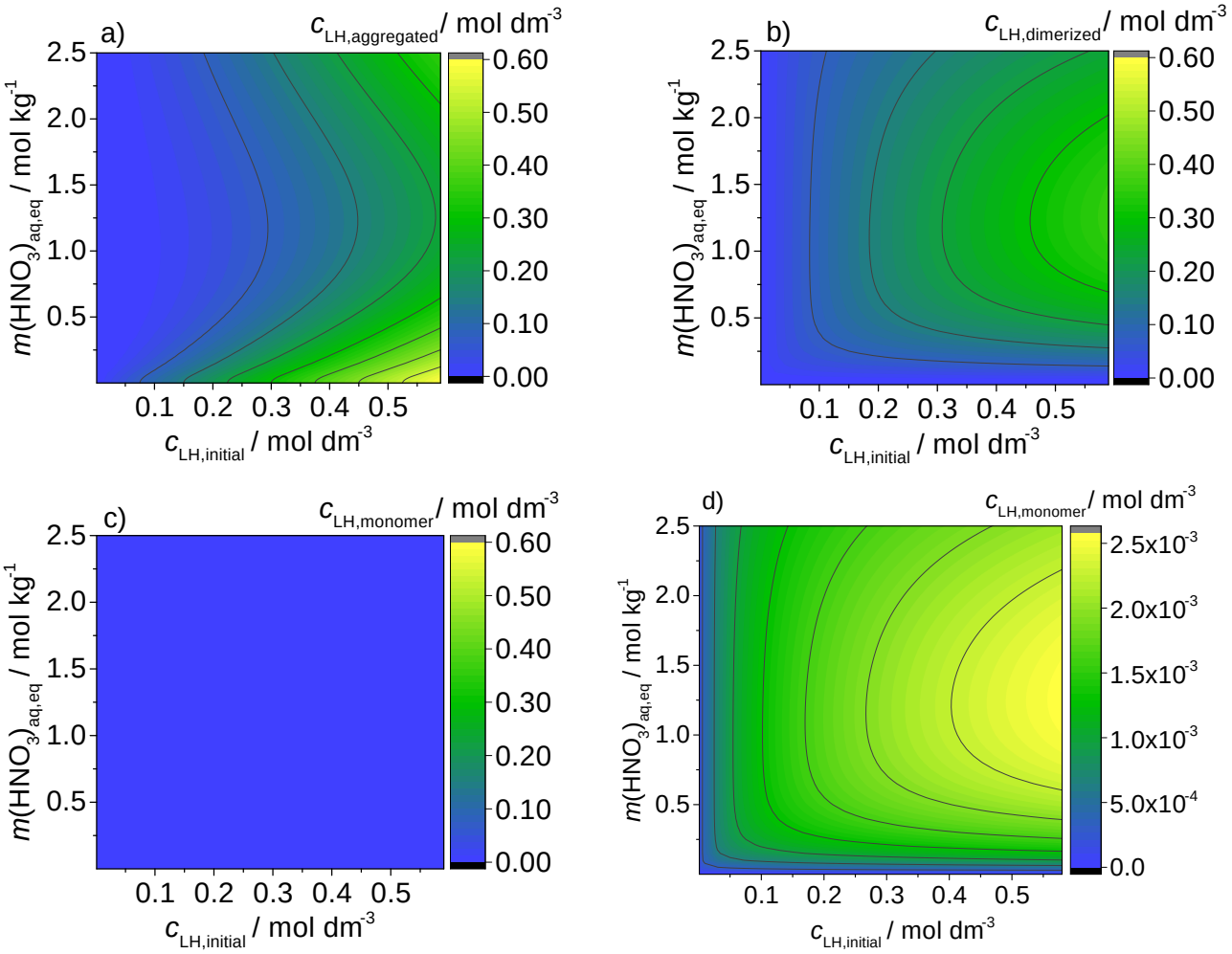

Figure 5.17 – Speciation maps of the extractant in the solvent as a function of $m(\mathrm{HNO_3})_{\mathrm{aq,eq}}$ and $c_{\mathrm{LH,monomeric}}$ in the solvent for $m(\mathrm{Eu^{3+}})_{\mathrm{eq,aq}} = 0.032$ mol kg^{-1}. a) aggregated extractant, b) dimerized, c) monomeric, d) equivalent to c), but scale is adjusted so that differences in $c_{\mathrm{LH,monomer}}$ can be clearly seen.

calculate CAC for each composition of the system. Figures 5.18a-c show respectively, the extraction maps of $\mathrm{Eu^{3+}}$, $\mathrm{HNO_3}$, and $\mathrm{H_2O}$, whereas Figure 5.18d shows a map of CAC. It can be seen in Figure 5.18a that a high $\mathrm{Eu^{3+}}$ extraction corresponds to $m(\mathrm{HNO_3})_{\mathrm{aq,eq}}$ lower than 1.5 mol kg^{-1}. A higher $m(\mathrm{HNO_3})_{\mathrm{aq,eq}}$ completely blocks $\mathrm{Eu^{3+}}$ extraction. The blocking $\mathrm{HNO_3}$ effect can be partially compensated with the increase of $m(\mathrm{Eu^{3+}})_{\mathrm{aq,eq}}$, as can be seen by broadening of $\mathrm{Eu^{3+}}$ extraction region (a pale blue color). This is a first major difference that is hard to detect by plotting a series of 2D graphs. By increasing the chemical potential of $\mathrm{Eu^{3+}}$, we can increase a working range in terms of $m(\mathrm{HNO_3})_{\mathrm{aq,eq}}$. Calculations also predict that high $\mathrm{Eu^{3+}}$ extraction region is accompanied by small $\mathrm{H_2O}$ uptake and $\mathrm{HNO_3}$ extraction (Blue region in Figures 5.18b-c). Yet, when $m(\mathrm{HNO_3})_{\mathrm{aq,eq}}$ is sufficiently high (after 1.5 mol kg^{-1}) the acid extraction takes hold. Consequently, a water uptake increases. Practically, it

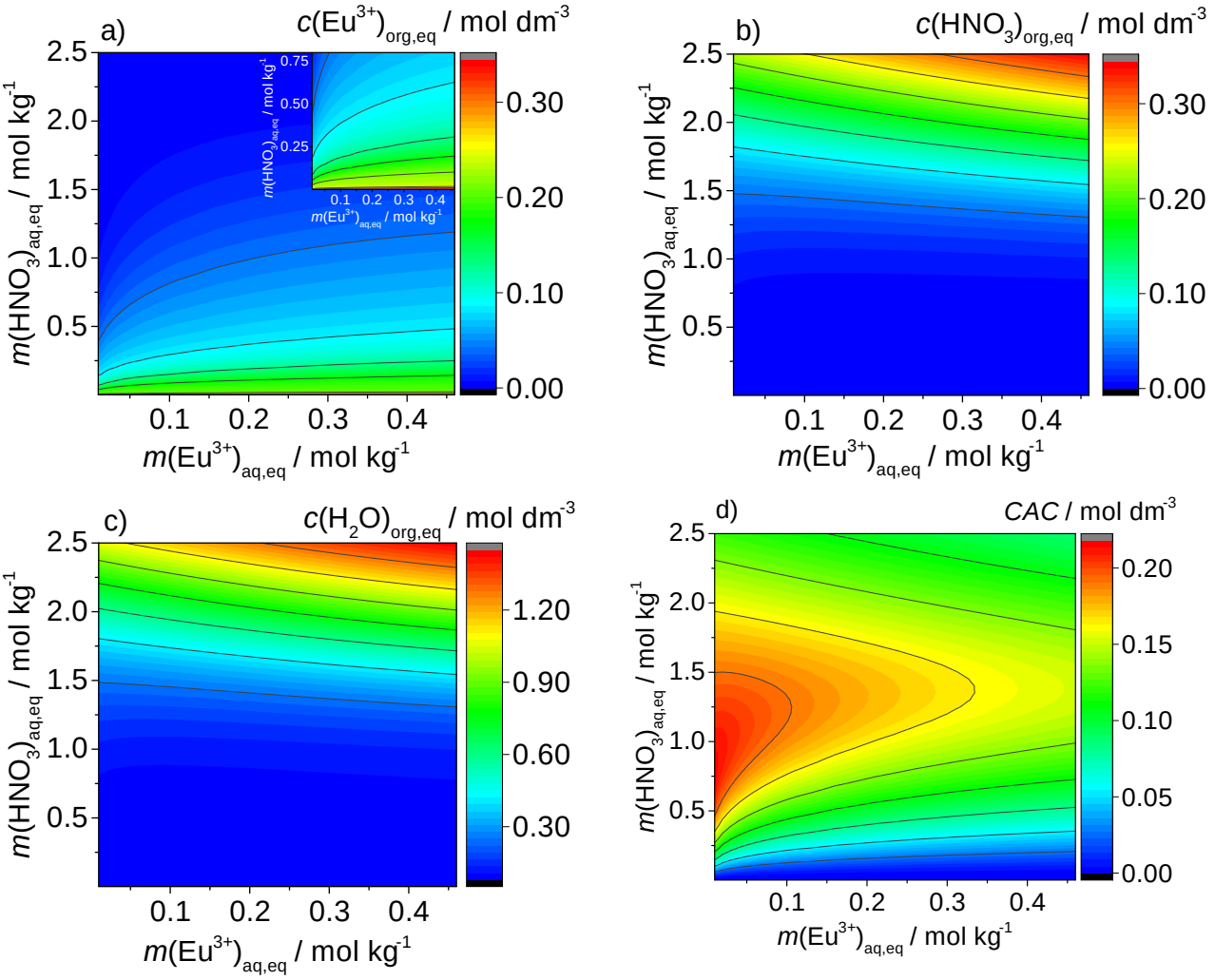

Figure 5.18 – Organic phase concentrations of extracted solutes (a-c) and CAC maps (d) in the solvent phase as a function $m(\mathrm{Eu}^{3+})_{\mathrm{aq,eq}}$ and $m(\mathrm{HNO_3})_{\mathrm{aq,eq}}$ for $c_{\mathrm{LH,initial}} = 0.6$ mol dm^{-3}. The inset in Figure a) shows enlarged region of the pronounced Eu^{3+} extraction.

means that the extractant is consumed not to extract the target cation, but is spent on the pure acid extraction. This can also be observed in HDEHP speciation maps in Figure 5.19, where aggregated extractant concentration increases, while dimers and monomers concentration decreases. This case obviously represents an undesired industrial formulation. In the case when both $m(\mathrm{HNO_3})_{\mathrm{aq,eq}}$ and $m(\mathrm{Eu}^{3+})_{\mathrm{aq,eq}}$ are high (right upper corners of extraction maps) $\mathrm{HNO_3}$ extraction is even more pronounced. At those conditions we have saturated aqueous phase with salts. Therefore chemical equilibrium is shifted towards the relaxation in terms of $\mathrm{HNO_3}$ transfer to the solvent (since Eu^{3+} extraction is impossible due to the high $m(\mathrm{HNO_3})_{\mathrm{aq,eq}}$). The water uptake (Figure 5.18c) follows the same trend to stabilize the core of the aggregates with multiple $\mathrm{HNO_3}$ present inside. It is worth to emphasize that water content around working point ($m(\mathrm{HNO_3})_{\mathrm{aq,eq}} \approx 1$ mol kg^{-1}, $m(\mathrm{Eu}^{3+})_{\mathrm{aq,eq}} \approx 0.05$ mol kg^{-1}) stays globally constant up

to moderate $m(HNO_3)_{aq,eq}$ level. Upon the additional increase of $m(HNO_3)_{aq,eq}$, an abrupt water co-extraction occurs. It must be emphasized that our model overestimates H_2O and HNO_3 extraction, but the order of magnitude is correct. This is a consequence of the fact that we neglected activity correction in the aqueous phase, which means that within the model, these issues can be easily solved. Also, Eu^{3+} extraction at very low $m(HNO_3)_{aq,eq}$ shows abrupt increase. We have traced the issue down to the error of the V_{core} calculation where we have neglected partial molar volume of Eu^{3+}. By doing so, we diminished the energy penalty F_{chain}, upon swelling the aggregate core. This can also be solved by taking tabulated values of molar volumes of mixed salts at finite concentration, but then the method loses a part of its generality. With drawback of the model emphasized, we must add that around working point of the industrial processes, the model shows remarkable prediction power and results are in the agreement with experimental data (as was seen from the previous section). These drawbacks appear only at the borderlines of the phase diagram, where we cannot even apply the model of the spherical micelles.

When it comes to the design of a desired reversible formulation, a knowledge of the aggregation behavior is crucial since it affects other properties important for industrial applications such as viscosity. In that sense, we have studied CAC dependence of the composition of the system (Figure 5.18d). Note that this graph is complementary to graphs in Figure 5.19. While inspecting Figure 5.18d it can be seen that the aggregation (regions of lower CAC) is controlled by two different competition reactions *i.e.* Eu^{3+} extraction at low $m(HNO_3)_{aq,eq}$ and pure HNO_3 extraction at high $m(HNO_3)_{aq,eq}$. Around the working point CAC landscape has a shape of a hill with slopes descending towards Eu^{3+} and HNO_3 extraction regions. "The CAC hill" (*i.e.* the minimum of the aggregation) corresponds to the case of poor Eu^{3+} extraction due to the presence of HNO_3, but HNO_3 concentration itself is not high enough to induce the aggregation by the pure acid extraction. This region of high CAC is manageable and therefore appropriate in the industry since it should correspond to the formulation of a moderate viscosity. The last thing to note here is that at high $m(Eu^{3+})_{aq,eq}$ and low $m(HNO_3)_{aq,eq}$ CAC is order of magnitude on a milimolar scale (the blue region in Figure 5.19d). This means that we have saturated completely the extractant and we are in the danger of the third phase formation. A question also arises here, with this being thermodynamically strongly favored extraction, how effective will be the stripping in the next stage of the cation recovery? Indeed, it was this issue that induced a development of the less efficient HDEHP extractant analogues[5].

Our model predicts that the design of the most appropriate extraction formulation would correspond to region between $m(HNO_3)_{aq,eq} \approx 0.5$ and 1 mol kg^{-1} and $m(Eu^{3+})_{aq,eq} \approx 0.1$ and

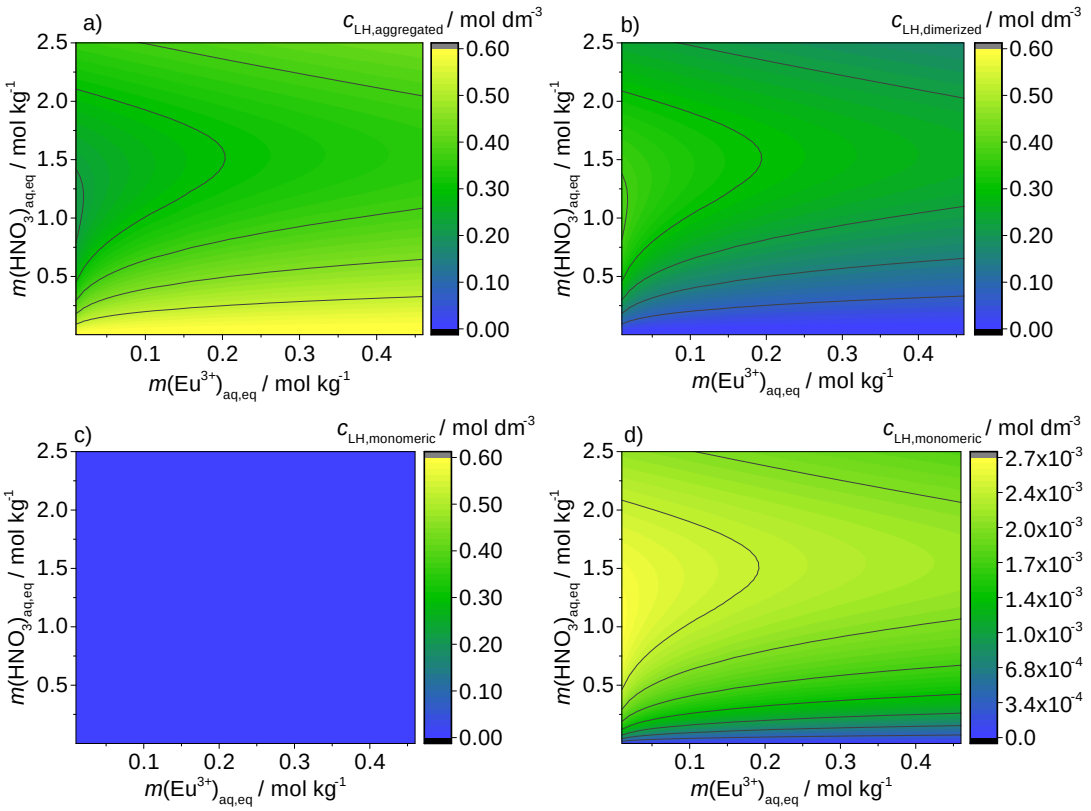

Figure 5.19 – Extractant speciation in the organic phase as a function of $m(\mathrm{Eu}^{3+})_{\mathrm{aq,eq}}$ and $m(\mathrm{HNO_3})_{\mathrm{aq,eq}}$ for $c_{\mathrm{LH,initial}} = 0.6$ mol dm^{-3}. Figures a-c) show respectively concentrations at equilibrium of aggregated, dimerized and monomeric form of the extractant in the solvent. Figure d) is equivalent to figure c), but scale is adjusted so that differences in $c_{\mathrm{LH,monomeric}}$ can be clearly seen.

0.2 mol kg^{-1}. Such formulations would have a reversible extraction character, while exhibit moderate viscosity and no danger to the third phase formation *i.e.* around half of the extractant is in form of dimers and not in fully aggregated form (see Figure 5.19a-d).

5.9 Complexation Energy and Formulation Design

In the previous section, we have discussed the efficiency of the extraction and the aggregation with the respect to concentrations of all constituents. Yet, we did not comment on the choice of the extractant molecule itself.

Within the model, the interaction between the extracted cation and the particular extractant molecule is described by the adjusted parameter $E_{Eu^{3+},LH}$. It reflects the affinity of the extractant molecule towards the target cation. Therefore, every cation/extractant molecule pair has its associated $E_{Eu^{3+},LH}$. If we set $E_{Eu^{3+},LH}$ as a continuous variable, then we can artificially represent different types of the possible extractants for the design of the extraction formulation. Figure 5.20 shows the negative value of the natural logarithm of the Eu^{3+} distribution coefficient, $-\ln D_{Eu^{3+}}$ as a function of the negative value of the complexation parameter per cation/extractant bond $-E_{Eu^{3+},LH}$ for three different $m(HNO_3)_{aq,eq}$, at $m(Eu^{3+})_{aq,eq} = 0.05$ mol kg^{-1} and $c_{LH,initial} = 0.6$ mol dm^{-3}. The negative values of $E_{Eu^{3+},LH}$ are taken for the purpose of visually easier understanding of the context. As we wrote in the previous section $-\ln D_{Eu^{3+}}$ is historically referred to as the apparent energy of the transfer of the cation between two phases. Results show two distinct regimes for any concentration of $m(HNO_3)_{aq,eq}$. At low $-E_{Eu^{3+},LH}$ (which which represents highly favorable interaction between extractant and cation) the apparent energy of transfer is constant. This regime corresponds to the complete saturation of the extractant *i.e.* the saturation threshold. It shows that practically we do not need to use a stronger complexing agent (the extractant) in order to improve the efficiency of the extraction. The limit of the extraction is given by the $m(Eu^{3+})_{aq,eq}$ to $c_{LH,initial}$ ratio[171]. For higher $-E_{Eu^{3+},LH}$ values (the lower affinity of the extractant to cation) the apparent energy of transfer increases, which means that these types of extractants will be less efficient for the extraction formulation design. Now if we change $m(HNO_3)_{aq,eq}$ in the system, results show that the saturation threshold will occur at lower $-E_{Eu^{3+},LH}$ for higher $m(HNO_3)_{aq,eq}$ in the aqueous phase (the lower pH). By decreasing $m(HNO_3)_{aq,eq}$, the saturation threshold occurs at higher $-E_{Eu^{3+},LH}$. These results are the consequence of the $pK_a^\circ - pH$ term which gives a distinct functionality of extraction isotherms. Note that weak extraction regimes of all three curves are equidistant after the saturation threshold (the curves are separated by the factor

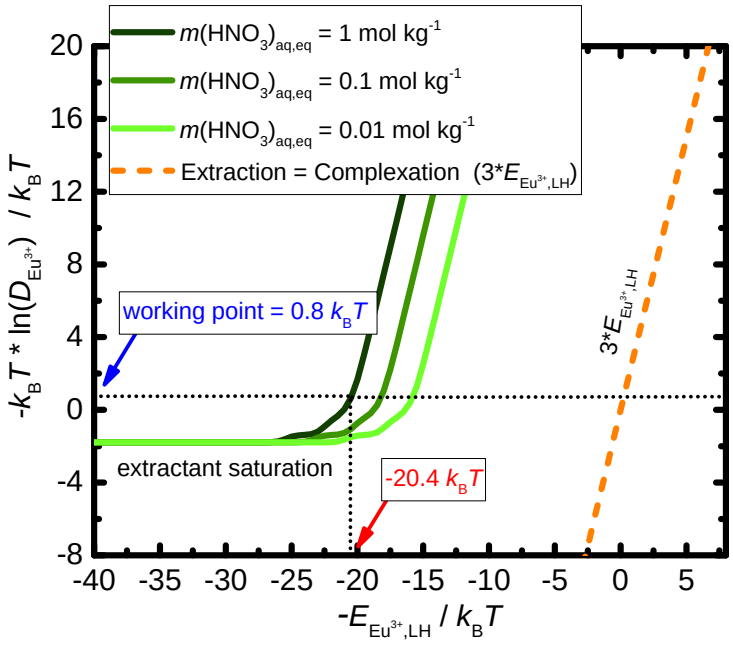

Figure 5.20 – The apparent energy of Eu^{3+} transfer as a function of the negative value of the complexation energy parameter per bond, $-E_{Eu^{3+},LH}$. The negative values of $E_{Eu^{3+},LH}$ are taken for the purpose of visually easier reading of the saturation limit. Results for various $m(HNO_3)_{aq,eq}$ are presented at $m(Eu^{3+})_{aq,eq} = 0.05$ mol kg^{-1} and $c_{LH,initial} = 0.6$ mol dm^{-3}. The dashed orange line represents the assumption that the apparent energy of transfer is equal to the total complexation energy in the aggregate.

$-N_L \cdot \ln(10)(pK_a^\circ - pH)$). A strong influence of $m(HNO_3)_{aq,eq}$ on the apparent energy of the transfer the gives the chemical engineering more liberty in the design of the extraction formulation. If the goal is to extract the same amount of Eu^{3+} like around working point, one can use a less efficient extractant (characterized by higher $-E_{Eu^{3+},LH}$ values) at the higher pH in the aqueous phase.

Examining results in Figure 5.20 reveals another important aspect of the aggregation phenomena leading the extraction of cations to the solvent. We have already stated that the extraction is sometimes identified as the complexation of the cation by the chelating agent, where the chelating agent represents the extractant molecule. In that representation, the apparent energy of transfer corresponds to the difference between the energy of similar complex (cation and chelating agents) and the hydration energy of cation in the aqueous phase (the first sphere interactions in both examples). If the extraction can be identified as the simplified picture of the complexation only, then the calculated apparent energy would correspond to the dashed orange line in Figure 5.20. The line has a value of 3 times $-E_{Eu^{3+},LH}$, since the

mentioned assumption deals only with the total complexation energy (note that x-axis values are in $-E_{\mathrm{Eu^{3+},LH}}$ per bond). The intersection of the dashed orange line with the horizontal dotted black line represents the extraction around working point in the chemical engineering and it corresponds to $-E_{\mathrm{Eu^{3+},LH}}$ less then $k_{\mathrm{B}}T$ per the extractant/cation bond. Such a small excess first sphere interaction energy between Eu^{3+} and dissociated HDEHP head group cannot account for the transfer of cation to the solvent phase. It would completely neglect any colloidal aspect, the self-assembly, or the influence of the organic solvent. Moreover, it would imply that the energy of first sphere around multivalent cation which includes 3 charged ligands (plus uncharged ligands and water molecules) is almost equal to the hydration energy of the multivalent cation.

As we have emphasized throughout the article that the system in study shows a complexity of extraction regimes. Therefore, we calculated complementary maps of the apparent energy of transfer as a function of $m(\mathrm{Eu^{3+}})_{\mathrm{aq,eq}}$ and $-E_{\mathrm{Eu^{3+},LH}}$ for three $m(\mathrm{HNO_3})_{\mathrm{aq,eq}}$. Results are presented in Figures 5.21a-c. The white dashed region on the maps depicts extraction efficiency which is equal to the extraction efficiency reported in reference experimental data (on which we based our fitting). The low $-E_{\mathrm{Eu^{3+},LH}}$ and $m(\mathrm{Eu^{3+}})_{\mathrm{aq,eq}}$ region corresponds to the extractant saturation threshold, as can be seen as a dark blue plateau for any $m(\mathrm{HNO_3})_{\mathrm{aq,eq}}$. After the working point region, the steep increase in the apparent energy of transfer occurs (as was demonstrated also in Figure 5.20). Results again show that $m(\mathrm{HNO_3})_{\mathrm{aq,eq}}$ has a pronounced effect on choice of $-E_{\mathrm{Eu^{3+},LH}}$ in order to achieve the extraction efficiency of the working point. By decreasing $m(\mathrm{HNO_3})_{\mathrm{aq,eq}}$ the higher $-E_{\mathrm{Eu^{3+},LH}}$ values (a weaker extractant) are sufficient for the reversible formulation. Another aspect observed in Figures 5.21a-c is worth to comment. The dotted rectangle enclosing the whited dashed is given as a guideline. It must be emphasized that the working point region broadens upon the increase of $m(\mathrm{HNO_3})_{\mathrm{aq,eq}}$. We have already shown throughout the article that those conditions correspond to the flat top of the aggregation 'the hill'. This gives the chemical engineering even more liberty in the design of the extraction process.

Naturally, we made a map of the apparent energy of transfer as a function of $m(\mathrm{HNO_3})_{\mathrm{aq,eq}}$ and $-E_{\mathrm{Eu^{3+},LH}}$. Results are presented in Figure 5.22. Once again results reflect the complexity of extraction systems since we have multiple solutions in the design of the extraction formulation just by changing the concentration of the acid.

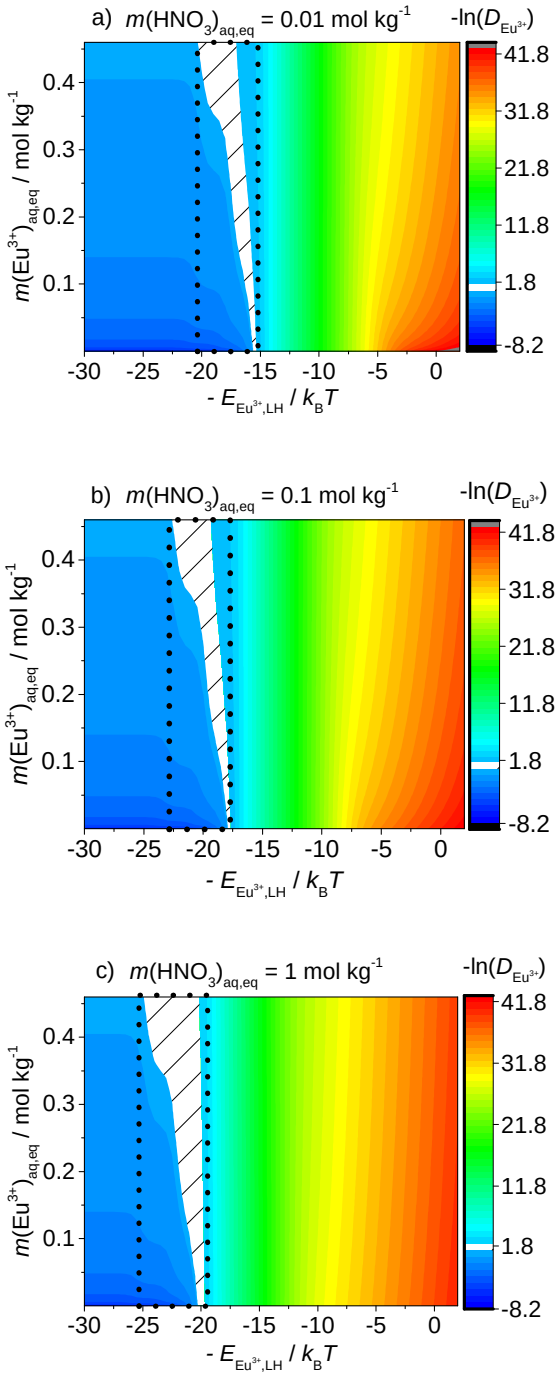

Figure 5.21 – Negative value of natural logarithm of the Eu^{3+} distribution coefficient, $-\ln D_{Eu^{3+}}$ as a function of $-E_{Eu^{3+},LH}$ and $m(Eu^{3+})_{aq,eq}$. Results are presented for various $m(HNO_3)_{aq,eq}$ (figures a-b) for $c_{LH,initial} = 0.6$ mol dm^{-3}. A white region depicts reference experimental data. The dotted rectangle enclosing the white region is given as a guideline to depict its broadness.

Elucidating the observed free energy of transfer

In our approach of the aggregate free energy calculation and completing the MAL afterward, the calculated apparent free energy of transfer corresponds to the interplay of the energy contributions. The leading complexation energy term (characterized by $E_{Eu^{3+},LH}$) shifts the equilibrium

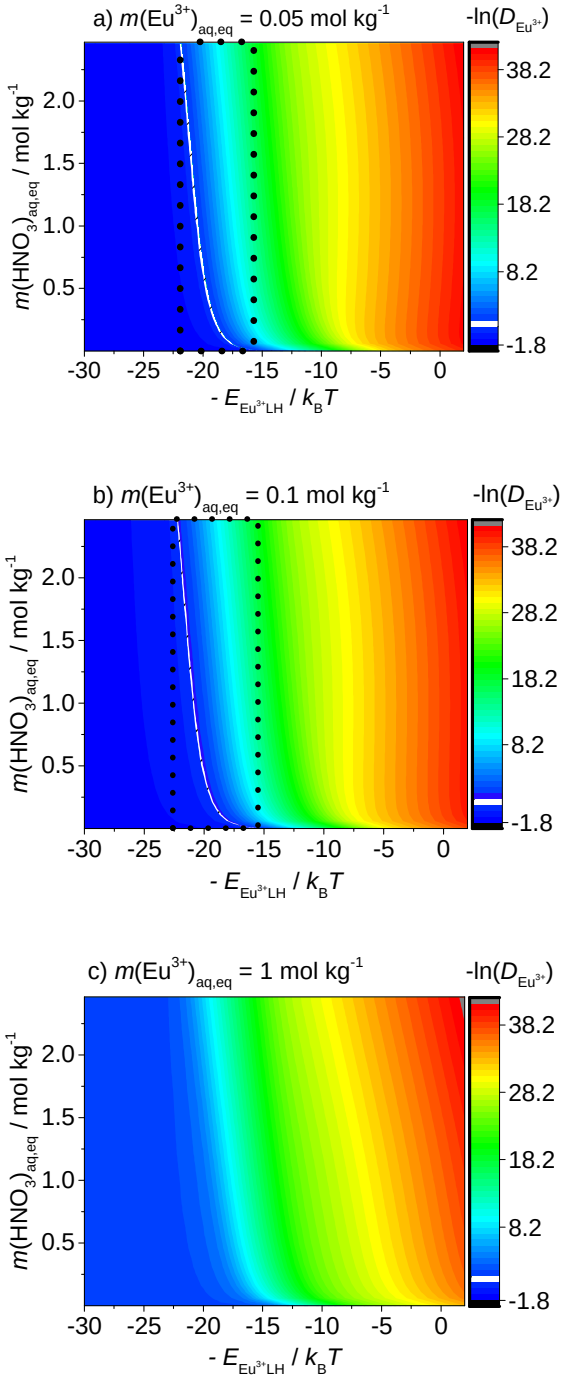

Figure 5.22 – Negative value of natural logarithm of the Eu^{3+} distribution coefficient, $-\ln D_{Eu^{3+}}$ as a function of $E_{Eu^{3+},LH}$ and $m(HNO_3)_{aq,eq}$. Results are presented for various $m(Eu^{3+})_{aq,eq}$ for $c_{LH,initial}$ = 0.6 mol dm^{-3}. A white region depicts reference experimental data.

towards the extraction of cation to the solvent but is counterbalanced by few terms. Terms like the energy penalty for the formation of the highly curved film of the extractant chains F_{chain} (Eq. 5.5), lateral head group repulsions in the extractant film $F_{extr.head}$ (Eq. 5.7), differences in ions and water molecules accessible volumes between the core of the aggregates and the aqueous phase, the difference between between an effective pK_a° and low pH are opposing the complexa-

tion, or the competing HDEHP dimerization. The sum of all contributions yields the apparent energy of transfer (dotted black line). The apparent energy of transfer for any $m(HNO_3)_{aq,eq}$ is far from the assumption Extraction = Complexation (dashed orange line in Figure 5.20). Once $-E_{Eu^{3+},LH}$ is high enough and unable to push the equilibrium towards the solvent phase with the respect to opposing quenching terms, the slope of the calculated apparent energy of transfer is equal to the dashed orange line. This is the regime of the weak extraction no longer interesting for the chemical engineering.

5.10 Conclusion

We have extended the Droplet model to predict the extraction efficiency using acidic extractants *e.g.* HDEHP. Moreover, we used the model to gain new insights in colloidal self-assembly phenomenon behind the extraction.

Additional terms included in this extension of the model were: the extractant head groups repulsions, the competing HDEHP dimerization, and the effect of reservoir pH given as a differences between an effective pK_a° and the reservoir pH. Extractant head groups repulsions and competing dimerization work in a way to quench the extraction. Low pH also quenches the extraction, while high pH values favor extractant dissociation and thus the extraction via complexation. A dominant term called the complexation energy is always favorable (by definition) and it sets the equilibrium towards the transfer of ions from the aqueous solution towards the oil phase. A small overall change of the free energy of the system upon the extraction of the ion between two phases (order of few k_BT or even less) is a consequence of the interplay of described forces. This interplay of the forces governs the reversibility of extraction systems and indeed allows them to be referred as a 'weak self-assembly'.

Obtained parameters for *n*-dodecane with HDEHP in contact to $Eu(NO_3)_3$ and HNO_3 aqueous solution system are: the standard chemical potential of HDEHP in dodecane $\mu^\circ_{LH} = 12.8$ kJ mol^{-1}, the generalized bending constant $\kappa^\star_{LH} = 14\ k_BT$, the spontaneous packing parameter for H_2O and HNO_3 $p_0 = 2.6$, the complexation energy for acid $E_{H^+,LH} = 4.2\ k_BT$, the spontaneous packing parameter of the dissociated extractant in the film $p_{0,Eu^{3+},LH} = 3.5$, the complexation energy of europium cation $E_{Eu^{3+},LH} = 20.4\ k_BT$ per bond, and the interaction between dissociated and undissociated extractant head groups $\chi_{LH,L^-} = 0.5\ k_BT$. It must be noted that χ_{LH,L^-} can be omitted from the calculation since we have shown that the free energy associated with lateral interactions of distinguishable head groups in the film are globally small compared to the total complexation energy (around 60 k_BT). The minimum aggregation

numbers found in our study correspond to 4 for aggregates cores filled with only H_2O and HNO_3, whereas the minimum aggregation number is 6 for cores containing at least one Eu^{3+}.

Furthermore, we used the model to study the speciation of the extractant in the solvent phase. Results show that the monomeric extractant concentration is globally small compared to the aggregated and the dimerized extractant. Both acid and metal cation concentrations in the aqueous phase exhibit a strong influence on the aggregation behavior. The low acid and the high metal concentrations in the aqueous phase favor the aggregation at the expense of the reduced dimer concentration.

The model predicts that the addition of the acid in the system diminishes the aggregation and quenches the extraction of metal cations. For sufficiently high acid concentration, the aggregation is again induced by the pure acid extraction. Our study also predicts the Langmuir-like isotherms for the extraction dependence on the concentration of cation in the aqueous phase as well as the fact that the apparent stoichiometry is not constant. It was quantitatively shown that the apparent stoichiometry depends on concentrations of all constituents of the system and that our model can be used to obtain the correct aggregation numbers of a given system of highly hydrophilic extractants.

Observed high complexity of the extraction system forced a change in the representation of results form traditional extraction isotherms to extraction and aggregation 'maps'. Such multidimensional representation allows us to trace and quantify different regimes in both the extraction of all solutes present, as well as the aggregation and the speciation of the extractant in the system. The Figure 5.18d is the central figure of this chapter. It directly shows how liquid-liquid extraction is complex, while at the same instant it provides a simple explanation for observed complexity, based on the competition of chemical reactions. It also reveals the detail concerning the speciation of the organic phase, which is the key for viscosity determination.

Calculations show that the choice of the extractant also matters, as was reflected in the complexation energy study. A lower pH in the aqueous phase demands the extractant with the higher affinity towards the target cation to balance the energy penalty for dissociation of the extractant in the media of the high acidity.

General behavior of HDEHP

HDEHP as a part of class of acidic ion exchange extractants, does not favor high dilution in the core of the aggregate. HDEHP is characterized by the strong dependency of the reservoir pH. With contrast to the non-ionic extractants the overall extraction efficiency increases with

the decrease in acid concentration in the system. Another major difference compared to DMDOHEMA is the fact that HDEHP can extract (quite moderately though) even before CAC. Similarly to non-ionic extractant, but now even more pronounced, the acidic extractants display their amphiphilic nature by self-assembling into organized structures. This is the consequence of the high energy associated in maintaining the single high dipole moment head group (in HDEHP case it is phosphate group) in apolar medium, without any association.

Chapter 6

Modelling of Liquid-Liquid Extraction: a Case of Synergistic Mixtures

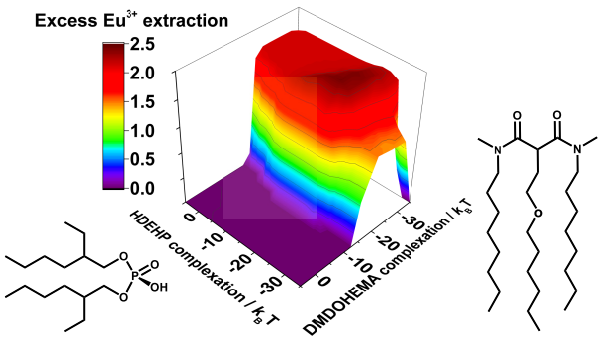

Figure 6.1 – Modelling liquid-liquid extraction: mixtures of extractants

Droplet model was generalized to account the mixtures of non-ionic and acidic extractants showing synergistic character. It is based on establishing the free energy contributions of the spherical aggregate formation in the organic phase. Results show that contrary to the current paradigm of simple stoichiometry behind liquid-liquid extraction, there is a severe polydispersity of aggregates completely different in compositions, but similar in the free energy. The change of the system variables governs the self-assembly to the set of possible aggregates mutually competing to achieve equilibrium. Mapping the polydispersity of self-assembled aggregates helped to rationalize the fraction of the synergy peak in metal cation extraction due to the formation of mixed and pure extractant species. The global overview of the complex nature of synergistic mixture shows different regimes in self-assembly, and thus in the extraction efficiency which can be tuned with respect to the green chemistry aspect.

6.1 Initial Remarks

The forth chapter of this thesis was devoted to establishing the colloidal thermodynamic model for spherical micelles using non-ionic extractants. We named it the Droplet model. Then in the following, fifth chapter, the Droplet model was extended to account for the specific properties of the acidic extractants. With the framework set, we can now study of the most complex system *i.e.* synergistic mixtures of extractants. Like in the previous section, the example is made on experimentally well-studied system: aqueous solution of $HNO_3/Eu(NO_3)_3$ in contact to the *n*-dodecane with dissolved DMDOHEMA, and HDEHP extractant. Throughout the following chapter we will emphasize the initial idea of the methodology: to abandon the paradigm of simple (single!) stoichiometry and to adopt polydispersity of self-assembled aggregates similar in free energy of formation that coexist at thermodynamic equilibrium.

The chapter will be organized such that in the end, it is a self-consistent unit able to be used for any multicomponent mixture of non-ionic and acidic extractants[1]. Throughout the theoretical section we will only describe the modifications and novelties needed in order to generalize the Droplet model for mixtures of extractants.

6.2 Theoretical Section: Generalization of Droplet Model to Mixtures of Extractants

The model system is the same as in previous two chapters and can be visualized using Figure 6.2. Schematic representation hints the variety of self-assembled structures that can in principle coexist at thermodynamic equilibrium. To further stress the huge number of possible equilibria needed to account for, we will provide (in contrast to previous two chapters) the chemical reaction of only major types of aggregates formation. Furthermore, each of those aggregates has its own polydispersity, as was demonstrated in detail in DMDOHEMA and HDEHP cases.

In the atempt to represent an ensemble of all possible chemical reactions that could partake in $Eu(NO_3)_3/HNO_3$ liquid-liquid extraction system[2] for the mixtures of extractants, we establish the following relation[53, 23, 9]:

$$2\overline{\mathrm{LH}} \rightleftharpoons \overline{\mathrm{LH_2}}$$

[1] With modifications, the model can be in principle used to for basic extractants also.

[2] Note that this only assumes formation of spherical aggregates and it was shown that additional higher-order morphologies can be observed by experimental techniques[217, 56].

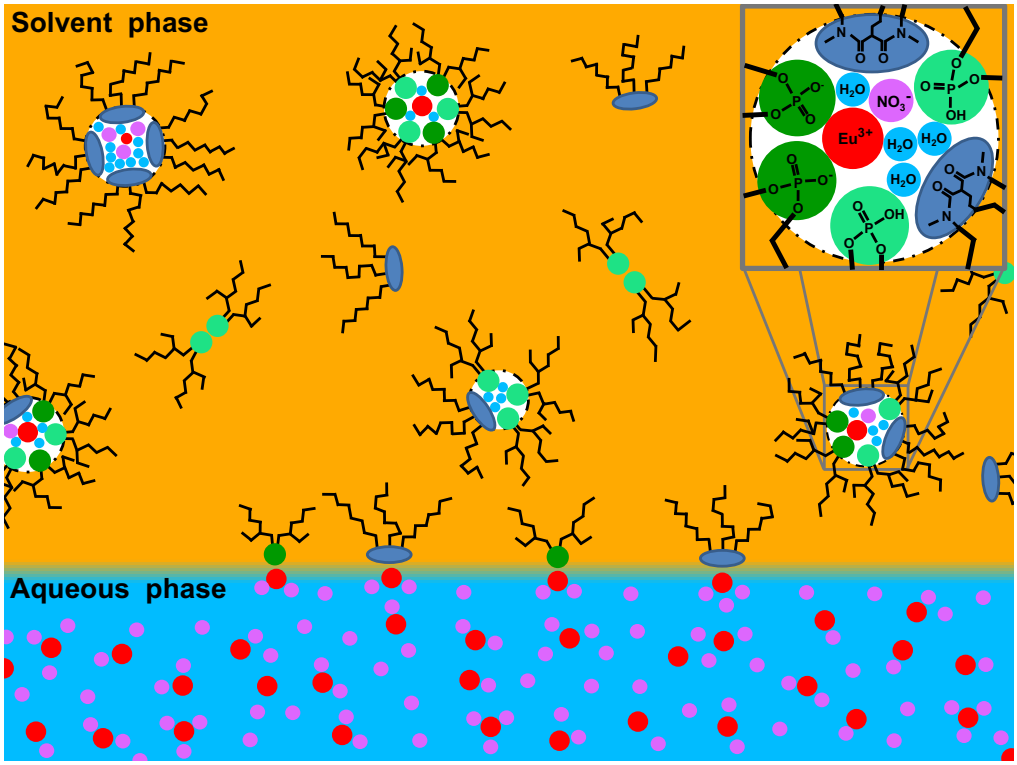

Figure 6.2 – Schematic representation of the bulk model for the liquid-liquid extraction using synergistic mixtures. Various types of aggregates are present in the organic phase (solvent phase), and their probability at equilibrium is determined by the composition of their cores and extractant film. Considering the surfactant nature of the extractant, the interface is at least partially covered by the extractant molecules (not shown here). The zoomed region shows the core of the aggregate with the europium cation (red), the nitrate anion (pink), water molecules (pale blue), and undissociated HDEHP head groups (dark green), and dissociated HDEHP head groups (pale green), and DMDOHEMA malonamide extractant head groups (dark blue). Extractant hydrophobic chains are presented in black.

$$N_{\mathrm{H_2O}} \cdot \mathrm{H_2O} + N_{\mathrm{Eu^{3+}}} \cdot \mathrm{Eu^{3+}} + N_{\mathrm{H^+}} \cdot \mathrm{H^+} + N_{\mathrm{NO_3^-}} \cdot \mathrm{NO_3^-} + N_{\mathrm{LH}} \cdot \overline{\mathrm{LH}} \rightleftharpoons \overline{\mathrm{A}_{N_{\mathrm{H_2O}};N_{\mathrm{Eu^{3+}}};N_{\mathrm{H^+}};N_{\mathrm{NO_3^-}};N_{\mathrm{L^-}};N_{\mathrm{LH,R}}}} + N_{\mathrm{L^-}} \cdot \mathrm{H^+}$$

$$N_{\mathrm{H_2O}} \cdot \mathrm{H_2O} + N_{\mathrm{Eu^{3+}}} \cdot \mathrm{Eu^{3+}} + N_{\mathrm{H^+}} \cdot \mathrm{H^+} + N_{\mathrm{NO_3^-}} \cdot \mathrm{NO_3^-} + N_{\mathrm{D}} \cdot \overline{\mathrm{D}} \rightleftharpoons \overline{\mathrm{A}_{N_{\mathrm{H_2O}};N_{\mathrm{Eu^{3+}}};N_{\mathrm{H^+}};N_{\mathrm{NO_3^-}};N_{\mathrm{D}}}}$$

$$N_{\mathrm{H_2O}} \cdot \mathrm{H_2O} + N_{\mathrm{Eu^{3+}}} \cdot \mathrm{Eu^{3+}} + N_{\mathrm{H^+}} \cdot \mathrm{H^+} + N_{\mathrm{NO_3^-}} \cdot \mathrm{NO_3^-} + N_{\mathrm{LH}} \cdot \overline{\mathrm{LH}} + N_{\mathrm{D}} \cdot \overline{\mathrm{D}} \rightleftharpoons \overline{\mathrm{A}_{N_{\mathrm{H_2O}};N_{\mathrm{Eu^{3+}}};N_{\mathrm{H^+}};N_{\mathrm{NO_3^-}};N_{\mathrm{L^-}};N_{\mathrm{LH,R}};N_{\mathrm{D}}}} + N_{\mathrm{L^-}} \cdot \mathrm{H^+} \quad (6.1)$$

where only new symbol corresponds to the mixed extractant aggregate in the organic phase

$\overline{\mathrm{A}}_{N_{\mathrm{H_2O}};N_{\mathrm{Eu^{3+}}};N_{\mathrm{H^+}};N_{\mathrm{NO_3^-}};N_{\mathrm{L^-}};N_{\mathrm{LH,R}};N_{\mathrm{D}}}$. All other symbols and stoichiometry numbers were previously defined for respectively individual DMDOHEMA and HDEHP cases. The first three chemical reaction (non-numerated) were already reported in previous chapters (Eq. 4.23, Eq. 5.1, and Eq. 5.2).

6.2.1 Free Energy of the Mixed Extractants Spherical Aggregate

To provide an analytical expression for the standard chemical potential of mixed extractants aggregates, we need to generalize expressions F_{complex}, F_{chain}, and $F_{\mathrm{extr.head}}$. Expressions F_{droplet} and $F_{\mathrm{correction}}$ are the same as before.

Generalized form of F_{complex}

Generalized complexation free energy contribution reads

$$F_{\mathrm{complex}} = -k_{\mathrm{B}}T \ln N_{\mathrm{complex}} - \sum_{z}\sum_{i} N_{i,z} N_{\mathrm{bond},i,z} E_{i,z} \tag{6.2}$$

where N_{complex} is number of microstates associated with the binding of cations to the 2D array of sites in case of mixtures[3], $N_{i,z}$ is the number of particular cations i in the core bonded to extractant type z, $N_{\mathrm{bond},i,z}$ is the number of sites of type z extractant that bonded particular cations take up, $E_{i,z}$ is the internal complexation energy parameter and represents the energy contribution for each bond created between cation and extractant head groups. It is adjusted parameter (fitting procedure is described in later in the text). Index z accounts for different extractant head groups. Since in oure case we are dealing with HDEHP and DMDOHEMA mixed aggregates, it follows that $z = 2$. In the case of Eu^{3+}, the number of HDEHP sites bonded per one cation can be from 1 to 3 *i.e.* $N_{\mathrm{bond,Eu^{3+},LH}} \in [1, 3]$, whereas for DMDOHEMA we can have maximum of two sites per cation *i.e.* $N_{\mathrm{bond,Eu^{3+},D}} \in [1, 2]$. For the acid (the proton), we have occupancy of only one site, $N_{\mathrm{bond,H^+,D}} = N_{\mathrm{bond,H^+,D}} = 1$[43, 34, 218, 37]. The imposed condition is given by the composition of the first coordination sphere, taken from quantum chemistry calculations[37]. Practically, it means that due to the steric constraints, we cannot violate the maximum coordination of the cation with its first-sphere ligands. Schematic representations of cation binding to multisite 2D plane was illustrated in Figure 6.3. We propose a general formula to calculate the number of microstates associated with binding of different

[3]In single mixed DMDOHEMA/HDEHP mixed aggregate, upon complexation of Eu^{3+} and dissociation of HDEHP we have three different sites.

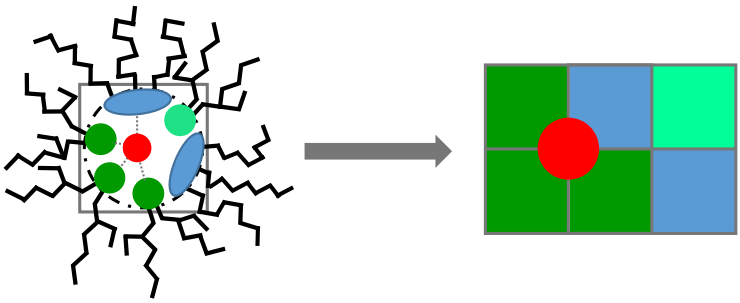

Figure 6.3 – Schematic representation of the calculation of the number of microstates (the entropy) associated with the binding of mixed extractant head group film N_{complex}. The extractant head groups film is approximated with 2D array of sites - an expanded lattice model. Eu^{3+} cation (red), dissociated HDEHP head groups (dark green), and undissociated HDEHP head groups (pale green), and DMDOHEMA malonamide extractant head groups (dark blue). Gray dashed lines connecting the cation with the head groups serve as guideline for bonding. It can be seen that Eu^{3+} can be bonded to different extractant head groups (bonded to HDEHP only, bonded to DMDOHEMA, or bonded to both HDEHP and DMDOHEMA), in this case to two deprotonated HDEHP and one DMDOHEMA head groups.

cations to mixed extractant film. It reads

$$N_{\text{complex}} = \frac{(\sum_z N_z)!}{\prod_z N_z!} \cdot \prod_z \left(\frac{N_z!}{\prod_i N_{i,z}! \, (N_z - \sum_i N_{i,z} N_{\text{bond},i,z})!} \cdot \frac{1}{\prod_i N_{\text{bond},i,z}!^{N_{i,z}}} \right) \tag{6.3}$$

where the factor $1/\prod_{\text{i}} N_{\text{bond},i,z}!^{N_i}$ accounts for intra-indistinguishability of sites binding a particle. In our particular case of mixed HDEHP and DMDOHEMA aggregates for synergistic systems considerations, we have

$$N_{\text{complex}} = \frac{(N_{\text{LH}} + N_{\text{D}})!}{N_{\text{LH}}! N_{\text{D}}!} \cdot \frac{N_{\text{LH}}!}{\prod_i N_{i,\text{LH}}! \, (N_{\text{LH}} - \sum_i N_{i,\text{LH}} N_{\text{bond},i,\text{LH}})!} \cdot \frac{1}{\prod_i N_{\text{bond},i,\text{LH}}!^{N_{i,\text{LH}}}} \cdot \frac{N_{\text{D}}!}{\prod_i N_{i,\text{D}}! \, (N_{\text{D}} - \sum_i N_{i,\text{D}} N_{\text{bond},i,\text{D}})!} \cdot \frac{1}{\prod_i N_{\text{bond},i,\text{D}}!^{N_{i,\text{D}}}} \tag{6.4}$$

where N_{LH}, N_{D}, $N_{i,\text{LH}}$, $N_{i,\text{D}}$, $N_{\text{bond},i,\text{LH}}$, and $N_{\text{bond},i,\text{D}}$ are respectively the aggregation numbers of HDEHP and DMDOHEMA, the number of cations of type i bonded to HDEHP sites, the number of cations of type i bonded to DMDOHEMA sites, the number of bonds that cation of type i creates with HDEHP sites, and the number of bonds that cation of type i creates with DMDOHEMA sites. From Eq. 6.4 it can be seen that Eq. 6.3 represents a general and consistent way to calculate the excess entropy associated with the possibilities of the arrangement of cations to multi-site 2D extractant film. It must be noted that in the case of pure DMDOHEMA, or HDEHP, this general expression for N_{complex} (presented by Eq. 6.3) reduces to respectively, Eq. 4.12 and Eq. 5.9.

Generalized form of F_{chain}

Free energy due to the curvature effects F_{chain} can be written as

$$F_{\text{chain}} = \sum_z \frac{\kappa_z^\star}{2} \left(\sum_i N_{i,z} N_{\text{bond},i,z} \left(p_{\text{eff}} - p_{0,i,z}\right)^2 + \left(N_z - \sum_i N_{i,z} N_{\text{bond},i,z}\right) \left(p_{\text{eff}} - p_{0,\text{H}_2\text{O},z}\right)^2 \right) \tag{6.5}$$

where $\kappa_z^\star$ represents the generalized bending constant of the molecule of the type z in the extractant film in a given solvent, p_{eff} is the effective packing parameter of the particular aggregate, $p_{0,i,z}$ is the spontaneous packing parameter for a certain type of extractant/cation pair in a given solvent (*e.g.* Eu^{3+} to DMDOHEMA or HDEHP), $p_{0,\text{H}_2\text{O},z}$ is the spontaneous packing parameter for a certain type of the extractant z when no cations are bound to it *i.e.* in contact to pure water. In the case of both HDEHP and DMDOHEMA, upon binding of the acid (the proton) the spontaneous packing parameter is the same as for the water in contact ($p_{0,\text{H}^+,z} = p_{0,\text{H}_2\text{O},z}$ for both HDEHP and DMDOHEMA).

In the case of aggregates containing different extractants, as well as dissociated and undissociated extractants, each aggregate is characterised by different effective packing parameter p_{eff}. If we assume that the length of the z extractant chains in the film is constant upon the change of composition of the core of the aggregate in the given solvent, and that the average length of the mixed extractant film is given through mean-field approximation, we can write p_{eff} in the explicit form as[47, 176]

$$p_{\text{eff}} = 1 + \frac{\langle l_{\text{chain}} \rangle}{R_{\text{core}}} + \frac{1}{3} \frac{\langle l_{\text{chain}} \rangle^2}{R_{\text{core}}^2} \tag{6.6}$$

where $\langle l_{\text{chain}} \rangle$ is the average length of mixed chains extractant film, and is defined as mean-field approximation of pure individual extractant chain lengths. It reads

$$\langle l_{\text{chain}} \rangle = \sum_z \frac{N_z}{\sum_z N_z} l_{\text{chain},z} \tag{6.7}$$

where $l_{\text{chain},z}$ is the average chain length of pure extractant of type z in a film. $l_{\text{chain},z}$ are measured quantities.

Generalized form of $F_{\text{extr.head}}$

A multicomponent $F_{\text{extr.head}}$ that takes into mixing and contact energies of different types of polar head-groups (in our case we have: $\overline{\text{LH}}$, $\overline{\text{L}^-}$, and $\overline{\text{D}}$) in 2D array of sites. We have

$$F_{\text{extr.head}} = (N_{\text{LH}} + N_{\text{D}})(x_{\text{LH}} x_{\text{L}^-} \chi_{\text{LH,L}^-} + x_{\text{LH}} x_{\text{D}} \chi_{\text{LH,D}} + x_{\text{L}^-} x_{\text{D}} \chi_{\text{L}^-,\text{D}}) - k_{\text{B}} T \ln \frac{(N_{\text{LH}} + N_{\text{D}})!}{N_{\text{LH,R}}! N_{\text{L}^-}! N_{\text{D}}!} \tag{6.8}$$

where $x_{\mathrm{LH}}, x_{\mathrm{L^-}}, x_{\mathrm{D}}$, $\chi_{\mathrm{LH,L^-}}$, $\chi_{\mathrm{LH,D}}$, and $\chi_{\mathrm{L^-,D}}$ are the number ratio of protonated HDEHP head groups, the number ratio of deprotonated HDEHP head groups, the number ratio of DMDOHEMA head groups in the monolayer, the exchange parameter describing the contact energy of $\overline{\mathrm{LH}}$-$\overline{\mathrm{L^-}}$ head groups contact, the exchange parameter describing the contact energy of $\overline{\mathrm{LH}}$-$\overline{\mathrm{D}}$ head groups contact, and the exchange parameter describing the contact energy of $\overline{\mathrm{L^-}}$-$\overline{\mathrm{D}}$ head groups contact[123]. Like in the HDEHP case, the entropic part of Eq. 6.8 will be omitted since the corrected N_{complex} accounts for all microstates of binding the multivalent cation to the mixed extractant film, and creating the additional site by deprotonation.

6.2.2 A Full Analytical Expression for the Standard Chemical Potential of the General Mixed Aggregate

A full expression for the standard chemical potential of the particular aggregate reads

$$\begin{aligned}
\mu^{\circ}_{\mathrm{Agg},x} = F_{\mathrm{complex}} + F_{\mathrm{correction}} + F_{\mathrm{droplet}} + F_{\mathrm{chain}} + F_{\mathrm{extr.head}} = \\
-k_{\mathrm{B}}T\,\ln N_{\mathrm{complex}} - \sum_z \sum_i N_{i,z} N_{\mathrm{bond},i,z} E_{i,z} + \\
k_{\mathrm{B}}T \ln\left(N_{\mathrm{H_2O}}! \prod_j N_j!\right) - k_{\mathrm{B}}T\left(N_{\mathrm{H_2O}} \ln N_{\mathrm{H_2O}} + \sum_j N_j \ln N_j - N_{\mathrm{H_2O}} - \sum_j N_j\right) + \\
N_{\mathrm{H_2O}}\mu^{\circ}_{\mathrm{H_2O}} - k_{\mathrm{B}}T N_{\mathrm{H_2O}} \frac{\sum_j x_j^{\mathrm{org}}}{x^{\mathrm{org}}_{\mathrm{H_2O}}} + \sum_j N_j \mu^{\circ}_j + k_{\mathrm{B}}T \sum_j N_j \ln\left(\frac{m_j^{\mathrm{org}}}{m_j^{\circ}}\right) + \\
\sum_z \frac{\kappa^{\star}_z}{2}\left(\sum_i N_{i,z} N_{\mathrm{bond},i,z}\,(p_{\mathrm{eff}} - p_{0,i,z})^2 + (N_z - \sum_i N_{i,z} N_{\mathrm{bond},i,z})\,(p_{\mathrm{eff}} - p_{0,\mathrm{H_2O},z})^2\right) + \\
(N_{\mathrm{LH}} + N_{\mathrm{D}})(x_{\mathrm{LH}} x_{\mathrm{L^-}} \chi_{\mathrm{LH,L^-}} + x_{\mathrm{LH}} x_{\mathrm{D}} \chi_{\mathrm{LH,D}} + x_{\mathrm{L^-}} x_{\mathrm{D}} \chi_{\mathrm{L^-,D}}) - k_{\mathrm{B}}T \ln\left(\frac{1}{N_{\mathrm{L^-}}!}\right)
\end{aligned} \tag{6.9}$$

with p_{eff} being described by Eq. 6.6, and N_{complex} being described by Eq. 6.3. The expression is valid for any composition of an aggregate, under the condition that overall the electroneutrality is preserved. Depending on the input of maximum aggregation numbers of both types of extractants, and the maximum water content (maximum number of water molecules present inside the core) the calculation goes over thousands of distinct species. In calculations we have accounted for the probabilities of almost 50000 different aggregates.

Calculation of equilibrium aggregate concentrations

We will show the calculation for the case presented by Eq. 6.1, which represents the most complex and most general example. We can write Eq. 6.1 expressed through chemical potentials

to obtain

$$\mu_{\mathrm{Agg},x} + \mathrm{N_{L^-}} \cdot \mu^{\mathrm{aq}}_{\mathrm{H^+}} = N_{\mathrm{LH}} \cdot \mu_{\mathrm{LH}} + N_{\mathrm{D}} \cdot \mu_{\mathrm{D}} + N_{\mathrm{H_2O}} \cdot \mu^{\mathrm{aq}}_{\mathrm{H_2O}} + \sum_j N_j \cdot \mu^{\mathrm{aq}}_j \tag{6.10}$$

in which we can insert definitions of chemical potentials (like in previous chapters) to obtain

$$\begin{aligned} \mu^{\circ}_{\mathrm{Agg},x} + k_{\mathrm{B}}T \ln\left(\frac{c_{\mathrm{Agg},x}}{c^{\circ}}\right) + N_{\mathrm{L^-}}\mu^{\circ}_{\mathrm{H^+}} + \mathrm{N_{L^-}} k_{\mathrm{B}}T \ln\left(\frac{m^{\mathrm{aq}}_{\mathrm{H^+}}}{m^{\circ}_{\mathrm{H^+}}}\right) = \\ N_{\mathrm{H_2O}}\mu^{\circ}_{\mathrm{H_2O}} - N_{\mathrm{H_2O}} k_{\mathrm{B}}T \frac{\sum_j x^{\mathrm{aq}}_j}{x^{\mathrm{aq}}_{\mathrm{H_2O}}} + \sum_j N_j \mu^{\circ}_j + \\ k_{\mathrm{B}}T \sum_j N_j \ln\left(\frac{m^{\mathrm{aq}}_j}{m^{\circ}_j}\right) + N_{\mathrm{LH}}\mu^{\circ}_{\mathrm{LH}} + N_{\mathrm{LH}} k_{\mathrm{B}}T \ln\left(\frac{c_{\mathrm{LH}}}{c^{\circ}}\right) + N_{\mathrm{D}}\mu^{\circ}_{\mathrm{D}} + N_{\mathrm{D}} k_{\mathrm{B}}T \ln\left(\frac{c_{\mathrm{D}}}{c^{\circ}}\right) \quad . \end{aligned} \tag{6.11}$$

Following the same tactics as in previous chapters we can: 1) collect the terms in reduced standard chemical potential $\mu^{\circ''}_{\mathrm{Agg},x}$, to make Eq. 6.11 neat, 2) cancel the standard chemical potentials of ions and water molecules, 3) collect standard chemical potentials multiplied by $N_{\mathrm{L^-}}$, 4) identify the standard reaction Gibbs energy of extractant head-group dissociation reaction $\Delta_{\mathrm{r}}G^{\circ}_{\mathrm{a}}$ and rewrite it in the form of the dissociation constant K°_{a}, 5) rearranging the final expression, 6) apply exponential function. Finally we recover

$$c_{\mathrm{Agg},x} = S_{\mathrm{Agg},x}\, c^{N_{\mathrm{LH}}}_{\mathrm{LH}}\, c^{N_{\mathrm{D}}}_{\mathrm{D}} \tag{6.12}$$

where $S_{\mathrm{Agg},x}$ is defined as

$$\begin{aligned} S_{\mathrm{Agg},x} = \exp\Bigg(-\beta\mu^{\circ''}_{\mathrm{Agg},x} + \sum_j N_j \ln\left(\frac{m^{\mathrm{aq}}_j}{m^{\mathrm{org}}_j}\right) + N_{\mathrm{H_2O}}\left(\frac{\sum_j x^{\mathrm{org}}_j}{x^{\mathrm{org}}_{\mathrm{H_2O}}} - \frac{\sum_j x^{\mathrm{aq}}_j}{x^{\mathrm{aq}}_{\mathrm{H_2O}}}\right) + \\ -N_{\mathrm{L^-}}\ln(10)(\mathrm{p}K^{\circ}_{\mathrm{a}} - \mathrm{pH}) + \beta N_{\mathrm{LH,R}}\mu^{\circ}_{\mathrm{LH}} + \beta N_{\mathrm{D}}\mu^{\circ}_{\mathrm{D}}\Bigg)\left(\frac{1}{c^{\circ}}\right)^{N_{\mathrm{LH}}+N_{\mathrm{D}}-1} \end{aligned} \tag{6.13}$$

with

$$\begin{aligned} \mu^{\circ''}_{\mathrm{Agg},x} = F_{\mathrm{complex}} + F_{\mathrm{correction}} + F_{\mathrm{chain}} + \\ k_{\mathrm{B}}T\,(N_{\mathrm{LH}} + N_{\mathrm{D}})(x_{\mathrm{LH}}x_{\mathrm{L^-}}\chi_{\mathrm{LH,L^-}} + x_{\mathrm{LH}}x_{\mathrm{D}}\chi_{\mathrm{LH,D}} + x_{\mathrm{L^-}}x_{\mathrm{D}}\chi_{\mathrm{L^-,D}}) - k_{\mathrm{B}}T \ln\left(\frac{1}{N_{\mathrm{L^-}}!}\right) \end{aligned}$$

Calculations were made in semi-grand canonical ensemble for a fixed $Eu(NO_3)_3$, HNO_3 and H_2O molecules chemical potentials in the reservoir (the bulk aqueous solution). MAL was fulfilled by two-dimensional minimization of system variables c_{LH}, and c_{D}. Calculated $c_{\mathrm{Agg},x}$ are normalized over the sample, with the exclusion of HDEHP dimers. Again, we emphasize that aggregates are only species filled with solutes.

6.3 Input for the Model and the Fitting the Experimental Data Set

To make calculations with generalized Droplet model, we take measured quantities and parameters obtained from previous studies, namely DMDOHEMA and HDEHP. The additional parametrization is forbidden in order to validate methodology.

6.3.1 Input for the Model

The minimum aggregation numbers for HNO_3 and H_2O filled aggregates were set to 4, for both pure DMDOHEMA, pure HDEHP, and mixed aggregates. The minimum pure HDEHP aggregation number for the case of Eu^{3+} was 6, while the minimum pure DMDOHEMA aggregation number for the case of Eu^{3+} was 4. The minimum mixed extractant aggregation number for the case of Eu^{3+} was 7. Such aggregation numbers are often reported in the literature [13, 44]. The maximum number of Eu^{3+}-filled mixed aggregates was set to 1. This is a drawback of the model, and it originates form the fact that we have neglected the partial molar volume of Eu^{3+} and attributed the total volume of salt to the volume of the counterion only.

The occupancy and the composition of Eu^{3+} first coordination sphere were taken form coordination chemistry considerations, as reported in the literature[37, 47, 43, 218]. The compositions of the first coordination sphere were plugged into the complexation free energy term, again in a additive manner. Within the model, this action provides physical restraint needed to block the unrealistic accumulation of Eu^{3+}-coordinated ligands, and thus limits the influence of F_{complex}.

6.3.2 Comparison of the Model and Experimental Data

For DMDOHEMA, the model parameters were derived, and discussed in detail in one of our previous papers[171]. In the same manner, HDEHP was studied, and parameters were obtained[193]. Now, in the case of the mixtures of aggregates, we may notice in the section Theory, that additional two parameters appeared. Two parameters correspond to head group interaction between HDEHP and DMDOHEMA $\chi_{\text{LH,D}}$, and deprotonated form of HDEHP and DMDOHEMA interaction parameter $\chi_{\text{L}^-,\text{D}}$. All other parameters, derived on individual pure DMDOHEMA and pure HDEHP were not readjusted. This is the only way to preserve generality of the approach. If the approach works on the individual, simpler cases, then it must work on more complex case. Therefore, synergistic case is sort of validation of our derived model.

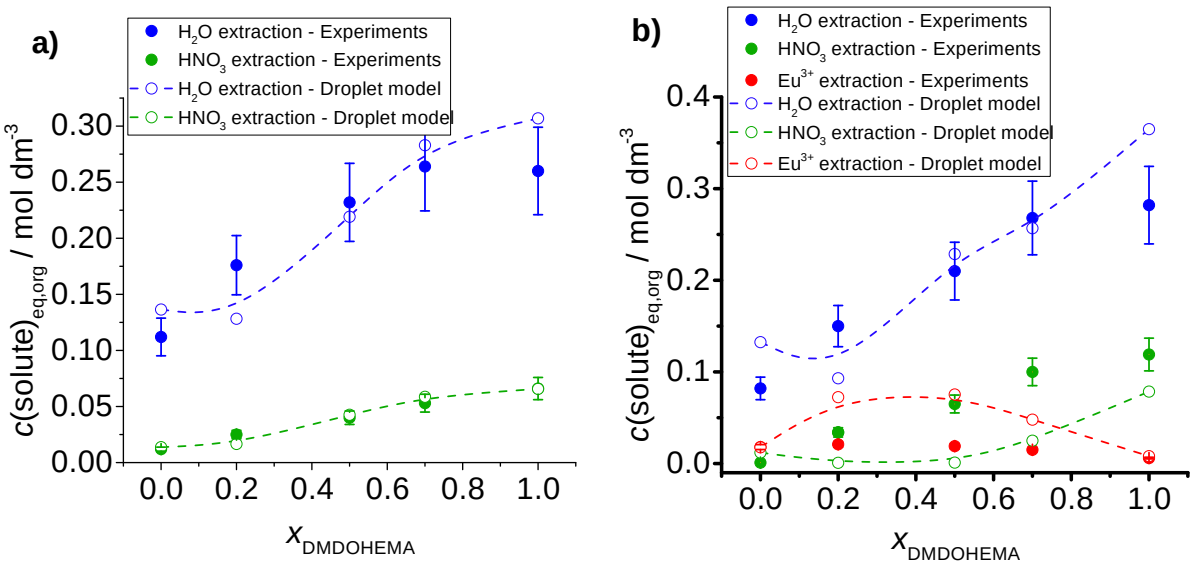

Figure 6.4 – Extraction of solutes are a function of x_{DMDOHEMA} at $c_{\mathrm{total}} = 0.6$ mol dm^{-3}. The organic phase is in contact to: a) $m(\mathrm{HNO_3})_{\mathrm{aq,eq}} = 1$ mol kg^{-1} (left), b) $m(\mathrm{HNO_3})_{\mathrm{aq,eq}} = 1$ mol kg^{-1}, $m(\mathrm{Eu^{3+}})_{\mathrm{aq,eq}} = 0.035$ mol kg^{-1} (right). The comparison of the reference experimental data by Rey *et al.* [54, 187] and predictions of the model are presented.

$\chi_{\mathrm{LH,D}}$ was obtained by fitting $\mathrm{HNO_3}$ system, since in the absence of multivalent cations, there is no HDEHP dissociation, thus no need for $\mathrm{L^-} - \mathrm{D}$. Results of the fitting, when just $\chi_{\mathrm{LH,D}}$ was added to the model are presented in Figure 6.4a. For the value $\chi_{\mathrm{LH,D}} = 4\ k_{\mathrm{B}}T$, we obtained a very good fit of the experimental data (recall that solute concentration determination in liquid-liquid extraction, the experimental error can easily be 100 % or grater!). $\chi_{\mathrm{L^-,D}} = 8\ k_{\mathrm{B}}T$ was obtained by fitting the extraction data of $\mathrm{Eu(NO_3)_3/HNO_3}$ system. Results are presented in Figure 6.4b. There is discrepancy between the fit and the experimental data, but order of magnitude on concentration (not log-log scale) is correct. Moreover, the results are within the experimental error of the reference literature[54, 187, 186].

It must be noted that as long as the aggregation numbers of aggregates are small (which indeed is the case), the influence of $F_{\mathrm{extr.head}}$ is small. $F_{\mathrm{extr.head}}$ is dominated by F_{complex} (see study made in reference[193]), which means that $\chi_{\mathrm{LH,D}}$ and $\chi_{\mathrm{L^-,D}}$ can almost be neglected (no extra parameters for the mixed extractant case). Yet, we used the values obtained by fitting.

6.4 Aggregates Diversity Behind the Self-Assembly: Influence of Independent System Variables

We start by presenting a direct output of calculations, *i.e.* aggregate probabilities at equilibrium. Calculations were made with equilibrium Eu^{3+} molality in the reservoir $m(Eu^{3+})_{aq,eq} = 0.035$ mol kg^{-1}, and the total concentration of extractant in the system, $c_{total} = 0.6$ mol dm^{-3}. The total concentration is the sum of the initial concentrations of both extractants in the system ($c_{total} = c_{LH,initial} + c_{D,initial}$, where $c_{LH,initial}$ is the initial HDEHP, and $c_{D,initial}$ is the initial DMDOHEMA concentration in the system). Results are presented in Figures 6.5a-c for three different equilibrium HNO_3 molalities in the reservoir $m(HNO_3)_{aq,eq}$, and different extractant mole fraction, $x_{DMDOHEMA}$. All the graphs presented in Figures 6.5a-c have been presented individually with additional zoomed regions for quantitative assessment in Appendix B.

The idea of presenting the probabilities as a sort of mass spectroscopy graphs follows from the wish of the authors to emphasize the diversity of self-assembled aggregates in a dilute extractant saturation regime that dictates later organic phase structuring, phase transitions in micro- or nanodomains, third phase formation, *etc.*

Figure 6.5a shows stacked probability $P_{Agg,x}$ plots as a function of the molar mass of the aggregates, $M_{agg,x}$ for $m(HNO_3)_{aq,eq} = 0.1$ mol kg^{-1} and $x_{DMDOHEMA}$ ranging form 0 to 1. In the case of $x_{DMDOHEMA} = 0$ (pure HDEHP system) the most probable aggregates are [3LH;3L$^-$;Eu^{3+};1-3H$_2$O], which is in accordance with the literature[120, 13, 44, 36]. The model also predicts a small probability of binuclear aggregates present at the equilibrium. For $x_{DMDOHEMA} = 0.2$, DMDOHEMA concentration is sufficiently high, which facilitates the formation of mixed HDEHP/DMDOHEMA aggregates (shortly mixed aggregates), as can be seen by the occurrence of multiple probability peaks at higher $M_{agg,x}$. Formation of mixed [2D;2LH;3L$^-$;Eu^{3+};1-3H$_2$O] and [3D;LH;3L$^-$;Eu^{3+};1-5H$_2$O] aggregates with the incorporation of respectively 2 or 3 DMDOHEMA molecules in the extractant film, accompanied by the replacement of HDEHP by DMDOHEMA in the first Eu^{3+} coordination sphere comes at the expense of lowered [3LH;3L$^-$;Eu^{3+};1-3H$_2$O] aggregate probability. Therefore, the model predicts that a sole change in $x_{DMDOHEMA}$ can induce a change in the stoichiometry of the aggregate for fixed values of other independent variables of the system. Instead of a single competition reaction, we obtained a severe polydispersity in aggregation. A further increase to $x_{DMDOHEMA} = 0.5$ decreases the polydispersity as probabilities cluster around single first-sphere composition along with 1 to 5 supporting H_2O molecules ([3LH;3L$^-$;Eu^{3+};1-3H$_2$O] aggregate). In this case, pure HDEHP aggregates have negligible probabilities, since HDEHP chemical potential is too low to

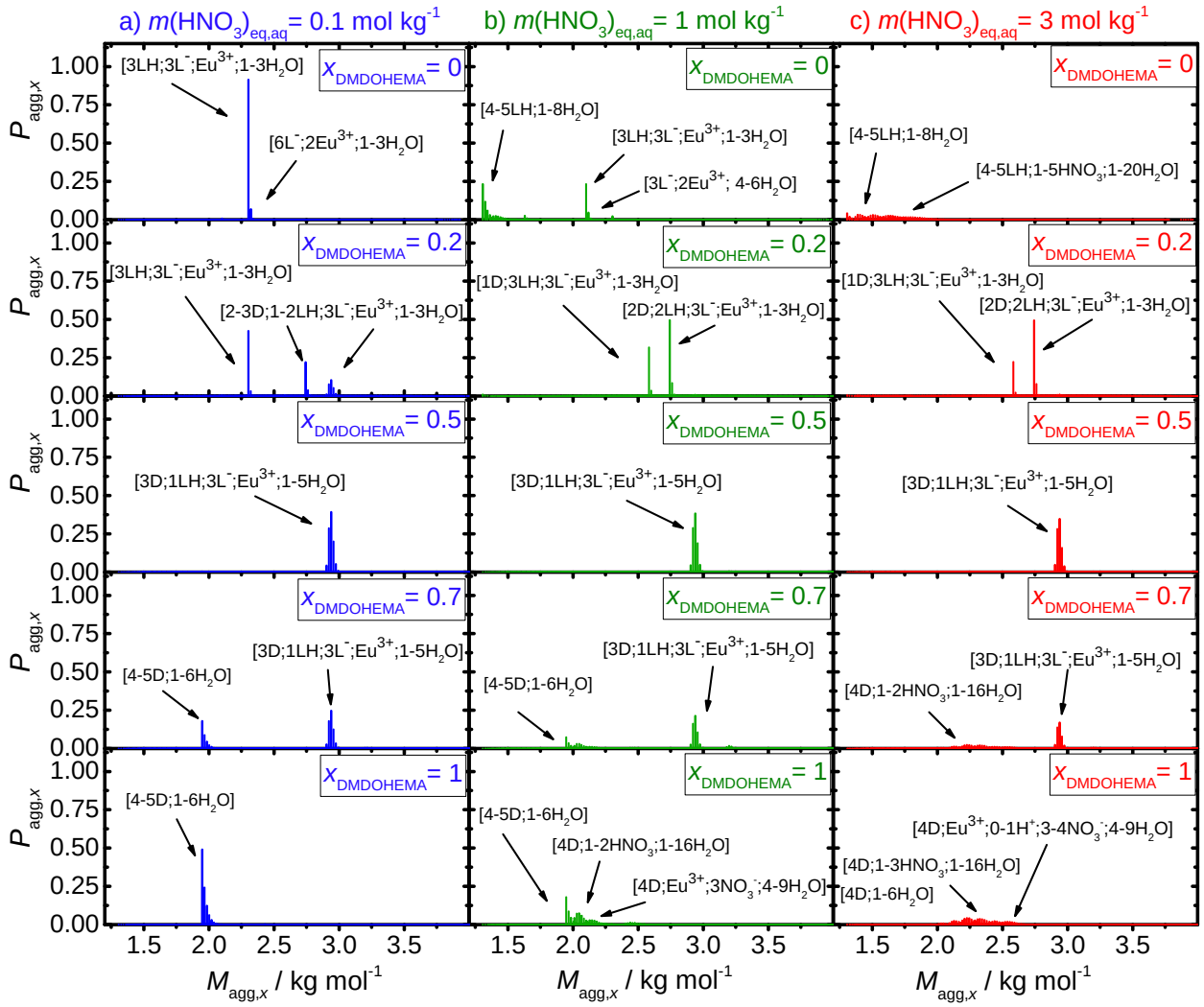

Figure 6.5 – Calculated aggregate probabilities $P_{\mathrm{Agg},x}$ as a function of the molar mass $M_{\mathrm{agg},x}$. Results are presented for different DMDOHEMA mole fraction, x_{DMDOHEMA} in the system. Symbol D stands for DMDOHEMA, whereas LH stands for HDEHP. Square brackets with text depict particular aggregate assignation. Calculations were made for $c_{\mathrm{total}} = 0.6$ mol dm^{-3}, and $m(\mathrm{Eu}^{3+})_{\mathrm{aq,eq}} = 0.035$ mol kg^{-1}. The three cases of different $\mathrm{HNO_3}$ in the bulk aqueous phase are presented. a) $m(\mathrm{HNO_3})_{\mathrm{aq,eq}} = 0.1$ mol kg^{-1}, b) $m(\mathrm{HNO_3})_{\mathrm{aq,eq}} = 1$ mol kg^{-1}, c) $m(\mathrm{HNO_3})_{\mathrm{aq,eq}} = 3$ mol kg^{-1}.

sustain them, especially since its complexation energy is quenched by the energy penalty to sustain highly curved interface along with LH-L$^-$ head groups repulsion and low accessible volume for the ions inside the polar core. Mixed aggregates, on the other hand, have highly favorable excess complexation energy of first-sphere interactions making their formation dominating competition reaction.

At $x_{\mathrm{DMDOHEMA}} = 0.7$ the self-assembly is now governed not only by the formation of mixed aggregates but also by the formation of pure DMDOHEMA aggregates filled only by $\mathrm{H_2O}$

molecules. This raises the water uptake in the organic phase. The trend of pure water uptake further extends for the case of $x_{\mathrm{DMDOHEMA}} = 1$, where for the pure DMDOHEMA system, the equilibrium is shifted to the formation of H_2O filled aggregates.

Figure 6.5b shows results of calculations for $m(\mathrm{HNO_3})_{\mathrm{aq,eq}} = 1$ mol kg^{-1}. Like in the case for lower bulk HNO_3 molality, at $x_{\mathrm{DMDOHEMA}} = 0$ the most probable aggregates again correspond to [3LH;3L$^-$;Eu^{3+};1-3H_2O]. But now there is an almost equal cumulative probability of pure HDEHP aggregates filled by H_2O molecules ([4LH;1-8H_2O]) which are in competition with Eu^{3+}-based aggregates. Remarkably, higher $m(\mathrm{HNO_3})_{\mathrm{aq,eq}}$ increases the polydispersity of the aggregates in both aggregation numbers and the water content. This prediction of the model, which is in accordance with the literature[218, 36], further stresses the influence of solutes (*e.g.* $m(\mathrm{HNO_3})_{\mathrm{aq,eq}}$) on the stoichiometry of mixed aggregate formation[193]. In terms of thermodynamics, the unfavorable acid influence in the system lowers the probabilities Eu^{3+} filled aggregates since dissociation of HDEHP in high acidity medium is needed to form the stable complex. The same argument holds also in the case of $x_{\mathrm{DMDOHEMA}} = 0.2$, where only mixed aggregates form, and [3LH;3L$^-$;Eu^{3+};1-3H_2O] have negligible probability.

A further increase of x_{DMDOHEMA} form 0.5 to 1 follows the trend like in Figure 6.5a, with a slight difference of additional probability of HNO_3/H_2O filled aggregates at higher DMDOHEMA concentrations in the system, caused by the increased HNO_3 chemical potential in the reservoir. It must be noted that at $x_{\mathrm{DMDOHEMA}} = 1$, [4D;Eu^{3+};3$NO_3^-$;4-9$H_2O$] starts to form, which is always observed experimentally, and recovered theoretically[219, 37, 34, 43, 46, 45, 32].

Results on Figure 6.5c correspond to $m(\mathrm{HNO_3})_{\mathrm{aq,eq}} = 3$ mol kg^{-1}. High HNO_3 molality smears probability peaks over a wide range of $M_{\mathrm{agg},x}$ at both $x_{\mathrm{DMDOHEMA}} = 0$, and 1. At $x_{\mathrm{DMDOHEMA}} = 1$, a small fraction of [4D;Eu^{3+};H$^+$;4NO_3^-;4-9H_2O] is observed (acid stabilization effect was reported before[46]). Aggregates formed in both cases are made of pure HDEHP or DMDOHEMA extractants, with several HNO_3 molecules in the polar core, accompanied by high dilution with H_2O. The trend similar to the $m(\mathrm{HNO_3})_{\mathrm{aq,eq}} = 1$ mol kg^{-1} case is observed for intermediate x_{DMDOHEMA} values.

Results from Figures 6.5a-c point to the fact that liquid-liquid extraction in the case of synergistic mixtures, cannot be fully (or even partially) described by a simple chemical equilibria where only a few aggregates form. Even the expansion of that concept in terms of variation of the total aggregation and the water content numbers is still missing the huge amount of information concerning the diversity of self-assembled aggregates. The presence of different species in the organic phase is a complex function of concentrations of all constituents in the system. This was illustrated, within the scope of our model, just by variation of x_{DMDOHEMA},

and $m(HNO_3)_{aq,eq}$ independent variables while keeping other variables fixed (c_{total} = 0.6 mol dm^{-3}, and $m(Eu^{3+})_{aq,eq}$ = 0.035 mol kg^{-1}). Note also that the organic solvent considered was *n*-dodecane. Changing the solvent would greatly affect the self-assembly phenomenon behind the liquid-liquid extraction efficiency even in the case of dilute gas-like dispersion of reverse aggregates[24, 220].

6.5 Decoupling the Total Extraction Efficiency Into Contributions

The advantage of the generalized Droplet model is the fact that it gives full distribution of aggregates. Therefore we can study in detail how polydispersity of self-assembled structures in the organic phase reflects on the efficiency of the liquid-liquid extraction system utilizing the synergistic mixtures of extractants.

6.5.1 Job's-like plots: Influence of Extractants Mole Fraction

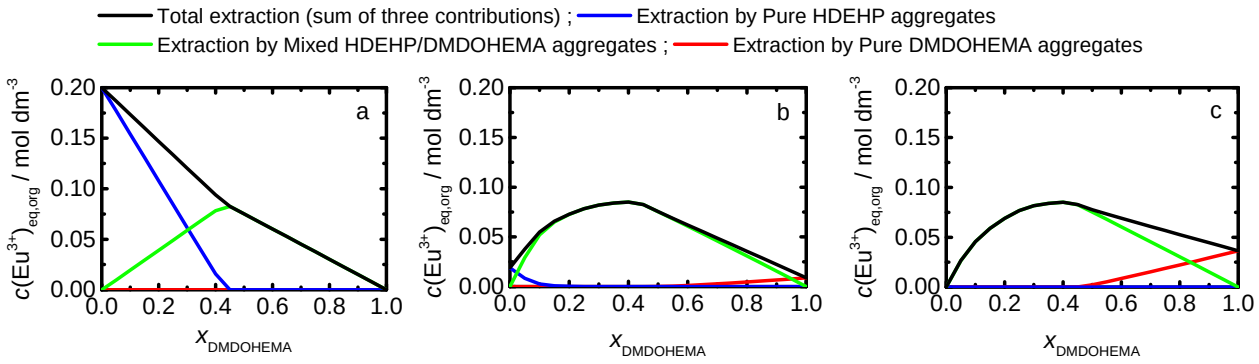

Figure 6.6 – Decoupling the extraction efficiency into contributions - an enhanced Job's plot. Calculated total Eu^{3+} extraction (black line), the contribution due to the mixed extractant aggregates (green line), the contribution due to the pure HDEHP extractant aggregates (blue line), and the contribution due to the pure DMDOHEMA extractant aggregates (red line) extraction as a function of DMDOHEMA mole fraction in the system, $x_{DMDOHEMA}$, for $m(Eu^{3+})_{aq,eq}$ = 0.035 mol kg^{-1}, and c_{total} = 0.6 mol dm^{-3}. The results are presented for three cases of HNO_3 in the bulk aqueous phase, $m(HNO_3)_{aq,eq}$. a) $m(HNO_3)_{aq,eq}$ = 0.01 mol kg^{-1}, b) $m(HNO_3)_{aq,eq}$ = 1 mol kg^{-1}, c) $m(HNO_3)_{aq,eq}$ = 3 mol kg^{-1}.

.

First thing is to study the effect of the DMDOHEMA to HDEHP mole fraction organic phase[167]. In that sense, we have calculated Job's-like plots and presented results in Fig-

ure 6.6a-c. To make a study complementary and consistent, we have plotted the concentration of Eu^{3+} in the organic phase (extracted amount) as a function of x_{DMDOHEMA} for three $m(\mathrm{HNO_3})_{\mathrm{aq,eq}}$, at $m(\mathrm{Eu^{3+}})_{\mathrm{aq,eq}} = 0.035$ mol kg^{-1}, and $c_{\mathrm{total}} = 0.6$ mol dm^{-3}. To improve understanding of the current Job's plots, we have quantitatively decoupled the total Eu^{3+} extraction to contributions by pure HDEHP aggregates (*e.g.* [3LH;3L$^-$;Eu^{3+};1-3H$_2$O]), pure DMDOHEMA aggregates (*e.g.* [4D;Eu^{3+};3NO$_3^-$;4-9H$_2$O]), and mixed aggregates responsible for synergistic behavior (*e.g.* [3D;LH;3L$^-$;Eu^{3+};1-5H$_2$O]) depicted by respectively the black, blue, red, and green lines in Figure 6.6a-c.

Results presented in Figure 6.6a, at $m(\mathrm{HNO_3})_{\mathrm{aq,eq}} = 0.01$ mol kg^{-1} represent so-called antagonistic case where mixtures extract less than individual extractant for given conditions[167]. Due to the dissociation of HDEHP at low HNO_3 molality (in our model the property has a form of $-N_{\mathrm{L^-}}\ln(10)(\mathrm{p}K_{\mathrm{a}}^{\circ} - \mathrm{pH})$, see Eq.6.13) the extraction is highly favorable for pure HDEHP system[193, 204]. The property is further reflected for low x_{DMDOHEMA}, where the system retains HDEHP-like behavior. The decoupled contributions (blue line) state that at low x_{DMDOHEMA}, HDEHP pure aggregates constitute almost the entire extraction (see also $x_{\mathrm{DMDOHEMA}} = 0$ and 0.2 cases in Figure 6.5a). Now, with a further increase of x_{DMDOHEMA} the extraction is becoming more influenced by the formation of mixed aggregates with the loss of irreversible antagonistic characteristics. Eventually, the total extraction curve collapses onto the extraction curve by mixed aggregates. Note that at low $m(\mathrm{HNO_3})_{\mathrm{aq,eq}}$ in the system and high x_{DMDOHEMA}, DMDOHEMA extractant is uselessly spent on the transfer of water molecules in the organic phase (see cases $x_{\mathrm{DMDOHEMA}} = 0.7, 1$ in Figure 6.5a).

The overlap of the total and the mixed aggregates extraction isotherms is the main property of the synergistic mixtures for the system conditions around working point ($m(\mathrm{HNO_3})_{\mathrm{aq,eq}} = 1$ mol kg^{-1}), as can be seen in Figure 6.6b. This extraction regime is often referred as the synergistic regime[54, 167]. Only at low, or at high x_{DMDOHEMA} we have contributions by either HDEHP or DMDOHEMA pure aggregates. The synergistic peak provided by our calculations is around $x_{\mathrm{DMDOHEMA}} = 0.4$. There is a slight discrepancy between calculations and reference literature data, but result is within the experimental error[187].

With the further increase in bulk acid molality (Figure 6.6c) the maximum of the total extraction *i.e.* the synergy peak slightly shifts towards higher x_{DMDOHEMA}. Moreover, for higher x_{DMDOHEMA} a substantial pure DMDOHEMA aggregates extraction takes hold (red line). Here we recover synergistic-to-linear regime. and it is a consequence of the acid-assisted cation extraction in the case of non-ionic extractants. The saturation of the aqueous phase with salts shifts the equilibrium towards the organic phase, as differences in molalities between

the polar core and the reservoir are reduced. For lower $m(\mathrm{Eu}^{3+})_{\mathrm{aq,eq}}$ we would recover also the so-called linear extraction regime.

To sum up, the three extraction regimes: the antagonistic, the synergistic, and the synergistic-to-linear regimes (Figure 6.6a-c) are completely controlled by concentrations of solutes in the aqueous phase and the extractant mole fraction for the fixed c_{total}. The change of compositions of the first- and second- Eu^{3+} coordination sphere induced by the change in independent system variables, is reflected in the extraction efficiency as the three regime emerge[218]. It follows, that it is the rule and not the exception.

6.5.2 Influence of Acid Molality

Results of decoupling the total extraction as a function of $m(\mathrm{HNO_3})_{\mathrm{aq,eq}}$ for a given x_{DMDOHEMA} are presented in Figure 6.7a-c. Figure 6.7a shows represented the case of $x_{\mathrm{DMDOHEMA}} = 0.2$.

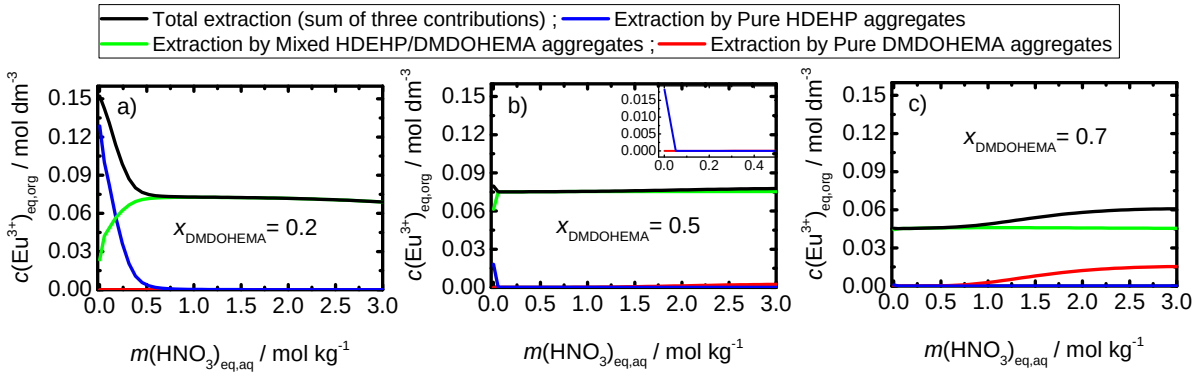

Figure 6.7 – Decoupling the extraction efficiency into contributions. Calculated total Eu^{3+} extraction (black line), extraction due to the mixed extractant aggregates (green line), extraction due to the pure HDEHP extractant aggregates (blue line), and extraction due to the pure DMDOHEMA extractant aggregates (red line) as a function of $m(\mathrm{HNO_3})_{\mathrm{aq,eq}}$. DMDOHEMA mole fraction in the system for $m(\mathrm{Eu}^{3+})_{\mathrm{aq,eq}} = 0.035$ mol kg^{-1}, and $c_{\mathrm{total}} = 0.6$ mol dm^{-3}. The results are presented for the three cases of DMDOHEMA mole ratio in the system. a) $x_{\mathrm{DMDOHEMA}} = 0.2$, b) $x_{\mathrm{DMDOHEMA}} = 0.5$, c) $x_{\mathrm{DMDOHEMA}} = 0.7$.

.

At low $m(\mathrm{HNO_3})_{\mathrm{aq,eq}}$, the system is in high extraction regime. The total Eu^{3+} extraction (depicted by the black line) shows a steep decrease upon increase of $m(\mathrm{HNO_3})_{\mathrm{aq,eq}}$. This is the typical phenomenon of the pure HDEHP system. In fact, the extraction contribution by the formation of pure HDEHP aggregates (depicted by the blue line) constitutes majority of the total extraction, while extraction by mixed aggregates formation is small. It follows that the mixed extractants system, at low x_{DMDOHEMA} and $m(\mathrm{HNO_3})_{\mathrm{aq,eq}}$ is controlled by pure

HDEHP aggregates. Behavior is thus the same as described in third chapter of this thesis. Pure DMDOHEMA contribution is negligible due to the small concentration of DMDOHEMA in the system. This was also demonstrated in Figure 6.5a. With the increase of $m(\mathrm{HNO_3})_{\mathrm{aq,eq}}$, the pure HDEHP contribution is completely damped, and once again the total extraction curve collapses onto the extraction utilized mixed aggregates.

The case of $x_{\mathrm{DMDOHEMA}} = 0.5$ (equal amounts of both extractants) presented in Figure 6.7b follows expected trend with dominant extraction by mixed aggregates. Figure 6.7c shows the case of $x_{\mathrm{DMDOHEMA}} = 0.7$. At low $m(\mathrm{HNO_3})_{\mathrm{aq,eq}}$ system is still completely controlled by the formation of mixed aggregates. The increase of $m(\mathrm{HNO_3})_{\mathrm{aq,eq}}$ causes the total extraction to increase. The increase was traced down to the extraction by pure DMDOHEMA aggregates (depicted by the red line). Indeed, in high acidity and high x_{DMDOHEMA}, the majority of extractant in the system is DMDOHEMA, which allows the increase in the total extraction. Now system is controlled by the DMDOHEMA, like in the second chapter.

6.6 Breaking the Synergy Paradigm

Within the abundant, and to some extent, scattered literature dealing with the liquid-liquid extraction and its colloidal aspect, there are typically two main approaches to study the occurrence of the synergy. One approach is by looking at the extractant mole fraction, and the other at the bulk acid concentration influence[187, 219, 37]. Therefore, the best way to elucidate what is synergy, or what is not, is to examine both approaches. Figure 6.8a shows Eu^{3+} extraction as a function x_{DMDOHEMA} for $m(\mathrm{HNO_3})_{\mathrm{aq,eq}} = 1$ mol kg^{-1}, $m(\mathrm{Eu^{3+}})_{\mathrm{aq,eq}} = 0.035$ mol kg^{-1}, and $c_{\mathrm{total}} = 0.6$ mol dm^{-3}. The solid green line depicts the synergistic extraction governed by mixed aggregates formation, whereas the dashed blue line depicts for the same system conditions a hypothetical extraction when no mixed aggregates are allowed to form. When no mixed aggregates are allowed, there is a minimum of the extraction at higher x_{DMDOHEMA}, due to the globally low HDEHP concentration in the system. The conclusion is that the entropy of mixing of extractants alone cannot be responsible for the synergy, since there is no characteristic peak at $x_{\mathrm{DMDOHEMA}} = 0.5$. Now, in the case when mixed aggregates are allowed (green line), we obtain the characteristic peak. Moreover, to incinerate the claim that additional entropy associated with the arrangements of different extractant molecules in the extractant film of mixed aggregates is sole factor to induce the synergy, we would like to emphasize that the peak in synergy is not at $x_{\mathrm{DMDOHEMA}} = 0.5$. At $x_{\mathrm{DMDOHEMA}} = 0.5$ the number of microstates is at maximum, but we see that extraction behavior does not correspond to it[187]. The excess entropy

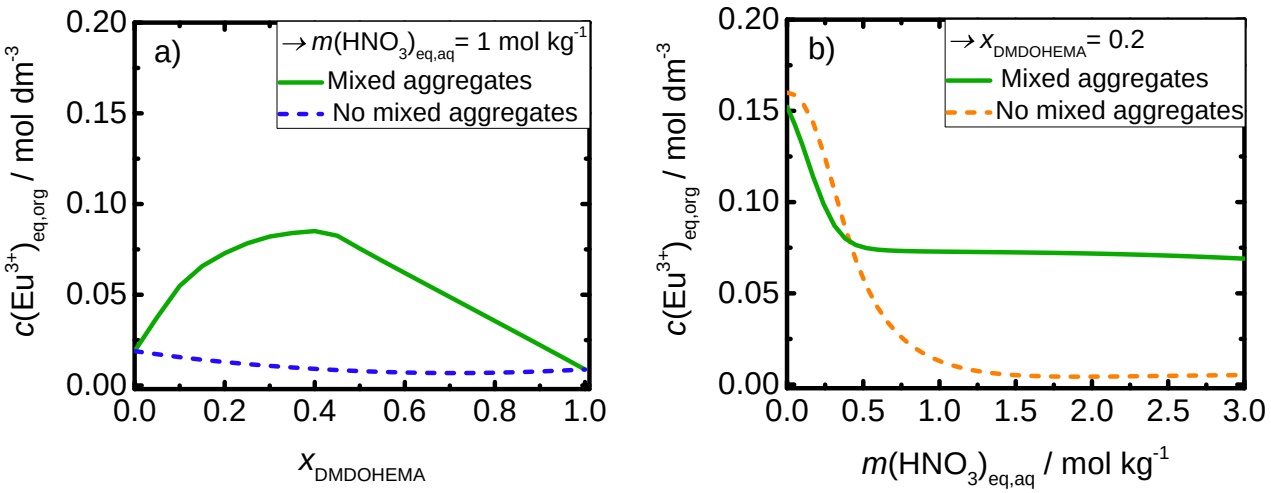

Figure 6.8 – The calculated Eu^{3+} extraction isotherms as function of: a) x_{DMDOHEMA} for $m(\mathrm{HNO_3})_{\mathrm{aq,eq}} = 1$ mol kg^{-1}, b) $m(\mathrm{HNO_3})_{\mathrm{aq,eq}}$, for $x_{\mathrm{DMDOHEMA}} = 0.2$. Both calculations were made for $m(\mathrm{Eu^{3+}})_{\mathrm{aq,eq}} = 0.035$ mol kg^{-1}, and $c_{\mathrm{total}} = 0.6$ mol dm^{-3}. Dashed lines in both graphs represent the calculated Eu^{3+} extraction isotherms when no mixed aggregates are allowed in the calculation *i.e.* only pure HDEHP or DMDOHEMA aggregates are present at equilibrium. Green solid curves represent synergistic mixtures.

would entirely compensate the loss of entropy due to the bringing the equal numbers of extractants monomers into a single aggregate. The most probable (and the only) aggregate would correspond to symmetrical occupancy of the first and the second Eu^{3+} coordination sphere *e.g.* the hypothetical [4D;4LH;Eu^{3+}] complex. Indeed, it is the enthalpic, or in our case, the internal energy contribution of the first-sphere complexation free energy that sets synergistic peak to a certain x_{DMDOHEMA} value. Furthermore, the case is even more complex than that, since we have shown that complexation excess free energy is in competition with various quenching energy terms, such as: the formation of curved extractant film, different head groups repulsion, branching of the extractant chains, diluent penetration power, shrinkage of the accessible volume of the ions and water molecules confined in the polar core, energy penalties due to the breaking of stable HDEHP dimers, dissociation of HDEHP, *etc.* Only by considering all energy terms that contribute to the formation of the particular aggregate, and all the independent system variables, the free energy of the system can be properly minimized[221].

Figure 6.8b is less intuitive concerning the thermodynamics of the system, but still it clearly demonstrates the difference between Eu^{3+} extraction driven by mixed aggregates (green line) and only pure HDEHP or DMDOHEMA aggregates formation (dashed orange line). The engineering aspect is notable here. Compared to rapid decrease of the extraction efficiency with increasing $m(\mathrm{HNO_3})_{\mathrm{aq,eq}}$ in the case when no mixed aggregates are allowed, the extraction

efficiency for synergistic mixtures stays globally the same. This broadens the search for new solutions in extraction formulation design. Chemical engineering aspect will be further addressed throughout the text.

To further demonstrate the acid influence on synergistic behavior of mixtures of extractant we have calculated Eu^{3+} extraction isotherms versus $m(HNO_3)_{aq,eq}$ for different $x_{DMDOHEMA}$ when mixed aggregation is allowed (Figure 6.9a), and when no mixed aggregation is allowed (Figure 6.9b). The difference between two cases is evident. First let us examine case with no

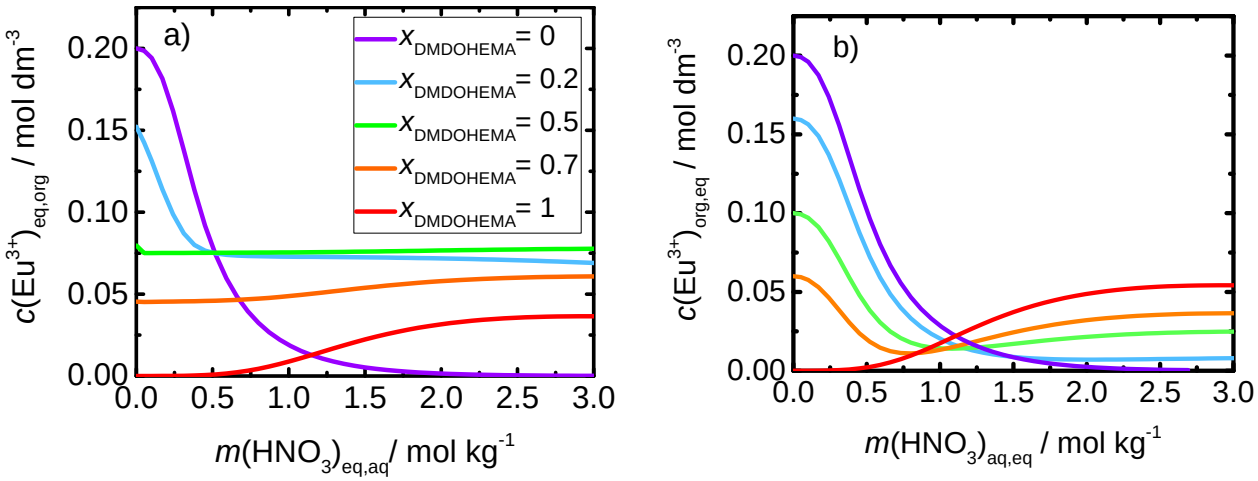

Figure 6.9 – The calculated Eu^{3+} extraction isotherms as function of $m(HNO_3)_{aq,eq}$ or for different $x_{DMDOHEMA}$ when: a) the specific synergistic interactions are included (mixed aggregates included), b) there are no specific synergistic interactions (pure aggregates only). Both calculations were made for $m(Eu^{3+})_{aq,eq} = 0.035$ mol kg^{-1}, and $c_{total} = 0.6$ mol dm^{-3}.

mixed aggregates formation. In the absence of the specific interactions that exhibit synergistic behavior, the acid molality controls competition between pure HDEHP and pure DMDOHEMA aggregation. At low $m(HNO_3)_{aq,eq}$, DMDOHEMA remains in form of monomers, whereas again, HDEHP is involved in the self-assembly and thus extracts. Opposite phenomenon happens when $m(HNO_3)_{aq,eq}$ is high. Then, HDEHP remains in dimeric form, whereas DMDOHEMA supports aggregation. Important aspect of the absence of specific mixed aggregation can be understood by examining the shape of extraction isotherms. They are in fact, a simple superposition of the pure DMDOHEMA and pure HDEHP extraction for a concentration of individual extractant given by $x_{DMDOHEMA}$ and c_{total}.

When mixed aggregates are allowed to form, wherever concentrations of individual extractant are sufficiently high (less than individual CAC), Eu^{3+} extraction is in moderate to high regime. The individual character of pure HDEHP at low $m(HNO_3)_{aq,eq}$ or pure DMDOHEMA at high $m(HNO_3)_{aq,eq}$ is almost completely lost. An important aspect of synergistic mixtures is

balancing the pH change by specific enthalpic interactions. It can be revealed when comparing isotherm corresponding to $x_{\mathrm{DMDOHEMA}} = 0.5$ from both figures. When no specific mixed aggregates are formed, the extraction due to the pure HDEHP diminishes with $m(\mathrm{HNO_3})_{\mathrm{aq,eq}}$ due to the mentioned acid blocking effect. In the case of mixed aggregates formation, the model predicts that there should not be a major differences in extraction efficiency. Quantitative analysis yielded a explanation that the additional contribution due to the complexation $F_{\mathrm{complexation}}$ is in fact able to overcome unfavorable acid blocking effect, which is in our model given by $-N_{\mathrm{L}}\text{-}\ln(10)(\mathrm{p}K_{\mathrm{a}}^{\circ} - \mathrm{pH})$ functionality (Eq. 6.13).

In order to understand what synergy is, we need to be sure what synergy is not. That is why, throughout the chapter, we will constantly readdress this issue.

6.7 Global Overview of Liquid-Liquid Extraction Systems: Towards the Mapping of the 'Extraction Landscape'

Like in the previous chapter, but now even more pronounced we can see the variety of extraction regimes, governed by the polydispersity of the self-assembly of spherical aggregates. Due to the complexity of the system, it is convenient to study extraction efficiency by simultaneously changing a few independent system variables. Therefore, we pass our considerations of probability plots and two-dimensional extraction isotherms to what we call: 'the extraction landscape maps' (shortly maps). These maps will provide us with a perspective of global behavior of liquid-liquid extraction by identifying various regimes.

6.7.1 Extraction Maps - Influence of Extractant Mole Fraction and Acid Molality

We can extend operating Job's plots (isotherms) into 'Job's maps' by calculating Eu^{3+} extraction efficiency as a function of $m(\mathrm{HNO_3})_{\mathrm{aq,eq}}$ and x_{DMDOHEMA} at constant $m(\mathrm{Eu}^{3+})_{\mathrm{aq,eq}} = 0.035$ mol kg^{-1}, and $c_{\mathrm{total}} = 0.6$ mol dm^{-3}. Results are presented in Figure 6.10a. Coextracted $\mathrm{HNO_3}$ map is presented in 6.10b. Coextraction of $\mathrm{HNO_3}$ is important to quantify since it is a strong competition reaction that can disrupt desirability of the chemical engineering formulations. Immediately, we can notice a few regimes in extraction. The high Eu^{3+} extraction is at low $m(\mathrm{HNO_3})_{\mathrm{aq,eq}}$ and low x_{DMDOHEMA}(HDEHP controlled). The moderate extraction regime expands for intermediate x_{DMDOHEMA} values (controlled by the formation of mixed aggregates). The low extraction regimes occurs at two cases, namely at high $m(\mathrm{HNO_3})_{\mathrm{aq,eq}}$

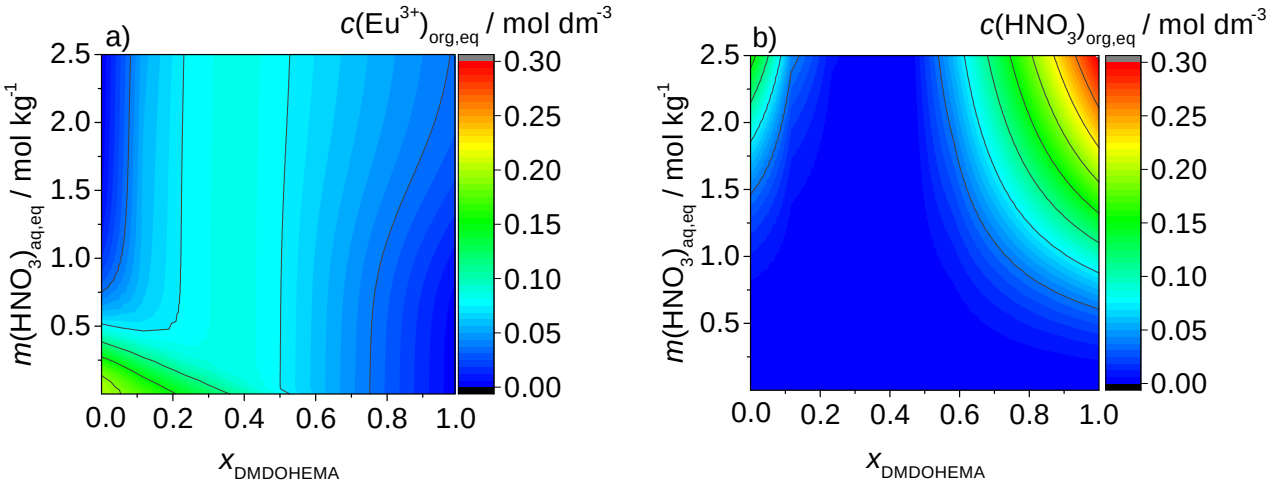

Figure 6.10 – The synergy hill. Concentrations of extracted solutes as a function $m(HNO_3)_{aq,eq}$ and $x_{DMDOHEMA}$ at $m(Eu^{3+})_{aq,eq} = 0.035$ mol kg^{-1}, and $c_{total} = 0.6$ mol dm^{-3}. a) Eu^{3+} extraction map, b) HNO_3 co-extraction map.

and low $x_{DMDOHEMA}$ (acid quenched HDEHP extraction), or at low $m(HNO_3)_{aq,eq}$ and high $x_{DMDOHEMA}$(DMDOHEMA controlled). Again, chemical potentials of solutes in the aqueous phase, and of extractants in the organic phase play a decisive role in controlling the extraction. Globally, Eu^{3+} extraction landscape presented in Figure 6.10a shows a type of hill, that corre-

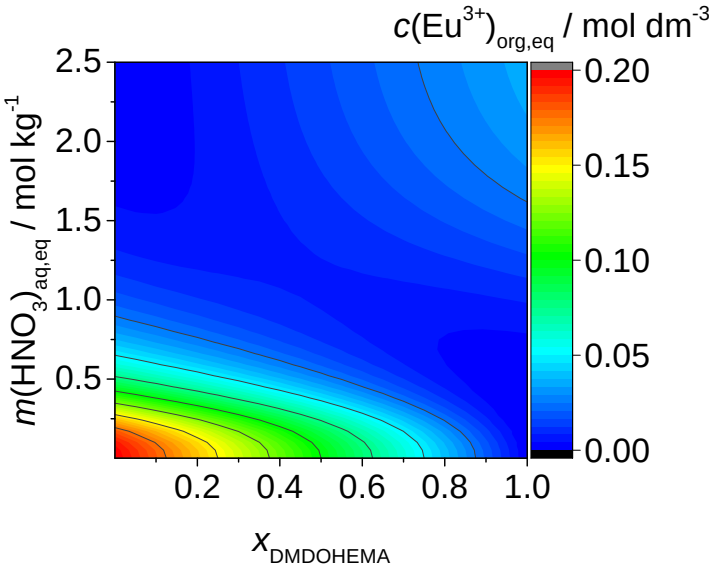

Figure 6.11 – The mountain pass. Concentrations of extracted solutes as a function $m(HNO_3)_{aq,eq}$ and $x_{DMDOHEMA}$ at $m(Eu^{3+})_{aq,eq} = 0.035$ mol kg^{-1}, and $c_{total} = 0.6$ mol dm^{-3}. No mixed aggregates are allowed to form.

sponds to synergistic mixtures. This can be easily noticed when following the isotherm for one particular $m(HNO_3)_{aq,eq}$. In the absence of mixed aggregates formation, instead of the hill, we would recover a depression in the extraction landscape (Figure 6.11). It follows that specific,

complexation governed interactions lead to formation of mixed aggregates that increase overall Eu^{3+} extraction, especially when the mole fraction of extractants is similar. A complementary HNO_3 coextraction maps reveals the two regimes of high acid uptake to the organic phase (Figure 6.10b). One occurring at low x_{DMDOHEMA} and high $m(\mathrm{HNO_3})_{\mathrm{aq,eq}}$ (see Figure 6.5c, case $x_{\mathrm{DMDOHEMA}} = 0$), and the other at high x_{DMDOHEMA} and low $m(\mathrm{HNO_3})_{\mathrm{aq,eq}}$ (see Figure 6.5c, cases $x_{\mathrm{DMDOHEMA}} = 0.7,\ 1$). The former case corresponds to the formation of pure HDEHP aggregates filled with acid and water molecules only, whereas the later corresponds to the formation of analogous pure DMDOHEMA aggregates. Acid coextraction maps resembles a sort of mountain pass in the landscape analogy. Once more, the diversity of competing chemical reactions is at display, this time on the expense of quenched Eu^{3+} extraction.

Speciation of the free extractant

The extraction efficiency map itself is insufficient to describe the self-assembly properties (recall severe polydispersity of aggregates!). That is why we have calculated complementary speciation maps of both extractants in the organic phase. Results are presented in Figures 6.12 a-d. Before examining results, let us first define the percentage of the 'free extractant' in the system. We have the percentage of the free extractant in the system $\Phi_{\mathrm{free,extractant}}$, is defined as

$$\Phi_{\mathrm{free,extractant}} = \Phi_{\mathrm{D,monomer}} + \Phi_{\mathrm{LH,monomer}} + \Phi_{\mathrm{LH,dimerized}} \tag{6.14}$$

where $\Phi_{\mathrm{D,monomer}}$, $\Phi_{\mathrm{LH,monomer}}$, $\Phi_{\mathrm{LH,dimerized}}$ are respectively the percentage of monomeric form of D, the percentage of monomeric form of LH, and the percentage of dimerized form of LH and can be written as

$$\begin{aligned} \Phi_{\mathrm{D,monomer}} &= c_{\mathrm{D,monomer}}/c_{\mathrm{total}} \\ \Phi_{\mathrm{LH,monomer}} &= c_{\mathrm{LH,monomer}}/c_{\mathrm{total}} \\ \Phi_{\mathrm{LH,dimerized}} &= c_{\mathrm{LH,dimerized}}/c_{\mathrm{total}} \end{aligned} \tag{6.15}$$

Speciation maps reveal that the synergy hill is accompanied by the high degree of micellization. This would give very low V-shaped canyon of measured critical micelle concentrations (or critical aggregate concentrations) in the organic phase, as fraction of free extractant in the system is low (Figure 6.12d). Indeed this result was already hinted experimentally, where strong aggregation was observed at the expense of free extractant concentration in the organic phase[54]. Figure 6.12a shows that HDEHP dimers dominate the mixture in the case of low x_{DMDOHEMA} and high $m(\mathrm{HNO_3})_{\mathrm{aq,eq}}$, where HDEHP remains in protonated form. Dimers concentration slightly decreases as pure acid extraction starts to induce self-assembly due to

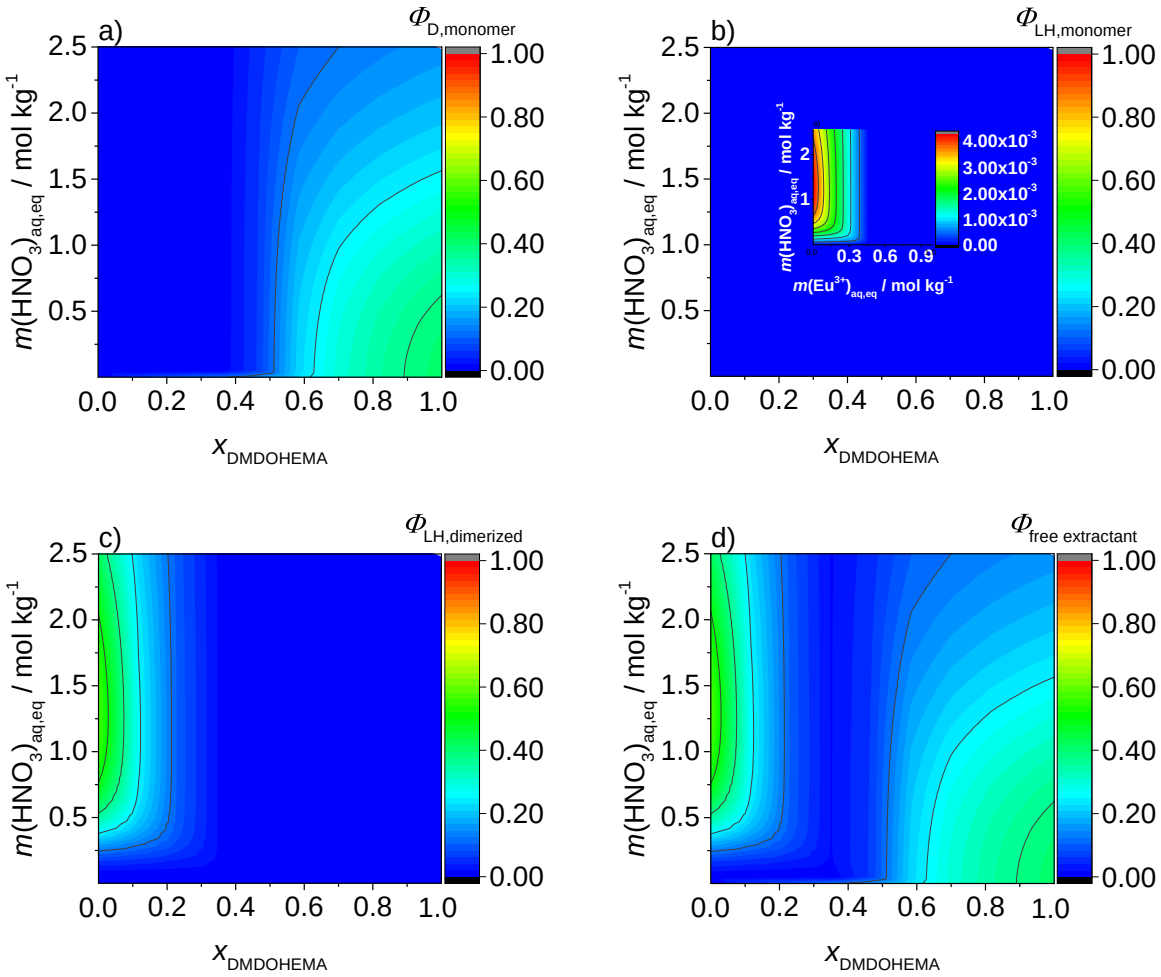

Figure 6.12 – Speciation of the extractant in the solvent as a function of x_{DMDOHEMA} and $m(\mathrm{HNO_3})_{\mathrm{aq,eq}}$, at $m(\mathrm{Eu^{3+}})_{\mathrm{aq,eq}} = 0.035$ mol kg^{-1} (pure HDEHP), and $c_{\mathrm{total}} = 0.6$ mol dm^{-3}. a) D in monomeric form, b) LH in monomeric form, c) LH in dimerized form, d) total percentage of the free extractant.

the high $\mathrm{HNO_3}$ chemical potential in the reservoir. HDEHP monomers concentration is globally small for all conditions. DMDOHEMA monomers are abundant for the low acidity, but decrease substantially upon the increase of $m(\mathrm{HNO_3})_{\mathrm{aq,eq}}$. It is the region of $\mathrm{Eu^{3+}}/\mathrm{HNO_3}$ co-extraction by pure DMDOHEMA aggregates. DMDOHEMA monomers are abundant at low $m(\mathrm{HNO_3})_{\mathrm{aq,eq}}$, since there is generally no aggregation. Concentrating the aqueous solution by increasing $m(\mathrm{HNO_3})_{\mathrm{aq,eq}}$, DMDOHEMA fraction decreases substantially, with aggregation being induced by pure acid transfer to the organic phase (complementary to Figure 6.10b).

Expanding Job's maps

We can exploit the calculated polydispersity of self-assembled aggregates to quantitatively decouple the total $\mathrm{Eu^{3+}}$ extraction map (presented in Figure 6.10a) into contributions as was

made on Job's plot in Figures 6.6a-c. Quantitative assessments of decoupled contributions is presented on Figures 6.13a-c. Figure 6.13a shows the contribution by mixed extractants aggre-

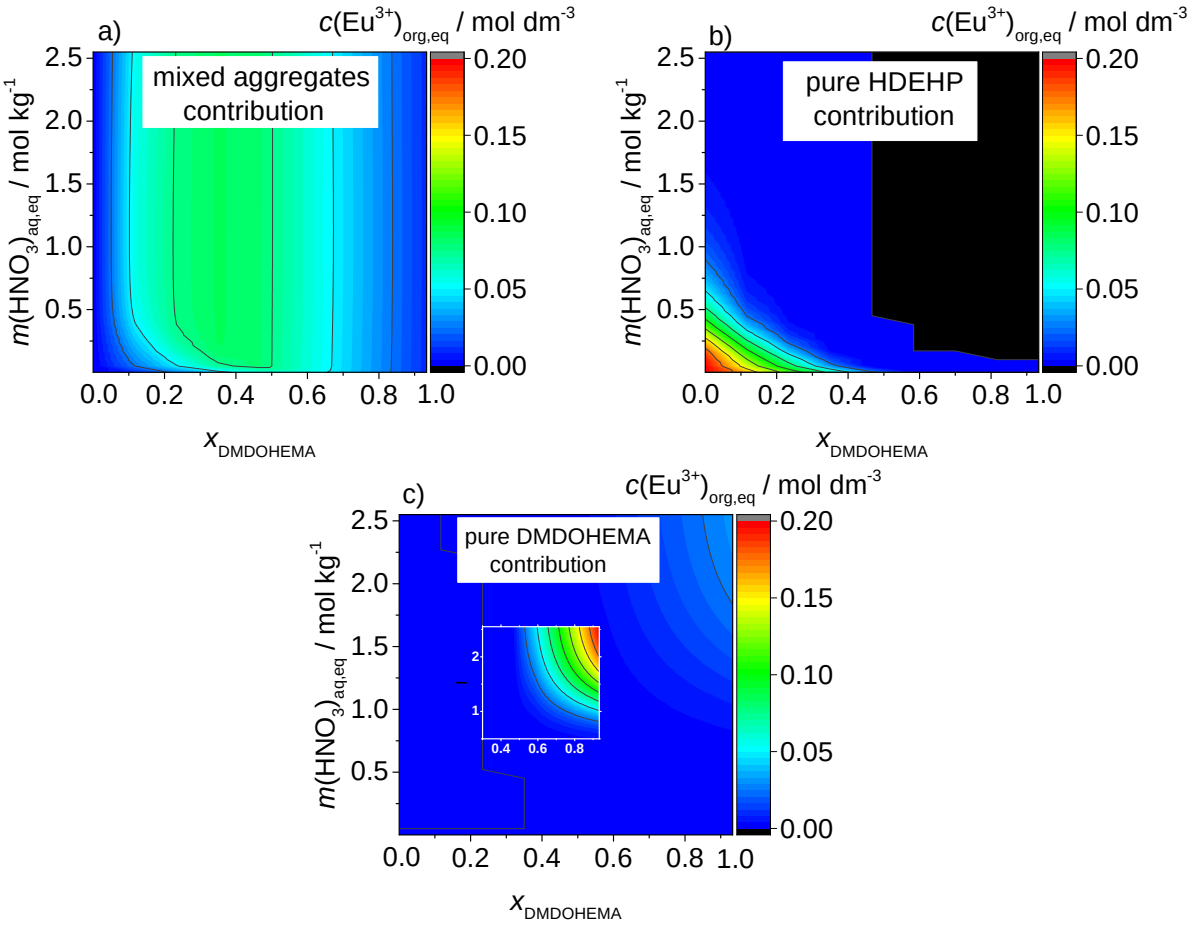

Figure 6.13 – Enhanced Job's map. Eu^{3+} concentration in the organic phase as a function $m(HNO_3)_{aq,eq}$ and $x_{DMDOHEMA}$ at $m(Eu^{3+})_{aq,eq} = 0.035$ mol kg^{-1}, and $c_{total} = 0.6$ mol dm^{-3}. a) extraction by Mixed HDEHP/DMDOHEMA aggregates, b) extraction by Pure HDEHP aggregates, c) extraction by Pure DMDOHEMA aggregates

gates. The synergy hill is now isolated. We can now observe the influence of the threshold of minimum concentration of individual extractant in the mixture. If there is insufficient concentration of individual extractant in the mixture (when $x_{DMDOHEMA} \to 0$, or $x_{DMDOHEMA} \to 1$), the influence of acid (which we sometimes referred as a crucial independent system variable) is irrelevant and cannot induce a mixed aggregates formation. Calculated aggregate concentrations at equilibrium are calculated in following manner: $c_{Agg,x} = S_{Agg,x}\, c_{LH}^{N_{LH}}\, c_{D}^{N_D}$ (Eq. 6.12). It can be seen the aggregate concentration is sensitive to the concentration of individual components. The functionality is power law, with power being the individual aggregation number. If the variation of the aggregation number is small, as is the case for pure DMDOHEMA type of aggregate (recall, we have huge polydispersity of types of aggregates and water content, but

not so much in aggregation number *e.g.* Figure 4.17), we can approximate true $c_{\mathrm{Agg},x}$ with one equilibria. It follows that $c_{\mathrm{Agg},x}$ scales with equilibrium monomer concentration to the power of the average individual aggregation number and is therefore very sensitive since we often have individual aggregation of 4 or even more. Practically, this means that if the concentrations of any of two extractants is sufficiently low, the system does not behave in synergistic manner, since the conditions for mixed aggregates formations are not fulfilled.

Figures 6.13b and c, show that the total Eu^{3+} extraction at two extremes of phase diagram are controlled by respectively pure HDEHP or pure DMDOHEMA aggregates. This was expected result, as was shown earlier. One more thing to note is the overlap of high HNO_3 co-extraction and Eu^{3+} extraction by pure DMDOHEMA aggregates. Indeed, this was illustrated in chapter dealing with DMDOHEMA, but on simple basis in form of apparent stoichiometry study. Normally, in this region the apparent stoichiometry fluctuates for the change of independent system variables.

6.7.2 Extraction Maps - Influence of Europium Nitrate and Acid Molality

The picture of extraction landscape is incomplete without the study of $m(Eu^{3+})_{\mathrm{aq,eq}}$ influence. Therefore we have calculated Eu^{3+} extraction as a function of $m(Eu^{3+})_{\mathrm{aq,eq}}$, and $m(HNO_3)_{\mathrm{aq,eq}}$ for different x_{DMDOHEMA}, and $c_{\mathrm{total}} = 0.6$ mol dm^{-3}. Results are presented in Figures 6.14a-e. Figure 6.14a shows characteristic irreversible behavior of pure HDEHP system ($x_{\mathrm{DMDOHEMA}} = 0$). The behavior is the same as in previous chapter for HDEHP case alone[193]. Same applies for the case for $x_{\mathrm{DMDOHEMA}} = 1$, where system is pure DMDOHEMA[171]. Two borderline cases are given as a guideline for easier understanding of the influence of synergistic mixtures on overall extraction efficiency.

At $x_{\mathrm{DMDOHEMA}} = 0.2$ (Figure 6.14b) there is a substantial change in the extraction landscape. Now the green color dominates the graph, suggesting the moderate extraction efficiency due to the mixed aggregates formation. $x_{\mathrm{DMDOHEMA}} = 0.2$ case still maintains partial HDEHP character, especially at low $m(HNO_3)_{\mathrm{aq,eq}}$, and high $m(Eu^{3+})_{\mathrm{aq,eq}}$. This is not surprising at all, since the total HDEHP concentration in the system is 0.42 mol dm^{-3}. Note that insets in Figures 6.14b-d are provided to simplify the determination of the differences in the extraction regimes in the case of synergistic mixtures. The differences are globally small, compared to the pure HDEHP and DMDOHEMA cases. When dealing with the synergistic mixtures, the question is no longer how to design efficient formulation, but to choose more efficient among

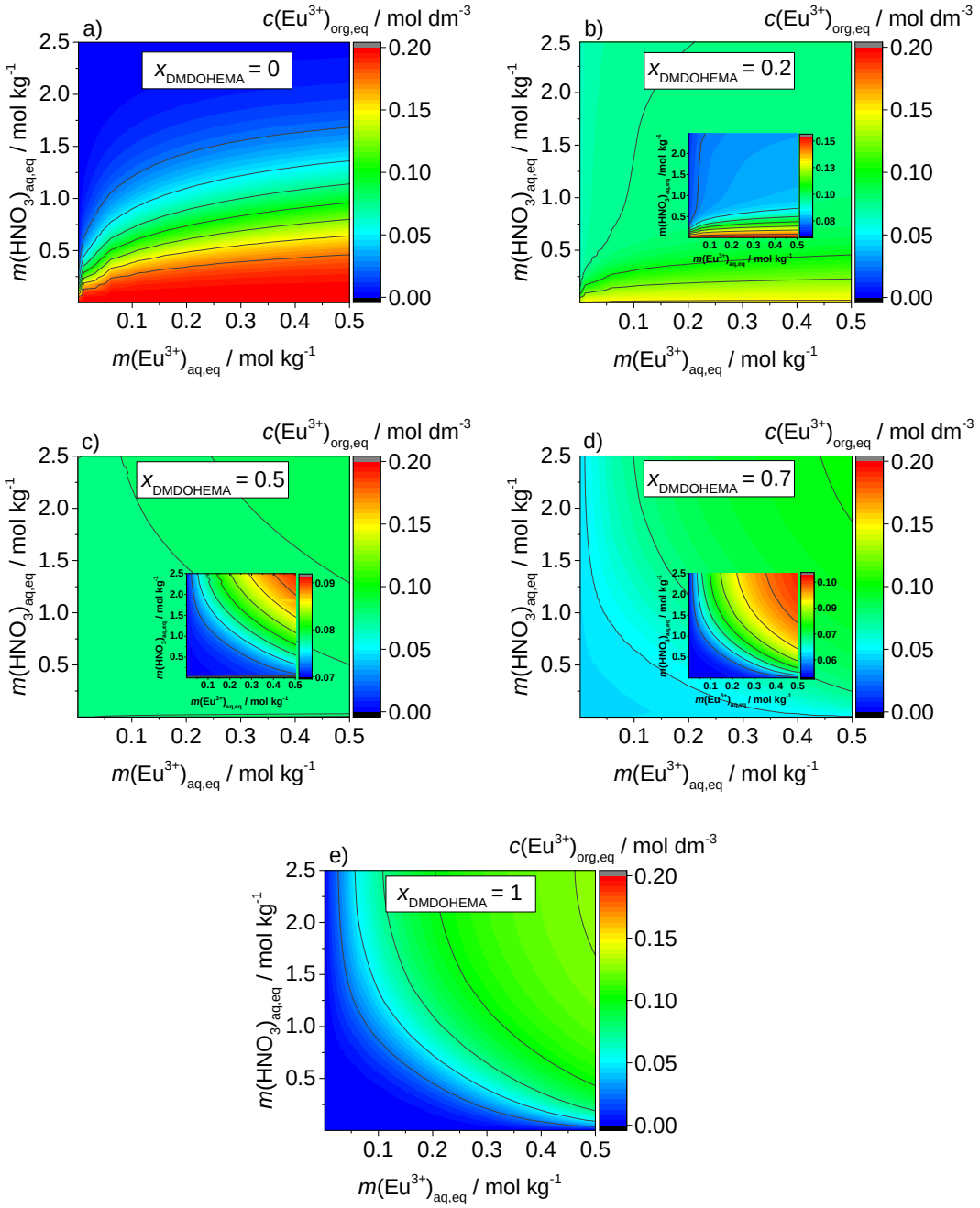

Figure 6.14 – Concentrations of extracted Eu^{3+} $c(Eu^{3+})_{org,eq}$, as a function $m(Eu^{3+})_{aq,eq}$ and $m(HNO_3)_{aq,eq}$ for different $x_{DMDOHEMA}$, and $c_{total} = 0.6$ mol dm^{-3} (a-e).

efficient formulations. This represents the core of the sustainability in the industry of metal cation recovery and the nuclear fuel reprocessing[3, 1]. The case of $x_{DMDOHEMA} = 0.5$ shows generally flat extraction landscape, but there is slight resemblance towards DMDOHEMA characteristics. Recall that the synergistic peak reported experimentally was around 0.35, and our experimentally observed was at 0.4. Therefore, an increase to $x_{DMDOHEMA} = 0.5$ is responsible for the slight resemblance of the DMDOHEMA behavior. Free extractant speciation shows that aggregation comes at the expense of HDEHP dimers. Surprisingly, DMDOHEMA monomers

still constitute around 10% of the free extractant in the system (Inset in Figure 6.15a). To elucidate this particular property of the synergistic mixture at $x_{\mathrm{DMDOHEMA}} = 0.5$ we need to back at the beginning of the chapter to study the aggregates probabilities in Figure 6.5. In order to assemble the mixed extractant aggregate, we need less large DMDOHEMA molecules, compared to HDEHP. Their role is, in terms of primitive explanation, to maintain the mixed aggregate by enclosing the polar core, while HDEHP is involved in complexation. Therefore, less DMDOHEMA is needed to boost the extraction. If there is no pure acid extraction by DMDOHEMA, then a part of its total concentration remains diluted as monomers. Indeed, when increasing $m(\mathrm{Eu}^{3+})_{\mathrm{aq,eq}}$ and $m(\mathrm{HNO_3})_{\mathrm{aq,eq}}$, now fraction of monomeric DMDOHEMA decreases and system is fully saturated. This state of the system is in principle characterized as unstable, and there is a danger of the third phase formation. The increase of x_{DMDOHEMA}

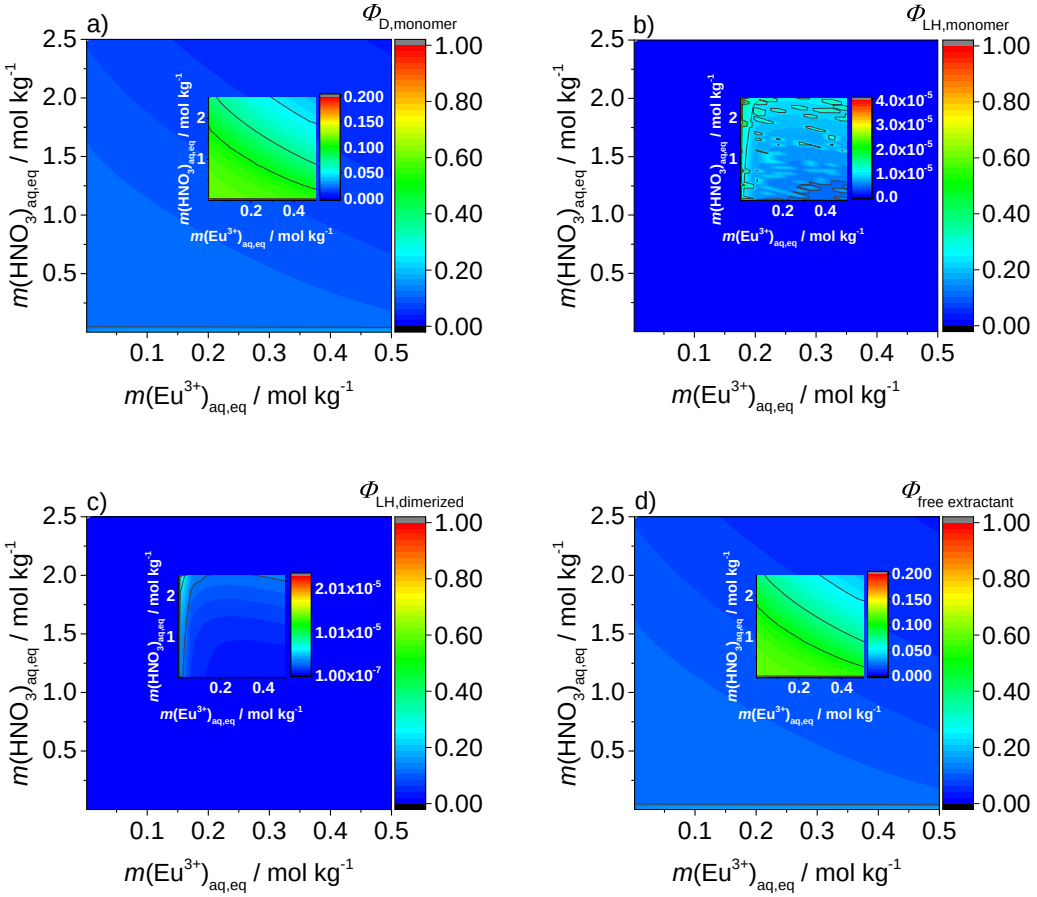

Figure 6.15 – Speciation of the extractant in the solvent as a function of $m(\mathrm{Eu}^{3+})_{\mathrm{aq,eq}}$ and $m(\mathrm{HNO_3})_{\mathrm{aq,eq}}$, at $x_{\mathrm{DMDOHEMA}} = 0.5$ (mixture), and $c_{\mathrm{total}} = 0.6$ mol dm^{-3}. a) D in monomeric form, b) LH in monomeric form, c) LH in dimerized form, d) total percentage of the free extractant.

towards 1 causes a moderate change in the extraction landscape. Gradually it ends up in the

pure DMDOHEMA case, but the change itself is not so severe due to the constant probability of mixed aggregates (recall the probability plots for different x_{DMDOHEMA} and $m(\mathrm{HNO_3})_{\mathrm{aq,eq}}$).

The severe change would be observed if there were no mixed aggregates formation. To emphasize the specificity that mixed aggregates exhibit to the global extraction landscape, we have calculated extraction maps with no mixed aggregation, and results are presented in Figures 6.16a-e. In the case of no mixed aggregates formation, the change in the extraction landscape is evident. The total extraction landscape in this case is a simple superposition of pure HDEHP and DMDOHEMA extraction maps, scaled by mole fraction. Since we consider ideal gas-like bulk micelle model, the change in extractant more fraction is the leading force for the change in the extraction regimes. Specific nature of synergistic mixture is in our approach given by generalized form of F_{complex} (Eq. 6.2) which is primitive additive potential for very cation/extractant site couple. Still, recall that we have respected the first coordination sphere on the basis of steric constraint. This argument was based on the reported set of optimized structures by DFT[37]. Note that in those studies, energies associated with removing or replacing particular extractant molecule in cation's first coordination sphere was the same order of magnitude as our reported complexation energy parameter $E_{i,z}$, obtained by fitting. Our model predicts that this specific nature of complexation (with strong emphasize on enthalpic contribution!) causes flattening of extraction landscape hence no major difference in extraction efficiency can be observed. This opens the question: are there multiple local maximums on the extraction map. If so, can we trace them if the mesh in calculations is fine enough. The speciation maps presented in Figure 6.15b shows situation similar to this, but we cannot claim if this is a consequence of the numerical noise within calculations. Still it is interesting aspect of the synergistic mixtures. Again we stress that dealing synergistic mixtures means choosing the more efficient among efficient liquid-liquid extraction formulations.

6.8 Complexation Energy Study and the Self-Assembly

In order to understand the internal energy (or the enthalpy) influence of coordination chemistry onto the liquid-liquid extraction efficiency of synergistic mixtures, as well as on its core phenomena *i.e.* the colloidal self-assembly, we need to go beyond our present results[4]. We start by defining the total Eu^{3+} distribution coefficient as: $D_{\mathrm{Eu^{3+},total}} = D_{\mathrm{Eu^{3+},LH}} + D_{\mathrm{Eu^{3+},D}} + D_{\mathrm{Eu^{3+},excess}}$, where $D_{\mathrm{Eu^{3+},LH}}$, $D_{\mathrm{Eu^{3+},D}}$, and $D_{\mathrm{Eu^{3+},excess}}$ are respectively the distribution coefficients of decou-

[4]Due to the intent to represent general classes of extractants, like ion-exchangers and solvating class, we abandon HDEHP and DMDOHEMA designations in this section and refer to extractants like LH and D.

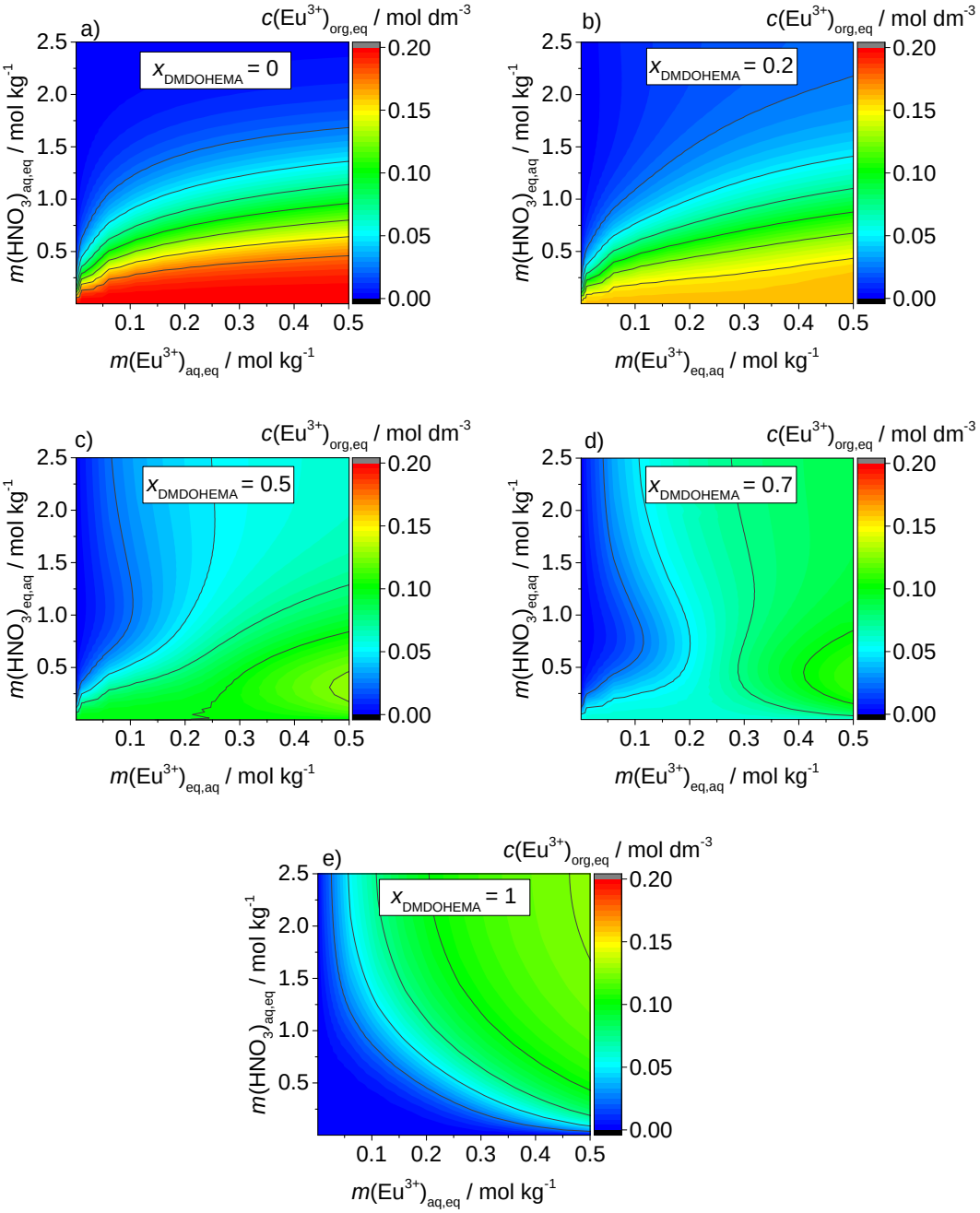

Figure 6.16 – Concentrations of extracted Eu^{3+} $c(Eu^{3+})_{org,eq}$, as a function $m(Eu^{3+})_{aq,eq}$ and $m(HNO_3)_{aq,eq}$ for different $x_{DMDOHEMA}$ and c_{total} = 0.6 mol dm^{-3} (a-e). Eu^{3+} extraction isotherms as a function of $m(HNO_3)_{aq,eq}$ for different $x_{DMDOHEMA}$, at $m(Eu^{3+})_{aq,eq}$ = 0.035 mol kg^{-1}, and c_{total} = 0.6 mol dm^{-3}. The extraction is attributed solely to the formation of pure HDEHP and DMDOHEMA aggregates only.

pled extraction by pure acidic extractant LH aggregates, extraction by pure non-ionic extractant D aggregates, and the excess extraction due to the formation of mixed aggregates. Each distribution coefficient is defined as a ratio of extracted Eu^{3+} in the organic phase and Eu^{3+} in the aqueous phase at equilibrium. $D_{Eu^{3+},total}$ definition holds as long as there are no interaction between two extractants, which is the case in our model (recall that we neglected formations of mixed extractants adducts).

In the case of the synergy, $D_{Eu^{3+},excess} > 0$, whereas in the absence of the synergy $D_{Eu^{3+},excess} = 0$. Practically it means that we have larger extraction than what would be expected if only individual pure extractants aggregates form. D represents any type of non-ionic extractant, and its affinity towards Eu^{3+} is characterized by complexation energy parameter $E_{Eu^{3+},D}$. In the same manner LH represents any acidic extractant with its affinity towards Eu^{3+} expressed by $E_{Eu^{3+},LH}$. Hypothetically, we can set $E_{Eu^{3+},D}$ and $E_{Eu^{3+},LH}$ as a continuous variables to artificially represent different types of extractant/Eu^{3+} metal cation couples. This tactics was made in every last section of previous two chapters, just on simpler cases. What we can further do is to investigate the influence of $E_{Eu^{3+},D}$ and $E_{Eu^{3+},LH}$ on Eu^{3+} extraction efficiency *i.e.* the distribution coefficients. Therefore, we have calculated $D_{Eu^{3+},total}$ and $D_{Eu^{3+},excess}$ as a function of $-E_{Eu^{3+},D}$ and $-E_{Eu^{3+},LH}$ for $x_{DMDOHEMA} = 0.5$, $m(HNO_3)_{aq,eq} = 1$ mol kg^{-1}, $m(Eu^{3+})_{aq,eq} = 0.035$ mol kg^{-1}, and $c_{total} = 0.6$ mol dm^{-3}. Negative values of $E_{Eu^{3+},D}$ and $E_{Eu^{3+},LH}$ are chosen for easier understanding of the phenomena (negative values by convention describe favorable contribution *e.g.* the enthalpy). Results are presented in Figure 6.17a-b.

From Figure 6.17a it can be seen that for the choice of two weak extractants in the system, with $-E_{Eu^{3+},D}$ and $-E_{Eu^{3+},LH}$ larger than $-10\ k_BT$, there is almost no extraction, thus $D_{Eu^{3+},total}$ and $D_{Eu^{3+},excess}$ are negligible. To obtain the additional information concerning the self-assembly at those conditions, we turn to extractant speciation maps presented in Figure 6.18a-d. It can be seen that extractant D is in its monomer form, whereas LH remains in the form of dimer (and monomer, as given by equilibrium). The percentage of free extractant (the sum of all monomeric and dimerized extractants in the system) is approaching 80%, which suggest that the conditions for substantial self-assembly are not fulfilled. A further inspection reveals that there is a small aggregation due to the pure water molecules extraction, but the fraction is rather small. That state of the system is characterised by the extractants present as monomers, dimers or other mixed adducts (if known to exist).

Now, if we decrease both complexation energy parameters along the diagonal (increase in affinity towards the cation to represent moderate strength of extractants) there is a gradual increase in $D_{Eu^{3+},total}$ (pale blue to green color transition), which means we started a moderate

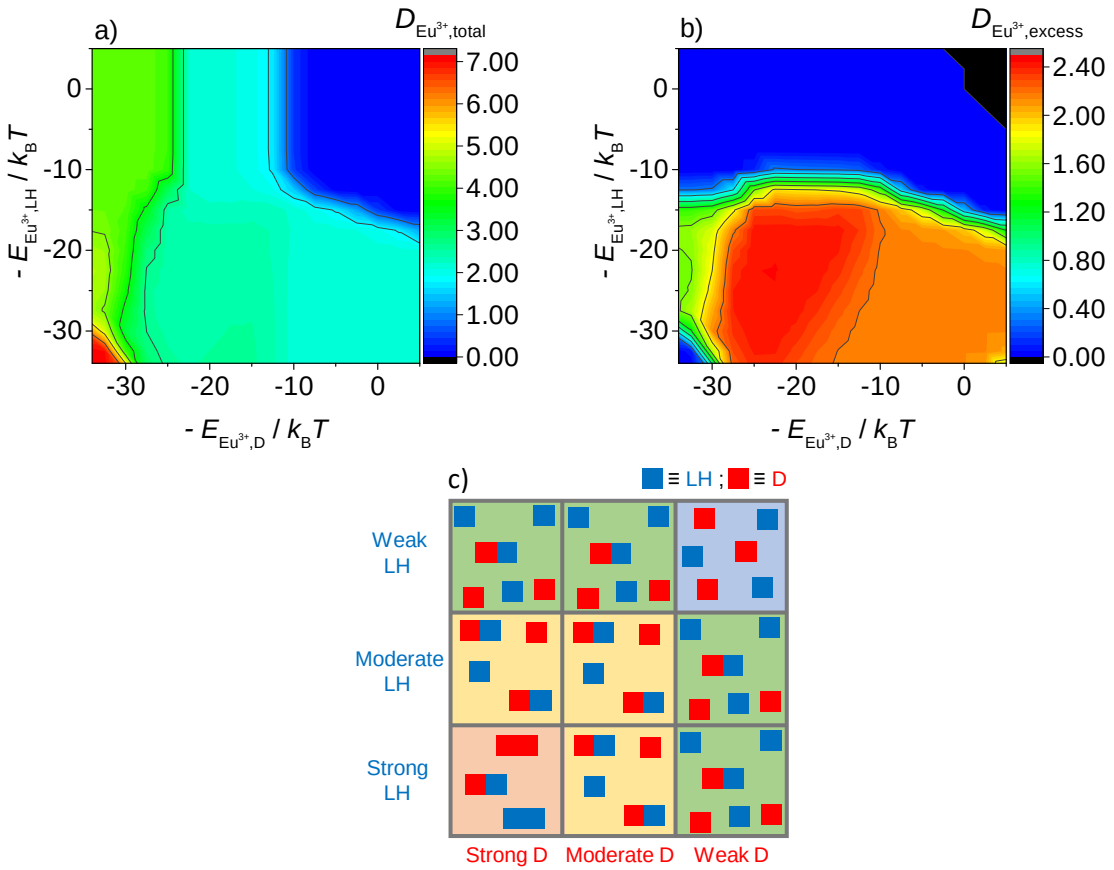

Figure 6.17 – Eu^{3+} distribution coefficient (a), and the excess Eu^{3+} distribution coefficient (b) as a function of the negative values of the complexation energy parameters per bond, $-E_{Eu^{3+},D}$, and $-E_{Eu^{3+},LH}$. System conditions are: $x_{DMDOHEMA} = 0.5$, $m(HNO_3)_{aq,eq} = 1$ mol kg^{-1}, $m(Eu^{3+})_{aq,eq} = 0.035$ mol kg^{-1}, and $c_{total} = 0.6$ mol dm^{-3}. Negative values of $E_{Eu^{3+},D}$ and $E_{Eu^{3+},LH}$ are chosen for easier understanding of the phenomena (negative values by convention describe favorable contribution *e.g.* the enthalpy). Figure (c) corresponds to schematic representation of the enthalpy control in the self-assembly of extractant mixtures. The abscissa corresponds to the complexation energy of extractant D, whereas the ordinate corresponds to complexation energy of LH. Red squares depict non-ionic extractant D, whereas blue squares depict acidic LH extractant. Merged squares depict aggregates.

extraction. On the other hand, its counterpart $D_{Eu^{3+},excess}$ map for those values showed an abrupt increase (red color). Very soon there is flat maximum recovered. This practically means that most of extraction in that region is attributed to the formation of mixed aggregates responsible for $D_{Eu^{3+},excess}$. The extractant is consumed for the formation of mixed aggregates with larger aggregation numbers (see Figure 6.18d). The fraction of free extractants rapidly diminishes. For the very low values of $-E_{Eu^{3+},D}$ and $-E_{Eu^{3+},LH}$ (in the case of very strong affinities that represent very strong extractants *e.g.* surfactants) $D_{Eu^{3+},total}$ further increases,

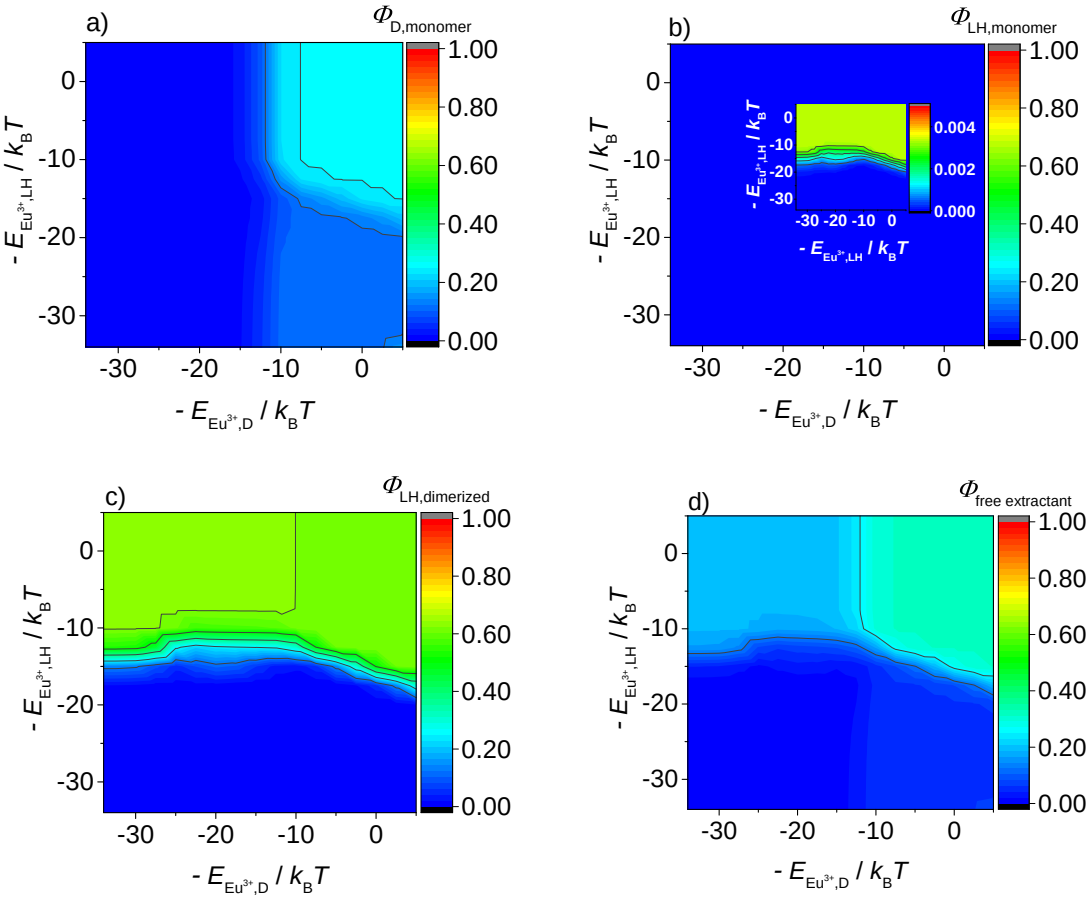

Figure 6.18 – Speciation of the extractant in the solvent as a function of the negative values of the complexation energy parameters per bond, $-E_{\mathrm{Eu^{3+},D}}$, and $-E_{\mathrm{Eu^{3+},LH}}$. System conditions are: $x_{\mathrm{DMDOHEMA}} = 0.5$, $m(\mathrm{HNO_3})_{\mathrm{aq,eq}} = 1$ mol kg^{-1}, $m(\mathrm{Eu^{3+}})_{\mathrm{aq,eq}} = 0.035$ mol kg^{-1}, and $c_{\mathrm{total}} = 0.6$ mol dm^{-3}. a) D in monomeric form, b) LH in monomeric form, c) LH in dimerized form, d) total percentage of the free extractant.

but surprisingly $D_{\mathrm{Eu^{3+},excess}}$ for those conditions decreases. What does it mean? It means that sufficiently strong extractants start to form pure D or LH aggregates. The restriction of the composition of the first sphere complex around lanthanide cation blocks the further decrease of the system free energy, since no additional extractant can be incorporated in the first Eu^{3+} coordination sphere due to the steric hindrance. As a consequence, additional extractants are being spent to constitute a second coordination sphere. In the case of pure D, or LH, the internal energy contribution is high enough to overcome all the quenching terms in the free energy approach. Globally, it is more favorable to utilize most of the extractant for the formation of the first-sphere in pure extractant aggregate complexes, than to maintain large mixed aggregates with extractants in the second sphere around cation unable to make favorable contributions. Note that in this region, we are approaching high cation loading conditions that

may easily cause a phase splitting *i.e.* the third phase formation. It must be emphasized that phase splitting cannot be directly predicted by our model, since aggregates activity coefficients are not included within MAL (recall the assumption of the ideal gas of aggregates in dilute regime). Still, extractant saturation provided by our model can serve as an indication of the phase instabilities.

Another very important core aspect of self-assembly of two extractant systems is lurking among results in Figures 6.17a-b. In the case that one extractant is strong and the other is weak, for a particular system conditions, there is a certain non-negligible extraction. The percentage of the free extractant in the system ranges from 20 to 50 %, indicating weak to moderate self-assembly properties. Conclusion is that we can have micellization even if one extractant is weak. The common example of such weak amphiphile molecule is 1-octanol, part of the class of phase modifiers. The fact that 1-octanol acts sometimes as a cosolvent or as a cosurfactant is nothing but the manifestation of its amphiphilic nature[222, 25]. If the overall system free energy is favoring the micellization with another surfactant, phase modifiers will be incorporated in the mixed film of the aggregate (cosurfactant behavior). Otherwise, phase modifiers will be present in the organic solvent in the form of monomers, dimers or other types of mixed adducts (cosolvent behavior).

Note also that these results are valid for certain system conditions (see Figure 6.17 caption), and there is influence of other independent system variables. We have made a study of the influence of different acidities in the system. Results are presented in Figures 6.19a-e. The lower acidity ($m(\mathrm{HNO_3})_{\mathrm{aq,eq}} = 0.1$ mol kg^{-1}) favor the LH dissociating, thus broadening the region of maximum extraction. Contrary to that, high acidity ($m(\mathrm{HNO_3})_{\mathrm{aq,eq}} = 3$ mol kg^{-1}) diminish LH working region, but increase the area of moderate extraction by boosting D-governed extraction. A phenomenon of increasing $D_{\mathrm{Eu^{3+},total}}$ but at the same time decreasing $D_{\mathrm{Eu^{3+},excess}}$, is more pronounced for low $m(\mathrm{HNO_3})_{\mathrm{aq,eq}}$. This is due to the fact that at low $m(\mathrm{HNO_3})_{\mathrm{aq,eq}} = 3$ mol kg^{-1}, LH extractant can dissociate and more easily complex the target cation. Once again, we can conclude that usage of mixtures provides chemical engineering with variety of system conditions that exhibit properties of desirable formulation.

Summary of the self-assembly regimes governed by enthalpic contributions

To sum up, there were four major phenomena identified in Figure 6.17a-b. In order to more easily understand these separate cases, we have provided a small scheme in Figure 6.17c. In the case that both hypothetical extractants are weak, there is no aggregation and the system is

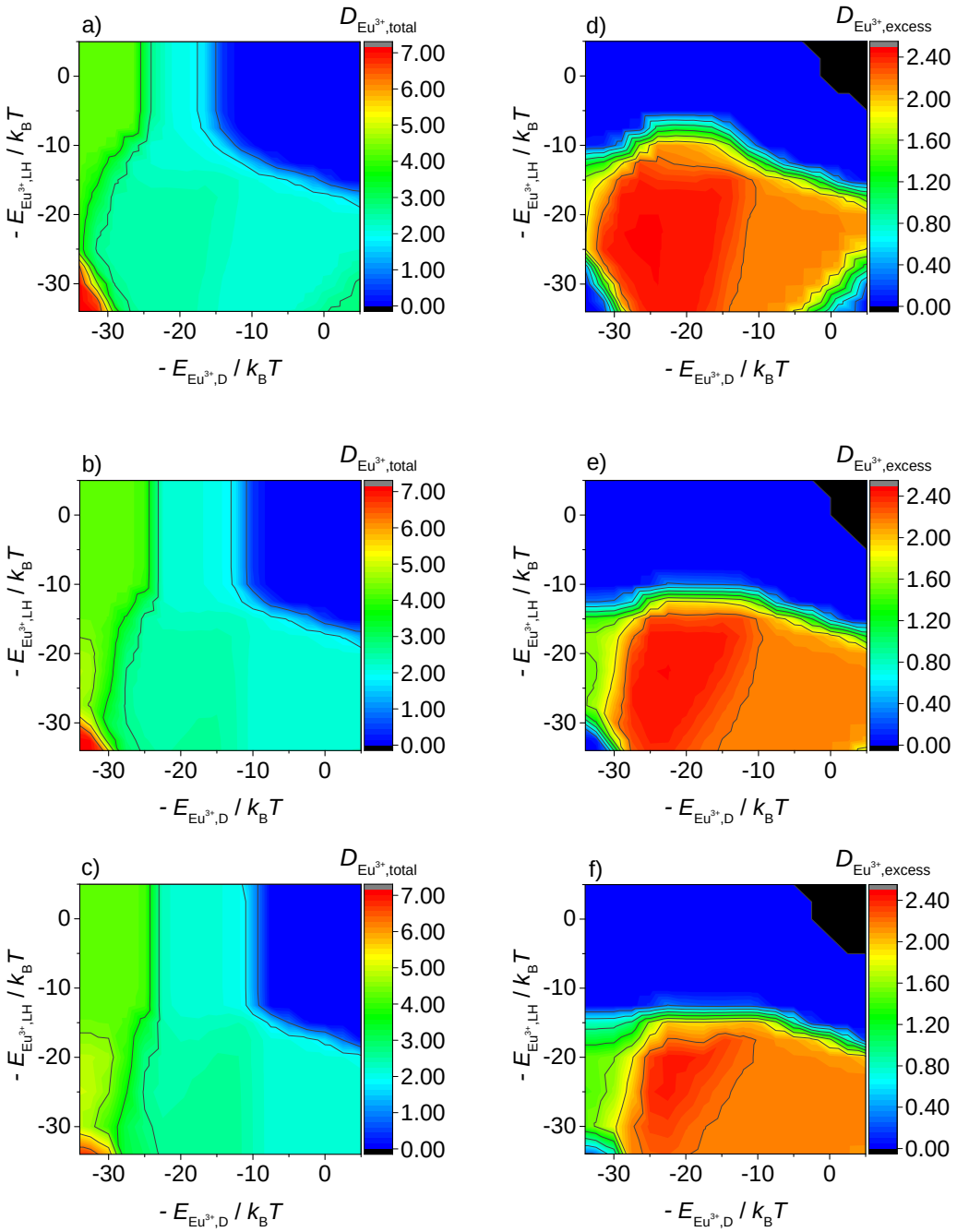

Figure 6.19 – Eu^{3+} distribution coefficient (a-c), and the excess Eu^{3+} distribution coefficient (d-f) as a function of the negative values of the complexation energy parameters per bond, $-E_{Eu^{3+},D}$, and $-E_{Eu^{3+},LH}$. Results are presented for three different acid concentrations in the bulk aqueous solution at $x_{DMDOHEMA} = 0.5$, $m(Eu^{3+})_{aq,eq} = 0.035$ mol kg^{-1}, and $c_{total} = 0.6$ mol dm^{-3}. a),d) $m(HNO_3)_{aq,eq} = 0.1$ mol kg^{-1}, b),e) $m(HNO_3)_{aq,eq} = 1$ mol kg^{-1}, c),f) $m(HNO_3)_{aq,eq} = 3$ mol kg^{-1}.

governed by global entropy of system, as represented by scattered blue end red squares (upper right corner of Figure 6.17c). There is no aggregation, hence extractants are dispersed as monomers, dimers, or adducts. In the second case of moderate extractant pairs, the system

was dominated by the formation of mixed aggregates, the extraction and self-assembly are also in moderate regime. The system is enthalpy driven. This is represented as majority of blue and red squares are connected (connected squares represent aggregates). The third case when both extractants very strong caused formation on pure D and LH aggregates, as represented by blue-blue and red-red connections (lower left corner of Figure 6.17c). The system approaches the third phase formation and is strongly governed by enthalpy. Lastly, the case of combination of strong and weak extractant provides weak extraction, and weak to moderate self-assembly (pale green squares), depending on the properties of the aqueous phase. Together, these four major phenomena underline the self-assembly in the case of the mixture of extractants. The majority of squares are scattered with small connected fraction to represent weak aggregation. Our calculations show that the synergy and mixed amphiphile aggregation in general, is simple displacement of amphiphile from apolar environment to nanodomains characterized by dual hydrophobic and hydrophilic nature *i.e.* reverse micelles. Therefore, the concept is not new, and is simple[223]. The only difference is the inclusion of the generality. It must be noted that idea for this study originates from, to some extent, similar studies but on different applications. Examples of the self-assembly to the surface of metal[172], or the protein stabilization and conformational stability of macromolecules in solutions in general [224, 225], are in fact studies of enthalpic or entropic control in the complex system.

6.9 Conclusion

We have developed a minimal thermodynamic model for the prediction of liquid-liquid extraction efficiency. The basis of the model is to calculate the free energy of every possible aggregate at infinite dilution, by establishing the relation that accounts for various terms that are involved in aggregation phenomena. The novelty is the fact that we consider every possible aggregate, while no additional parametrization is required. Therefore, we have abandoned the historical picture of simple stoichiometry involved in the extraction process.

The initial idea that the model should be general is reflected in the result of calculations, as we have identified dozens of different aggregates at equilibrium. The aggregates compositions are under influence of system independent variables. It was shown that aggregates compositions are prone to changes upon the change of independent variable *e.g.* the change of first, and second coordination sphere by increase of the bulk acid concentration, or the mole fraction of the extractants in the system. It follows that Figure 6.5 is the central figure of this chapter. In one composite figure, the huge variety of aggregates different in composition but similar in free

energy can be observed. This variety is reflected in every macroscopic property of the system.

Diversity of aggregates enabled us to quantitatively decouple the extraction efficiency into contributions. The most of the synergistic maximum in extraction isotherm was attributed to the self-assembly of mixed extractant aggregates, but for some system conditions the total extraction is partly controlled by creation of pure extractant aggregates also. The sum of all contributions gives total extraction isotherm. The polydispersity of aggregates (mutually competing reactions) at chemical equilibrium, suggests the change in current paradigm that synergy is the occurrence of one particular mixed aggregate.

The severe differences in aggregates compositions induced by the change in system conditions inspired a change from evaluation of historical extraction isotherms, to extraction "maps" in three-dimensional representation. This enabled us to observed a system on more global scale. As a results, different regimes in self-assembly, and thus the liquid-liquid extraction efficiency have been investigated. Within the calculation of the speciation as a function of multiple independent variables, a new aspect of "greener" chemistry emerged. Calculations show that liquid-liquid extraction can be tuned, which in principle, can reduce the usage of effluents or lower the usage of expensive extractant molecules just by utilizing the mixtures. Furthermore, proper speciation of the organic phase is crucial for the study of mass transfer, since viscosity (one of crucial parameters of efficient industrial formulations) depends on it.

A hypothetical study of global entropy and the internal energy (or enthalpy) influences, showed that in the case of mixture of extractants there is a complex interplay that underlines the self-assembly. We distinguished entropy driven weak association extractant systems at one hand, and enthalpy driven strong association between strong extractants mediated by coordination to multivalent cation.

A present work on micellization in dilute regime predates the organic phase structuring, thus is complementary to it[33]. The enlightening view of liquid-liquid extraction proposes a symmetric global maximum in the probability of observation landscape by taking into account formation of aggregates, their morphology, size and further higher-order interactions[226]. We take a liberty of expanding this view to a multiple maximum (with one global) probability map, where the essential building blocks are polydisperse smaller structures that form in the dilute regime.

Summary of the behavior of mixture of HDEHP and DMDOHEMA

Mixture of HDEHP and DMDOHEMA represents the mixtures of acidic and solvating extractants. Simple prediction of the behavior of such system would correspond to superposition of the two separate cases if both concentrations of extractants are above their individual CAC, like presented in Figures 6.16a-e. Experimentally, and predicted by our model also, this is not the case. Strong non-linear effects are observed that cannot be accounted simple equilibrium. Depending of the choice of variables to change, the occurrence of specific mixed aggregates causes resilience of extraction efficiency when changing the independent system variables (a slight to moderate changes), as can be seen in Figures 6.14a-e. Analogy to this resilience is the buffer, which opposes the change to solution pH. In other cases it can causes a severe fluctuation of extraction efficiency (Figure 6.10). To conclude: the mixture does not always yield macroscopic property which is the superposition of individual constituents *i.e.* we need model to elucidate the phenomenon at hand.

Chapter 7

General Conclusion

In this work we have addressed two common problematic that are interesting from both fundamental science, as well as in chemical engineering, industrial aspect. We studied examples of systems involving highly porous solid adsorbents dispersed in the aqueous solutions of ions, and on liquid-liquid extraction assisted by weak amphiphiles *i.e.* extractant molecules. In order to give tools and new insights for chemical engineering, in case of former porous materials, the crucial issues is to quantify the adsorption inside pores. By experimental techniques, this is not possible because of the high disorder of such systems. In the case of later, liquid-liquid extraction modelling, the important aspect is to provide a method for reducing experimental plans that is of everyday work for chemical engineers. Moreover, by keeping the molecular picture of constituents it is in principle possible to propose new solutions for the design of liquid-liquid extraction processes.

We have focused on mesoscopic modelling since it is suitable to capture the physics and chemistry of constituents of the system but also manageable enough to be scaled to engineering scale. No theory is without drawbacks, same applies for the levels of theories we have used throughout this thesis. Still, with well described approximations and limitations, microscopic modelling is still a good framework to bridge the fundamental science and chemical engineering.

Study of TiO_2 Nanotubes in an Aqueous Solution

In order to study the decontamination or any type of adsorption in case of nanotubular structures, the first thing is to obtain a proper description of the charge properties. Charge properties assume two important parts (but mutually dependent), namely the charge of surface and the ion distributions that characterize the medium in contact to surfaces. Since the surface charge exhibits the electric field on the solution in contact and creates inhomogenities, and ions affect

the surface charge by direct association, it is natural to couple a charge regulation method with the theory of inhomogenous liquids.

In our approach, we have used the simplest case of the classical density function theory: the Poisson-Boltzmann theory. The charge regulation was taken into account as two successive protonations of surface site. Ion distributions set the concentration of protons at interface, which regulates that charge. Since ions distributions and surface charge are dependent we calculated the system of Poisson-Boltzmann non-linear differential equations with charge regulated boundary conditions in a self-consistent manner.

The novelty of the approach was the fact that we studied the system as whole, starting from the cylinder axis of symmetry (at which we set the origin of the cylindrical coordinate system) towards the bulk solution far from the outer surface. If follows that we had to solve two non-linear PB equations along with four regulated boundary conditions.

Fitting of the experimental polyelectrolyte titration data, we have obtained protonation constants, which have correct order of magnitude. Moreover, by considering Bjerrum definition of ion pair dielectric continuum with only electrostatic potential between surface site and proton at the interface, it was shown that obtained constants have acceptable values.

With the parametrized model, we have studied the charge properties of TiO_2 nanotubes in an aqueous solution. We have shown the needed conditions in terms of the inner radius of nanotubes and the salt concentration in the reservoir, for which the interior of nanotubes behaves like bulk solution. The study was further expanded with the influence of reservoir pH. As expected for the inner nanotubes radius equal 4 nm in the case of low salt concentration in the reservoir, electroneutrality condition is not fulfilled inside the cavity and aqueous solution in contact the outer surface is needed to equilibrate the overall system. In those conditions the ions confined inside are under influence by the electric field. Increasing the reservoir salt concentration, causes more efficient screening and ions distributions show bulk-like behavior.

The key finding proposed by our work is the dissimilarity of the total charge of two surface which does not follow the ratio of their radii, in low salt regime. The unexpected accumulation of the charge at the outer surface was attributed to the lack of electroneutrality inside the nanotubes. This phenomenon is important from the fundamental point of view, but also for any applications. Charge governed adsorption or photocatalysis would be more efficient at the outer surface, if our predictions are correct. In the absence of any experimental technique that can provide enlightening proof, the only choice is to use some of the known and better theories and see if the charge accumulation occurs. Keeping this in mind, we must be careful with the choice of theory, since at low salt concentrations, MD simulations are particularly useful.

Currently, the modified PB and coupled PB-MSA approaches are being utilized to study this issue.

Modelling Liquid-Liquid Extraction

Modelling liquid-liquid extraction presented in this thesis manuscript was split into three parts. Three parts, even though intimately mixed, demanded a separate considerations.

In the first part we have introduced the model based on the idea that aggregates different by composition but similar in the free energy are coexist in chemical equilibrium. The idea involves two major aspects: 1) establishing the multiple chemical equilibrium, 2) proposing the framework in terms of analytical expressions to calculate the free energy of any possible aggregate, as proposed by multiple chemical equilibrium. Practically, what we had to do is to establish multicomponent general MAL, but not to try to fit the constants. Instead we had to calculate the free energy of any possible aggregate at infinite dilution *i.e.* its standard chemical potential.

The developed model was named Droplet model. The model is ideal and no potentials among aggregates are taken into account. We have demonstrated strengths and weaknesses of the model on the example of non-ionic solvating DMDOHEMA extractant, which is important for the nuclear industry of fuel reprocessing. The key finding of the chapter was identification of different types of aggregates present. The speciation was tuned by the change of system variables, namely salts concentrations, pH, extractant concentration[1]. Furthermore, for each type of aggregate a certain degree of polydispersity of the aggregation number and the water content was predicted. It was then made clear that the change in the behavior (or the trend) of the overall extraction efficiency is in fact governed by the strong competing self-assembly of aggregates different by compositions, but similar in the free energy.

The second part involved the extension of the Droplet model to the class of acidic extractants. These extractants are especially interesting since upon the dissociation, they readily complex the target cation. Extension required accounting for the dissociation, strong dimerization, just to mention some of the effects. Again to demonstrate the validity of our approach, we have chose industrially common and well documented HDEHP extractant. In contrast DMDOHEMA case, acidic extractants disfavored the acid in the system. Also, system was more or less monodisperse. It was shown that strong complexation between HDEHP and target cation is the leading force for the self-assembly in the organic phase. The key finding came of in the

[1] We did not study the influence of the temperature.

form of the mapping of the extraction and the self-assembly landscape for different independent system variables. This provided a global overview of the liquid-liquid extraction. Throughout the manuscript, we have adopted this way of studying the overall liquid-liquid extraction.

The third part involved the combination of the previous two models, along with minor adjustments to make the final model general but consistent. Combining the DMDOHEMA and HDEHP cases was to yield the experimentally observed synergy. Without additional parametrization but for a certain constraints, we have obtained the synergistic peak which is in accordance with the reference experimental data. Our model predicts that behavior of the synergistic mixture of the extractants completely different compared to the individual DMDOHEMA and HDEHP cases. Out of few surprising findings, the most striking is the calculated variety of aggregates coexisting at equilibrium. This underlining diversity of the self-assembly of aggregates in the dilute regime that reflects on extraction efficiency is most likely the reason for experimentally observed strong non-linearities. Moreover, we have addressed the current paradigm, which states that combination of one or few chemical equilibria is responsible for synergistic mixtures behavior. Quantitative decoupling the total extraction efficiency into contributions revealed that the peak of synergy is not solely attributed to the formation of mixed extractant aggregates, but to the formation of pure extractant aggregates also. At the very end of chapter, we made a hypothetical study to obtain insights into macroscopic enthalpy or entropy influence on the complex two-extractant system self-assembly. Similar to recent studies that show how delicate interplay of enthalpy or entropy control can lead to hierarchy of self-assembly at metal substrate interface, or for example on protein conformation, in our case the variety of regimes were identified. Like described in the bachelor thermodynamic courses, our study shows how entropy control favors no aggregation and uniform dispersion of non-interacting extractants, while strong enthalpy favors ordered systems. In between is the working point for the experimental chemists, where they can tune and choose desired system conditions.

It is worth to add that we have also demonstrated how the simple choice of the ensemble in which we perform calculations can be useful to interpret the different the experimental scales in liquid-liquid extraction. In particular, canonical ensemble is quite pleasant to interpret laboratory-scale experiments which are usually done in small flask, whereas inadequate for large engineering systems. Grand-canonical ensemble on the other hand can elegantly solve the problem by considering the aqueous phase as a infinite reservoir that fixes the chemical potentials of ions and water. This is also a good example for students who are taught that some ensembles are better for some purposes, whereas bad for others. Our work provides a

simple practical example.

Concluding remarks

At the very end, we need to make a realistic statement. This General Conclusion chapter started with statement that no theory is perfect. Our models are far from perfect. Either the subject is porous materials and ions in confined media, or the subject is liquid-liquid extraction, currently it is impossible to account for every effect and, at the same instant, to make prediction for the practical engineering scale. Still, improving current models and theories step-by-step, does give a hope to include chemistry, not just numerical analysis, into engineering world.

The List of Publications

- M. Špadina, A. Selmani, G. Drazić, S. Gourdin, J.-F. Dufrêche, K. Bohinc, Charge Properties of TiO_2 Nanotubes in $NaNO_3$ Aqueous Solution, *ACS Applied Materials & Interfaces* **2018**, 10, 13130-13142.

- M. Špadina, M. K. Bohinc, T. Zemb, J.-F. Dufrêche, Multicomponent Model for the Prediction of Nuclear Waste/Rare-Earth Extraction Processes. *Langmuir*, **2018**, 34, 10434-10447.

- M. Špadina, K. Bohinc, T. Zemb, J.-F. Dufrêche, A colloidal model of prediction of the extraction of rare earths assisted by the acidic extractant. *Langmuir* **2019**, 35, 3215-3230.

- M. Špadina, K. Bohinc, T. Zemb, J.-F. Dufrêche, Modeling rare earth cations extraction by the mixture of extractants: can we trace the origin of the synergy? *Submitted.*

- M. Špadina, J. Rey, S. Dourdain, S. Pellet-Rostaing, K. Bohinc, J.-F. Dufrêche, T. Zemb, Synergy and Anti-Synergy in Liquid-Liquid Extraction: The Rule Rather Than the Exception, *In preparation.*

- M. Špadina, A. Selmani, G. Drazić, B. Radatović, D. Kovačević, J.-F. Dufrêche, K. Bohinc, Mesoscopic Modelling of Cs^+ Decontamination Process Utilizing TiO_2 Nanotubular Adsorbent, *In preparation.*

Appendix A

7.1 Experimental Support for TiO_2 nanotubes part

7.1.1 Materials

For the synthesis of the TiO_2 NTs the TiO_2 P25 (75% Antase, 25% Rutil) from Degussa was used. The NaOH solution used (c = 10 mol dm^{-3}) was prepared by dissolving the NaOH pellets (Reidel-de Haen) in the CO_2-free deionized water (the CO_2 was removed by boiling and bubbling of the deionized water with N_2). $NaNO_3$ was analytical grade and was purchased from Fluka. HNO_3 ($c = 0.1$ mol dm^{-3}) and NaOH ($c = 0.1$ mol dm^{-3}) titrivals were obtained from Reidel-de Haen. Tris(hydroxymethyl)aminomethane (TRIS) was obtained from Sigma Aldrich. Five standard buffers, pH = 2, 4, 6, 8, and 10 that were purchased from Reidel-de Haen were used for the potentiometric measurements, *i.e.* electrode calibration. Poly-diallyldimethylammonium chloride (PDDA, molar mass 100 - 200 kDa; 20% wt , density 1.04 g cm^{-3}) which was used as titrant was purchased from Sigma Aldrich.

7.1.2 Synthesis of TiO_2 NTs

TiO_2 NTs were prepared by alkaline hydrothermal routine by suspending 2.0 g TiO_2 P25 (75% Antase, 25% Rutil) in aqueous 65 cm^{-3} NaOH solution ($c = 10$ mol dm^{-3})[134]. The suspension was stirred with a magnetic stirrer and the ultrasound (1500 V, 20 kHz, Sonicator Ultrasonic Processor XL, Misonix Inc.) was applied in order to achieve homogeneity, using the following procedure: five minutes on followed for by five minutes off. The procedure lasted for a total of two hours. The prepared homogeneous suspension was placed to the Teflon lined autoclave. Synthesis temperature was kept at $\Theta = 146$ °C for 48 hours. The obtained sample was filtered and washed with de-ionized water respectively until the conductivity has approached to approximate conductivity of de-ionized water ($\kappa < 10$ μS cm^{-1}). The sample was incubated with 0.1 mol dm^{-3} HCl for three hours to remove excess of the adsorbed sodium ions. The resulting

sample was again filtered and washed with deionized water respectively until the conductivity of the supernatant fluid was below 10 μS cm^{-1}. The TiO_2 NTs were dried at 80 °C for six hours in the air and stored in a glass bottle.

7.1.3 Characterization the TiO_2 NTs: HR-TEM

The morphology and size of TiO_2 NTs were studied by high-resolution transmission electron microscopy (HR-TEM)[78]. A 200 kV Cs-probe-corrected cold-field-emission transmission electron microscope (Jeol ARM 200 CF), coupled with a Gatan Quantum ER electron energy-loss spectroscopy (EELS) system and an energy-dispersive X-ray spectroscopy (EDXS) system Jeol Centurio with a 100 mm^2 SDD detector was used. Samples with TiO_2 NTs powder were dispersed in ethanol and placed on a copper lacy-carbon grid. EELS and EDXS spectra and mappings were collected in scanning-transmission mode.

7.1.4 Characterization the TiO_2 NTs: AFM

Atomic force microscope (AFM) images of nanotubes were taken with JPK Nanowizard Ultra Speed AFM under ambient conditions. Non-contact AC (tapping) mode was used for acquisition with setpoint of 52%. AppNano silicon tips with a nominal spring constant of 45 - 90 N/m, a tip radius less than 5 nm and a nominal resonant frequency of 160 – 225 kHz were used. Images were processed with Gwyddion software[227].

7.1.5 Electrophoretic Mobility of the TiO_2 NTs

Electrophoretic mobility of the TiO_2 NTs was determined using the Zetasizer Nano ZS (Malvern, UK) equipped with a green laser ($\lambda = 532$ nm). The intensity of scattered light was detected at the angle of 173°. For electrokinetic measurements the TiO_2 NTs suspension with mass concentration, $\gamma = 0.1$ g dm^{-3} was prepared in the 0.001 mol dm^{-3} $NaNO_3$ aqueous solution. Initial pH was adjusted with NaOH ($c = 0.1$ mol dm^{-3}). Suspensions were sonicated for three minutes using the bath sonicator (35 kHz, 320 W, Bandelin Sonorex Rk 100 H) before mobility measurements[228]. The electrophoretic mobility of the TiO_2 NTs as a function of pH was measured where HNO_3 ($c = 0.1$ mol dm^{-3}) was used as a titrant. After each addition of the HNO_3, the system was left for equilibration for ten minutes to obtain stable pH electrode signal response with the potentiometer accuracy of 0.01 mV. In order to prevent sedimentation, stirring was applied during the measurement. Then pH was recorded with combined microglass electrode (6.0228.010, Metrohm) which was calibrated with five standard buffers (pH = 2, 4,

6, 8 and 10). All experiments were carried under a nitrogen atmosphere at $\Theta = (25 \pm 0.1)$°C. Data were collected with five runs per measurement for two measurements in total. All data processing was done by the Zetasizer software 6.32 (Malvern instruments).

7.1.6 Surface Charge Density of the TiO_2 NTs

Surface charge density of the NTs was measured with the Mütec-PCD03 (BTG Instruments, Switzerland). 1 g dm^{-3} TiO_2 NTs suspension was prepared by suspending 25 mg of solid NTs in 25 mL of aqueous $NaNO_3$ ($c(NaNO_3) = 0.001$ mol dm^{-3}) solution. To increase homogeneity, the suspension was shaken and then the sonication treatment was applied twice for three minutes. The prepared suspensions for both polyelectrolyte titration and electrophoretic measurements the sonication treatment of only two times three minutes was applied to lower the risk of breakage of TiO_2 NTs. The mechanical breakage of TiO_2 NTs has been reported before[160, 80]. The pH of suspension was adjusted with NaOH ($c = 0.1$ mol dm^{-3}). The suspensions with pH between 2 and 10 were prepared. The suspension was added into the Mütec-PCD03 cell. The polyelectrolyte titrant solution, c(PDDA) = 1.3×10^{-4}mol dm^{-3}), was added in the Mutek-PCD05 sample cell containing the suspension of TiO_2 NTs. The streaming potential signal was monitored as titration is conducted. The PDDA denotes concentration of monomer (diallyldimethylammonium chloride) units. The titration was conducted manually. After the streaming potential signal changed sign, the procedure was stooped and total charge σ_{tot} (C g^{-1}) of particles was computed from:

$$\sigma_{\mathrm{tot}} = \frac{Fc(\mathrm{PDDA})V(\mathrm{PDDA})}{m(\mathrm{TiO_2})\, s} \tag{7.1}$$

where s is the specific surface area in m^2 g^{-1}, F is the Faraday's constant in C mol^{-1}, c(PDDA) is the concentration of the titrant, V(PDDA) is the volume of the titrant necessary to obtain the point of the zero charge and $m(TiO_2)$ is the mass of the TiO_2 NTs added in the suspension. Specific surface s of TiO_2 NTs sample is obtained from BET measurements and is 200 m^2 g^{-1}. The total charge per unit of mass was converted to charge per unit length $Q_{\mathrm{tot}}L^{-1}$ in C m^{-1}.

Appendix B

7.2 Calculated Aggregate Probabilities

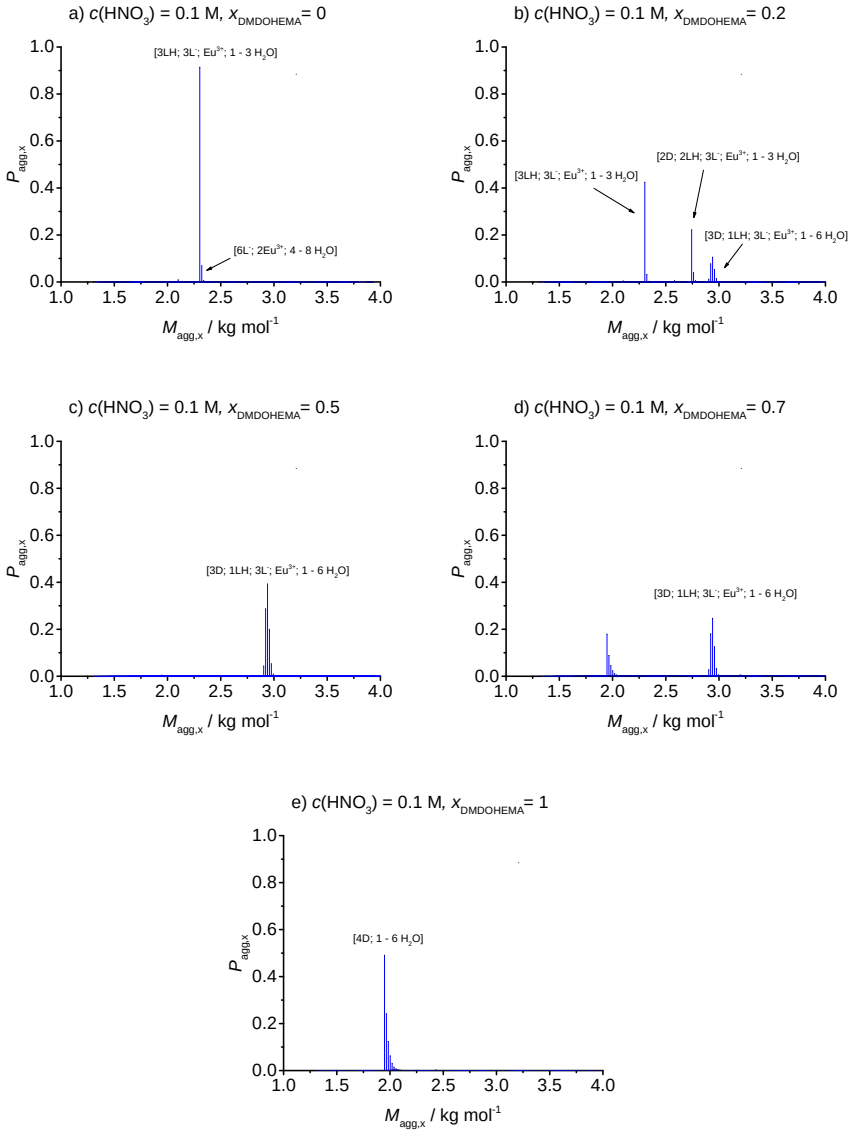

Figure 7.1 – Calculated aggregate probabilities as a function of the molar mass for $c_{\mathrm{total}} = 0.6$ mol dm^{-3}, $m(\mathrm{Eu}^{3+})_{\mathrm{aq,eq}} = 0.035$ mol kg^{-1}, and $m(\mathrm{HNO_3})_{\mathrm{aq,eq}} = 0.1$ mol kg^{-1}. Results are presented for various x_{DMDOHEMA} (a-e).

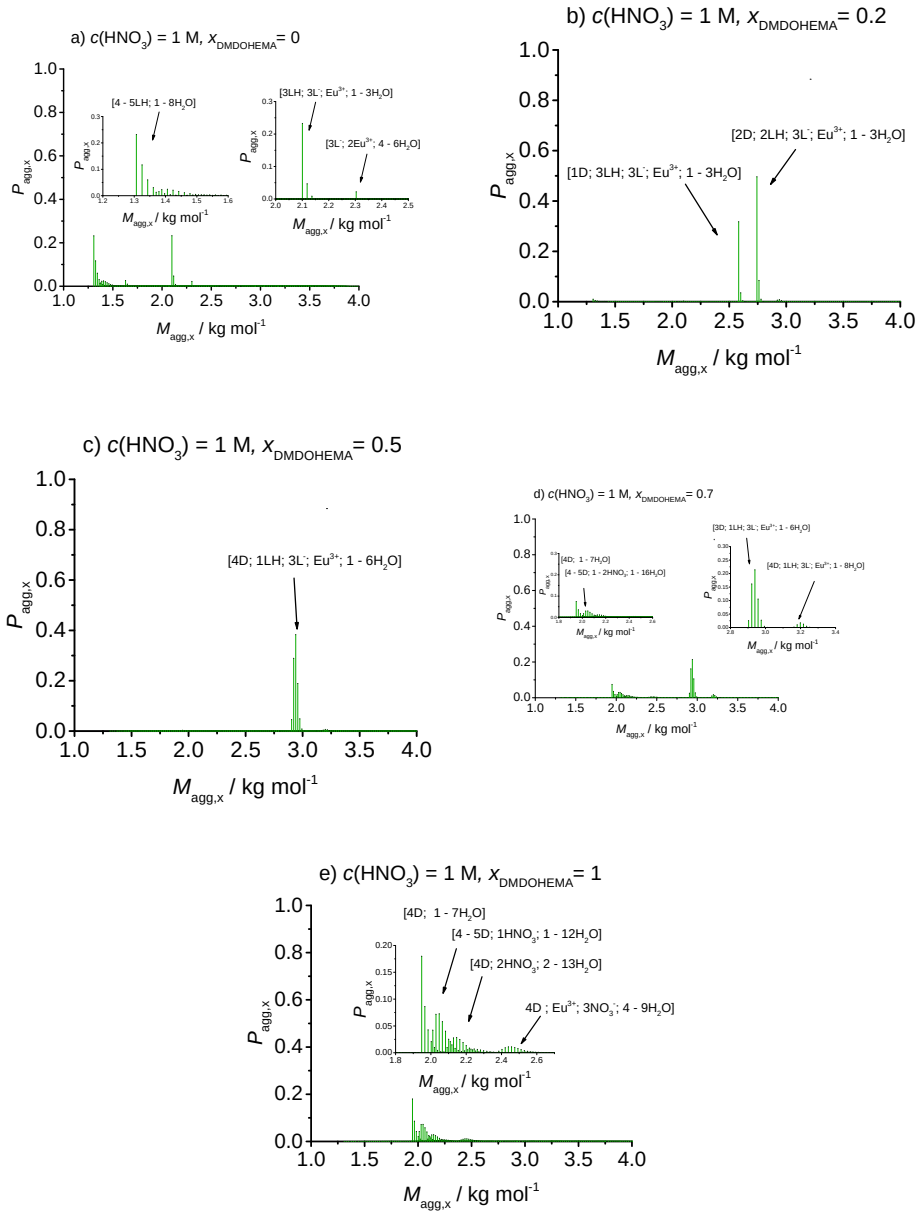

Figure 7.2 – Calculated aggregate probabilities as a function of the molar mass for $c_{\text{total}} = 0.6$ mol dm^{-3}, $m(\text{Eu}^{3+})_{\text{aq,eq}} = 0.035$ mol kg^{-1}, and $m(\text{HNO}_3)_{\text{aq,eq}} = 1$ mol kg^{-1}. Results are presented for various x_{DMDOHEMA} (a-e).

7.3 Speciation of the Extractant: a Mole Fraction Representation

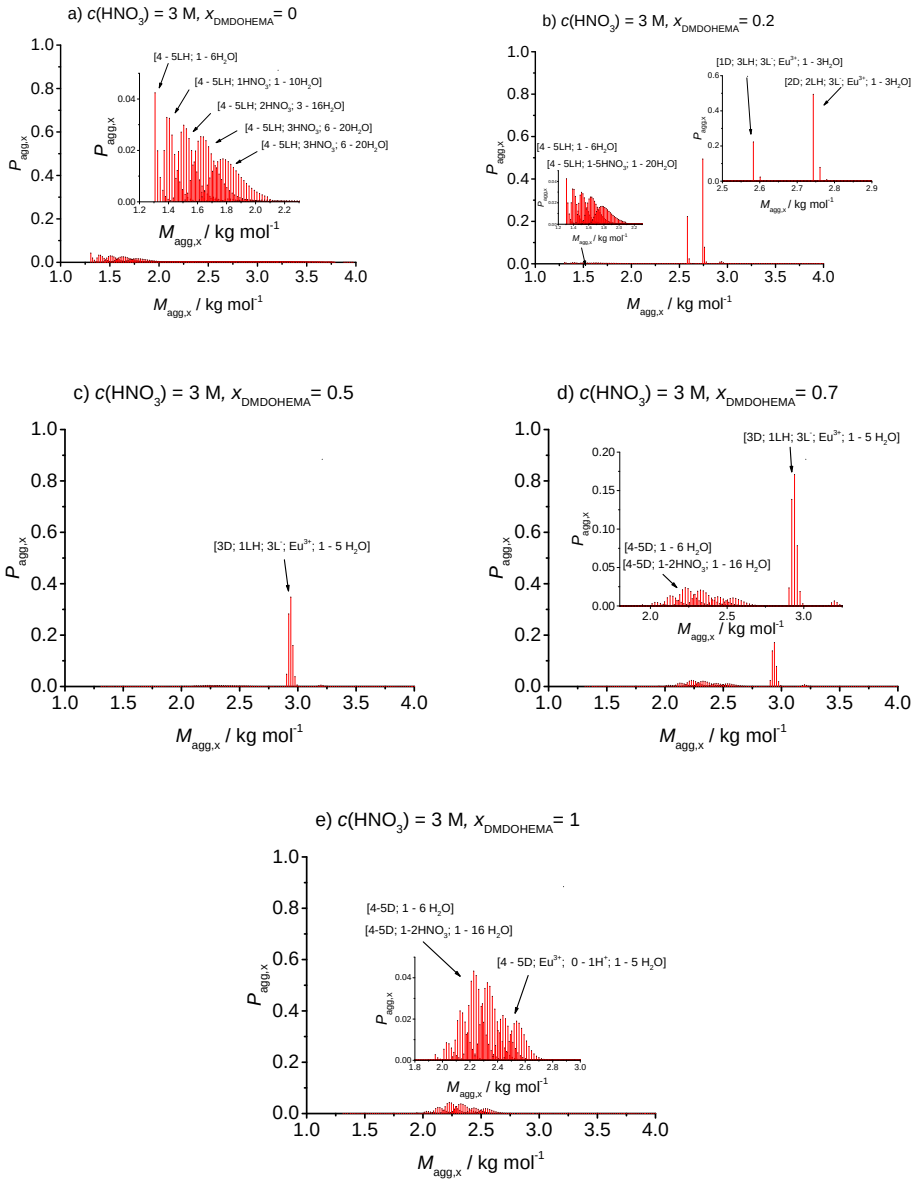

Figure 7.3 – Calculated aggregate probabilities as a function of the molar mass for $c_{\text{total}} = 0.6$ mol dm^{-3}, $m(\text{Eu}^{3+})_{\text{aq,eq}} = 0.035$ mol kg^{-1}, and $m(\text{HNO}_3)_{\text{aq,eq}} = 3$ mol kg^{-1}. Results are presented for various x_{DMDOHEMA} (a-e).

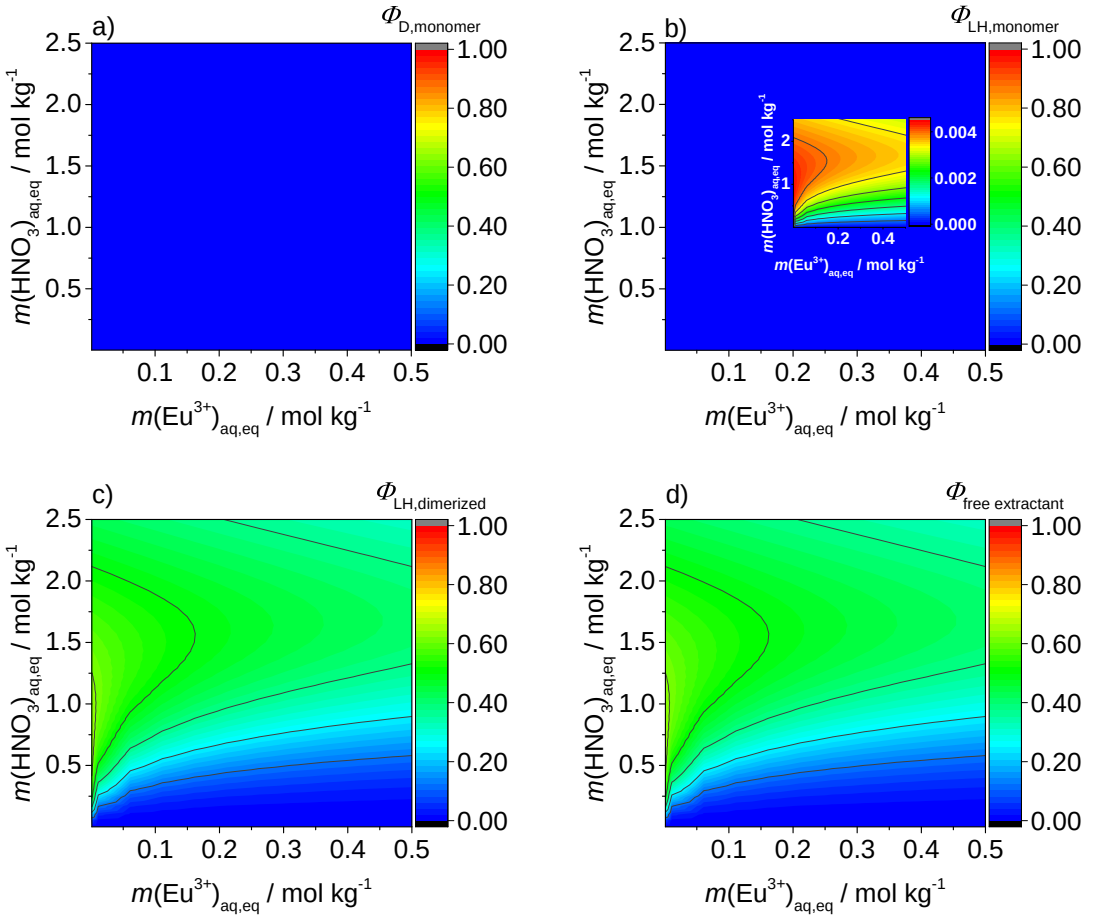

Figure 7.4 – Speciation of the extractant in the solvent as a function of $m(\mathrm{Eu}^{3+})_{\mathrm{aq,eq}}$ and $m(\mathrm{HNO_3})_{\mathrm{aq,eq}}$, at $x_{\mathrm{DMDOHEMA}} = 0$ (pure HDEHP), and $c_{\mathrm{total}} = 0.6$ mol dm^{-3}. a) D in monomeric form, b) LH in monomeric form, c) LH in dimerized form, d) total percentage of the free extractant. Figure a) does not have the inset since at $x_{\mathrm{DMDOHEMA}} = 0$ there is no DMDOHEMA in the system.

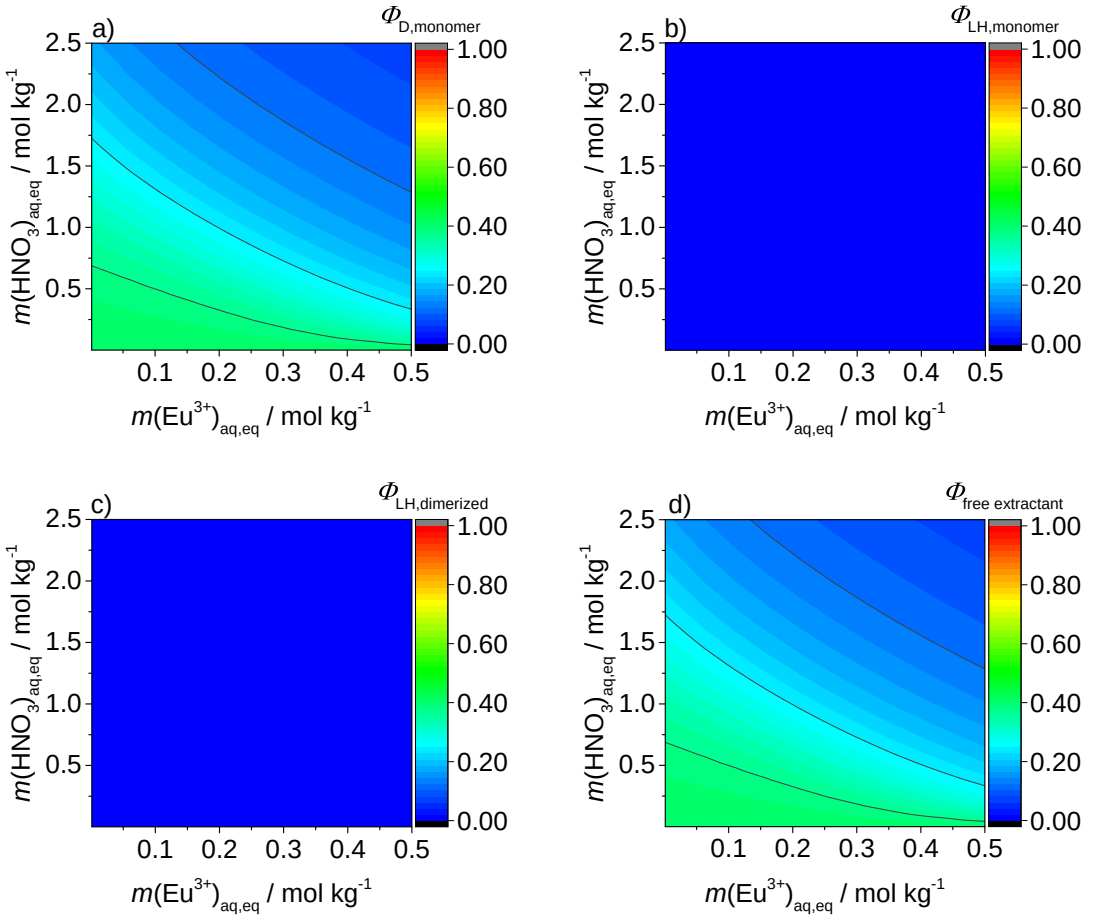

Figure 7.5 – Speciation of the extractant in the solvent as a function of $m(\mathrm{Eu}^{3+})_{\mathrm{aq,eq}}$ and $m(\mathrm{HNO_3})_{\mathrm{aq,eq}}$, at $x_{\mathrm{DMDOHEMA}} = 1$ (pure DMDOHEMA), and $c_{\mathrm{total}} = 0.6$ mol dm^{-3}. a) D in monomeric form, b) LH in monomeric form, c) LH in dimerized form, d) total percentage of the free extractant. Figure b) and c) do not have the inset since at $x_{\mathrm{DMDOHEMA}} = 1$ there is no HDEHP in the system.

Résumé

7.4 Introduction

La durabilité est une question importante de l'industrie chimique et pour la communauté scientifique[1]. Si l'industrie chimique est le lien entre la croissance industrielle et la recherche fondamentale, sa durabilité se manifeste sous différentes formes qui concernent des pans entiers de la chimie. Actuellement, l'une des principales manifestations de cela est la séparation chimique sélective des métaux des terres rares (REEs - pour Rare Earth Elements) à partir de solutions aqueuses, en particulier dans les cas des grandes dilutions [3]. Ce domaine de l'hydrométallurgie en plein essor est la conséquence du fait que les terres rares jouent un rôle majeur dans le maintien d'une économie verte et à faible émission de carbone. Leurs nombreuses applications concernent les aimants permanents, les lampes à phosphore, les batteries des voitures hybrides, *etc*[4, 5, 6]. L'application des terres rares, à l'inverse, signifie également un potentiel de recyclage à partir des déchets de production et des produits en fin de vie[7, 5, 2, 6]. Il faut souligner que seule une petite partie des déchets produits annuellement est recyclée afin de récupérer les terres rares [6]. La demande énorme, le marché restreint et l'absence de recyclage placent certains métaux de terres rares dans un groupe critique en termes d'importance pour l'énergie propre et de risque dans l'offre. Ceci est démontré dans la Figure 1.1. Par conséquent, l'amélioration des méthodes de séparation est au cœur de la durabilité de l'industrie chimique, l'Union européenne ayant d'ailleurs reconnu cette nécessité en finançant un projet European Research Council (ERC) REE-CYCLE (2013-2018)[2].

Parmi les nombreuses méthodes déjà établies, l' extraction solide-liquide (adsorption) et liquide-liquide (extraction par solvant), ainsi que la flottation sont toujours considérées comme des techniques de référence. Bien que les technologies parvenues à maturité en termes d'utilisation prévue et d'améliorations aient déjà été appliquées dans des cas pratiques, leur simplicité et leur potentiel de mise à l'échelle poussent à la nécessité d'un développement plus poussé [8].

[2]ERC REE-CYCLE (2013-2018) est le projet qui a cofinancé cette thèse.

Dans le cadre de cette thèse, des cas de méthodes d'extraction solide-liquide et liquide-liquide seront traités.

En effet, on peut reconnaître l'efficacité globale du procédé dépend des ions et de leurs propriétés de solvatation. Le sujet de cette thèse est ainsi la modélisation des propriétés des ions dans ces milieux complexes pour permettre, grâce à la théorie utilisée, de rationaliser les effets responsables du transfert des ions entre deux domaines. Deux exemples seront donnés : 1) le transfert d'ions de la solution aqueuse à la phase organique sous forme d'agrégats faiblement liés, 2) le transfert d'ions de la solution aqueuse à l'intérieur d'une cavité adsorbante solide sous l'influence du champ électrique. La connaissance du comportement des ions et de leur solubilisation est donc au cœur de la durabilité de l'industrie chimique.

7.5 Methodes

Pour trouver des solutions à ces deux problèmes, nous avons dû adopter deux méthodologies différentes, comme nous le verrons dans cette section.

Modèle d'adsorbants solides en solution aqueuse

Dans ce chapitre, nous avons abordé l'une des questions centrales concernant les ions dans les milieux confinés sous l'influence du champ électrique. Dans le cadre de cette étude, nous avons ainsi présenté un cadre pour quantifier les propriétés de charge des nanotubes de TiO_2 et d'autres matériaux poreux en solution aqueuse faiblement concentrées en sel.

Le modèle théorique a été développé afin de comprendre et d'interpréter les données expérimentales. La base du modèle théorique comprend l'équation de Poisson-Boltzmann (qui est le cas le plus simple de la théorie de la fonctionnelle de la densité classique pour les solutions électrolytiques) et la méthode de régulation de la charge de surface par la loi de l'action de masse. Un système de deux équations différentielles non linéaires de second ordre couplées a été résolu numériquement d'une manière cohérente par rapport à quatre conditions aux limites couplées. L'algorithme proposé prédit la dépendance de la charge superficielle initiale en fonction du pH par extrapolation à l'aide d'un polynôme de second ordre de Lagrange, et des méthodes de réinjection pour le calcul couplé de $\sigma_{o,i}$ et $\Psi_{i,o}$.

Les considérations générales sur le système, ainsi que la méthode de régulation de la charge par des protonations de type grand canonique (adsorption à partir du réservoir) sont représentées sur la Figure. 7.6.

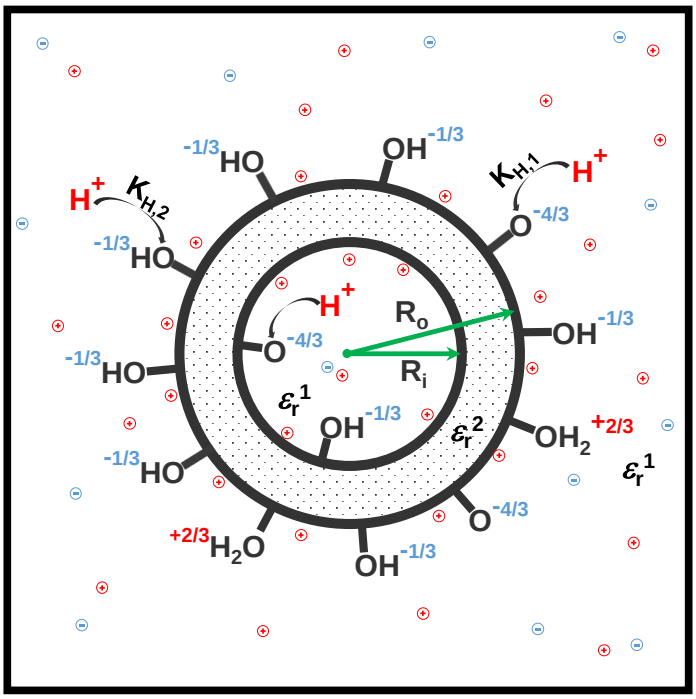

Figure 7.6 – Coupe transversale des nanotubes d'oxyde de titane TiO_2. La section transversale est perpendiculaire à l'axe de symétrie du cylindre. R_i et R_o correspondent respectivement aux rayons intérieur et extérieur du cylindre. $\epsilon_{\mathrm{r},1}$ et $\epsilon_{\mathrm{r},2}$ correspondent respectivement aux constantes diélectriques des couches TiO_2 et de la solution électrolytique. Les groupes de surface $\equiv \mathrm{TiO}^{-\frac{4}{3}}$, $\equiv \mathrm{TiOH}^{-\frac{1}{3}}$ et $\equiv\equiv \mathrm{TiOH}_2^{+\frac{2}{3}}$ sont en équilibre avec la solution d'électrolyte. $K_{\mathrm{H},1}$ et $K_{\mathrm{H},2}$ sont des constantes de réactions de surface. Les ions protons H^+ se distinguent des autres ions uniquement par les équilibres de surface et l'autoprotolyse de l'eau. Dans le modèle, tous les ions sont considérés ponctuels.

Modèle pour l'extraction liquide-liquide

Notre approche consiste à établir l'expression de l'énergie libre d'un agrégat particulier dans le solvant organique. Nous permettons la formation de tous les agrégats sphériques possibles à l'équilibre, tels que définis par la loi de l'action de masse. L'énergie libre est la somme de différentes contributions énergétiques, qui sont décrites aux chapitres 4, 5 et 6. L'énergie libre d'un agrégat individuel est par définition son potentiel chimique standard. Lorsque le potentiel chimique standard est connu, il nous permet de compléter la loi d'action de masse, mais pas seulement : si nous connaissons la fonctionnalité des termes énergétiques, nous pouvons calculer tous les agrégats possibles. C'est l'idée maîtresse de cette partie de la thèse et elle peut s'écrire dans un vocabulaire plus général de chimie colloïdale : tous les agrégats sont possibles et peuvent coexister en équilibre, et leur probabilité est déterminée par la composition. Une image simplifiée du processus d'extraction à l'échelle nanométrique à l'équilibre peut être comprise à partir de la Figure 7.7.

7.6 Résultats majeurs

Étude des nanotubes d'oxyde de titane TiO_2

La principale conclusion proposée par notre travail est la dissimilarité de la charge totale de deux surfaces qui ne suit pas le rapport de leurs rayons, en régime peu salin. Les résultats sont présentés sur la Figure 7.8.

L'accumulation inattendue de la charge sur la surface externe est attribuée à l'absence d'électroneutralité à l'intérieur des nanotubes. Ce phénomène est important d'un point de vue fondamental, mais aussi pour toutes les applications. L'adsorption contrôlée par la charge ou la photocatalyse seraient plus efficace sur la surface externe, si nos prédictions sont exactes. En l'absence de toute technique expérimentale pouvant fournir des preuves éclairantes, le seul choix serait d'utiliser d'autres cadres théoriques et de voir si l'accumulation de charges se produit.

Le modèle de la goutte liquide pour l'extraction liquide-liquide

Le modèle développé a été nommé le modèle de la goutte liquide. Le modèle est idéal et aucun potentiel entre les agrégats n'est pris en compte. Nous avons démontré les forces et les faiblesses du modèle sur l'exemple de l'extractant DMDOHEMA solvant non-ionique, qui est important pour l'industrie nucléaire du retraitement du combustible. La principale conclusion de ce chapitre est l'identification des différents types d'agrégats présents à l'équilibre, comme

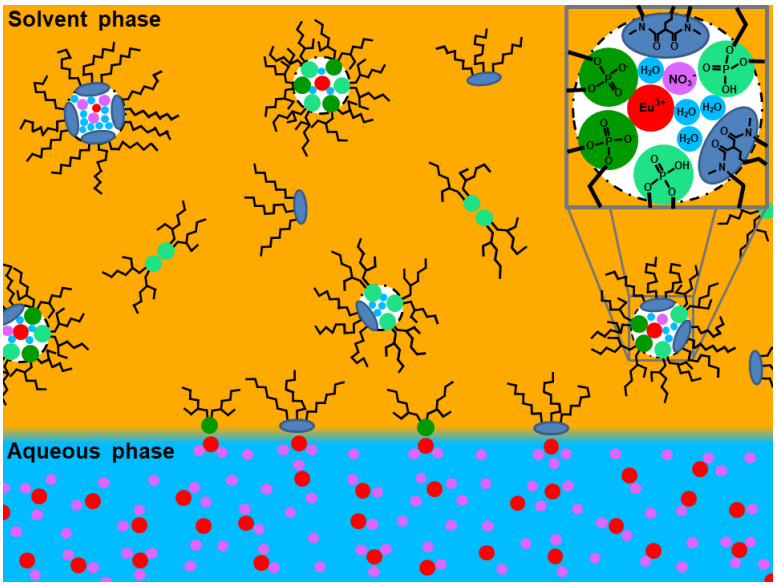

Figure 7.7 – Représentation schématique du modèle pour l'extraction liquide-liquide dans le cas de mélanges synergiques. Différents types d'agrégats sont présents dans la phase organique (phase solvant), et leur probabilité à l'équilibre est déterminée par la composition de leurs noyaux et du film extracteur. Compte tenu de la nature tensioactive de l'agent d'extraction, l'interface est au moins partiellement recouverte par les molécules de l'agent d'extraction (non représentées ici). La région agrandie montre le noyau de l'agrégat avec le cation europium (rouge), l'anion nitrate (rose), les molécules d'eau (bleu pâle), les groupes de têtes HDEHP non dissociés (vert foncé), et les groupes de têtes HDEHP dissociés (vert pâle), et les groupes de têtes malonamides DMDOHEMA (bleu foncé). Les chaînes hydrophobes des extractants sont représentées en noir.

le montre la Figure 7.9. On peut voir que le paradigme de la stœchiométrie unique de la loi d'action de masse ne peut pas être responsable des phénomènes complexes tels que l'extraction liquide-liquide puisque de nombreux agrégats sont probables. Les calculs ont en outre montré que cette spéciation dans la phase organique est contrôlé par la valeur des variables du système, à savoir les concentrations de sels, le pH et la concentration de l'extractant. De plus, pour chaque type d'agrégat, un certain degré de polydispersité du nombre d'agrégats et de la teneur en eau a été prédit. Il a ensuite été précisé que le changement de comportement (ou de tendance) de l'efficacité d'extraction globale est en fait régi par le fort auto-assemblage concurrentiel d'agrégats différents en composition, mais similaires en énergie libre. La stœchiométrie simple doit donc être abandonnée au profit d'une cartographie des probabilités des agrégats.

La deuxième partie portait sur l'extension du modèle de la goutte liquide à la classe des extractants acides. Ces extractants sont d'autant plus intéressants qu'en se dissociant, ils com-

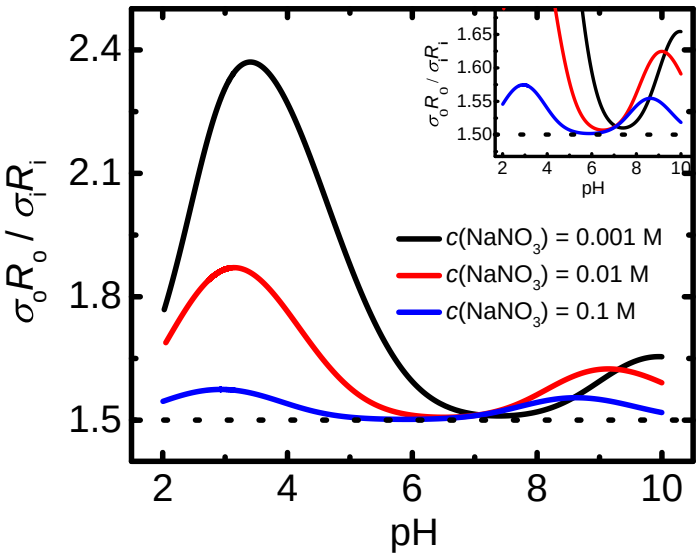

Figure 7.8 – Rapport de la charge entre la surface extérieure et la surface intérieure en fonction du pH. Les résultats sont donnés pour trois concentrations différentes de sel dans le réservoir : la ligne noire correspond à $c(\mathrm{NaNO_3}) = 0{,}001$ M, la ligne rouge à $c(\mathrm{NaNO_3}) = 0{,}01$ M, et la ligne bleue à $c(\mathrm{NaNO_3}) = 0{,}1$ M.

plexent plus facilement le cation cible. L'extension exigeait de tenir compte de la dissociation, de la forte dimérisation, pour ne mentionner que certains des effets. Encore une fois pour démontrer la validité de notre approche, nous avons choisi un extractant HDEHP industriel commun et bien documenté. Contrairement au cas du DMDOHEMA, les extractants acides ont désavantagé l'extraction de l'acide. De plus, le système était plus ou moins monodispersé. Il a été démontré qu'une forte complexation entre le HDEHP et le cation cible est la force motrice de l'auto-assemblage en phase organique.

Avant cette étape de la thèse, la nouveauté principale était le passage de la stœchiométrie aux cartes de probabilité. Mais, à partir de cette étape, nous nous sommes également intéressés à la vue plus globale de l'extraction comme une sorte d'imitation des diagrammes de phase puisqu'elle permet la prédiction pour l'ingénierie chimique. La principale conclusion est venue de la cartographie du paysage d'extraction et d'auto-assemblage pour différentes variables système indépendantes. Ceci a fourni un aperçu global de l'extraction liquide-liquide, tel que présenté sur la Figure 7.10. Tout au long du manuscrit, nous avons adopté cette façon d'étudier l'extraction liquide-liquide globale. Dans notre modèle, nous pouvons maintenant distinguer l'extraction et la saturation de l'extractant en fonction de quelques variables indépendantes du système.

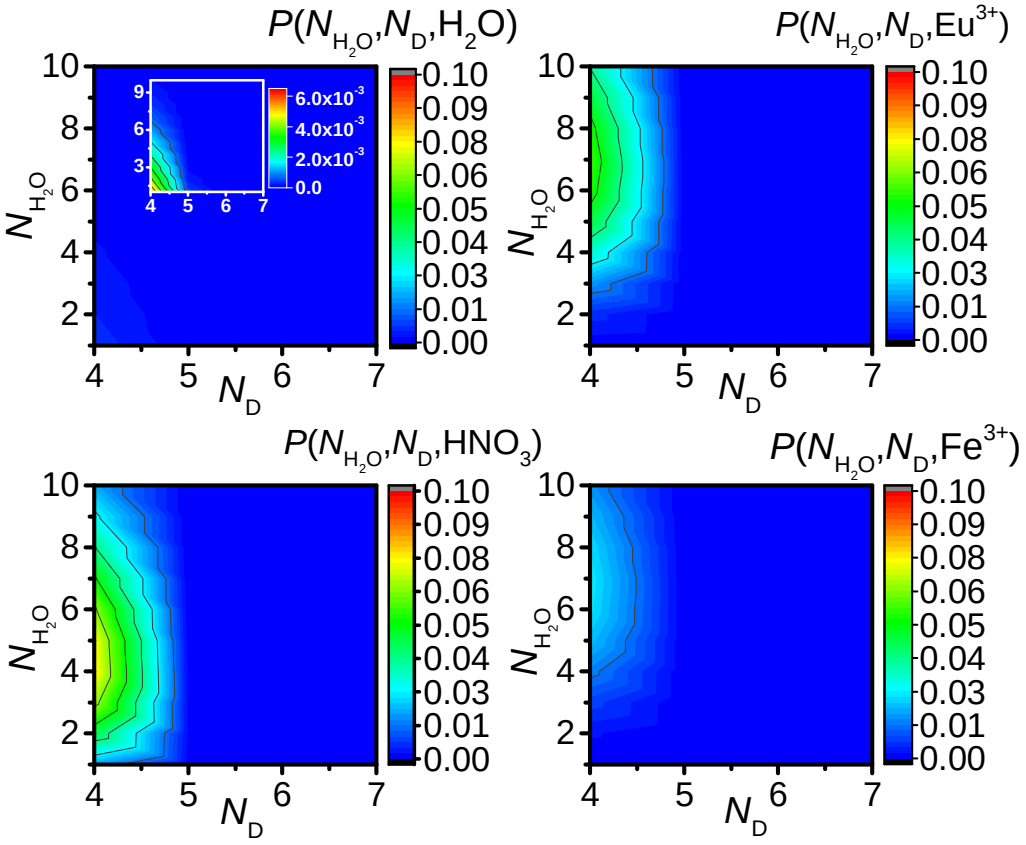

Figure 7.9 – Influence de la phase aqueuse initiale sur les probabilités globales d'équilibre calculées en fonction de la composition du noyau. Système étudié: $c_{\mathrm{D,initial}} = 0.6$ mol dm^{-3}, $m_{\mathrm{HNO_3,initial}} = 3$ mol kg^{-1} and $m_{\mathrm{Eu(NO_3)_3,initial}} = m_{\mathrm{Fe(NO_3)_3,initial}} = 0.05$ mol kg^{-1}. Cette figure est complémentaire de la Figure 4.16b.

La troisième partie consistait à combiner les deux modèles précédents avec des ajustements mineurs pour rendre le modèle final général mais cohérent. La combinaison des cas DMDOHEMA et HDEHP devait produire la synergie observée expérimentalement. Sans paramétrage supplémentaire mais pour certaines contraintes, nous avons obtenu le pic synergique qui est conforme aux données expérimentales de référence.

Notre modèle prédit que le comportement du mélange synergique des extractants est complètement différent par rapport aux cas individuels DMDOHEMA et HDEHP. Parmi les quelques résultats surprenants, le plus frappant est la variété calculée d'agrégats coexistant à l'équilibre. Cette diversité représente celle de l'auto-assemblage des agrégats dans le régime dilué et elle se reflète sur l'efficacité de l'extraction en étant très probablement la raison des fortes non-linéarités observées expérimentalement. De plus, nous avons abordé le paradigme actuel, qui stipule que la combinaison d'un ou plusieurs équilibres chimiques est responsable du comportement synergique des mélanges. Le découplage quantitatif de l'efficacité d'extraction totale

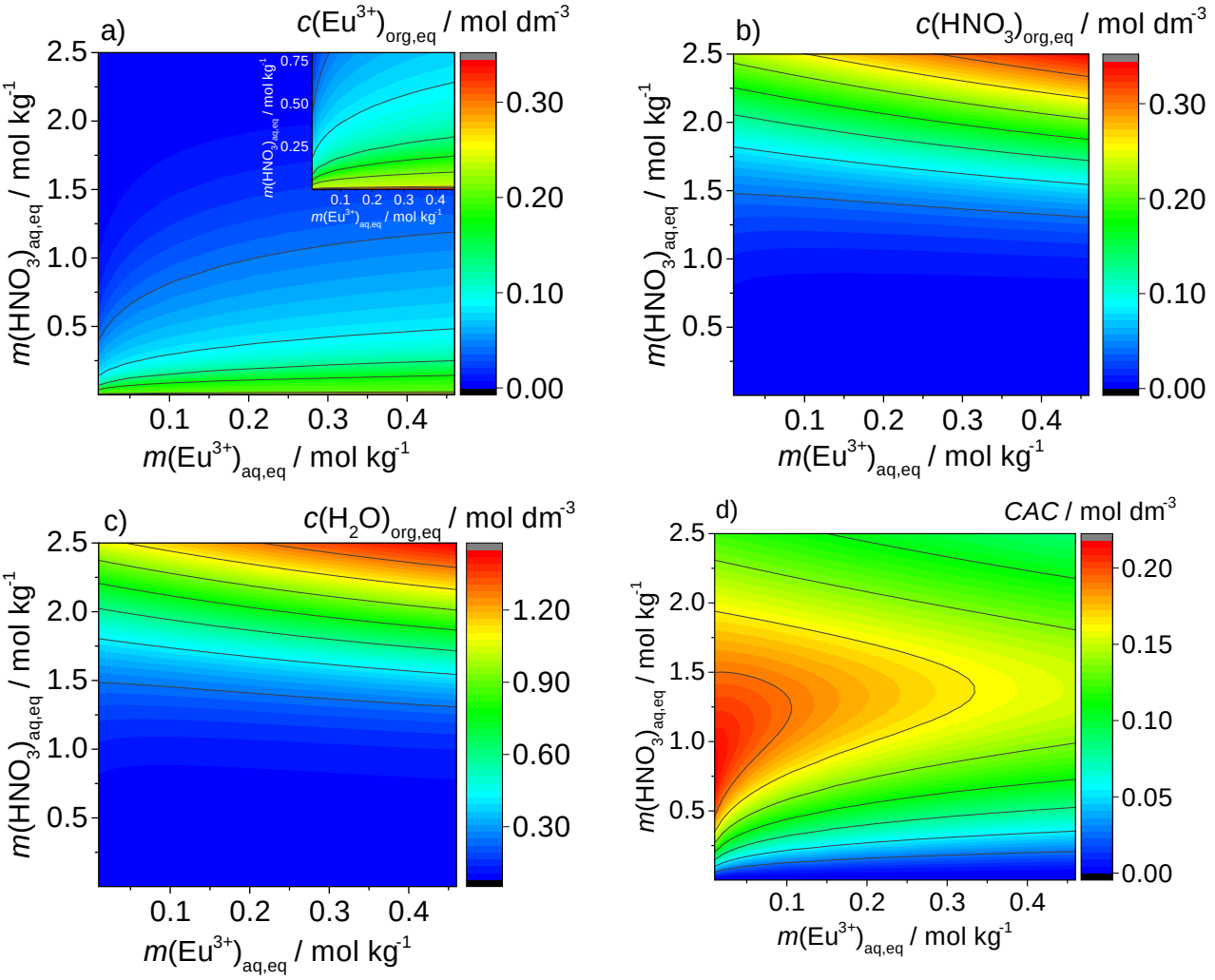

Figure 7.10 – Concentration en phase organique des solutés extraits (a-c) et cartes de concentration d'agrégation critique (CAC)(d) dans la phase solvant en fonction de $m(Eu^{3+})_{aq,eq}$ et $m(HNO_3)_{aq,eq}$ pour $c_{LH,initial} = 0.6$ mol dm^{-3}. L'encadré de la Figure a) montre un agrandissement de la région où l'extraction de Eu^{3+} est forte.

en contributions a révélé que le pic de synergie n'est pas uniquement attribué à la formation d'agrégats d'extraction mixtes, mais aussi à la formation d'agrégats d'extraction à un seul type d'extractant. A la toute fin du chapitre, nous avons fait une étude hypothétique pour obtenir des informations sur l'enthalpie macroscopique ou l'influence de l'entropie sur l'auto-assemblage complexe du système à deux extractants. Comme dans les études récentes qui montrent comment le couplage des contrôles enthalpiques et entropiques peut conduire à une hiérarchie de l'auto-assemblage à l'interface d'un substrat métallique, ou par exemple sur la conformation des protéines, dans notre cas les différents régimes ont été identifiés. Comme décrit dans les cours de thermodynamique, notre étude montre comment le contrôle de l'entropie favorise l'absence d'agrégation et la dispersion uniforme des extractants non interactifs, tandis que la forte en-

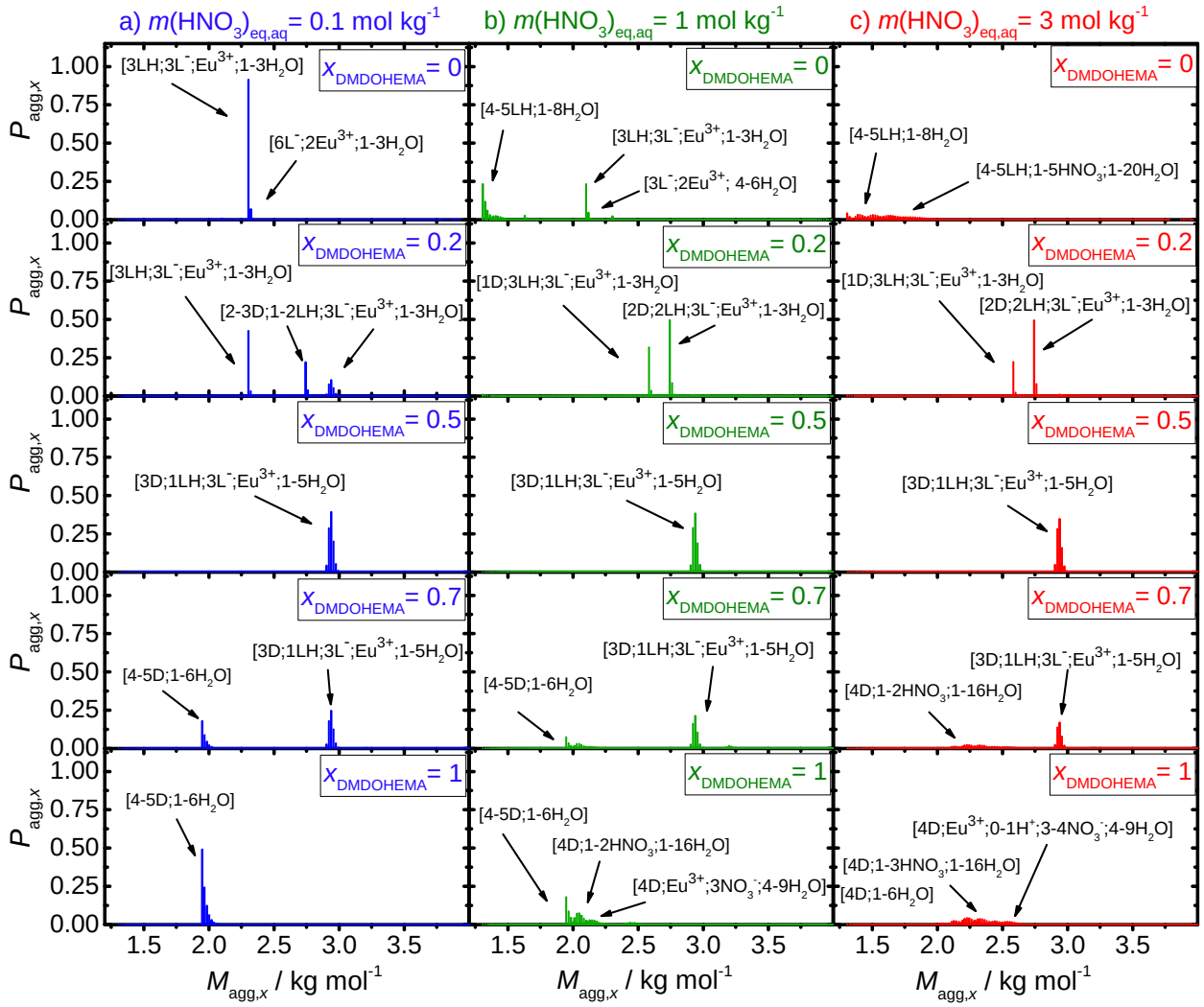

Figure 7.11 – Probabilités globales calculées en fonction de la masse molaire. Les résultats sont présentés pour différentes fractions molaires de DMDOHEMA, x_{DMDOHEMA} dans le système. Le symbole D représente DMDOHEMA, tandis que LH représente HDEHP. Le texte entre crochets représentent l'affectation d'agrégats particuliers. Les calculs ont été effectués pour $c_{\mathrm{total}} = 0.6$ mol dm^{-3}, and $m(\mathrm{Eu}^{3+})_{\mathrm{aq,eq}} = 0.035$ mol kg^{-1}. Trois concentrations de HNO_3 dans la phase aqueuse sont présentées. a) $m(\mathrm{HNO_3})_{\mathrm{aq,eq}} = 0.1$ mol kg^{-1}, b) $m(\mathrm{HNO_3})_{\mathrm{aq,eq}} = 1$ mol kg^{-1}, c) $m(\mathrm{HNO_3})_{\mathrm{aq,eq}} = 3$ mol kg^{-1}.

thalpie favorise les systèmes ordonnés. Entre les deux se trouve le point de travail des chimistes expérimentaux, où ils peuvent régler et choisir les conditions de système souhaitées.

7.7 Observations finales

Dans le cadre de cette thèse, nous avons démontré la nécessité d'une modélisation mésoscopique des ions et de leurs propriétés de solvatation. Au-delà de l'aspect fondamental, nous avons

essayé de fournir un cadre qui peut être utilisé par les ingénieurs chimistes pour la simplification des plans d'expériences. Même si elle est loin d'être parfaite, la modélisation mésoscopique a un énorme potentiel pour faire le pont entre la description atomistique et la description par le génie chimique du phénomène en question.

Bibliography

[1] National Research Council (U. S.). *Sustainability in the Chemical Industry: Grand Challenges And Research Needs – a Workshop Book.* National Academies Press, 1 edition, 2005.

[2] Koen Binnemans, Peter Tom Jones, Bart Blanpain, Tom Van Gerven, Yongxiang Yang, Allan Walton, and Matthias Buchert. Recycling of rare earths: A critical review. *Journal of Cleaner Production*, 51:1–22, 2013.

[3] David S Sholl and Ryan P. Lively. Comment. *Nature*, 532(435):6–9, 2016.

[4] Feng Xie, Ting An Zhang, David Dreisinger, and Fiona Doyle. A critical review on solvent extraction of rare earths from aqueous solutions. *Minerals Engineering*, 56:10–28, 2014.

[5] Manis Kumar Jha, Archana Kumari, Rekha Panda, Jyothi Rajesh Kumar, Kyoungkeun Yoo, and Jin Young Lee. Review on hydrometallurgical recovery of rare earth metals. *Hydrometallurgy*, 165:2–26, 2016.

[6] Abigail Walters and Paul Lusty. Rare earth elements. *British Geological Survey*, (November):54, 2011.

[7] Ho Sung Yoon, Chul Joo Kim, Kyeong Woo Chung, Sung Don Kim, Jin Young Lee, and Jyothi Rajesh Kumar. Solvent extraction, separation and recovery of dysprosium (Dy) and neodymium (Nd) from aqueous solutions: Waste recycling strategies for permanent magnet processing. *Hydrometallurgy*, 165:27–43, 2016.

[8] Humphrey Jimmy and Keller George. *Separation Process Technology.* McGraw-Hill, 1 edition, 1997.

[9] Jan Rydberg, Michael Cox, Claude Musikas, and Gregory R. Choppin. *Solvent Extraction Principles and Practice, Revised and Expanded.* Taylor & Francis, 2004.

[10] Hans-Jorg Bart. *Reactive extraction.* Springer-Verlag Berlin Heidelberg, 1 edition, 2001.

[11] A. Matthew Wilson, Phillip J. Bailey, Peter A. Tasker, Jennifer R. Turkington, Richard A. Grant, and Jason B. Love. Solvent extraction: the coordination chemistry behind extractive metallurgy. *Chem. Soc. Rev.*, 43(1):123–134, 2014.

[12] Artem V Gelis and Gregg J Lumetta. Actinide Lanthanide Separation Process - ALSEP. *Ind. Eng. Chem. Res.*, 53:1624–1631, 2014.

[13] Elizabeth Krahn, Cécile Marie, and Kenneth Nash. Probing organic phase ligand exchange kinetics of 4f/5f solvent extraction systems with NMR spectroscopy. *Coord. Chem. Rev.*, 316:21–35, 2016.

[14] Boyd Weaver and F.A. Kappelmann. Preferential extraction of lanthanides over trivalent actinides by monoacidic organophosphates from carboxylic acids and from mixtures of carboxylic and aminopolyacetic acids. *Journal of Inorganic and Nuclear Chemistry*, 30(1):263 – 272, 1968.

[15] Gregg J. Lumetta, Artem V. Gelis, and George F. Vandegrift. Review: Solvent systems combining neutral and acidic extractants for separating trivalent lanthanides from the transuranic elements. *Solvent Extraction and Ion Exchange*, 28(3):287–312, 2010.

[16] Peter Tkac, George F. Vandegrift, Gregg J. Lumetta, and Artem V. Gelis. Study of the interaction between hdehp and cmpo and its effect on the extraction of selected lanthanides. *Industrial & Engineering Chemistry Research*, 51(31):10433–10444, 2012.

[17] Charles Madic, Michaël Lecomte, Pascal Baron, and Bernard Boullis. Separation of long-lived radionuclides from high active nuclear waste. *Comptes Rendus Physique*, 3(7-8):797–811, 2002.

[18] Gregg J. Lumetta, Artem V. Gelis, and George F. Vandegrift. Review: Solvent systems combining neutral and acidic extractants for separating trivalent lanthanides from the transuranic elements. *Solvent Extr. Ion Exch.*, 28(3):287–312, 2010.

[19] Daniel M. Whittaker, Tamara L. Griffiths, Madeleine Helliwell, Adam N. Swinburne, Louise S. Natrajan, Frank W. Lewis, Laurence M. Harwood, Stephen A. Parry, and Clint A. Sharrad. Lanthanide speciation in potential SANEX and GANEX actinide/lanthanide separations using tetra-N-donor extractants. *Inorganic Chemistry*, 52(7):3429–3444, 2013.

[20] Giuseppe Modolo, Hendrik Vijgen, Daniel Serrano-Purroy, Birgit Christiansen, Rikard Malmbeck, Christian Sorel, and Pascal Baron. DIAMEX counter-current extraction process for recovery of trivalent actinides from simulated high active concentrate. *Separation Science and Technology*, 42(3):439–452, 2007.

[21] D.F. Peppard, S.W. Moline, and G.W. Mason. Isolation of berkelium by solvent extraction of the tetravalent species. *Journal of Inorganic and Nuclear Chemistry*, 4(5):344 – 348, 1957.

[22] Thomas Zemb, Caroline Bauer, Pierre Bauduin, Luc Belloni, Christophe Déjugnat, Olivier Diat, Véronique Dubois, Jean-François Dufrêche, Sandrine Dourdain, Magali Duvail, Chantal Larpent, Fabienne Testard, and Stéphane Pellet-Rostaing. Recycling metals by controlled transfer of ionic species between complex fluids: en route to "ienaics". *Colloid and Polymer Science*, 293(1):1–22, Jan 2015.

[23] M. R. Antonio, R. Chiarizia, B. Gannaz, L. Berthon, N. Zorz, C. Hill, and G. Cote. Aggregation in solvent extraction systems containing a malonamide, a dialkylphosphoric acid and their mixtures. *Separation Science and Technology*, 43(9-10):2572–2605, 2008.

[24] J. Rey, S. Dourdain, L. Berthon, J. Jestin, S. Pellet-Rostaing, and T. Zemb. Synergy in Extraction System Chemistry: Combining Configurational Entropy, Film Bending, and Perturbation of Complexation. *Langmuir*, 31(25):7006–7015, 2015.

[25] Andrew W Knight, Baofu Qiao, Renato Chiarizia, Tori Forbes, Ross J Ellis, and L Soderholm. Subtle Effects of Aliphatic Alcohol Structure on Water Extraction and Solute Aggregation in Biphasic Water/n-Dodecane. 2017.

[26] Yushu Chen, Magali Duvail, Philippe Guilbaud, and Jean-François Dufrêche. Stability of reverse micelles in rare-earth separation: a chemical model based on a molecular approach. *Phys. Chem. Chem. Phys.*, 25:7094–7100, 2017.

[27] Minh Nguyen Vo, Vyacheslav S. Bryantsev, J. Karl Johnson, and John A. Keith. Quantum chemistry benchmarking of binding and selectivity for lanthanide extractants. *International Journal of Quantum Chemistry*, 118(7):e25516.

[28] Ross J. Ellis, Thomas Demars, Guokui Liu, Jens Niklas, Oleg G. Poluektov, and Ilya A. Shkrob. In the Bottlebrush Garden: The Structural Aspects of Coordination Polymer Phases formed in Lanthanide Extraction with Alkyl Phosphoric Acids. *J. Phys. Chem. B*, 119(35):11910–11927, 2015.

[29] Yu Jing, Ji Chen, Li Chen, Wenrou Su, Yu Liu, and Deqian Li. Extraction behaviors of heavy rare earths with organophosphoric extractants: The contribution of extractant dimer dissociation, acid ionization, and complexation. a quantum chemistry study. *The Journal of Physical Chemistry A*, 121(12):2531–2543, 2017. PMID: 28263616.

[30] Eléonor Acher, Thomas Dumas, Christelle Tamain, Nathalie Boubals, Pier Lorenzo Solari, and Dominique Guillaumont. Inner to outer-sphere coordination of plutonium(iv) with N,N-dialkyl amide: Influence of nitric acid. *Dalt. Trans.*, 46(12):3812–3815, 2017.

[31] Pauline Moeyaert, Thomas Dumas, Dominique Guillaumont, Kristina Kvashnina, Christian Sorel, Manuel Miguirditchian, Philippe Moisy, and Jean François Dufrêche. Modeling and Speciation Study of Uranium(VI) and Technetium(VII) Coextraction with DEHiBA. *Inorg. Chem.*, 55(13):6511–6519, 2016.

[32] Anna G Baldwin, Alexander S Ivanov, Neil J Williams, Ross J Ellis, Bruce A Moyer, Vyacheslav S Bryantsev, and Jenifer C Shafer. Outer-Sphere Water Clusters Tune the Lanthanide Selectivity of Diglycolamides. *ACS Central Science*, 4:739–747, 2018.

[33] Ryuhei Motokawa, Tohru Kobayashi, Hitoshi Endo, Junju Mu, Christopher D. Williams, Andrew J. Masters, Mark R. Antonio, William T. Heller, and Michihiro Nagao. A Telescoping View of Solute Architectures in a Complex Fluid System. *ACS Cent. Sci.*, 5(1):85–96, 2019.

[34] Ross J. Ellis, Yannick Meridiano, Renato Chiarizia, Laurence Berthon, Julie Muller, Laurent Couston, and Mark R. Antonio. Periodic behavior of lanthanide coordination within reverse micelles. *Chemistry - A European Journal*, 19(8):2663–2675, 2013.

[35] Derek M. Brigham, Alexander S. Ivanov, Bruce A. Moyer, Laetitia H. Delmau, Vyacheslav S. Bryantsev, and Ross J. Ellis. Trefoil-shaped outer-sphere ion clusters mediate lanthanide(iii) ion transport with diglycolamide ligands. *Journal of the American Chemical Society*, 139(48):17350–17358, 2017. PMID: 29083173.

[36] Brian J Gullekson, Andrew T Breshears, M Alex Brown, Jeremy B Essner, Gary A Baker, Justin R Walensky, Alena Paulenova, and Artem V Gelis. Extraction of Water and Speciation of Trivalent Lanthanides and Americium in Organophosphorus Extractants. *Inorganic Chemistry*, 55:12675–12685, 2016.

[37] Julie M. Muller, Claude Berthon, Laurent Couston, Dominique Guillaumont, Ross J. Ellis, Nicole Zorz, Jean Pierre Simonin, and Laurence Berthon. Understanding the synergistic effect on lanthanides(III) solvent extraction by systems combining a malonamide and a dialkyl phosphoric acid. *Hydrometallurgy*, 169:542–551, 2017.

[38] Riccardo Spezia, Valentina Migliorati, and Paola D'Angelo. On the development of polarizable and Lennard-Jones force fields to study hydration structure and dynamics of actinide(III) ions based on effective ionic radii. *J. Chem. Phys.*, 147(16), 2017.

[39] Elsa Galbis, Jorge Hernández-Cobos, Christophe Den Auwer, Ciaire Le Naour, Dominique Guillaumont, Eric Simoni, Rafael R. Pappalardo, and Enrique Sánchez Marcos. Solving the hydration structure of the heaviest actinide aqua ion known: the californium(III) case. *Angew. Chemie - Int. Ed.*, 49(22):3811–3815, 2010.

[40] Cécile Marie, Manuel Miguirditchian, Dominique Guillaumont, Arnaud Tosseng, Claude Berthon, Philippe Guilbaud, Magali Duvail, Julia Bisson, Denis Guillaneux, Muriel Pipelier, and Didier Dubreuil. Complexation of lanthanides(III), americium(III), and uranium(VI) with bitopic N,O ligands: An experimental and theoretical study. *Inorg. Chem.*, 50(14):6557–6566, 2011.

[41] Xudong Wang, Zhaodong Li, Jian Shi, and Yanhao Yu. One-dimensional titanium dioxide nanomaterials: Nanowires, nanorods, and nanobelts. *Chem. Rev.*, 114(19):9346–9384, 2014.

[42] Philippe Guilbaud and Thomas Zemb. Solute-induced microstructural transition from weak aggregates towards a curved film of surface-active extractants. *ChemPhysChem*, 13(3):687–691, 2012.

[43] Ross J. Ellis, Yannick Meridiano, Julie Muller, Laurence Berthon, Philippe Guilbaud, Nicole Zorz, Mark R. Antonio, Thomas Demars, and Thomas Zemb. Complexation-induced supramolecular assembly drives metal-ion extraction. *Chemistry - A European Journal*, 20(40):12796–12807, 2014.

[44] Baofu Qiao, John V. Muntean, Monica Olvera de la Cruz, and Ross J. Ellis. Ion transport mechanisms in liquid-liquid interface. *Langmuir*, 33(24):6135–6142, 2017.

[45] Baofu Qiao, Geoffroy Ferru, Monica Olvera De La Cruz, and Ross J. Ellis. Molecular origins of mesoscale ordering in a metalloamphiphile phase. *ACS Central Science*, 1(9):493–503, 2015.

[46] Baofu Qiao, Thomas Demars, Monica Olvera De La Cruz, and Ross J. Ellis. How hydrogen bonds affect the growth of reverse micelles around coordinating metal ions. *Journal of Physical Chemistry Letters*, 5(8):1440–1444, 2014.

[47] Magali Duvail, Steven van Damme, Philippe Guilbaud, Yushu Chen, Thomas Zemb, and Jean-François Dufrêche. The role of curvature effects in liquid–liquid extraction: assessing organic phase mesoscopic properties from MD simulations. *Soft Matter*, 13(33):5518–5526, 2017.

[48] O. Pecheur, S. Dourdain, D. Guillaumont, J. Rey, P. Guilbaud, L. Berthon, M. C. Charbonnel, S. Pellet-Rostaing, and F. Testard. Synergism in a HDEHP/TOPO Liquid-Liquid Extraction System: An Intrinsic Ligands Property? *Journal of Physical Chemistry B*, 120(10):2814–2823, 2016.

[49] Geoffroy Ferru, Donatien Gomes Rodrigues, Laurence Berthon, Olivier Diat, Pierre Bauduin, and Philippe Guilbaud. Elucidation of the structure of organic solutions in solvent extraction by combining molecular dynamics and X-ray scattering. *Angewandte Chemie - International Edition*, 53(21):5346–5350, 2014.

[50] C Tanford. *The Hydrophobic Effect: Formation of Micelles and Biological Membranes*. Garland Science, 2 edition, 1980.

[51] D. John Mitchell and Barry W. Ninham. Micelles, vesicles and microemulsions. *Journal of the Chemical Society, Faraday Transactions*, 77(4):601, 1981.

[52] R. Nagarajan. Molecular packing parameter and surfactant self-assembly: The neglected role of the surfactant tail. *Langmuir*, 18(1):31–38, 2002.

[53] Christophe Déjugnat, Sandrine Dourdain, Véronique Dubois, Laurence Berthon, Stéphane Pellet-Rostaing, Jean-François Dufrêche, and Thomas Zemb. Reverse aggregate nucleation induced by acids in liquid-liquid extraction processes. *Physical Chemistry Chemical Physics*, 16:7339, 2014.

[54] J. Rey, S. Dourdain, J. F. Dufrêche, L. Berthon, J. M. Muller, S. Pellet-Rostaing, and T. Zemb. Thermodynamic Description of Synergy in Solvent Extraction: I. Enthalpy of Mixing at the Origin of Synergistic Aggregation. *Langmuir*, 32(49):13095–13105, 2016.

[55] Thomas Zemb and Olivier Diat. How Do Anions A ff ect Self-Assembly and Solubility of Cetylpyridinium Surfactants in Water. 2013.

[56] Maximilian Pleines. *Viscosity-control and prediction of microemulsions. Thése de l'Université de Montpellier*. PhD thesis, 2018.

[57] Fabienne Testard, Laurence Berthon, and Thomas Zemb. Liquid-liquid extraction: An adsorption isotherm at divided interface? *Comptes Rendus Chimie*, 10(10-11):1034–1041, 2007.

[58] Sandrine Dourdain, Christophe Déjugnat, Laurence Berthon, Véronique Dubois, Stéphane Pellet-Rostaing, Jean-François Dufrêche, and Thomas Zemb. Liquid-Liquid Extraction of Acids by a Malonamide: II-Anion Specific Effects in the Aggregate-Enhanced Extraction Isotherms. *Solvent Extraction and Ion Exchange*, 32(6):620–636, 2014.

[59] Thomas Zemb, Magali Duvail, and Jean-François Dufrêche. Reverse Aggregates as Adaptive Self-Assembled Systems for Selective Liquid-Liquid Cation Extraction. *Israel Journal of Chemistry*, 53:108–112, 2013.

[60] G. Cote. Hydrometallurgy of strategic metals. *Solvent Extr. Ion Exch.*, 18(4):703–727, 2000.

[61] A. A. Leopold, M. T. Coll, A. Fortuny, N. S. Rathore, and A. M. Sastre. Mathematical modeling of cadmium(II) solvent extraction from neutral and acidic chloride media using Cyanex 923 extractant as a metal carrier. *J. Hazard. Mater.*, 182(1-3):903–911, 2010.

[62] P. Moeyaert, M. Miguirditchian, M. Masson, B. Dinh, X. Hérès, S. De Sio, and C. Sorel. Experimental and modelling study of ruthenium extraction with tri-n-butylphosphate in the purex process. *Chem. Eng. Sci.*, 158(October 2016):580–586, 2017.

[63] Shaohua Yin, Wenyuan Wu, Xue Bian, Yao Luo, and Fengyun Zhang. Solvent extraction of La(III) from chloride medium in the presence of two water soluble complexing agents with di-(2-ethylhexyl) phosphoric acid. *Ind. Eng. Chem. Res.*, 52(25):8558–8564, 2013.

[64] Denis Beltrami, Alexandre Chagnes, Mansour Haddad, Hugo Laureano, Hamid Mokhtari, Bruno Courtaud, Sylvain Jugé, and Gérard Cote. Solvent extraction studies of uranium(VI) from phosphoric acid: Role of synergistic reagents in mixture with bis(2-ethylhexyl) phosphoric acid. *Hydrometallurgy*, 144-145:207–214, 2014.

[65] Adrien Dartiguelongue, Alexandre Chagnes, Elise Provost, Walter Fürst, and Gérard Cote. Modelling of uranium(VI) extraction by D2EHPA/TOPO from phosphoric acid within a wide range of concentrations. *Hydrometallurgy*, 165:57–63, 2016.

[66] Y. Meridiano, L. Berthon, X. Crozes, C. Sorel, P. Dannus, M. R. Antonio, R. Chiarizia, and T. Zemb. Aggregation in organic solutions of malonamides: Consequences for water extraction. *Solvent Extraction and Ion Exchange*, 27(5-6):607–637, 2009.

[67] Epaminondas B. Leodidis and T. Alan Hatton. Amino acids in AOT reversed micelles. 1. Determination of interfacial partition coefficients using the phase-transfer method. *J. Phys. Chem.*, 94(16):6400–6411, 1990.

[68] Epaminondas B. Leodidis and T. Alan Hatton. Amino acids in AOT reversed micelles. 2. The hydrophobic effect and hydrogen bonding as driving forces for interfacial solubilization. *J. Phys. Chem.*, 94(16):6411–6420, 1990.

[69] Epaminondas B. Leodidis, Andreas S. Bommarius, and T. Alan Hatton. Amino acids in reversed micelles. 3. Dependence of the interfacial partition coefficient on excess phase salinity and interfacial curvature. *J. Phys. Chem.*, 95(15):5943–5956, 1991.

[70] Epaminondas B. Leodidis and T. Alan Hatton. Amino Acids in Reversed Micelles. 4. Amino Acids as cosfurfactants. *J. Phys. Chem.*, 95(6):5957–5965, 1991.

[71] Jean-François Dufrêche and Thomas Zemb. Effect of long-range interactions on ion equilibria in liquid-liquid extraction. *Chemical Physics Letters*, 622:45–49, 2015.

[72] Michael Bley, Bertrand Siboulet, Anwesa Karmakar, Thomas Zemb, and Jean François Dufrêche. A predictive model of reverse micelles solubilizing water for solvent extraction. 479:106–114, 2016.

[73] Anwesa Karmakar, Magali Duvail, Michael Bley, Thomas Zemb, and Jean-François Dufrêche. Combined supramolecular and mesoscale modelling of liquid–liquid extraction of rare earth salts. *Colloids and Surfaces A: Physicochemical and Engineering Aspects*, 555:713 – 727, 2018.

[74] Y G Berube and P L De Bruyn. Adsorption at the rutile-solution interface. *J. Colloid Interface Sci.*, 28(1):92–105, 1968.

[75] T Hiemstra, W H Van Riemsdijk, and G H Bolt. Multisite proton adsorption modeling at the solid/solution interface of (hydr) oxides: A new approach: I. Model description and evaluation of intrinsic reaction constants. *J. Colloid Interface Sci.*, 133(1):91–104, 1989.

[76] W Van Riemsdijk, G Bolt, L K Koopal, and J Blaakmeer. Electrolyte adsorption on heterogenous surfaces: adsorption models. *J. Colloid Interface Sci.*, 109(1):219–228, 1986.

[77] K. Bourikas, T. Hiemstra, and W. H. Van Riemsdijk. Ion pair formation and primary charging behavior of titanium oxide (anatase and rutile). *Langmuir*, 17(3):749–756, 2001.

[78] Greta R Patzke, Frank Krumeich, and Reinhard Nesper. Oxidic nanotubes and nanorods - Anisotropic modules for a future nanotechnology. *Angew. Chemie - Int. Ed.*, 41(14):2446–2461, 2002.

[79] A. Charlot, F. Cuer, and A. Grandjean. The effect of pore diameter in the arrangement of chelating species grafted onto silica surfaces with application to uranium extraction. *New J. Chem.*, 41(2):503–511, 2017.

[80] Atida Selmani, Mario Špadina, Milivoj Plodinec, Ida Delač Marion, Marc Georg Willinger, Johannes Lützenkirchen, Harry D Gafney, and Engelbert Redel. An Experimental and Theoretical Approach to Understanding the Surface Properties of One-Dimensional TiO2 Nanomaterials. *J. Phys. Chem. C*, 120(7):4150, 2016.

[81] Helena Kaper, Jimmy Nicolle, Julien Cambedouzou, and Agnès Grandjean. Multi-method analysis of functionalized single-walled carbon nanotubes for cesium liquid-solid extraction. *Mater. Chem. Phys.*, 147(1-2):147–154, 2014.

[82] Jie Li, Xiangxue Wang, Guixia Zhao, Changlun Chen, Zhifang Chai, Ahmed Alsaedi, Tasawar Hayat, and Xiangke Wang. Metal–organic framework-based materials: superior adsorbents for the capture of toxic and radioactive metal ions. *Chem. Soc. Rev.*, 47:2322–2356, 2018.

[83] Daniel T. Sun, Li Peng, Washington S. Reeder, Seyed Mohamad Moosavi, Davide Tiana, David K. Britt, Emad Oveisi, and Wendy L. Queen. Rapid, Selective Heavy Metal Removal from Water by a Metal-Organic Framework/Polydopamine Composite. *ACS Cent. Sci.*, 4(3):349–356, 2018.

[84] Christian S. Diercks, Markus J. Kalmutzki, Nicolas J. Diercks, and Omar M. Yaghi. Conceptual Advances from Werner Complexes to Metal-Organic Frameworks. *ACS Cent. Sci.*, 4(11):1457–1464, 2018.

[85] Selvan Demir, Nicholas K. Brune, Jeffrey F. Van Humbeck, Jarad A. Mason, Tatiana V. Plakhova, Shuao Wang, Guoxin Tian, Stefan G. Minasian, Tolek Tyliszczak, Tsuyoshi Yaita, Tohru Kobayashi, Stepan N. Kalmykov, Hideaki Shiwaku, David K. Shuh, and Jeffrey R. Long. Extraction of lanthanide and actinide ions from aqueous mixtures using a carboxylic acid-functionalized porous aromatic framework. *ACS Cent. Sci.*, 2(4):253–265, 2016.

[86] Baiyan Li, Yiming Zhang, Dingxuan Ma, Zhan Shi, and Shengqian Ma. Removal of mercury (II) from aqueous solution. *Nat. Commun.*, 5(May):1–7, 2014.

[87] Aurélie Merceille, Evelyne Weinzaepfel, Yves Barré, and Agnès Grandjean. The sorption behaviour of synthetic sodium nonatitanate and zeolite A for removing radioactive strontium from aqueous wastes. *Sep. Purif. Technol.*, 96:81–88, 2012.

[88] Caroline Michel, Yves Barré, Caroline de Dieuleveult, Agnès Grandjean, and Laurent De Windt. Cs ion exchange by a potassium nickel hexacyanoferrate loaded on a granular support. *Chem. Eng. Sci.*, 137:904–913, 2015.

[89] Arnaud Villard, Bertrand Siboulet, Guillaume Toquer, Aurélie Merceille, Agnès Grandjean, and Jean François Dufrêche. Strontium selectivity in sodium nonatitanate Na4Ti9O20·xH2O. *J. Hazard. Mater.*, 283:432–438, 2015.

[90] Arnaud Villard, Guillaume Toquer, Bertrand Siboulet, Philippe Trens, Agnès Grandjean, and Jean François Dufrêche. Sorption pH dependance of strontium/calcium by sodium nonatitanate. *Chemosphere*, 202:33–39, 2018.

[91] Célia Guévar, Audrey Hertz, Emmanuelle Brackx, Yves Barré, and Agnès Grandjean. Mechanisms of strontium removal by a Ba-titanate material for the wastewater treatment. *J. Environ. Chem. Eng.*, 5(5):4948–4957, 2017.

[92] Caroline Michel, Yves Barré, Laurent De Windt, Caroline De Dieuleveult, Emmanuelle Brackx, and Agnès Grandjean. Ion exchange and structural properties of a new cyanoferrate mesoporous silica material for Cs removal from natural saline waters. *J. Environ. Chem. Eng.*, 5(1), 2017.

[93] Alexander Sachse, Aurélie Merceille, Yves Barré, Agnès Grandjean, François Fajula, and Anne Galarneau. Macroporous LTA-monoliths for in-flow removal of radioactive strontium from aqueous effluents: Application to the case of Fukushima. *Microporous Mesoporous Mater.*, 164:251–258, 2012.

[94] Marie Jardat, Jean-François Dufrêche, Virginie Marry, Benjamin Rotenberg, and Pierre Turq. Salt exclusion in charged porous media: a coarse-graining strategy in the case of montmorillonite clays. *Phys. Chem. Chem. Phys.*, 11:2023–2033, 2009.

[95] Nadine Schwierz, Dominik Horinek, and Roland R. Netz. Anionic and cationic hofmeister effects on hydrophobic and hydrophilic surfaces. *Langmuir*, 29(8):2602–2614, 2013.

[96] Jean-François Dufrêche, T. O. White, and Jean-Pierre Hansen. Charged-stabilized colloidal suspensions: Counterion condensation and phase diagrams. *Mol. Phys.*, 101(11):1741–1759, 2003.

[97] Sarah Hocine, Remco Hartkamp, Bertrand Siboulet, Magali Duvail, Benoit Coasne, Pierre Turq, and Jean François Dufrêche. How Ion Condensation Occurs at a Charged Surface: A Molecular Dynamics Investigation of the Stern Layer for Water-Silica Interfaces. *J. Phys. Chem. C*, 120(2):963–973, 2016.

[98] Filippo De Angelis, Cristiana Di Valentin, Simona Fantacci, Andrea Vittadini, and Annabella Selloni. Theoretical studies on anatase and less common TiO2phases: Bulk, surfaces, and nanomaterials. *Chem. Rev.*, 114(19):9708–9753, 2014.

[99] Remco Hartkamp, Anne Laure Biance, Li Fu, Jean François Dufrêche, Oriane Bonhomme, and Laurent Joly. Measuring surface charge: Why experimental characterization and molecular modeling should be coupled. *Curr. Opin. Colloid Interface Sci.*, 37:101–114, 2018.

[100] Pierre Andre Cazade, Remco Hartkamp, and Benoit Coasne. Structure and dynamics of an electrolyte confined in charged nanopores. *J. Phys. Chem. C*, 118(10):5061–5072, 2014.

[101] Bertrand Siboulet, Sarah Hocine, Remco Hartkamp, and Jean-François Dufrêche. Scrutinizing electro-osmosis and surface conductivity with molecular dynamics. *J. Phys. Chem. C*, 121(12):6756–6769, 2017.

[102] Christian D. Lorenz and Alex Travesset. Charge inversion of divalent ionic solutions in silica channels. *Phys. Rev. E - Stat. Nonlinear, Soft Matter Phys.*, 75(6):2–6, 2007.

[103] Klemen Bohinc, Jurij Res, Jean-François Dufrêche, and Leo Lue. Recycling of Uranyl from Contaminated Water. 2013.

[104] Klemen Bohinc, Jurij Reščič, and Sylvio May. Electrostatic adsorption and orientational order of inhomogeneously charged particles on flat surfaces. *J. Mol. Liq.*, 228:201–207, 2017.

[105] Bo Jönsson, C. Labbez, and B. Cabane. Interaction of nanometric clay platelets. *Langmuir*, 24(20):11406–11413, 2008.

[106] Bo Jönsson, A. Nonat, C. Labbez, B. Cabane, and H. Wennerström. Controlling the cohesion of cement paste. *Langmuir*, 21(20):9211–9221, 2005.

[107] Jonathan W Lee, Robert H Nilson, Jeremy A Templeton, Stewart K Gri, Andy Kung, and Bryan M Wong. Comparison of Molecular Dynamics with Classical Density Functional and Poisson−Boltzmann Theories of the Electric Double Layer in Nanochannels. *J. Chem. Theory Comput.*, 8:2012–2022, 2012.

[108] Robert Evans. The nature of the liquid-vapour interface and other topics in the statistical mechanics of non-uniform, classical fluids. *Adv. Phys.*, 28(2):143–200, apr 1979.

[109] A. Gonzalez, J. White, F. Roman, S. Velasco, and R. Evans. Density Functional Theory for Small Systems: Hard Spheres in a Closed Spherical Cavity. *Phys. Rev. Lett.*, 79:2466–2469, 1997.

[110] Yan Xin, Yuan-Xiang Zheng, and Yang-Xin Yu. Density functional theory study on ion adsorption and electroosmotic flow in a membrane with charged cylindrical pores. *Mol. Phys.*, 8976(July 2016):1–9, 2015.

[111] Emmanuel Trizac and J.-P Hansen. Wigner-Seitz model of charged lamellar colloidal dispersions. *Phys. Rev. E*, 56(3):3137, 1997.

[112] Gregor Trefalt, Sven Holger Behrens, and Michal Borkovec. Charge Regulation in the Electrical Double Layer: Ion Adsorption and Surface Interactions. *Langmuir*, 32(2):380–400, 2016.

[113] S H Behrens and M Borkovec. Exact Poisson-Boltzmann solution for the interaction of dissimilar charge-regulating surfaces. *Phys. Rev. E. Stat. Phys. Plasmas. Fluids. Relat. Interdiscip. Topics*, 60(6 Pt B):7040–8, 1999.

[114] Christian Fleck, Roland R Netz, and Hans Hennig von Grünberg. Poisson-Boltzmann theory for membranes with mobile charged lipids and the pH-dependent interaction of a DNA molecule with a membrane. *Biophys. J.*, 82(1 Pt 1):76–92, 2002.

[115] Natasa Adzic and Rudolf Podgornik. Charge regulation in ionic solutions: Thermal fluctuations and Kirkwood-Schumaker interactions. *Phys. Rev. E - Stat. Nonlinear, Soft Matter Phys.*, 91(2), 2015.

[116] Jérôme F L Duval, Jenny Merlin, and Puranam a L Narayana. Electrostatic interactions between diffuse soft multi-layered (bio)particles: beyond Debye-Hückel approximation and Deryagin formulation. *Phys. Chem. Chem. Phys.*, 13(3):1037–1053, 2011.

[117] Aleš Iglič, Ekaterina Gongadze, and Klemen Bohinc. Excluded volume effect and orientational ordering near charged surface in solution of ions and Langevin dipoles. *Bioelectrochemistry*, 79(2):223–227, 2010.

[118] Dan Ben-Yaakov, David Andelman, Rudi Podgornik, and Daniel Harries. Ion-specific hydration effects: Extending the Poisson-Boltzmann theory, 2011.

[119] Jean-Pierre Hansen and Hartmut Löwen. Effective interaction between electric double-layers. *Annu. Rev. Phys. Chem.*, 51(1):209–242, 2000.

[120] Beibei Huang, Stefano Maset, and Klemen Bohinc. Interaction between Charged Cylinders in Electrolyte Solution; Excluded Volume Effect. *J. Phys. Chem. B*, 121(38):9013–9023, 2017.

[121] Herbert B. Callen. *Thermodynamics and an Introduction to Thermostatistics, 2nd Edition*. Wiley, 1985.

[122] Jean-Louis Barrat and Hansen. Jean-Pierre. *Thermodynamics and an Introduction to Thermostatistics, 2nd Edition*. Cambridge University Press, 2003.

[123] K A Dill and S Bromberg. *Molecular Driving Forces: Statistical Thermodynamics in Biology, Chemistry, Physics, and Nanoscience*. Garland Science, 2 edition, 2011.

[124] S. Krimm. The hydrophobic effect: Formation of micelles and biological membranes, Charles Tanford, Wiley-Interscience, New York, 1980, 233 pp. price: $18.50. *Journal of Polymer Science: Polymer Letters Edition*, 18(10):687–687, oct 1980.

[125] Jacob N. Israelachvili, D. John Mitchell, and Barry W. Ninham. Theory of self-assembly of hydrocarbon amphiphiles into micelles and bilayers. *Journal of the Chemical Society, Faraday Transactions 2*, 72:1525, 1976.

[126] S. T. Hyde, I. S. Barnes, and B. W. Ninham. Curvature Energy of Surfactant Interfaces Confined to the Plaquettes of a Cubic Lattice. *Langmuir*, 6(6):1055–1062, 1990.

[127] Krisztián Kordás, Melinda Mohl, Zoltán Kónya, and Ákos Kukovecz. Layered titanate nanostructures: perspectives for industrial exploitation. *Transl. Mater. Res.*, 2(1):15003, 2015.

[128] Wen Liu, Weiling Sun, Yunfei Han, Muhammad Ahmad, and Jinren Ni. Adsorption of Cu(II) and Cd(II) on titanate nanomaterials synthesized via hydrothermal method under different NaOH concentrations: Role of sodium content. *Colloids Surfaces A Physicochem. Eng. Asp.*, 452(1):138–147, 2014.

[129] Inderpreet Singh Grover, Satnam Singh, and Bonamali Pal. The preparation, surface structure, zeta potential, surface charge density and photocatalytic activity of TiO2 nanostructures of different shapes. *Appl. Surf. Sci.*, 280:366–372, 2013.

[130] Poulomi Roy, Steffen Berger, and Patrik Schmuki. TiO2 nanotubes: Synthesis and applications. *Angew. Chemie - Int. Ed.*, 50(13):2904–2939, 2011.

[131] Henrique Antonio Mendonça Faria and Alvaro Antonio Alencar de Queiroz. A novel drug delivery of 5-fluorouracil device based on TiO2/ZnS nanotubes. *Mater. Sci. & Eng. C, Mater. Biol. Appl.*, 56:260–268, 2015.

[132] Wei-Wan Yang, Ying Wang, Bin Huang, Ning-Xin Wang, Zhong-Bo Wei, Jun Luo, Ai-Jun Miao, and Liu-Yan Yang. TiO2 Nanoparticles Act As a Carrier of Cd Bioaccumulation in the Ciliate Tetrahymena thermophila. *Environ. Sci. Technol.*, 48(13):7568–7575, 2014.

[133] Kiyoung Lee, Anca Mazare, and Patrik Schmuki. One-Dimensional Titanium Dioxide Nanomaterials : Nanotubes. 2014.

[134] Tomoko Kasuga, Masayoshi Hiramatsu, Akihiko Hoson, and Toru Sekino. Formation of Titanium Oxide Nanotube. *Langmuir*, 7463(5):3160–3163, 1998.

[135] Kyriakos Bourikas, John Vakros, Christos Kordulis, and Alexis Lycourghiotis. Potentiometric Mass Titrations: Experimental and Theoretical Establishment of a New Technique for Determining the Point of Zero Charge (PZC) of Metal (Hydr) Oxides. *J. Phys. Chem. B*, 107:9441–9451, 2003.

[136] Robert J Hunter. No Title. In *Zeta Potential Colloid Sci.* Academic Press, 1 edition, 1981.

[137] Luc Belloni. Ionic condensation and charge renormalization in colloidal suspensions. *Colloids Surfaces A Physicochem. Eng. Asp.*, 140(1-3):227–243, 1998.

[138] Lene Haugaard Mikkelsen. Applications and limitations of the colloid titration method for measuring activated sludge surface charges. *Water Res.*, 37(10):2458–2466, 2003.

[139] Sang K Kam and John Gregory. Charge determination of synthetic cationic polyelectrolytes by colloid titration. *Colloids Surfaces A Physicochem. Eng. Asp.*, 159(1):165–179, 1999.

[140] A. Elisabet Horvath, Tom Lindström, and Janne Laine. On the indirect polyelectrolyte titration of cellulosic fibers. Conditions for charge stoichiometry and comparison with ESCA. *Langmuir*, 22(2):824–830, 2006.

[141] Klemen Bohinc, Jan Gimsa, Veronika Kralj-Iglič, Tomaž Slivnik, and Aleš Iglič. Excluded volume driven counterion condensation inside nanotubes in a concave electrical double layer model. *Bioelectrochemistry*, 67(1):91–99, 2005.

[142] Grégoire Allaire, Jean-François Dufrêche, Andro Mikelić, and Andrey Piatnitski. Asymptotic analysis of the Poisson - Boltzmann equation describing electrokinetics in porous media. *Nonlinearity*, 26(3):881–910, 2013.

[143] Barry W Ninham and V Adrian Parsegian. Electrostatic potential between surfaces bearing ionizable groups in ionic equilibrium with physiologic saline solution. *J. Theor. Biol.*, 31(3):405–428, 1971.

[144] Linus Pauling. the Principles Determining the Structure of Complex Ionic Crystals. *J. Am. Chem. Soc.*, 51(4):1010–1026, 1929.

[145] T Hiemstra and W H Van Riemsdijk. A Surface Structural Approach to Ion Adsorption: The Charge Distribution (CD) Model. *J. Colloid Interface Sci.*, 508(179):488–508, 1996.

[146] George D Panagiotou, Theano Petsi, Kyriakos Bourikas, Christos S Garoufalis, Athanassios Tsevis, Nikos Spanos, Christos Kordulis, and Alexis Lycourghiotis. Mapping the surface (hydr)oxo-groups of titanium oxide and its interface with an aqueous solution: The state of the art and a new approach. *Adv. Colloid Interface Sci.*, 142(1-2):20–42, 2008.

[147] K. Bourikas, T. Hiemstra, and W. H. Van Riemsdijk. Ion pair formation and primary charging behavior of titanium oxide (anatase and rutile). *Langmuir*, 17(3):749–756, 2001.

[148] T Gisler, H Sticher, P Schurtenberger, Bruno D'Aguanno, and Rudolf Klein. Understanding colloidal charge renormalization from surface chemistry: Experiment and theory. *J. Chem. Phys.*, 101(11):9924, 1994.

[149] Dimitri A. Sverjensky. Standard states for the activities of mineral surface sites and species. *Geochim. Cosmochim. Acta*, 67(1):17–28, jan 2003.

[150] Nikola Kallay, Tajana Preocanin, Davor Kovacevic, Johannes Lutzenkirchen, and Emil Chibowski. Electrostatic Potentials at Solid/Liquid Interfaces. *Croat. Chem. Acta*, 83(3):357–370, 2010.

[151] David A. Smith and William F. Ford. Numerical Comparisons of Nonlinear Convergence Accelerators. *Math. Comput.*, 38(158, April):481–499, 2007.

[152] Markus Deserno, Christian Holm, and Sylvio May. Fraction of condensed counterions around a charged rod: Comparison of Poisson-Boltzmann theory and computer simulations. *Macromolecules*, 33(1):199–206, 2000.

[153] Robert Pelton, Bernard Cabane, Yuguo Cui, and Howard Ketelson. Shapes of polyelectrolyte titration curves. 1. Well-behaved strong polyelectrolytes. *Anal. Chem.*, 79(21):8114–8117, 2007.

[154] K Böckenhoff and W R Fischer. Determination of electrokinetic charge with a particle-charge detector, and its relationship to the total charge. *Fresenius. J. Anal. Chem.*, 371(5):670–674, 2001.

[155] David A Dzombak and François M M Morel. *Surface Complexation Modeling: Hydrous Ferric Oxide*. John Wiley & Sons Ltd, New York, 1990.

[156] John J Molina, Jean-Francois Dufrêche, Mathieu Salanne, Olivier Bernard, and Pierre Turq. Primitive models of ions in solution from molecular descriptions: A perturbation approach. *J. Chem. Phys.*, 135(23):234509, 2011.

[157] John Jairo Molina, Jean-Francois Dufrêche, Mathieu Salanne, Olivier Bernard, Marie Jardat, and Pierre Turq. Models of electrolyte solutions from molecular descriptions: The example of NaCl solutions. *Phys. Rev. E*, 80(6):65103, dec 2009.

[158] Rui Wang and Zhen-Gang Wang. On the theoretical description of weakly charged surfaces. *J. Chem. Phys.*, 142(10):104705, 2015.

[159] Nadine Schwierz and Roland R. Netz. Effective interaction between two ion-adsorbing plates: Hofmeister series and salting-in/salting-out phase diagrams from a global mean-field analysis. *Langmuir*, 28(8):3881–3886, 2012.

[160] Dmitry V Bavykin and Frank C Walsh. Kinetics of Alkali Metal Ion Exchange into Nanotubular and Nanofibrous Titanates. *J. Phys. Chem. C*, 25:14644–14651, 2007.

[161] Thiago Colla, Matheus Girotto, Alexandre P. Dos Santos, and Yan Levin. Charge neutrality breakdown in confined aqueous electrolytes: Theory and simulation. *J. Chem. Phys.*, 145(9):94704, 2016.

[162] Jenny Perez Holmberg, Elisabet Ahlberg, Johan Bergenholtz, Martin Hassellöv, and Zareen Abbas. Surface charge and interfacial potential of titanium dioxide nanoparticles: Experimental and theoretical investigations. *J. Colloid Interface Sci.*, 407:168–176, 2013.

[163] Zhu Liang, Wei Bu, Karl J. Schweighofer, David J. Walwark, Jeffrey S. Harvey, Glenn R. Hanlon, Daniel Amoanu, Cem Erol, Ilan Benjamin, and Mark L. Schlossman. Nanoscale view of assisted ion transport across the liquid–liquid interface. *Proceedings of the National Academy of Sciences*, 2018.

[164] Jennifer K. Hensel, Andrew P. Carpenter, Regina K. Ciszewski, Brandon K. Schabes, Clive T. Kittredge, Fred G. Moore, and Geraldine L. Richmond. Molecular characterization of water and surfactant aot at nanoemulsion surfaces. *Proceedings of the National Academy of Sciences*, 114(51):13351–13356, 2017.

[165] Wenrou Su, Ji Chen, and Yu Jing. Aqueous Partition Mechanism of Organophosphorus Extractants in Rare Earths Extraction. *Ind. Eng. Chem. Res.*, 55(30):8424–8431, 2016.

[166] Krystyna Prochaska. Interfacial activity of metal ion extractant. *Advances in colloid and interface science*, 95(1):51—72, January 2002.

[167] Julie M. Muller, Claude Berthon, Laurent Couston, Nicole Zorz, Jean Pierre Simonin, and Laurence Berthon. Extraction of Lanthanides(III) by a Mixture of a Malonamide and a Dialkyl Phosphoric Acid. *Solvent Extraction and Ion Exchange*, 34(2):141–160, 2016.

[168] Jean-Pierre Hansen, , and Ian R. McDonald. *Theory of Simple Liquids*. Academic Press, Burlington, 3 edition, 2006.

[169] Shaghayegh Vafaei, Bruno Tomberli, and C. G. Gray. McMillan-Mayer theory of solutions revisited: Simplifications and extensions. *Journal of Chemical Physics*, 141(15), 2014.

[170] Beate Moeser and Dominik Horinek. Biophysical Chemistry The role of the concentration scale in the de fi nition of transfer free energies. *Biophysical Chemistry*, 196:68–76, 2015.

[171] Mario Špadina, Klemen Bohinc, Thomas Zemb, and Jean-François Dufrêche. Multicomponent Model for the Prediction of Nuclear Waste/Rare-Earth Extraction Processes. *Langmuir*, 34(35):10434–10447, 2018.

[172] Daniel M. Packwood, Patrick Han, and Taro Hitosugi. Chemical and entropic control on the molecular self-assembly process. *Nat. Commun.*, 8:1–8, 2017.

[173] S Hyde, Z Blum, T Landh, S Lidin, BW Ninham, S Andersson, and K Larsson. *The Language of Shape*. Garland Science, 1 edition, 1996.

[174] S. Krimm. The hydrophobic effect: Formation of micelles and biological membranes, charles tanford, wiley-interscience, new york, 1980. *Journal of Polymer Science: Polymer Letters Edition*, 18(10):687–687, 1980.

[175] T. N. Zemb. The DOC model of microemulsions: Microstructure, scattering, conductivity and phase limits imposed by sterical constraints. *Colloids and Surfaces A: Physicochemical and Engineering Aspects*, 129-130:435–454, 1997.

[176] Michael Bley, Bertrand Siboulet, Anwesa Karmakar, Thomas Zemb, and Jean-François Dufrêche. A predictive model of reverse micelles solubilizing water for solvent extraction. *Journal of Colloid and Interface Science*, 479:106–114, 2016.

[177] Anwesa Karmakar, Magali Duvail, Michael Bley, Thomas Zemb, and Jean-François Dufrêche. Combined supramolecular and mesoscale modelling of liquid-liquid extraction of rare earth salts. *In preparation.*

[178] Yizhak Marcus. *Ions in Solution and their Solvation*. John Wiley & Sons Inc, New York, 2015.

[179] William H. Press, Saul A. Teukolsky, William T. Vetterling, and Brian P. Flannery. *Numerical Recipes in Fortran77: The Art of Scientific Computing*. Cambridge University Press, New York, USA, 2 edition, 1992.

[180] Yizhak Marcus. Electrostriction in electrolyte solutions. *Chem. Rev.*, 111(4):2761–2783, 2011.

[181] Jan Lipfert, Linda Columbus, Vincent B. Chu, Scott A. Lesley, and Sebastian Doniach. Size and shape of detergent micelles determined by small-angle X-ray scattering. *Journal of Physical Chemistry B*, 111(43):12427–12438, 2007.

[182] L. Berthon, L. Martinet, F. Testard, C. Madic, and Th Zemb. Solvent penetration and sterical stabilization of reverse aggregates based on the DIAMEX process extracting molecules: Consequences for the third phase formation. *Solvent Extraction and Ion Exchange*, 25(5):545–576, 2007.

[183] Florence Ricoul, Monique Dubois, Luc Belloni, Thomas Zemb, and Christiane Andre. Phase Equilibria and Equation of State of a Mixed Cationic Surfactant-Glycolipid Lamellar System. 7463(97):2645–2655, 1998.

[184] J. Meridiano. *Organisation des molécules extractantes de type diamide : lien avec les propriétés extractantes? Thése de l'Université Paris XI.* Rapport CEA-R-6228, 2009.

[185] L. Bosland. *Etude thermodynamique et cinétique de l'extraction des nitrates de lanthanides par un malonamide (N,N diméthyl-N,N dioctylhexylethoxy malonamide ou DMDOHEMA). Thése de l'Ecole Centrale Paris.* Rapport CEA-R-6099, 2006.

[186] J. Muller. *Spéciation dans les phases organiques des systémes d'extraction liquide-liquide contenant un malonamide et un acide alkylphosphorique , Thése de l'Université Pierre et Marie Curie.* Rapport CEA-R-6159, 2012.

[187] J. Rey, M. Bley, J. F. Dufrêche, S. Gourdin, S. Pellet-Rostaing, T. Zemb, and S. Dourdain. Thermodynamic Description of Synergy in Solvent Extraction: II Thermodynamic Balance of Driving Forces Implied in Synergistic Extraction. *Langmuir*, 33(46):13168–13179, 2017.

[188] Christophe Déjugnat, Laurence Berthon, Véronique Dubois, Yannick Meridiano, Sandrine Dourdain, Dominique Guillaumont, Stéphane Pellet-Rostaing, and Thomas Zemb. Liquid-Liquid Extraction of Acids and Water by a Malonamide: I-Anion Specific Effects on the Polar Core Microstructure of the Aggregated Malonamide. *Solvent Extraction and Ion Exchange*, 32(6):601–619, 2014.

[189] C. Cuillerdier, C. Musikas, P. Hoel, L. Nigond, and X. Vitart. Malonamides as New Extractants for Nuclear Waste Solutions. *Separation Science and Technology*, 26(9):1229–1244, 1991.

[190] F. Testard, P. Bauduin, L. Martinet, B. Abécassis, L. Berthon, C. Madic, and Th Zemb. Self-assembling properties of malonamide extractants used in separation processes. *Radiochimica Acta*, 96(4-5):265–272, 2008.

[191] J Ennis. Spontaneous Curvature of Surfactant Films. *Journal of Chemical Physics*, 97(1):663–678, 1992.

[192] Anwesa Karmakar, Magali Duvail, Michael Bley, and Thomas Zemb. Supporting Information Combined supramolecular and mesoscale modelling of liquid-liquid extraction of rare earth salts. pages 1–8.

[193] Mario Špadina, Klemen Bohinc, Thomas N Zemb, and Jean-Francois Dufrêche. A colloidal model of prediction of the extraction of rare earths assisted by the acidic extractant. *Langmuir*, 35:3215–3230, 2019.

[194] N. Condamines and C. Musikas. *The extraction by n, n-dialk ylamides. II. extraction of actinide cations*, volume 10. 1992.

[195] Q. Tian and M. A. Hughes. The mechanism of extraction of HNO3 and neodymium with diamides. *Hydrometallurgy*, 36(3):315–330, 1994.

[196] Petra J. Panak and Andreas Geist. Complexation and extraction of trivalent actinides and lanthanides by triazinylpyridine N-donor ligands. *Chemical Reviews*, 113(2):1199–1236, 2013.

[197] Peter Kaufholz, Giuseppe Modolo, Andreas Wilden, Fabian Sadowski, Christoph Wagner, Andreas Geist, Petra J Panak, Frank W Lewis, Laurence M Harwood, Peter Kaufholz, Giuseppe Modolo, Andreas Wilden, Fabian Sadowski, Dirk Bosbach, Christoph Wagner, Andreas Geist, Petra J Panak, and Frank W Lewis. Solvent Extraction and Fluorescence Spectroscopic Investigation of the Selective Am(III) Complexation with TS-BTPhen. *Solvent Extraction and Ion Exchange*, 34(2):126–140, 2016.

[198] Youcai Lu and Wuping Liao. Extraction and separation of trivalent rare earth metal ions from nitrate medium by p-phosphonic acid calix[4]arene. *Hydrometallurgy*, 165:300–305, 2016.

[199] C. Erlinger, L. Belloni, Th Zemb, and C. Madic. Attractive interactions between reverse aggregates and phase separation in concentrated malonamide extractant solutions. *Langmuir*, 15(7):2290–2300, 1999.

[200] Frank J. Millero, Fen Huang, Antonio Lo Surdo, and Faina Vinokurova. Partial molal volumes and compressibilities of phosphoric acid and sodium phosphates in 0.725 molal NaCl at 25°C. *J. Phys. Chem. B*, 114(49):16099–16104, 2010.

[201] Zdenek Kolarik. Critical evaluation of some equilibrium constants involving acidic organophosphorus extractants. *Pure Appl. Chem.*, 54(12):2593–2674, 1982.

[202] K. Rama Swami, R. Kumaresan, P. K. Nayak, K. A. Venkatesan, and M. P. Antony. Effect of pKaon the extraction behavior of Am(III) in organo phosphorus acid and diglycolamide solvent system. *Radiochim. Acta*, 106(2):107–118, 2018.

[203] Wang Tao and Yukio Nagaosa. Evaluation of some prediction models for the determination of physicochemical constants of dialkylphosphoric acids. *Sep. Sci. Technol.*, 38(7):1621–1631, 2003.

[204] Pulak Dutta, Sangjun Yoo, Monica Olvera de la Cruz, Yihao Liang, Miaoqi Chu, Wei Bu, Mitchell Miller, and Honghao Li. Electrostatic Origin of Element Selectivity during Rare Earth Adsorption. *Phys. Rev. Lett.*, 122(5):58001, 2019.

[205] Z. Kolarik. Review: Dissociation, self-association, and partition of monoacidic organophosphorus extractants. *Solvent Extraction and Ion Exchange*, 28(6):707–763, 2010.

[206] Yu Jing, Ji Chen, Li Chen, Wenrou Su, Yu Liu, and Deqian Li. Extraction Behaviors of Heavy Rare Earths with Organophosphoric Extractants: The Contribution of Extractant Dimer Dissociation, Acid Ionization, and Complexation. A Quantum Chemistry Study. *J. Phys. Chem. A*, 121(12):2531–2543, mar 2017.

[207] R. K. Biswas, M. A. Habib, and M. N. Islam. Some Physicochemical Properties of (D2EHPA). 1. Distribution, Dimerization, and Acid Dissociation Constants of D2EHPA in a Kerosene/0.10 kmol m^{-3} $(Na^+,H^+)Cl^-$ System and the Extraction of Mn(II). *Ind. Eng. Chem. Res.*, 39(1):155–160, 2000.

[208] Werner Kunz, Fabienne Testard, and Thomas Zemb. Correspondence between curvature, packing parameter, and hydrophilic-lipophilic deviation scales around the phase-inversion temperature. *Langmuir*, 25(1):112–115, 2009.

[209] Diptendu Das, V. A. Juvekar, V. H. Rupawate, K. Ramprasad, and R. Bhattacharya. Effect of the nature of organophosphorous acid moiety on co-extraction of U(VI) and

mineral acid from aqueous solutions using D2EHPA, PC88A and Cyanex 272. *Hydrometallurgy*, 152:129–138, 2015.

[210] Ronald D. Neuman, Nai-Fu Zhou, Jinguang Wu, Matthew A. Jones, Anilkumar G. Gaonkar, S. J. Park, and M. L. Agrawal. General model for aggregation of metal-extractant complexes in acidic organophosphorus solvent extraction systems. *Separation Science and Technology*, 25(13-15):1655–1674, 1990.

[211] Benoît Gannaz, Mark R. Antonio, Renato Chiarizia, Clément Hill, and Gérard Cote. Structural study of trivalent lanthanide and actinide complexes formed upon solvent extraction. *Dalt. Trans.*, (38):4553–4562, 2006.

[212] Wei Bu, Hao Yu, Guangming Luo, Mrinal K. Bera, Binyang Hou, Adam W. Schuman, Binhua Lin, Mati Meron, Ivan Kuzmenko, Mark R. Antonio, L. Soderholm, and Mark L. Schlossman. Observation of a rare earth ion-extractant complex arrested at the oil-water interface during solvent extraction. *J. Phys. Chem. B*, 118(36):10662–10674, 2014.

[213] D. Darvishi, D. F. Haghshenas, S. Etemadi, E. Keshavarz Alamdari, and S. K. Sadrnezhaad. Water adsorption in the organic phase for the D2EHPA-kerosene/water and aqueous Zn^{2+}, Co^{2+}, Ni^{2+} sulphate systems. *Hydrometallurgy*, 88(1-4):92–97, 2007.

[214] Totaro Goto. Separation factor for the extraction systems, YCl_3-$ErCl_3$-HCl , YCl_3 - $HoCl_3$-HCl and some lanthanide chlorides-hydrochloric acid with phosphoric acid in n-heptane. *Journal of Inorganic and Nuclear chemistry*, 30(1967):3305–3315, 1968.

[215] Taichi Sato. Liquid-Liquid Extraction of Rare-Earth Elements from Aqueous Acid Solutions by Acid Organophosphorus Compounds. *Hydrometallurgy*, 22:121–140, 1989.

[216] Yuji Sasaki, Yumi Sugo, Keisuke Morita, and Kenneth L. Nash. The Effect of Alkyl Substituents on Actinide and Lanthanide Extraction by Diglycolamide Compounds. *Solvent Extraction and Ion Exchange*, 33(7):625–641, 2015.

[217] Tobias Lopian. *Characterization of metal-extracting water-poor microemulsions, Thése de l'Université de Montpellier.* PhD thesis, 2017.

[218] Ross J. Ellis. Acid-switched Eu(III) coordination inside reverse aggregates: Insights into a synergistic liquid-liquid extraction system. *Inorganica Chim. Acta*, 460:159–164, 2017.

[219] Julie M. Muller, Claude Berthon, Laurent Couston, Nicole Zorz, Jean Pierre Simonin, and Laurence Berthon. Extraction of Lanthanides(III) by a Mixture of a Malonamide and a Dialkyl Phosphoric Acid. *Solvent Extraction and Ion Exchange*, 34(2):141–160, 2016.

[220] Remi Poirot, Le Goff, Olivier Diat, Damien Bourgeois, and Daniel Meyer. Metal Recognition Driven by Weak Interactions : A Case Study in Solvent Extraction. *ChemPhysChem*, 17:1–7, 2016.

[221] Haim Diamant and David Andelman. Free energy approach to micellization and aggregation: Equilibrium, metastability, and kinetics. *Curr. Opin. Colloid Interface Sci.*, 22:94–98, 2016.

[222] B. Abrécassis, F. Testard, Th Zemb, L. Berthon, and C. Madic. Effect of n-octanol on the structure at the supramolecular scale of concentrated dimethyldioctylhexylethoxymalonamide extractant solutions. *Langmuir*, 19(17):6638–6644, 2003.

[223] Songling Han, Siyu Chen, Lanlan Li, Jin Li, Huijie An, Hui Tao, Yi Jia, Shan Lu, Ruibing Wang, and Jianxiang Zhang. Multiscale and Multifunctional Emulsions by Host-Guest Interaction-Mediated Self-Assembly. *ACS Cent. Sci.*, 4(5):600–605, 2018.

[224] Liel Sapir and Daniel Harries. Is the depletion force entropic? Molecular crowding beyond steric interactions. *Curr. Opin. Colloid Interface Sci.*, 20(1):3–10, 2015.

[225] Liel Sapir and Daniel Harries. Macromolecular compaction by mixed solutions: Bridging versus depletion attraction. *Curr. Opin. Colloid Interface Sci.*, 22:80–87, 2016.

[226] Aurora E. Clark. Amphiphile-Based Complex Fluids: The Self-Assembly Ensemble as Protagonist. *ACS Cent. Sci.*, 5(1):10–12, 2019.

[227] D. Nečas and P. Klapetek. Gwyddion: an Open-Source Software for SPM Data Analysis. *Central European Journal of Physics*, 10:181–188, 2012.

[228] N. Mandzy, E. Grulke, and T. Druffel. Breakage of TiO2 agglomerates in electrostatically stabilized aqueous dispersions. *Powder Technol.*, 160(2):121–126, 2005.